2013

Principles and Biophysical Applications of Single Particle Super-Localization and Rotational Tracking

Yan Gu
Iowa State University

Recommended Citation

Gu, Yan, "Principles and Biophysical Applications of Single Particle Super-Localization and Rotational Tracking" (2013). *Graduate Theses and Dissertations*. 13264.
https://lib.dr.iastate.edu/etd/13264

Principles and biophysical applications of single particle super-localization and rotational tracking

by

Yan Gu

A dissertation submitted to the graduate faculty
In partial fulfillment of the requirements for the degree of
DOCTOR OF PHILOSOPHY

Major: Analytical Chemistry

Program of Study Committee:
Ning Fang, Major Professor
Emily Smith
Robert (Sam) Houk
Edward Yu
Michael McCloskey

Iowa State University

Ames, Iowa

2013

TABLE OF CONTENTS

CHAPTER 2

CHAPTER 3

CHAPTER 4

CHAPTER 5

CHAPTER 6

CHAPTER 7

ACKNOWLEDGMENTS

I have been given many during the past five years. I learned a lot as a graduate student, I had a lot done as a researcher, I grew up a lot as a young scientist, and I made a lot of friends in the small city of Ames. There are many people I would like to acknowledge and say thank you to for all their support and help.

First of all, I want to express my heartfelt thanks to Prof. Ning Fang, my research advisor, for his efforts to teach me and advice me with infinite patience. The work presented in the dissertation is not possible without his advice and support. He has been the one that I can go to whenever I have questions and doubts. He encouraged me when I lost my confidence and belief. He is always easy-going and understanding. He taught me how to think as a scientist, how to go gold-mining with limited tools, how to find the treasures in the data, how to write a paper with good quality, and many aspects that would influence my research, life and future.

I would like to gratefully thank my other Program of Study Committee members, Dr. Emily Smith, Dr. Sam Houk, Dr. Ed Yu and Dr Michael McCloskey. Their help on my research and their critical advice pushed me to think and do things more scientifically. I thank them for their time and effort put on being on my committee for my research and for my thesis.

I would like to thank Prof. Gufeng Wang in North Carolina State University who was a post-doctor in our group and Dr. Wei Sun, a post-doctor in University of Washington who was a senior student in the group when I was new. I learned a lot from them when I was fresh in course works and research in graduate school. They were patient, encouraging, and taught me everything without reservation. Gufeng mentored me with basic knowledge and taught me how to do research. Wei showed me many experimental techniques hand by hand and was always available when I had questions. I want to thank Prof. Yong Luo in Dalian University of Science and Technology for his encouragement and friendship when he was doing his post-doctoral work in the group. I also want to thank Dr. Mary Jo Schmerr, who told me to be strong and independent, and always try to be excellent. Because of her, I have been really proud of being a female chemist. I also want to thank other group members, Anthony Stender, Kyle Marchuk, Rui Han, Ji Won Ha, Ashley Augspurger, Kuangcai Chen, Bin Dong, Amanda Nguy, Tian Tian and Jiaheng Yin, for their kindly help and friendship during the past years.

I have to express my special thanks to my husband, Yi Wang, who has been very supportive and encouraging on my research and career, and made my daily life full of joy. I want to thank my son, Bernard Ming-Han Wang, who has been a good baby giving me strength and wisdom. I thank my in-laws, for their lots of help and encouragement. Finally, I cannot finish without saying thanks to my parents who educated me, supported me and encourage me to pursue my Ph.D., especially my mom who always has confidence in me.

This research is supported by a research assistantship offered by the Department of Chemistry and Ames Laboratory, U.S. Department of Energy.

This dissertation is dedicated to my family and friends who love me and who I love.

ABSTRACT

While conventional Single Particle Tracking (SPT) techniques acquire 2D or 3D trajectories of particle probes, we have developed Single Particle Orientation and Rotational Tracking (SPORT) techniques to extract orientation and rotational information. Combined with DIC microscopy, the SPORT technique has been applied in biophysical studies, including membrane diffusion and intracellular transport.

The rotational dynamics of nanoparticle vectors on live cell membranes was recorded and its influence on the fate of these nanoparticle vectors was elucidated. The rotational motions of gold nanorods with various surface modifiers were tracked continuously at a temporal resolution of 5 ms under a DIC microscope. We found that the rotational behaviors of gold nanorod vectors are strongly related to their surface charge, specific surface functional groups, and the availability of receptors on cell membranes. The study of rotational Brownian motion of nanoparticles on cell membranes will lead to a better understanding of the mechanisms of drug delivery and provide guidance in designing surface modification strategies for drug delivery vectors under various circumstances.

To characterize the rotation mode of surface functionalized gold nanorods on cell membranes, the SPORT technique is combined with the correlation analysis of the bright and dark DIC intensities. The unique capabilities of visualizing and understanding rotational motions of functionalized nanoparticles on live cell membranes allow us to correlate rotational and translational dynamics in unprecedented detail and provide new insights for

complex membrane processes, including electrostatic interactions, ligand-receptor binding, and lateral (confined and hopping) diffusion of membrane receptors. Surface-functionalized nanoparticles interact with the membrane in fundamentally different ways and exhibit distinct rotational modes. The early events of particle-membrane approach and attachment are directly visualized for the first time.

The rotational dynamics of cargos in both active directional transport and pausing stages of axonal transport was also visualized using high-speed SPORT with a temporal resolution of 2 ms. Both long and short pauses are imaged, and the correlations between the pause duration, the rotational behaviour of the cargo at the pause, and the moving direction after the pause are established. Furthermore, the rotational dynamics leading to switching tracks are visualized in detail. These first-time observations of cargo's rotational dynamics provide new insights on how kinesin and dynein motors take the cargo through the alternating stages of active directional transport and pause.

To improve the localization precision of the SPT technique with DIC microscopy, a precise three-dimensional (3D) localization method of spherical gold nanoparticle probes using model-based correlation coefficient mapping was introduced. To accomplish this, a stack of sample images at different z-positions are acquired, and a 3D intensity profile of the probe serving as the model is used to map out the positions of nanoparticles in the sample. By using this model-based correlation imaging method, precise localization can be achieved in imaging techniques with complicated point spread functions (PSF) such as differential interference contrast (DIC) microscopy. The 3D superlocalization method was applied to tracking gold nanospheres during live endocytosis events.

Finally, a novel dual-modality imaging technique has been developed to super-localize a single gold nanorod while providing its orientation and rotational information. The super-localization of the gold nanorod can be accomplished by curve fitting the modified bright-field images generated by one of the two beams laterally shifted by the first Nomarski prism in a DIC microscope. The orientation and rotational information is derived from the DIC images of gold nanorods. The new imaging setup has been applied to study the steric hindrance induced by relatively large cargos in the microtubule gliding assay and to track nanocargos in the crowded cellular environment.

CHAPTER 1 INTRODUCTION

This thesis is composed of eight chapters. Chapter 1 is the general introduction outlining the composition of the thesis. Chapter 2 is a feature article introducing current single particle orientation and rotational tracking techniques and their applications in biophysical studies. Chapter 3 is a paper published in Journal of the Ameircan Chemical Society, demonstrating the application of SPORT technique combining DIC microscopy and gold nanorods in rotational dynamic studies of nanoparticles modified with drug delivery agents on live cell membranes. Chapter 4 is a paper published in Small. It investigates the rotation modes of surface modified gold nanorods on cell membranes. Chapter 5 is a paper published in Nature Communications, reporting the rotataonal behaviors of cargos at the pauses stages during the axonal transport and their relationship with motor protein arrangement. Chapter 6 is a paper published in Analytical Chemistry, demontrating a 3D superlocalization approach for gold nanospheres. Chapter 7 is a paper published in ACS Nano. It describes a dual-mode microscope that is devised for sinultaneous super-localization and rotataional tracking of gold nanorods. Chapter 8 is the general conclusions of the thesis and the outlook.

CHAPTER 2

SINGLE PARTICLE ORIENTATION AND ROTATIONAL TRACKING (SPORT) IN BIOPHYSICAL STUDIES

A feature article submitted to Nanoscale

Yan Gu[a,b], Ji Won Ha[a,b], Ashley E. Augspurger[a], Kuangcai Chen[a,b], Shaobin Zhu[a], and Ning Fang[a,b]*

[a] Department of Chemistry, Iowa State University, Ames, Iowa, 50011

[b] Ames Laboratory, U.S. Department of Energy, Ames, Iowa, 50011

Abstract

The single particle orientation and rotational tracking (SPORT) techniques have seen rapid development in the past 5 years. Recent technical advances have greatly expanded the applicability of SPORT in biophysical studies. In this feature article, we survey the current development of SPORT and discuss its potential applications in biophysics, including cellular membrane processes and intracellular transport.

1. Introduction

The real-time tracking of biological processes is essential in digging out mechanisms that are otherwise hidden in static observations. With the advances of optical microscopy techniques and photodetectors, sophisticated micro- and nano-scale biological phenomena can now be observed in real time with relative ease. It is usually necessary to label biomolecules of interest in live cells or bioengineered systems with contrast agents for observation under light microscopes. Most single molecule tracking techniques employed in biophysical studies rely on fluorescent labeling of target molecules. For example, the lateral diffusion of membrane lipids and proteins[1], signaling processes of membrane receptors[2], and infection pathways of single viruses[3] were observed by using fluorescent tags. However, the single molecule fluorescence techniques are usually limited by the stochastic intensity fluctuations, relatively short observation time due to the intrinsic photobleaching of organic dyes, and high autofluorescence background. Single particle tracking (SPT), as an alternative approach, sometimes serves as a more reliable imaging method. The SPT techniques typically incorporate labeling using fluorescent quantum dots (Q-dots)[4] or non-fluorescent noble metal nanoparticles[5, 6]. They have been widely applied in biophysical studies, such as membrane diffusion[7, 8], cellular uptake of extraneous substances[9-11], and intracellular transport[12-14].

The conventional SPT techniques investigate biophysical phenomena from two-dimensional (2D) or three-dimensional (3D) translational movement of imaging probes. However, many biological processes involve orientation and rotational information, e.g., DNA polymerization[15], ATP synthase self-rotation[16], and the stepping of molecular motors[17, 18]. Recent advances of imaging techniques have greatly expanded our ability to resolve not only the translational dynamics but also the rotational dynamics of imaging probes in cellular and engineered environments.

It is our belief that the acronym “SPORT” for Single Particle Orientation and Rotational

Tracking is an appropriate name to encompass all of the techniques that are designed to resolve the orientation and rotational motion of single nanoparticle probes.

A brief introduction to various SPORT techniques that utilize either fluorescent Q-dots or plasmonic nanoparticles will be provided. Readers are encouraged to read a recent comprehensive review on the technical details of single-cell optical imaging techniques[19]. In the present perspective, we will put more emphasis on the practical considerations and biophysical applications of SPORT and provide future perspectives on technical developments and experimental designs.

2. SPORT with Fluorescent Probes

The fluorescence-based SPORT techniques have been widely used for biological studies, and they typically rely on the detection of the transition dipole orientation of fluorescent probes such as organic dye molecules, conjugated polymers, and Q-dots. The dipole orientation of an optical probe is obtained by measuring the fluorescence polarization anisotropy, or polarization-dependent absorption. In this section, we will focus on fluorescent Q-dots used as probes in SPORT.

Using fluorescence polarization microscopy, the 3D orientation of a single CdSe Q-dot can be resolved by measuring its 2D transition dipole in multiple polarization channels at room temperature[20]. Toprak et al. combined defocused orientation and position imaging (DOPI) with fluorescence imaging with one-nanometer accuracy (FIONA) to resolve the step sizes and behaviors of myosin V motor protein walking on actin filaments[21]. In their work, the Q-dots were imaged with circularly polarized light under a total internal reflection fluorescence (TIRF) microscope. For the orientation tracking, the sample was imaged out of focus (~ 500 nm from the focal plane) and the 3D orientation was determined by comparing the defocused images with the theoretical models. The position tracking with 1.5-nm accuracy was realized by taking focused images of Q-dots under the principle of FIONA. Compared with conventional organic dyes, Q-dots are photophysically more stable and brighter to allow a ~5-fold increase in temporal resolution.

In addition to Q-dots, fluorescent quantum rods (Q-rods) with proper aspect ratios (>10:1) emit approximately linearly polarized light; therefore, they can also be used as rotational probes[22-24]. In another attempt to measure the stepping behaviors of myosin V, the fluorescence signals from the Q-rods emitters excited by a circularly polarized laser beam were split to 4 polarization components (0°, 45°, 90°, and 135°) and projected onto the same CCD chip by installing a half-mirror and a Wollaston prism in the light path[23]. In this way, the 3D orientation of Q-rods was determined with better than 10° accuracy at the temporal resolution of ~30 ms, while the 2D trajectories were acquired simultaneously.

In another interesting study using Q-dots as rotational probes, instead of tracking the dipole orientation of Q-dots with polarized light, as in other experiments discussed in this section, Q-dots were labeled on single viruses, and the interferometric scattering of viruses and super-localization of Q-dots are combined for tracking the position and orientation of viruses on synthetic lipid bilayers[25].

3. SPORT with Plasmonic Nanoparticles

The non-fluorescence SPORT techniques typically utilize anisotropic plasmonic metal nanoparticles as imaging probes. Gold nanorods[26] (AuNRs) have been the most popular choice in orientation sensing and rotational tracking due to their photostability (non-photobleaching and non-blinking), easy surface modification, low toxicity to biological samples, and most importantly, the high scattering and absorption cross sections resulting from the localized surface plasmon resonance (LSPR). The plasmon band, which depends on the size and shape of the nanoparticles, as well as the dielectric constant of the surrounding medium, allow one to tune the desired LSPR frequency. The anisotropic AuNRs possess two geometrically confined LSPR bands: the longitudinal LSPR along the long axis and the transverse LSPR along the short axis. The single dipolar character of the plasmon bands enables AuNRs to be used as rotational probes in ways similar to fluorescent molecular dipoles.

In this section, we will focus on the working principles and experimental designs of several far-field optical imaging-based SPORT techniques that have been widely employed to measure the orientation of single AuNR probes. (See **Fig. 2.1** for the definitions of the orientation angles.) The optical techniques include the scattering-based dark field microscopy, planar illumination microscopy, total internal reflection scattering (TIRS) microscopy, the absorption-based photothermal heterodyne imaging, and the interferometry-based differential interference contrast (DIC) microscopy.

3.1 Scattering-based optical techniques in SPORT

The first demonstration of AuNRs as rotational probes was carried out with a dark field microscope by Sönnichsen and Alivisatos[27]. The AuNRs were illuminated with a tungsten lamp and the scattered light was split into two orthogonal polarization directions by a birefringent calcite crystal. The intensity signals of AuNRs loosely attached to the surface of a glass flow cell were recorded and the rotational diffusion time was estimated by calculating the autocorrelation of the intensity traces. The fastest rotation diffusion time was 60 ms, reflecting the large effective local viscosity near the surface. This technique was later applied in the study of rotational diffusion of surface modified AuNRs on synthetic lipid bilayers.[28] The characteristic rotation times were calculated by fitting the power spectral density of the reduced linear dichroism of the scattering intensities with the Lorentzian function.

Xiao et al. described a planar illumination (or light-sheet) scattering microscope to directly track the rotational and translational diffusion dynamics of AuNRs in live cells[29]. Through illuminating AuNRs with two orthogonal light sheets and resolving the polarized scattering signals with a birefringent crystal, the rotational dynamics of individual AuNRs was recorded successfully. Moreover, the translational and rotational movements of individual AuNRs transported on the microtubules inside live cells were imaged. The light-sheet illumination resulted in a simple continuous excitation probability function for AuNRs compared with dark field microscopy, and the background noise was also reduced.

More recently, Fang and coworkers demonstrated a TIRS microscopy imaging system to probe rotational dynamics of AuNRs interacting with functional surfaces[30]. The orientation-dependent scattering intensity fluctuations of the longitudinal and transverse LSPR modes of AuNRs were used to determine the 3D orientation of the surface-bound AuNRs and resolve their conformations in unprecedented detail. Furthermore, the same research group also developed a TIRS-based method based on the far-field scattering patterns of in-focus AuNRs supported on a dielectric gold film[31]. The 3D orientation of AuNRs within a single frame can be extracted from the characteristic image patterns. Further discussion on the 3D orientation of AuNRs will be provided in Section 4.

3.2 Absorption-based optical techniques in SPORT

There are few reports on absorption-based polarization measurements of AuNRs. Valle et al. have developed spatial modulation spectroscopy, an extinction-based technique, to measure the extinction spectrum of single AuNRs[32]. They also reported the polarization dependence of the extinction cross section of a single AuNR at the longitudinal and transverse LSPR. The maximum intensity of the longitudinal LSPR indeed occurs at the polarization direction orthogonal to the transverse LSPR. Boyer et al. have developed another absorption-based technique, called photothermal imaging, to study the absorption properties of nanostructures[33]. Briefly, they employed a frequency-modulated absorption beam to excite the plasmon band overlaid with another probe beam that probes the change in refractive index of the medium caused by the heat generated from the energy relaxation. Recently, Chang et al. demonstrated the photothermal imaging technique for determining the 2D orientation of single AuNRs[34]. AuNRs (25 nm × 73 nm) were sparsely deposited onto a glass slide, and the polarized photothermal images were obtained as a function of polarization angle. The photothermal polarization traces were then fitted to an equation used to extract the orientation and conformation of a conjugated polymer in the isotropic environment. The photothermal measurement agreed well with the scanning electron microscopy (SEM) measurement.

3.3 Differential interference contrast microscopy in SPORT

DIC microscopy has long been used as a complementary technique to image cells because it provides better visualization (higher contrast, better resolution, and shallower depth of field) of cellular features than other far-field optical microscopy techniques. The recent efforts in the Fang laboratory have transformed DIC microscopy into a primary research tool for tracking plasmonic nanoparticles in biological samples.

Nomarski DIC is the primary microscope design for imaging in the visible and near-IR range, and a Nomarski DIC microsope is equipped with two polarizers and two Nomarski prisms. The first Nomarski prism splits the illumination beam into two orthogonally polarized beams that are separated by a sub-wavelength shear distance. Two intermediate images are generated behind the microscope objective and then laterally shifted back by the second Nomarski prism to overlay and form the interference DIC image. In essence, the Nomarski DIC microscope works as a two-beam interferometer that detects the optical path difference of the two beams passing through the specimen.

Under a DIC microscope, anisotropic AuNRs display disproportionate bright and dark spots depending on their orientation relative to the optical axes and the illumination wavelength[35]. AuNRs with an average size of 25 nm × 73 nm may be imaged at the longitudinal LSPR wavelength of 700 nm or the transverse LSPR wavelength of 540 nm. DIC polarization anisotropy is defined in a way similar to fluorescence anisotropy with the bright and dark DIC intensities[36].

4. Recent Technical Advances of SPORT

Although the optical techniques described above have been widely used to determine the orientation of AuNRs, it is still highly desirable to further improve these techniques for practical applications of SPORT in biophysical studies. In this section, we will therefore discuss the recent advances in far-field optical imaging-based SPORT techniques, in terms of the 3D orientation determination, lateral localization precision, temporal resolution, etc. This section is organized by features, and some papers may be discussed more than once in different subsections.

4.1 Resolving 3D orientation of rotational probes

The ability to precisely resolve the 3D orientation of rotational probes is important because it can greatly enhance our understanding of interactions in complex biological systems. All of the aforementioned SPORT techniques can track a rotational probe’s in-plane orientation (azimuthal angle) reliably, while the out-of-plane orientation (polar or elevation angle) remains difficult to resolve with high accuracy. Recently, there have been several technical advances to overcome this limitation.

4.1.1 Defocused dark-field microscopy

The defocused orientation and position imaging (DOPI) techniques have been reported to have the capability of determining the 3D orientation of out-of-focus AuNRs without angular degeneracy. The DOPI techniques are based on the electron transition dipole approximation and the fact that the dipole radiation exhibits an angular anisotropy. The direct detection of the spatial distribution of the scattered field of a single dipole becomes possible when an aberration is deliberately applied to the imaging system. However, the DOPI techniques have major drawbacks in that both signal and resolution are sacrificed to devolve 3D information, and it is necessary to alternate between defocused and focused imaging for more precise simultaneous position and orientation measurements[21]. Recently, Xiao et al. reported a dual-wavelength dark field microscope to detect both the longitudinal and transverse SPR modes from individual AuNRs, and the well-focused transverse LSPR mode was used for translational localization, while the 3D orientation information was simultaneously determined through the defocused longitudinal SPR mode[37] (**Fig. 2.2a**).

4.1.2 Differential interference contrast microscopy

It has been demonstrated that DIC polarization anisotropy can be used to resolve both the in-plane azimuthal angle and the out-of-plane polar/elevation angles. However, it is important to note that the method can only resolve the azimuthal angle in the range of 0-90°, instead of 0-360°. In other words, there is an angular degeneracy that prevents one from determining in which quadrant the azimuthal angle resides. The four quadrants are defined using the polarization directions of the two light beams after the first Nomarski prism of the DIC microscope. Another consequence of the angular degeneracy is the inability to tell the rotational direction (right-handed or left-handed).

Recently, Xiao et al. overcame the limitations described above by combining DIC image pattern recognition with DIC polarization anisotropy measurement[38]. This approach was developed based on the finding that a AuNR that is *tilted* relative to the horizontal specimen plane would generate different DIC image patterns depending on the quadrant the azimuthal angle belongs (**Fig. 2.2b**). In this two-step process, the DIC polarization anisotropy measurement is first carried out to find the polar angle and the azimuthal angles in the range of 0-90°, and then the pattern recognition determines the quadrant for the exact azimuthal angle in the range of 0-360°. Using this technique, the rocking motion of *tilted* AuNRs was detected on the cell membrane, and the rotational direction (clockwise or counter-clockwise) was determined[38].

This technique determines the orientation of AuNRs in the focal plane of the objective lens; therefore, it is attractive over the defocused imaging techniques in some applications. However, the requirement of a *tilted* AuNR is a major limitation. The estimated minimal polar angle for generating recognizable image patterns in each quadrant is ~70°. The 3D orientation tracking cannot be realized for a AuNR that settles flat relative to the horizontal plane. Furthermore, the tilted position results in reduced signals that affects the angular resolution in DIC microscopy.

4.1.3 Total internal reflection scattering microscopy

Ha et al. developed a high-throughput TIRS-based technique that enables the determination of the 3D orientation of single AuNRs within single frames without suffering from angular degeneracy[31]. This technique is based on the strong interaction of plasmonic AuNRs with dielectric substrates (**Fig. 2.2c**). When AuNRs deposited on a 50-nm thick gold film are illuminated with p-polarized laser light, the point spread function (PSF) of the scattered light from a single AuNR becomes donut-shaped. P-polarized excitation selectively excites the AuNR's out-of-plane transverse dipole perpendicular to the substrate and creates an image charge dipole that is in phase with the AuNR's out-of-plane dipole, resulting in constructive interference. The doughnut-shaped scattering pattern is formed by the net out-of-plane transverse dipole and directly portrays the scattering intensity distribution from this dipole. When the nanorod is tilted from the surface and measured by p-polarized light, the spatial intensity distribution is no longer circularly symmetric. The characteristic image patterns allow the determination of the 3D spatial orientation of the AuNR in the focal plane of the objective lens. Unlike the DOPI techniques[21], this focused orientation and position imaging (FOPI) technique provides the angular information from in-focus single framed images. As a result, such techniques allow high-throughput determination of the 3D orientation of single AuNRs without angular degeneracy and the sacrifice of image quality.

The necessary interaction between the AuNR and the substrate limits the applicability of the FOPI technique in biological samples such as living cells. However, it can still be used in many artificial systems, such as synthetic lipid membranes. Considering its high 3D angular resolution, the FOPI technique may be used in surface studies that that require high-precision orientation information.

Besides the FOPI technique, Marchuk et al. recently demonstrated another TIRS technique that can dynamically track 3D orientation changes of multiple AuNRs under a dual-color TIRS microscope (**Fig. 2.2d**)[30]. The p-polarized excitation light (perpendicular to the horizontal plane) at the longitudinal LSPR wavelength was used for tracking the out-of-plane angle, while the s-polarized excitation light (parallel to the horizontal surface) at the transverse LSPR wavelength was used for tracking the in-plane angle. This technique is capable of resolving the out-of-plane angle with a high angular resolution comparable to that for the in-plane angle. However, it does suffer from the angular degeneracy (only 0-90°) for a AuNR in the focal plane of the objective lens.

4.2 Simultaneous super-localization and rotational tracking

High-precision localization of single molecule or nanoparticle probes is necessary to resolve nanoscale biological structures and dynamics. The localization precision in rotational tracking is significantly influenced by the 3D orientation of the emission dipole[39, 40]. The worst localization precision usually occurs when the dipole orientation is perpendicular to the polarization direction of the excitation beam.

In the defocused imaging techniques, it is rather challenging to super-localize single imaging probes from the orientation-dependent image patterns. Therefore, switching back and forth between focused and defocused imaging is required to obtain both the orientation and the accurate centroid of the emitting dipoles[21]. By splitting the fluorescence signals to four polarization channels, the Yanagida group devised a simultaneous 3D orientation and position tracking technique using fluorescent QRs[23].

For super-localization of single AuNRs in dark field microscopy, Xiao et al. utilized a dual-wavelength setup to create a focused image plane and a defocused image plane simultaneously[37]. The precise location of a AuNR can be determined in the focused image plane at the transverse LSPR wavelength, while its 3D orientation is determined in the defocused image plane at the longitudinal LSPR wavelength. Using this technique, the rotational and translational diffusion of AuNRs on live cell membranes were found to be unsynchronized.

Under a TIRS microscope, Marchuk et al. presented a method in which one can simultaneously track 3D rotational dynamics in AuNRs while super-localizing their lateral motions across a surface. In combination with superlocalization through PSF fitting, they overcame the four-quadrant angular degeneracy of AuNRs in the focal plane of objective and resolve conformations of surface-bound anisotropic AuNRs in detail.

For AuNRs under a DIC microscope, the varying image patterns also make it challenging to super-localize the particles while their orientations are being tracked. Due to the complicated PSF of the DIC microscope, the images under the microscope cannot be simply fitted by a 2D Gaussian function. Gu et al. developed the correlation mapping method to localize isotropic gold nanospheres[41]. Further endeavors are needed to develop new techniques that combine the SPORT technique and the super-localization of the AuNRs.

4.3 Improving temporal resolution

In studying biological systems, 3D trajectories of biological objects such as transport vesicles often need to be acquired with high temporal resolution. In particular, measuring rotational dynamics at the nanoscale require sub-millisecond time resolution. Therefore, it is highly desirable to improve temporal resolution in SPORT techniques for in-depth biophysical studies. Recently, there have been several reports to achieve high temporal resolution. For example, Gu et al. tracked rotational motions of AuNRs with various surface modifiers at 2-5 ms temporal resolution under a DIC microscope[42, 43]. The high temporal resolution made it possible to reveal that the rotational behaviors of AuNR probes on live cell membranes are strongly related to their surface charges. In addition to enhancing temporal resolution, a way to semi-quantify the rotational dynamics needs to be found in order to analyze the rotational dynamics of AuNRs and compare the rotational dynamics at different time points and among various conditions. In the study of the rotational dynamics of AuNRs on synthetic bilayers, the power spectral density of the dark-field signals fitted by a Lorentzian function was applied[44]. However, the power spectral density of the time series of the fast rotating AuNR is usually noisy and affects the fitting result. To semi-quantify the rotational dynamics of AuNRs observed with the SPORT technique, Gu et al. calculated the autocorrelation of the DIC intensities and fitted with a stretched exponential function[45], and the rotation time is semi-quantified as the characteristic time of the stretched exponential decay.

4.4 Revealing fundamental rotational modes

In addition to the technical advances in the SPORT techniques, simulations together with statistical correlation coefficient analysis are also essential in SPORT to provide important insights into the rotational mode, rotational rate and rotational behaviors of AuNRs interacting with cell membranes. A correlation analysis method was developed to extract information about the rotational mode from the DIC intensities of the AuNRs rotating on the membranes[46].

Three fundamental rotational modes, as depicted in **Fig. 2.3**, are defined according to the orientation of the rotation axis relative to the horizontal plane and AuNR. The in-plane rotation is around a rotation axis perpendicular to the horizontal plane. The out-of-plane tilting is around a rotation axis in the horizontal plane. In either of these two rotational modes, the longitudinal and transverse SPR modes of anisotropic AuNRs change orientations to result in orientation-dependent signal intensities and/or image patterns. The third rotational mode, i.e., the rotation around the AuNR's long axis, cannot be resolved directly as it does not give rise to any orientation changes. However, it should be pointed out that AuNRs, if firmly bound to other rotating objects, may resolve this type of rotation. For example, Wang et al. resolved the self-rotation of microtubules transported by kinesin motor proteins immobilized on the substrate surface[35]. All the other rotational motions of AuNRs can be deemed as the combination of these fundamental modes at different proportions.

The rotational modes of AuNRs are reflected by the correlation between the bright and dark DIC intensities[46]. When the nanorod performs in-plane rotation, the bright and dark DIC intensities are correlated, with the correlation coefficient approaching 1. When the nanorod performs out-of-plane tilting motions, the bright and dark DIC intensities are anti-correlated, with the correlation coefficient approaching -1. Other rotational patterns can be considered as a mixture of the in-plane rotation and out-of-plane tilting motions at different proportions and with different restrictions on the rotational angle ranges. The correlation coefficient would approach 0 if a AuNR rotates freely in space. This special case may be referred to as the 3D wandering mode.

5. Biophysical Applications of SPORT

5.1 Rotational motions of F_1-ATP synthase

The first biophysical application of AuNRs was reported by the Frasch group[47, 48]. The rotational behavior of F_1-ATP synthase, a rotary molecular motor, was revealed by tracking single AuNRs attached to the γ-subunit of F_1-ATP synthase. The employment of a single photon counting avalanche photodiode as detector improved the achievable temporal resolution to 2.5 μs, and the rotations of F_1-ATP synthase at ~7.6 rad/ms were observed. The Frasch group also studied F_0F_1-ATP synthase using the same technique. They resolved the average time of the F_0 subunit's transient dwell interaction spent in the formation (163 μs) and dissociation (175 μs) processes.[49] These experiments achieved the fastest temporal resolution in single particle tracking to date.

5.2 Nanoparticle diffusion on membranes

Membrane diffusion of various biomolecules and extraneous substances has aroused great interest as it is closely related with cross-membrane transport and drug delivery. The ensemble measurements of both lateral and rotational diffusion of membrane biomolecules can be dated back to the early 1970s with techniques such as flash photolysis, fluorescence autocorrelation spectroscopy, fluorescence anisotropy, and polarized fluorescence photobleaching[50-53]. In the past two decades, single molecule and particle tracking techniques have emerged as the tools of choice. The discussion here will be focused on the rotational tracking with nanoparticle probes.

AuNRs have been demonstrated to be a good model system for studying nanoparticle-based drug delivery[42]. The rotational dynamics of AuNRs can provide rich information on the interactions between nanoparticles and cell membranes. AuNRs were functionalized with various biomolecules including a cell penetrating peptide (CPP) from the HIV-1 protein Tat[12, 13, 54] and transferrin (a glycoprotein used as a drug delivery agent[55]), and their rotational dynamics was followed at a temporal resolution of 5 ms to reveal the effects of electrostatic interactions and specific binding interactions between nanoparticles and cell membranes.

In the follow-up study from the same group, the different rotational modes of functionalized AuNRs at first contact with live cell membranes were elucidated[46]. The Tat CPP modified AuNRs showed generally random rotational motions at first contact under the influence of electrostatic interactions and tended to perform in-plane rotations as the interactions between the AuNRs and the cell membranes got stronger likely through additional hydrogen bonds. The transferrin-modified AuNRs showed larger fractions of in-plane rotational modes at first contact with the cell membranes due to the existence of specific receptors. The calibration of the rotational modes of AuNRs with various surface modifications was carried out on synthetic lipid bilayers.

5.3 Cargo transport by molecular motors

Molecular motors, including kinesin, dynein and myosin, are largely responsible for intracellular trafficking of biomolecules, vesicles, and organelles along microtubules and actin filaments of the cytoskeleton. These molecular motors are evolutionarily developed to perform their functions extremely efficiently and precisely[56]. Direct visualization of cargo transportation in living cells and engineered systems with high localization precision and fast temporal resolution has contributed significantly to our current understanding of this complicated transport system.

5.3.1 In-vitro microtubule gliding assays

In microtubule gliding assays, reconstituted microtubules act as shuttles to move cargos and they are transported by the kinesin motors immobilized on the substrate surface upon the addition of Adenosine-5'-triphosphate (ATP). Microtubules are normally composed of 13 linear protofilaments in eukaryotic cells. These 13-protofilament microtubules glide on the substrate surface without rotating around their longitudinal axis. Under various assembly conditions, however, one can also make reconstituted microtubules that are composed of non-13 protofilaments[57]. The protofilaments in non-13-mers may not be linear but twisted left-handedly (14-mers) or right-handedly (12-mers); therefore, these microtubules can rotate around their longitudinal axis when being driven to move laterally.

Efforts have been taken to elucidate the 3D rotation of the gliding 12- or 14-protofilament microtubules, including using microtubules with a side arm[57,58], Q-dot-assisted fluorescence interference contrast microscopy (FLIC)[59], and placing a wedge prism at the back focal plane to track the 3D position[60]. More recently, the DIC microscopy-based SPORT technique has been employed to make arguably the most direct measurement of the microtubule's rotation[35].

AuNRs (10 nm × 35 nm) were attached to the microtubules through the strong biotin-neutravidin linkage (**Fig. 2.4A**). These AuNRs were small enough to avoid obstructing the rotation of the microtubules. The rotation was detected by monitoring the periodic DIC signal changes corresponding to the orientation changes of the AuNRs.

It is important to note that the greatest advantage of the AuNR and DIC microscopy-based SPORT technique is the ability to track the rotational motions of cargos in live intracellular transport (**Fig. 2.4B**). The rest of this section is devoted to the recent applications of SPORT on intracellular transport.

5.3.2 Intracellular transport

Although there have been many reports on the intracellular transport of subcellular organelles or nanoprobes, e.g., Tat modified Q-dots[9], the orientation and rotational tracking of cargos during the transport has rarely been studied until recently. The AuNR and DIC microscopy-based SPORT technique show great potential in elucidating the working mechanisms of molecular motors by visualizing the rotational motions of cargos in live cells[35]. In this new approach, transferrin-conjugated AuNRs (25 nm × 73 nm) are endocytosed and contained within the lipid membranes of small endocytic vesicles. These AuNRs are chosen for their sufficiently high DIC contrast and angular resolution at the longitudinal SPR wavelength (~700 nm) and for their size matching with typical endocytic vesicles. Furthermore, these AuNRs are bound to the transferrin receptors imbedded in the lipid membranes to keep them stationary with respect to the vesicle on the time scale of the transport events.

It has been found that the AuNR-containing vesicles usually show relatively constant DIC image patterns during the active directional transport along linear protofilaments in eukaryotic cells. The restriction on the cargo's rotational motion during the directional transport is believed to be caused by tension applied by multiple motor proteins bound to the cargo. Two examples are provided in the supplementary movies. In **Supplementary Movie 2.1**, a cargo (indicated by the red arrow) takes a 90^o turn in the transport direction while the DIC image pattern changes drastically from dark to bright, indicating a 90° turn in the cargo's orientation. In **Supplementary Movie 2.2**, the cargo (indicated by the red arrow) goes back and forth on the same microtubule track while maintaining relatively constant DIC image patterns.

A dual-modality SPORT technique has also been developed to image fluorescent microtubule tracks and AuNRs in live cells simultaneously[61]. Using this technique, one can localize the AuNRs while they dock to or undock from the microtubule tracks in real time. Co-localization of AuNRs and associated fluorescent biomolecules or cellular structures is an essential requirement in drawing conclusions on nearly all of dynamic tracking experiments in live cells.

The orientation and rotational studies of cargo transport on microtubule tracks promise further investigations into the intracellular transport, e.g., the navigation of cargos among the cytoskeleton network[62] and the motions of cargos in front of road blocks such as microtubule or actin associated proteins[63-65].

5.3.3 Axonal transport

Axonal transport, as a special type of intracellular transport, is of vital importance to neuronal growth and functions. On the other hand, axonal transport is a good platform for studying the working mechanisms of kinesin and dynein motors because of the simplicity of the unidirectional microtubule cytoskeleton with plus end outwards in the slender axons. Axonal transport has mainly been studied using fluorescence-based imaging techniques to follow fluorescently-labeled organelles[66-68] or nerve growth factor-modified Q-dots in endosomes[69]. The ability to resolve the rotational motions of cargos during the active directional transport and pauses offers new experimental and theoretical perspectives in studying axonal transport[45].

Using a similar approach discussed in the previous section, transferrin-modified AuNRs are endocytosed by the differentiated PC12 cells and contained in the endocytic vesicles. The rotational motions of cargos during short and long pauses can be captured and analyzed. The correlation analysis of the bright and dark DIC intensities of the AuNRs performing rotational motions during the pauses compared with free rotational diffusions indicates that the cargos were still tethered to the microtubule tracks during the pauses. The rotational motion and the transport direction right after a pause are also correlated with the pause duration, indicating that certain regulatory mechanisms likely exist in the cargo transport by kinesin and dynein motors.

Cultured PC12 cells provide a simplified platform because of the convenient access to the cell line, the robustness of the cells and easy manipulation of cell differentiation. However, they still differ from the primary neuronal cells since they lack many neuronal functions and regulatory factors. Here we want to emphasize that it is possible to track the axonal transport of endocytosed functionalized AuNRs in primary neuronal cells. **Fig. 2.5** shows the DIC intensities and corresponding lateral displacement of a AuNR-containing vesicle (particle **a** in **Fig. 2.5A**, **Supplementary Movie 2.3)** undergoing directional transport, pause and directional transport again in the same direction. During the directional transport, the AuNR moves at a speed of ~ 1 μm/s and generally kept constant DIC image patterns except when the smooth transport was interrupted by the short pauses (at 1.8 s, 2.4 s, etc.).

Starting at 2.9 s, the AuNR pauses for 1.2 s, which was accompanied by a ~180^o turn of the AuNR, and the DIC intensity changed from dark to bright and to dark again. The nanorod then resumed the directional transport, with short pauses and fluctuations during the short pauses. As a comparison, the nanorod (particle **b** in **Figure 2.5A**) highlighted on the top of **Supplementary Movie 2.3** shows quite different behaviors. The DIC intensities and the lateral displacement are shown in **Figure 2.5C**. The AuNR continues to rotate while moving back and forth along the axon. No directional transport with constant DIC image patterns was observed. Although there are many small reversals during the movement, transport along the axon is still observed from the general trend of the displacement. The nanorod generally moved downwards at 0-0.8 s, 1.4-2.5 s, and 3.1-3.4 s, while moved upwards at 1.2-1.5 s and 2.5-3.1 s. One likely explanation of the frequent reversals and rotational motions of the cargo is that kinesin and dynein motors are constantly competing with each other to move the cargo on the microtubule track.

Direct visualization of the cargo’s rotational dynamics during the active transport and the pauses provides a novel approach to acquire new knowledge about the working mechanisms of motor proteins and associated regulatory proteins that were unattainable previously using other imaging techniques.

6. Summary and outlook

SPORT has been realized with a variety of microscopy modalities, including fluorescence microscopy, dark field microscopy, total internal reflection scattering microscopy, photothermal imaging, and DIC microscopy. Recent advances, such as the full 3D orientation tracking with high angular resolution and high precision localization of single nanoparticle probes, have greatly expanded the applicability of SPORT in biophysical studies. However, a number of key improvements are still necessary in order to fully realize the potential of SPORT. First, dynamic tracking in the axial direction remains challenging and the axial localization precision is still more than an order of magnitude worse than the lateral precision. As such, it is necessary to develop new SPORT techniques that provide accurate measurements of both 3D position and orientation of rotational probes. Second, the temporal resolution of SPORT is usually much worse than the conventional SPT, as a larger number of photons need to be collected in order to resolve the orientation. Faster image rates and innovative data analysis methods are desirable to elucidate fast rotational motions encountered in live biological systems. The current state-of-the-art SPORT techniques are mainly applicable to study rotational probes that are restrained by certain factors, such as being tethered to membrane receptors or encapsulated inside small compartments.

Most of the current biophysical studies using SPORT are technical demonstrations or reports of direct observations of rotational motions. Future SPORT studies should be focused on elucidating the underlying mechanisms that govern the observed rotational motions. The arguably most important topic of SPORT is nanoparticle-based drug delivery. Functionalized nanoparticles can be fashioned as model systems to allow the studies on the detailed mechanisms of membrane diffusion/interactions, internalization, targeted delivery to the diseased organ, controlled drug release, and nanotoxicity.

Finally, live rotational motions captured by SPORT provide a significant new dimensionality to the computational efforts. As the translational freedom does not necessarily correlate directly with the rotational freedom, the new dimension in experimental and simulated data will provide a more accurate interpretation of the influences of individual factors.

References

1. Kusumi, A.; Nakada, C.; Ritchie, K.; Murase, K.; Suzuki, K.; Murakoshi, H.; Kasai, R. S.; Kondo, J.; Fujiwara, T., *Annu. Rev. Biophys. Biomol. Struct.*, 2005; Vol. 34, pp 351-378.
2. Sako, Y.; Minoguchi, S.; Yanagida, T. *Nat. Cell Biol.* **2000,** 2, (3), 168-172.
3. Seisenberger, G.; Ried, M. U.; Endress, T.; Buning, H.; Hallek, M.; Brauchle, C. *Science* **2001,** 294, (5548), 1929-1932.
4. Alivisatos, A. P. *Science* **1996,** 271, (5251), 933-937.
5. Anker, J. N.; Hall, W. P.; Lyandres, O.; Shah, N. C.; Zhao, J.; Van Duyne, R. P. *Nature Materials* **2008,** 7, (6), 442-453.
6. Jain, P. K.; Huang, X.; El-Sayed, I. H.; El-Sayed, M. A. *Accounts Chem. Res.* **2008,** 41, (12), 1578-1586.
7. Kusumi, A.; Sako, Y.; Yamamoto, M. *Biophys. J.* **1993,** 65, (5), 2021-2040.
8. Saxton, M. J.; Jacobson, K. *Annu. Rev. Biophys. Biomol. Struct.* **1997,** 26, 373-399.
9. Ruan, G.; Agrawal, A.; Marcus, A. I.; Nie, S. *J. Am. Chem. Soc.* **2007,** 129, (47), 14759-14766.
10. Moore, A.; Weissleder, R.; Bogdanov, A. *Jmri-Journal of Magnetic Resonance Imaging* **1997,** 7, (6), 1140-1145.
11. Panyam, J.; Labhasetwar, V. *Pharm. Res.* **2003,** 20, (2), 212-220.
12. Tkachenko, A. G.; Xie, H.; Liu, Y. L.; Coleman, D.; Ryan, J.; Glomm, W. R.; Shipton, M. K.; Franzen, S.; Feldheim, D. L. *Bioconjugate Chem.* **2004,** 15, (3), 482-490.
13. de la Fuente, J. M.; Berry, C. C. *Bioconjugate Chem.* **2005,** 16, (5), 1176-1180.
14. Yezhelyev, M. V.; Qi, L.; O'Regan, R. M.; Nie, S.; Gao, X. *J. Am. Chem. Soc.* **2008,** 130, (28), 9006-9012.

15. Waga, S.; Stillman, B. *Annu. Rev. Biochem.* **1998,** 67, 721-751.
16. Yasuda, R.; Noji, H.; Yoshida, M.; Kinosita, K.; Itoh, H. *Nature* **2001,** 410, (6831), 898-904.
17. Kural, C.; Kim, H.; Syed, S.; Goshima, G.; Gelfand, V. I.; Selvin, P. R. *Science* **2005,** 308, (5727), 1469-1472.
18. Forkey, J. N.; Quinlan, M. E.; Shaw, M. A.; Corrie, J. E. T.; Goldman, Y. E. *Nature* **2003,** 422, (6930), 399-404.
19. Stender, A. S.; Marchuk, K.; Liu, C.; Sander, S.; Meyer, M. W.; Smith, E. A.; Neupane, B.; Wang, G.; Li, J.; Cheng, J.-X.; Huang, B.; Fang, N. *Chem. Rev.* **2013,** 113, (4), 2469-2527.
20. Chung, I. H.; Shimizu, K. T.; Bawendi, M. G. *Proc. Natl. Acad. Sci. U. S. A.* **2003,** 100, (2), 405-408.
21. Toprak, E.; Enderlein, J.; Syed, S.; McKinney, S. A.; Petschek, R. G.; Ha, T.; Goldman, Y. E.; Selvin, P. R. *Proc. Natl. Acad. Sci. U. S. A.* **2006,** 103, (17), 6495-6499.
22. Hu, J. T.; Li, L. S.; Yang, W. D.; Manna, L.; Wang, L. W. *Science* **2001,** 292, (5524), 2060-2063.
23. Ohmachi, M.; Komori, Y.; Iwane, A. H.; Fujii, F.; Jin, T.; Yanagida, T. *Proc. Natl. Acad. Sci. U. S. A.* **2012,** 109, (14), 5294-5298.
24. Tsay, J. M.; Doose, S.; Weiss, S. *J. Am. Chem. Soc.* **2006,** 128, (5), 1639-1647.
25. Kukura, P.; Ewers, H.; Muller, C.; Renn, A.; Helenius, A.; Sandoghdar, V. *Nat. Methods* **2009,** 6, (12), 923-927.
26. Jana, N. R.; Gearheart, L.; Murphy, C. J. *J. Phys. Chem. B* **2001,** 105, (19), 4065-4067.
27. Sonnichsen, C.; Alivisatos, A. P. *Nano Lett.* **2005,** 5, (2), 301-304.
28. Pierrat, S.; Hartinger, E.; Faiss, S.; Janshoff, A.; So□nnichsen, C. *J. Phys. Chem. C* **2009,** 113, (26), 11179-11183.
29. Xiao, L.; Qiao, Y.; He, Y.; Yeung, E. S. *J. Am. Chem. Soc.* **2011,** 133, (27), 10638–10645.
30. Marchuk, K.; Ha, J. W.; Fang, N. *Nano Lett.* **2013**.
31. Ha, J. W.; Marchuk, K.; Fang, N. *Nano Lett.* **2012,** 12, (8), 4282-4288.
32. Billaud, P.; Marhaba, S.; Cottancin, E.; Arnaud, L.; Bachelier, G.; Bonnet, C.; Del Fatti, N.; Lerme, J.; Vallee, F.; Vialle, J. L.; Broyer, M.; Pellarin, M. *J. Phys. Chem. C* **2008,** 112, (4), 978-982.
33. Boyer, D.; Tamarat, P.; Maali, A.; Lounis, B.; Orrit, M. *Science* **2002,** 297, (5584), 1160-1163.
34. Chang, W.-S.; Ha, J. W.; Slaughter, L. S.; Link, S. *Proc. Natl. Acad. Sci. U. S. A.* **2010,** 107, (7), 2781-2786.
35. Wang, G.; Sun, W.; Luo, Y.; Fang, N. *J. Am. Chem. Soc.* **2010,** 132, (46), 16417-16422.
36. Ha, J. W.; Sun, W.; Wang, G.; Fang, N. *Chem. Commun.* **2011,** 47, 7743-7745.
37. Xiao, L.; Wei, L.; Liu, C.; He, Y.; Yeung, E. S. *Angew. Chem. Int. Ed.* **2012,** 51, (17), 4181-4184.
38. Xiao, L.; Ha, J. W.; Wei, L.; Wang, G.; Fang, N. *Angew. Chem. Int. Ed.* **2012,** 51, (31),

7734-7738.

39. Enderlein, J.; Toprak, E.; Selvin, P. R. *Opt. Express* **2006,** 14, (18), 8111-8120.
40. Mortensen, K. I.; Churchman, L. S.; Spudich, J. A.; Flyvbjerg, H. *Nat. Methods* **2010,** 7, (5), 377-381.
41. Gu, Y.; Di, X.; Sun, W.; Wang, G.; Fang, N. *Anal. Chem.* **2012,** 84, (9), 4111-4117.
42. Gu, Y.; Sun, W.; Wang, G.; Fang, N. *J. Am. Chem. Soc.* **2011,** 133, (15), 5720-5723.
43. Gu, Y.; Sun, W.; Wang, G.; Jeftinija, K.; Jeftinija, S.; Fang, N. *Nat. Commun.* **2012,** 3, 1030.
44. Pierrat, S.; Hartinger, E.; Faiss, S.; Janshoff, A.; Soennichsen, C. *J. Phys. Chem. C* **2009,** 113, (26), 11179-11183.
45. Roecker, C.; Poetzl, M.; Zhang, F.; Parak, W. J.; Nienhaus, G. U. *Nat. Nanotechnol.* **2009,** 4, (9), 577-580.
46. Gu, Y.; Sun, W.; Wang, G.; Zimmermann, M. T.; Jernigan, R. L.; Fang, N. *Small* **2013,** 9, (5), 785-792.
47. York, J.; Spetzler, D.; Xiong, F.; Frasch, W. *Lab Chip* **2008,** 8, (3), 415-419.
48. Spetzler, D.; York, J.; Daniel, D.; Fromme, R.; Lowry, D.; Frasch, W. *Biochemistry* **2006,** 45, (10), 3117-3124.
49. Ishmukhametov, R.; Hornung, T.; Spetzler, D.; Frasch, W. D. *EMBO J* **2010,** 29, (23), 3911-3923.
50. Edidin, M. *Current Topics in Membranes and Transport* **1987,** 29, 91-127.
51. Cherry, R. J. *Biochim. Biophys. Acta* **1979,** 559, (4), 289-327.
52. Yuan, Y.; Axelrod, D. *Biophys. J.* **1995,** 69, (2), 690-700.
53. Chakrabarti, A.; Matko, J.; Rahman, N. A.; Barisas, B. G.; Edidin, M. *Biochemistry* **1992,** 31, (31), 7182-7189.
54. Heitz, F.; Morris, M. C.; Divita, G. *Br. J. Pharmacol.* **2009,** 157, (2), 195-206.
55. Qian, Z. M.; Li, H. Y.; Sun, H. Z.; Ho, K. *Pharmacol. Rev.* **2002,** 54, (4), 561-587.
56. Mickler, M.; Schleiff, E.; Hugel, T. *ChemPhysChem* **2008,** 9, (11), 1503-1509.
57. Ray, S.; Meyhofer, E.; Milligan, R. A.; Howard, J. *J. Cell Biol.* **1993,** 121, (5), 1083-1093.
58. Yajima, J.; Cross, R. A. *Nat. Chem. Biol.* **2005,** 1, (6), 338-341.
59. Nitzsche, B.; Ruhnow, F.; Diez, S. *Nat. Nanotechnol.* **2008,** 3, (9), 552-556.
60. Yajima, J.; Mizutani, K.; Nishizaka, T. *Nat. Struct. Mol. Biol.* **2008,** 15, (10), 1119-1121.
61. Sun, W.; Gu, Y.; Wang, G.; Fang, N. *Anal. Chem.* **2012,** 84, (2), 1134-1138.
62. Ross, J. L.; Ali, M. Y.; Warshaw, D. M. *Curr. Opin. Cell Biol.* **2008,** 20, (1), 41-47.
63. Telley, I. A.; Bieling, P.; Surrey, T. *Biophys. J.* **2009,** 96, (8), 3341-3353.
64. Schmidt, C.; Kim, B.; Grabner, H.; Ries, J.; Kulomaa, M.; Vogel, V. *Nano Lett.* **2012,** 12, (7), 3466-71.
65. Crevel, I.; Nyitrai, M.; Alonso, M. C.; Weiss, S.; Geeves, M. A.; Cross, R. A. *EMBO J.* **2004,** 23, (1), 23-32.
66. Droz, B.; Leblond, C. P. *Science* **1962,** 137, (3535), 1047-1048.

67. Nan, X. L.; Sims, P. A.; Chen, P.; Xie, X. S. *J. Phys. Chem. B* **2005,** 109, (51), 24220-24224.
68. Roy, S.; Coffee, P.; Smith, G.; Liem, R. K. H.; Brady, S. T.; Black, M. M. *J. Neurosci.* **2000,** 20, (18), 6849-6861.
69. Cui, B. X.; Wu, C. B.; Chen, L.; Ramirez, A.; Bearer, E. L.; Li, W. P.; Mobley, W. C.; Chu, S. *Proc. Natl. Acad. Sci. U. S. A.* **2007,** 104, (34), 13666-13671.

Figures

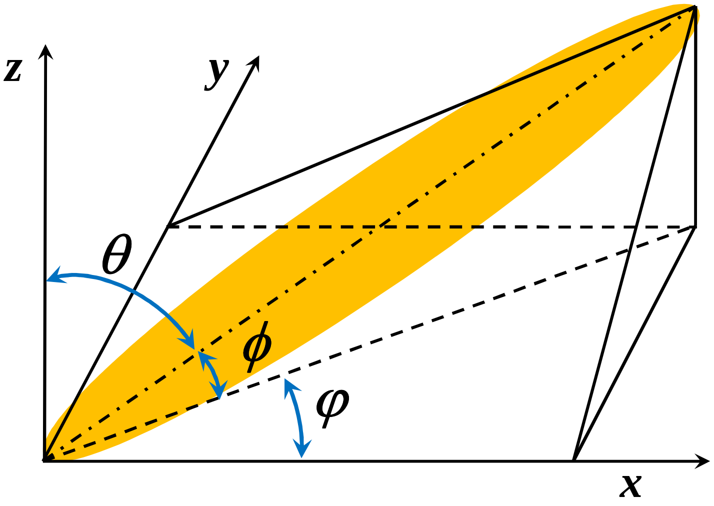

Figure 2.1 3D orientation angles of a AuNR: azimuthal angle φ, polar angle θ, and elevation angle ϕ. The *x*- and *y*-axes are typically set according to the polarization direction(s) of the illumination light.

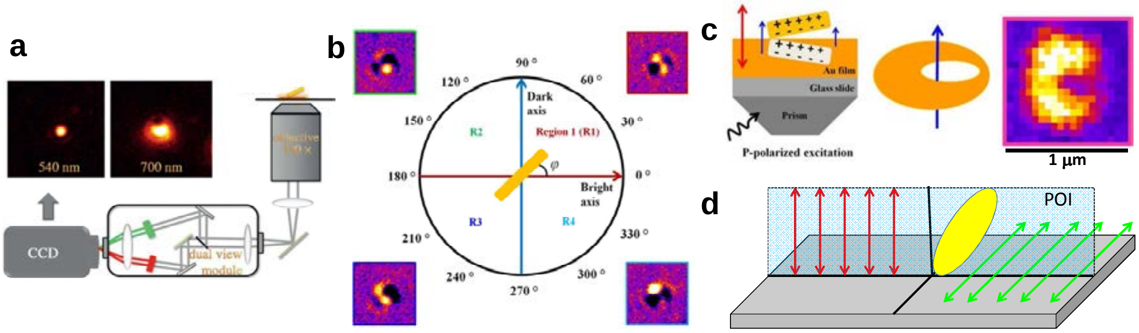

Figure 2.2. New strategies for resolving the orientation of AuNRs. **(a)** Dual-view dark-field optics for single particle translational and rotational tracking which provide a well-focused image at 540 nm and a defocused image at 700 nm. The focused image is used to determine the position and the defocused image is used to determine the 3D orientation of the gold nanorod. Reprinted with permission from ref. 37. Copyright 2012 John Wiley & Sons, Inc. **(b)** Changes in DIC image patterns of a tilted gold nanorod as a function of azimuthal angle. The red (bright) and blue (dark) axes correspond to the polarization directions of the two light beams after the first Nomarski prism in a DIC microscope. When illuminated under the longitudinal LSPR wavelength, a AuNR gives rise to a mostly bright (dark) image when its LSPR mode is aligned with the bright (dark) axis. Reprinted with permission from ref. 38. Copyright 2012 John Wiley & Sons, Inc. **(c)** Schematic diagram for a tilted AuNR on the Au film under a TIRS microscope with p-polarized excitation. The red arrow indicates the direction of the excitation polarization. The net out-of-plane dipole torus is no longer circularly symmetric and results in Pac-Man-like patterns. Reprinted with permission from ref. 31. Copyright 2012 American Chemical Society. **(d)** Schematic diagram for a AuNR illuminated with p (red) & s (green) polarized light under a dual-color TIRS microscope. POI: plane of incident. Reprinted with permission from ref. 30. Copyright 2013 American Chemical Society.

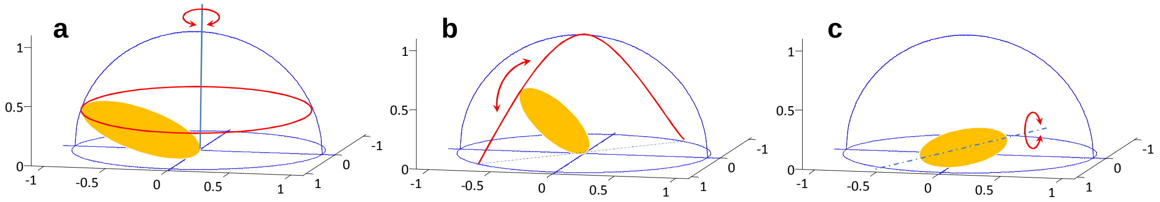

in-plane rotation **out-of-plane tilting** **rotation around own long axis**

Fig. 2.3. Three fundamental rotational modes. Adapted with permission from ref. 46. Copyright 2013 John Wiley & Son, Inc.

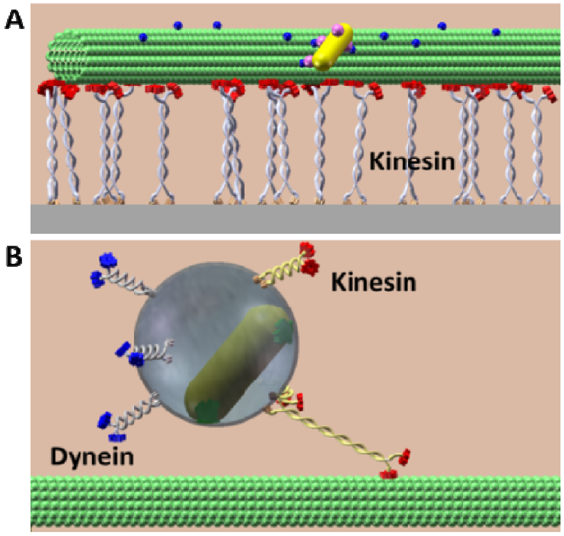

Fig. 2.4. Cargo transport by molecular motors. (A) Schematic illustration of a piece of gliding microtubule serving as the shuttle on a kinesin-coated glass slide. The blue dots are biotin, and the purple dots are neutravidin. (B) Schematic illustration of the microtubule-associated intracellular transport of a AuNR-containing vesicle. The red and blue motor proteins represent kinesin and dynein motors, respectively. Adapted with permission from ref. 35. Copyright 2010 American Chemical Society.

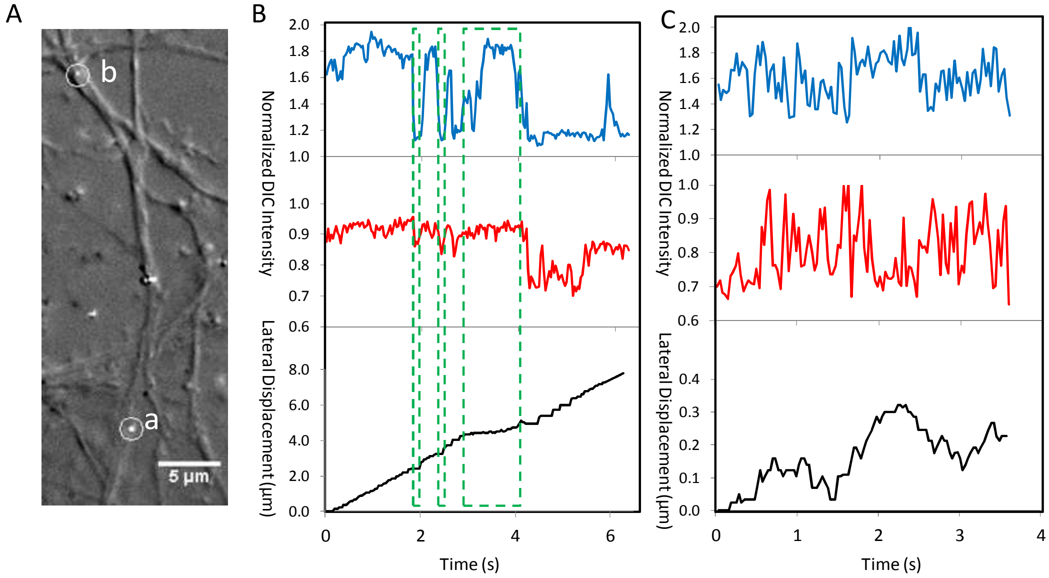

Fig. 2.5. (A) The DIC image of two gold nanorods (a and b) transported in the axon of a neuron cell. (B) The normalized DIC intensities and the lateral displacement of particle a during the 6.4 s of active transport. The green rectangles highlight the pauses during the transport. (C) The normalized DIC intensities and the lateral displacement of particle b during the 4 s of active transport.

CHAPTER 3

SINGLE PARTICLE ORIENTATION AND ROTATION TRACKING DISCLOSES DISTINCTIVE ROTATIONAL DYNAMICS OF DRUG DELIVERY VECTORS ON LIVE CELL MEMBRANES

A paper published in the Journal of the American Chemical Society
2011, 133, 5720-5723

*Yan Gu, Wei Sun, Gufeng Wang, and Ning Fang**

Ames Laboratory, U.S. Department of Energy and Department of Chemistry, Iowa State University,
Ames, Iowa, 50011

Abstract

Engineered nanoparticles have emerged as potentially revolutionary drug and gene delivery vectors. Using rod-shaped gold nanoparticles as a model, we studied for the first time the rotational dynamics of nanoparticle vectors on live cell membranes and its impact on the fate of these nanoparticle vectors. The rotational motions of gold nanorods with various surface modifiers were tracked continuously at 200 frames per second under a differential interference contrast (DIC) microscope. We found that the rotational behaviors of gold nanorod vectors are strongly related to their surface charges. Specific surface functional groups and the availability of receptors on cell membranes also contribute to the rotational dynamics. The study of nanoparticle's rotational Brownian motion on cell membranes will lead to a better understanding of the mechanisms of drug delivery and provide guidance in

designing surface modification strategies for drug delivery vectors under different circumstances.

Introduction

Among the numerous drug delivery strategies that have been developed to overcome the physiological barrier of the cell and nuclear membranes,[1] engineered nanoparticles have emerged as potentially revolutionary drug carriers for diagnosis and treatment of many diseases,[2] for their advantages including enhanced drug solubility, improved internalization efficiency, targeted delivery to the diseased organ, controlled drug release, and reduced side effects. For example, gold nanoparticles have been used to deliver drugs[3-5] and biological molecules.[6-10]

In order to rationally design nanoparticle carriers, it is imperative to understand the influences of nanoparticle's physical and chemical properties, including particle size, shape, and surface characteristics, on nanoparticle-based drug delivery.[2,11] Most of the reported research efforts in this area were focused on identifying these effects from static fluorescence and electron micrographs taken at different stages;[12-17] however, characteristic translational and rotational dynamics of functionalized nanoparticle carriers resulting from their interactions with the cellular environment have not been fully elucidated.

Conventional single particle tracking (SPT)[18] techniques are useful to probe the structure and biological functions of cell membrane at the molecular level, but its usefulness is limited to translational motions. To overcome this limitation, plasmonic gold nanorods with anisotropic absorption and scattering properties have been utilized as orientation probe under dark field microscopy,[19,20] photothermal imaging,[21] and Nomarski-type differential interference contrast (DIC) microscopy.[22] These methods were successful in characterizing well-defined rotational motions, e.g., the rotational motion of the center domain of F1-ATPase immobilized on glass substrate,[20] by resolving the nanorod orientation in each image frame of a recorded rotation sequence. On the other hand, the characterization of the rotational Brownian motion requires statistical analysis on a large number of consecutive images taken at fast frame rates. Pierrat *et al.* demonstrated that 2-D rotational dynamics of laterally frozen nanoparticles on synthetic membranes is controlled in part by dragging forces introduced by the surface viscosity of the membrane;[23] however, the rotational Brownian motion has never been elucidated for functionalized nanoparticles on live cell membranes.

In the present study, the integrated imaging platform based on DIC microscopy for single particle orientation and rotation tracking (SPORT)[22] was employed for direct visualization of the distinctive rotational dynamics of gold nanorods functionalized with different surface modifiers on live cell membranes. The images of both the cell and nanoparticle vectors were acquired at 200 frames per second (fps) under a DIC microscope, which provides a unique advantage of visualizing fast rotational and translational motions of nanoparticle probes and the cellular environment simultaneously with sufficient angular resolution.[22,24,25]

Gold nanorods with an average size of 25 nm × 73 nm were surface-modified with polyethylene glycol (PEG), carboxyl-terminated PEG (PEG-CO_2^{2-}), transferrin[26] through PEG linkers, trans-activating transcriptional (TAT) activator (a cell penetrating peptide from Human Immunodeficiency Virus 1[17,27,28]) through PEG linkers, and two forms of polyether imide (PEI): linear 22 kDa and branched 25 kDa. (See Supplementary Figure 2 for the illustrations of the functionalized nanorods.) All of these modifiers, except PEG-CO_2^{2-}, have been used as either gene/drug delivery agents or agents that promote the delivery efficiencies of nanoparticle carriers.

The functionalized gold nanorods were tracked continuously to reveal their rotational dynamics until they were internalized by the cells or stayed on the membrane sufficiently long (> 2 hours) in non-internalization cases. **Movie 3.1** shows such an example that a PEG-CO_2^{2-}-modified gold nanorod was undergoing both translational and rotational motions on the membrane of an A549 human lung cancer cell. Unlike spherical probes, the gold nanorods displayed flickering bright/dark images for active rotational motions under the DIC microscope. Figure 2 shows the DIC intensities of the gold nanorod in 4000 consecutive images acquired at 200 fps. The two DIC intensity traces present typical fast (Figure 2C) and slow (Figure 1D) rotations of the gold nanorod as revealed by the frequencies of the DIC intensity variations in both the bright and dark parts.

To semi-quantify the rotational dynamics of gold nanorods, we analyze the stochastic DIC intensity fluctuations using the autocorrelation function.[29-31] The DIC contrast, which is defined as the difference between the bright intensity and the dark intensity divided by the background intensity, is used as the signal in computing an autocorrelation function for 4000 consecutive images in each movie. The autocorrelation curve can be satisfactorily fitted with a stretched exponential function.[29-31] (See the Supporting Information for details.) The mean relaxation time (<τ>) of decay of the autocorrelation function reflects the rotation speed of the gold nanorod, with a smaller <τ> value corresponding to a faster rotation. The mean relaxation times are 0.02 s for the fast rotation in Figure 2C and 0.48 s for the slow rotation in Figure 2D through non-linear least squares fittings (Supplementary Figure 2.2).

Using the autocorrelation analysis, we found that the time evolution of rotational dynamics of gold nanorods was tightly related to their surface charges. The functionalized nanoprobes can be categorized according to their surface charges: positively charged (TAT, linear or branched PEI), neutral (PEG), and negatively charged (PEG-CO_2^{2-}, transferrin). The positively charged particles were adsorbed quickly by the negatively charged cell membrane through electrostatic interactions, while the neutral or negatively charged particles were captured at much slower rates and usually had much longer active rotation durations on the cell membrane. For each type of functionalized nanoparticle vector, multiple examples were recorded and all of them demonstrated similar characteristic rotational dynamics.

We begin our detailed discussion with the simplest case: the linear or branched PEI-modified gold nanorods. These nanorods were strongly positively charged, and they lost their rotation almost immediately after appearing on the cell membrane due to strong electrostatic interactions. In **Movie 3.2**, a nanorod modified with branched 25-kDa PEI showed little rotation for the entire 20-s recording time. Some slight changes of DIC intensities were likely caused by the fluidity of the membranes.

TAT peptide is among the most widely used cell penetrating reagents. Although how TAT peptide enters cell membranes is still under debate, it is generally believed that a multiplicity of pathways are involved in the internalization process.[32] The TAT-modified gold nanorods with a zeta potential (ζ) of +22.3 mV had much weaker positive charges than the PEI-modified nanorods, resulting in longer periods of active rotation on the membrane. **Movie 3.3** shows six movie segments, displayed side-by-side, of the same TAT-modified nanorod at different times after its appearance on the cell membrane. The corresponding DIC intensity traces are displayed in **Supplementary Figure 3.3**. The mean relaxation time increased gradually within the first 4 minutes (**Figure 3.2A**), most likely because the TAT peptides on the nanorod surface incorporated more and more effectively into the membrane. The nanorod rotation became very slow, and nearly came to a stop after ~4 minutes on the membrane. This nanorod was eventually internalized by the cell. Similar observations were recorded for other TAT-modified gold nanorods.

PEG is a neutral polymer that is well known for resisting non-specific adsorption.[33] The PEG-modified gold nanorods (ζ = +1.5 mV) showed evident reluctance to bind firmly to the cell membrane. Desorption of the PEG-modified nanorods from the membrane occurred frequently. During the whole time these nanorods were adsorbed onto the membrane, they showed active lateral movement while maintaining high speed of rotation (**Figure 3.2B**, **Movie 3.4**, and Supplementary **Figure 3.4**). No internalization events were observed before the cells lost their viability on the microscope stage.

The PEG-CO_2^{2-}-modified gold nanorods had negative surface charges (ζ = -20 mV); thus, it was difficult for them to be adsorbed onto the negatively charged cell membrane due to electrostatic repulsion. When they did land on the membrane through nonspecific binding to the cationic sites, many of them desorbed from the membrane within seconds to minutes, which was similar to the PEG-modified nanorods. For those nanorods that stayed on the membrane, the fluctuation in rotation speed was much more significantly than that for the PEG-modified nanorods. They could slow down the rotation significantly or even come to full stop for up to a few minutes, and then resumed back to fast rotation, showing the struggles between weak binding interactions and thermal activities of the nanorod and its surrounding environment. **Figure 3.2C**, **Movie 3.5** and **Supplementary Figure 3.5** shows such an example that a nanorod rotated for a prolonged period, stopped rotation occasionally, before finally anchored on the membrane.

Finally, transferrin is a naturally occurring plasma protein involved in iron delivery. The internalization of transferrin involves the specific binding to the transferrin receptors on the cell membrane.[34] Similar to the PEG-CO_2^{2-}-modified gold nanorods, the transferrin-modified nanorods (ζ = -11.2 mV) also showed reluctance to bind onto the cell membrane due to negative charges on their surfaces. However, once they bound to the cell surface, their active rotation lasted much shorter than the PEG-CO_2^{2-}-modified ones. **Figure 3.2D**, **Movie 3.6**, and **Supplementary Figure 3.6** show such an event, during which the transferrin-modified nanorod was endocytosed within 7 minutes after it was adsorbed onto the membrane. While staying at the initial landing site on the membrane, the nanorod rotation started at fast rates, then slowed down significantly, followed by a quick return to fast rotation. This pattern of speed change happened twice before the nanorod moved laterally to a new site. At this new location, the nanorod stopped rotating for ~25 s and then was endocytosed by the cell. The lateral movement likely involved a change of binding from a non-specific site to transferrin receptors, thus facilitating receptor mediated endocytosis. As a comparison, it usually takes a much longer time (tens of minutes to hours) for the PEG-CO_2^{2-}-modified gold nanorods to be anchored on the cell membrane due to the lack of specific receptors. Thus for the first time, the distinctive rotational behaviors of the transferrin- and PEG-CO_2^{2-}-modified nanorods were revealed and convincingly attributed to the availability of specific binding sites on the cell membrane.

Conclusions

In summary, we studied real-time rotational dynamics of differently functionalized gold nanoparticle vectors on live cell membranes for the first time. The rotational behaviors of the gold nanorods were strongly related to the surface charges. Specific surface functional groups and the availability of receptors on cell membranes also contribute to the rotational dynamics of the gold nanorods. Because the gold nanorods are non-blinking and non-bleaching, they can be tracked continuously for a much longer time compared to fluorophore-based techniques. The study of rotational behaviors of gold nanoparticles on live cells can be extended to other cellular processes, such as endocytosis, exocytosis, intracellular transport and cell-cell communication, and thus bring us further on the exploration into the cell kingdom. More significantly, the studies of nanoparticle's rotational Brownian motion on cell membranes will lead to a better understanding of the nanoparticle-based drug delivery mechanisms and provide guidance in designing modification strategies for drug delivery vectors under different circumstances.

Acknowledgement

This work was supported by U.S. Department of Energy, Office of Basic Energy Sciences, Chemical Sciences, Geosciences, and Biosciences Division. The Ames Laboratory is operated for the U.S. Department of Energy by Iowa State University under contract no. DE-AC02-07CH11358.

References

(1) Dass, C. R.; Choong, P. F. M. *Peptides* 2006, *27*, 3020.

(2) Petros, R. A.; DeSimone, J. M. *Nat. Rev. Drug. Discov.* 2010, *9*, 615.

(3) Cheng, Y.; Samia, A. C.; Li, J.; Kenney, M. E.; Resnick, A.; Burda, C. *Langmuir*, 2010, *26*, 2248.

(4) Dreaden, E. C.; Mwakwari, S. C.; Sodji, Q. H.; Oyelere, A. K.; El-Sayed, M. A. *Bioconjugate Chem.* 2009, *20*, 2247.

(5) Patra, C. R.; Bhattacharya, R.; Mukherjee, P. *J. Mater. Chem.* 2009, *20*, 547.

(6) Giljohann, D. A.; Seferos, D. S.; Prigodich, A. E.; Patel, P. C.; Mirkin, C. A. *J. Am. Chem. Soc.* 2009, *131*, 2072.

(7) Kawano, T.; Yamagata, M.; Takahashi, H.; Niidome, Y.; Yamada, S.; Katayama, Y.; Niidome, T. *J. Controlled Release* 2006, *111*, 382.

(8) Lee, J.-S.; Green, J. J.; Love, K. T.; Sunshine, J.; Langer, R.; Anderson, D. G. *Nano Lett.* 2009, *9*, 2402.

(9) Wijaya, A.; Schaffer, S. B.; Pallares, I. G.; Hamad-Schifferli, K. *ACS Nano* 2009, *3*, 80.

(10) Zheng, B.; Yamashita, I.; Uenuma, M.; Iwahori, K.; Kobayashi, M.; Uraoka, Y. *Nanotechnology*, 2010, *21*, 045305/1.

(11) Verma, A.; Stellacci, F. *Small* 2010, *6*, 12.

(12) Chithrani, B. D.; Chan, W. C. W. *Nano Lett.* 2007, *7*, 1542.

(13) Chithrani, B. D.; Ghazani, A. A.; Chan, W. C. W. *Nano Lett.* 2006, *6*, 662.

(14) Cho, E. C.; Xie, J. W.; Wurm, P. A.; Xia, Y. N. *Nano Lett.* 2009, *9*, 1080.

(15) Huang, H.-C.; Barua, S.; Kay, D. B.; Rege, K. *ACS Nano* 2009, *3*, 2941.

(16) Callahan, J.; Kopeček, J. *Biomacromolecules* 2006, *7*, 2347.

(17) Tkachenko, A. G.; Xie, H.; Liu, Y. L.; Coleman, D.; Ryan, J.; Glomm, W. R.; Shipton, M. K.; Franzen, S.; Feldheim, D. L. *Bioconjugate Chem.* 2004, *15*, 482.

(18) Saxton, M. J. *Nat. Methods* 2008, *5*, 671.

(19) Sonnichsen, C.; Alivisatos, A. P. *Nano Lett.* 2005, *5*, 301.

(20) Spetzler, D.; York, J.; Daniel, D.; Fromme, R.; Lowry, D.; Frasch, W. *Biochemistry* 2006, *45*, 3117.

(21) Chang, W. S.; Ha, J. W.; Slaughter, L. S.; Link, S. *Proc. Natl. Acad. Sci. U. S. A.* 2010, *107*, 2781.

(22) Wang, G. F.; Sun, W.; Luo, Y.; Fang, N. *J. Am. Chem. Soc.* 2010, *132*, 16417.

(23) Pierrat, S.; Hartinger, E.; Faiss, S.; Janshoff, A.; Sonnichsen, C. *J. Phys. Chem. C* 2009, *113*, 11179.

(24) Pluta, M. *Advance light microscopy*; Elsevier Science Publishing Co. Inc.: New York, 1989; Vol. 2.

(25) Sun, W.; Wang, G.; Fang, N.; Yeung, E. S. *Anal. Chem.* 2009, *81*, 9203.

(26) Qian, Z. M.; Li, H. Y.; Sun, H. Z.; Ho, K. *Pharmacol. Rev.* 2002, *54*, 561.

(27) de la Fuente, J. M.; Berry, C. C. *Bioconjugate Chem.* 2005, *16*, 1176.

(28) Heitz, F.; Morris, M. C.; Divita, G. *Br. J. Pharmacol.* 2009, *157*, 195.
(29) Hess, S. T.; Webb, W. W. *Biophys. J.* 2002, *83*, 2300.
(30) Martin, J. E.; Wilcoxon, J.; Odinek, J. *Phys. Rev. A* 1991, *43*, 858.
(31) Rocker, C.; Potzl, M.; Zhang, F.; Parak, W. J.; Nienhaus, G. U. *Nat. Nanotechnol.* 2009, *4*, 577.
(32) Brooks, H.; Lebleu, B.; Vives, E. *Adv. Drug. Deliv. Rev.* 2005, *57*, 559.
(33) Xie, J.; Xu, C.; Kohler, N.; Hou, Y.; Sun, S. *Adv. Mater.* 2007, *19*, 3163.
(34) Li, H.; Qian, Z. M. *Med. Res. Rev.* 2002, *22*, 225.

Figures

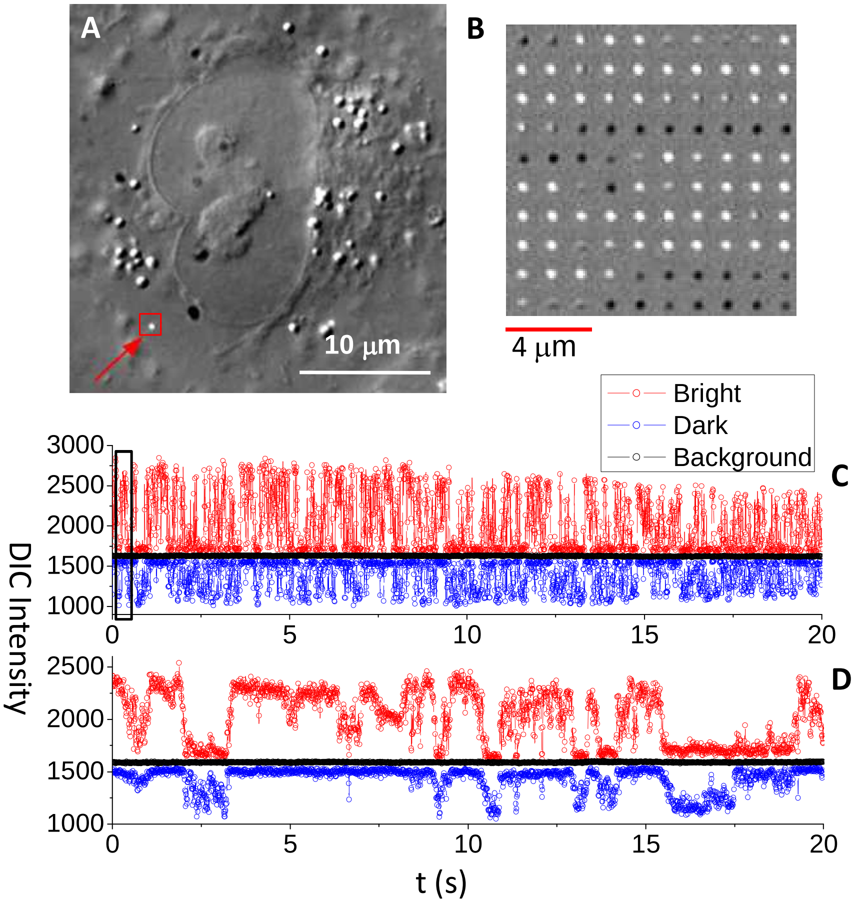

Figure 3.1. (A) DIC image of an A549 cell with a PEG-CO_2^{2-}-modified gold nanorod highlighted in the red square. (B) 100 consecutive images of the gold nanorod. (C, D) Typical DIC intensity traces as a function of time for a fast rotation (C) and a slow rotation (D). The rectangle in (C) distinguishes the intensities of the 100 DIC images shown in (B). The fast rotation trace was recorded right after the nanorod landed on the cell membrane and the slow rotation trace was recorded 7 minutes later for the same nanorod.

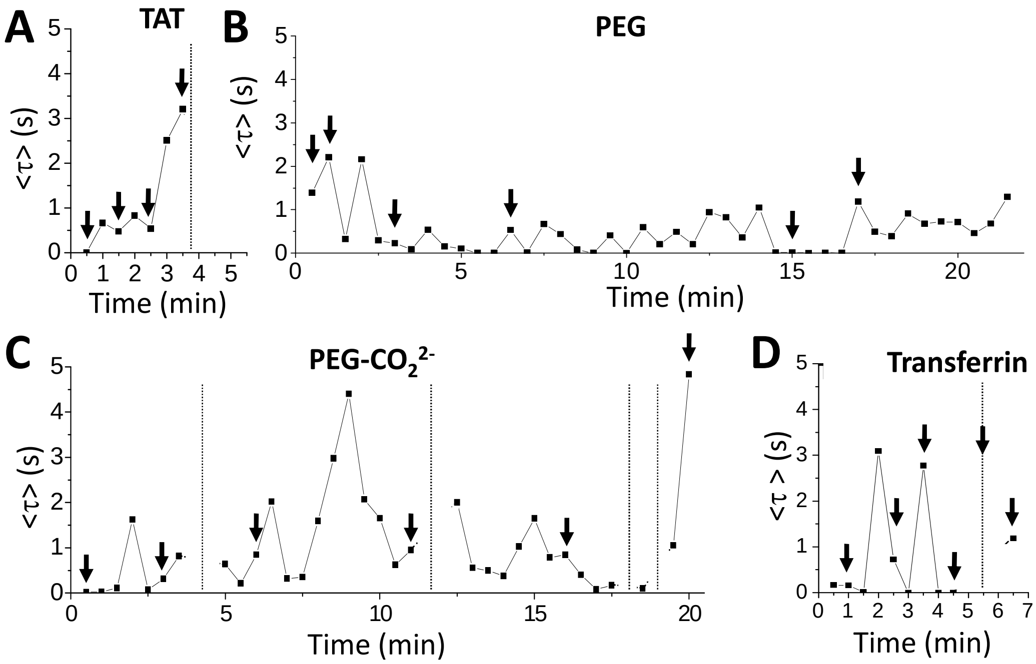

Figure 3.2. The representative evolution (at a time interval of 0.5 min) of the mean relaxation time $<\tau>$ of (A) TAT-; (B) PEG-; (C) PEG-CO$_2^{2-}$-; and (D) transferrin-modified gold nanorods on live cell membranes. Each data point was calculated from 4000 frames in a 20-s movie. The dotted vertical lines indicate the pauses of rotation, for which no mean relaxation times were calculated. The arrows point out the movie segments that are included in the corresponding movies in the Supporting Information.

Supporting Information

for

Single Particle Orientation and Rotation Tracking Discloses Distinctive Rotational Dynamics of Drug Delivery Vectors on Live Cell Membranes

*Yan Gu, Wei Sun, Gufeng Wang, and Ning Fang**
Ames Laboratory, U.S. Department of Energy and Department of Chemistry, Iowa State University,
Ames, Iowa, 50011

Experimetnal Section

DIC microscopy. An upright Nikon Eclipse 80i microscope with a pair of Nomarski prisms and two polarizers was used in this study. The microscope was equipped with a 100× 1.40 numerical aperture (NA) Plan Apo oil immersion objective and 1.4 NA oil immersion condenser. A 700-nm optical filter (Semrock, Rochester, NY) with a bandwidth of 20 nm was inserted at the illumination side. The movies were taken by an Andor iXon^{EM}+ 897 camera. The collected videos were analyzed with MATLAB and NIH ImageJ.

Surface modification of gold nanorods. The carboxylic and ctab-stabilized gold nanorods (25 nm × 73 nm) were purchased from nanopartz (salt lake city, ut). Gold nanorods were modified with peg, peg-transferrin, pei and peg-tat molecules according to the protocols below. The ctab-stabilized gold nanorods were washed twice with 18.2 mΩ deionized water to remove excessive ctab in the solution to reduce cytotoxicity.

PEG-TAT modified gold nanorods: 2 μL of 20 mM NHS-PEG-thiol solution in DMSO (Sigma Aldrich) was added to react with 200 μL pre-cleaned gold nanorod solution for 2 hours. The solution was cleaned up by centrifugation and resuspended in 2 mM borate buffer. Then, 2 μL of 2 mg/mL trans-activating transcriptional activator (TAT) peptide solution (sequence: YGRKKRRQRRR, AnaSpec, San Jose, CA) in deionized water was added for reaction for 2 hours. The final solution was washed again with 18.2 MΩ deionized water.

PEG-transferrin modified gold nanorods: 2 μL of 20 mM NHS-PEG-thiol solution in DMSO was added to react with 200 μL pre-cleaned gold nanorod solution for 2 h. The gold nanorods were then washed with 18.2 MΩ deionized water and mixed with 20 μg transferrin (Sigma-Aldrich) for 8 hours. The final solution was washed and resuspended in 18.2 MΩ deionized water.

Poly(ethylene glycol) (PEG) modified gold nanorods: 2 μL PEG-thiol (MW 5000, Sigma Aldrich, Catalog #11124, diluted to 20 mM in DMSO) was added to 200 μL pre-cleaned gold nanorods solution to react under room temperature for 2 h. The gold nanorods were then washed and resuspended in 18.2 MΩ deionized water.

Polyethyleneimine (PEI) modified gold nanorods: Two types of PEI polymers were chosen: branched PEI polymer (MW ~ 25,000, Sigma Aldrich #408727), and linear PEI polymer (MW ~ 22,000, Exgen 500 in vitro, United States Biological). In preparation, 200 μL pre-cleaned gold nanorod solution were reacted with 0.2 mg 11-mercaptoundecanoic acid

(Sigma Aldrich) for 30 min and then washed and resuspended in 1 mM NaCl solution. The gold nanorods then reacted with 0.2 mg PEI for 30 minutes at room temperature. The solution was finally washed and resuspended in 1 mM NaCl solution.

Cell culture and imaging. A549 human lung cancer cells (ATCC, CCL-185) were cultured on 22 mm × 22 mm poly-lysine coated glass coverslips in a six-well tissue culture plate. Minimum essential cell culture medium (ATCC) with 10% fetal bovine serum supplement was added to the plates. The cell culture was incubated at 37ºC under 5% CO_2. After the cell culture covered 70% of a coverslip, the coverslip was rinsed with a 10-mM phosphate buffered saline (PBS) at pH 7.4 and then placed on a clean glass slide for observation. Two pieces of double-sided tape served as spacers between the glass slide and the coverslip to form a chamber. 30 μL of the cell culture medium without BSA was added into the chamber to keep the cells from drying out and to provide the cells with some nutrition.

It is well known that proteins can be adsorbed onto the surface of functionalized nanoparticles and change the surface properties, such as the zeta potential. To minimize this effect, we took the following steps to introduce the surface-modified nanoparticles to the cell surface: (1) The cell coverslips were rinsed with the PBS buffer to remove BSA and other proteins on cell membranes; (2) A surface-modified gold nanorod solution was diluted to a final concentration of 1.0×10^9 particles/mL in the cell culture medium without BSA; (3) Immediately after the dilution, 20 μL of the gold nanorod solution was added into the chamber. Movies of single nanorod rotation were recorded when or right after a single nanorod adsorbed onto the cell membrane. The size of region of interest (ROI) was limited to 64×64 pixels in order to increase the camera's recording speed. All of the movies were taken at 200 fps.

Measurement of zeta potential in water. After the gold nanorods were functionalized with one of the surface modifiers, they were cleaned up by centrifugation and resuspension in 1 ml Milli-Q water. The zeta potential of the surface-modified gold nanoparticle, which refers to the electrostatic potential created as a result of the accumulation of electrons at the surface, was measured in Nano-ZS90 Zetasizer (Malvern Instruments, United Kingdom).

All of the surface-modified gold nanorods, except the PEI-modified ones, were stable in water at sufficiently high concentrations for measuring their zeta potentials. The zeta potentials of TAT-, PEG-, PEG-CO_2^{2-}-, and transferrin-modified nanorods in water were measured to be +22.3, +1.5, -20, and -11.2 mV, respectively. These zeta potentials did not change much during the time we carried out the experiments (up to several days).

The zeta potential for the PEI-modified nanorod was not provided here for two reasons: (1) PEI is so highly positively charged that there is no doubt that the PEI-modified nanorod is also highly positively charged, which explains its distinctive rotational dynamics on the cell membrane; (2) Due to the relatively long PEI chain and high charge density, the PEI-modified nanorod solution could only be kept relatively stable at low concentrations, which made it difficult to measure the zeta potential reliably.

Measurement of zeta potential of TAT-modified gold nanorods in the cell culture

medium. To understand how the protein adsorption to the surface of nanoparticles change their surface charges, we measured the zeta potentials of the TAT-modified gold nanorod solution diluted in the cell culture medium over a time span that is comparable to the rotation duration time. An equal amount of the cell culture medium was added into the nanorod solution for a dilution factor of two. The zeta potential was +17.8 mV in the first measurement (the measurement lasted for 1.5 min), which was a little smaller than the zeta potential measured in water (+22.3 mV). The zeta potential changed to +11.2 mV in the second measurement that occurred 1.5 min after the first measurement, and then to +6.85 mV in the third measurement. Within the duration of rotation (~3.5 min), the zeta potential changed gradually, but was still positive as it was supposed to be.

It should be noted that the surface charge in the first few minutes from the moment a gold nanoparticle starts to interact with the cell membrane is of greater significance to the present study. After the first contact, the gold nanorod was embedded gradually on the cell membrane and was less affected by the cell culture medium.

Calculation of characteristic relaxation time. The autocorrelation curve can be fitted by a stretched exponential function:[1]

$$f(t) = f_0 e^{-(t/\tau)^{\beta}}, \qquad (1)$$

where f_0 is the pre-exponential factor that is used in the fitting, τ is the characteristic time

---

constant, and β is the stretching exponent. The mean relaxation time ($<\tau>$) can be calculated as:

$$<\tau>=\int_0^\infty dt\exp(-(t/\tau)^\beta)=\frac{\tau}{\beta}\Gamma(\frac{1}{\beta}), \qquad (2)$$

where Γ denotes the Gamma function. $<\tau>$ of the decay reflects the rotating speed of the gold nanorod, with a smaller $<\tau>$ value corresponding to a faster rotation. The mean relaxation times of the stretched exponential decays are 0.02 s for the fast rotation and 0.48 s for the slow rotation through non-linear least squares fittings (**Supplementary Figure 3.2**).

It should be noted that this analysis gives accurate rotational information only if the nanorods rotate neither too fast nor too slow. The imaging rate of 200 fps used in this study is adequate to characterize the rotation of the functionalized nanorods that are restricted and slowed down by electrostatic and binding interactions on the cell membrane. The fastest rotation rate that can be resolved by the 200-fps imaging rate is 100π radians/s or 50 rounds/s, which happens when a nanorod rotates 90° during the 5-ms time interval between two consecutive frames. On the other hand, if a nanorod is fixed or rotates very slowly, which can be identified by inspecting the recorded intensity series, the uncertainties in DIC intensity measurement become a dominant factor, thus leading to inaccurate assessment of rotational motions. The slowest observable rotation happens when a nanorod takes only one full circle in the entire 20-s recording time for each movie.

References:

1. S. T. Hess and W. W. Webb, *Biophysical Journal* **83** (4), 2300 (2002).
2. J. E. Martin, J. Wilcoxon, and J. Odinek, *Physical Review A* **43** (2), 858 (1991).
3. C. Rocker, M. Potzl, F. Zhang et al., *Nature Nanotechnology* **4** (9), 577 (2009).

Figures

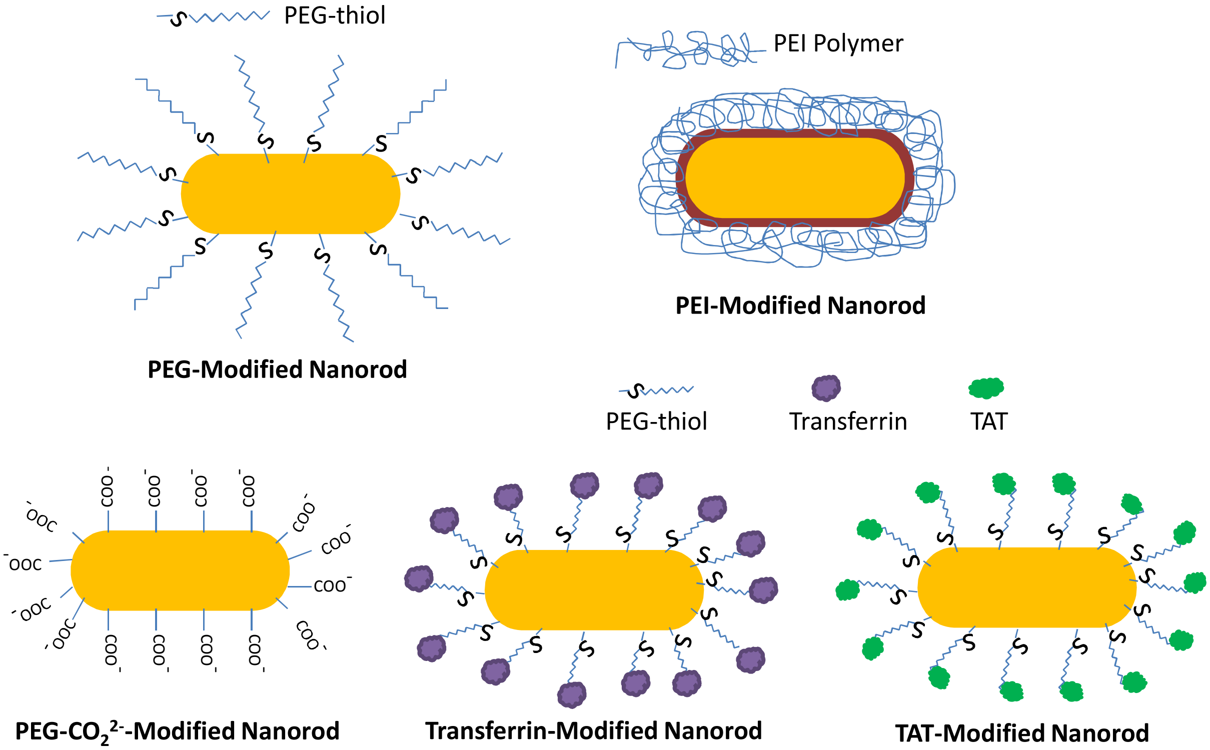

PEG-Modified Nanorod

PEI-Modified Nanorod

PEG-CO$_2$$^{2-}$-Modified Nanorod

Transferrin-Modified Nanorod

TAT-Modified Nanorod

Figure 3.S1. The schematic illustrations of the functionalized nanorods.

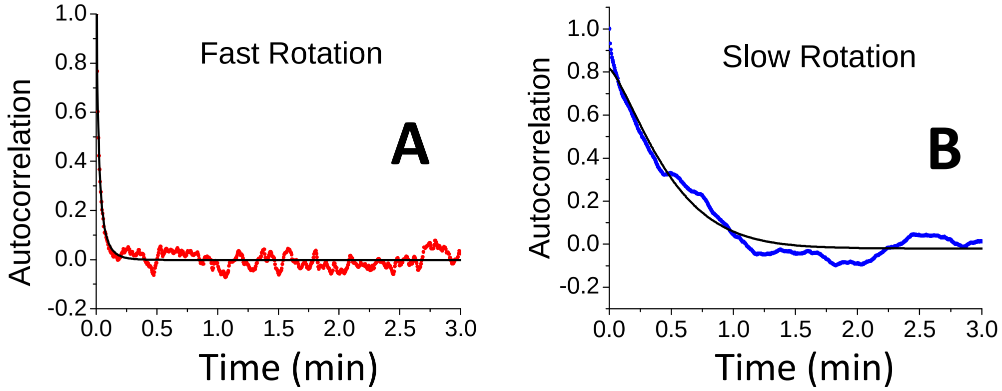

Figure 3.S2. Autocorrelation analysis for (A) fast and (B) slow rotational dynamics. The autocorrelation curves (red and blue) are satisfactorily fitted with a stretched exponential function (black). The mean relaxation times are 0.02 s for the fast rotation (raw data in Figure 2.1C) and 0.48 s for the slow rotation (raw data in Figure 2.1D).

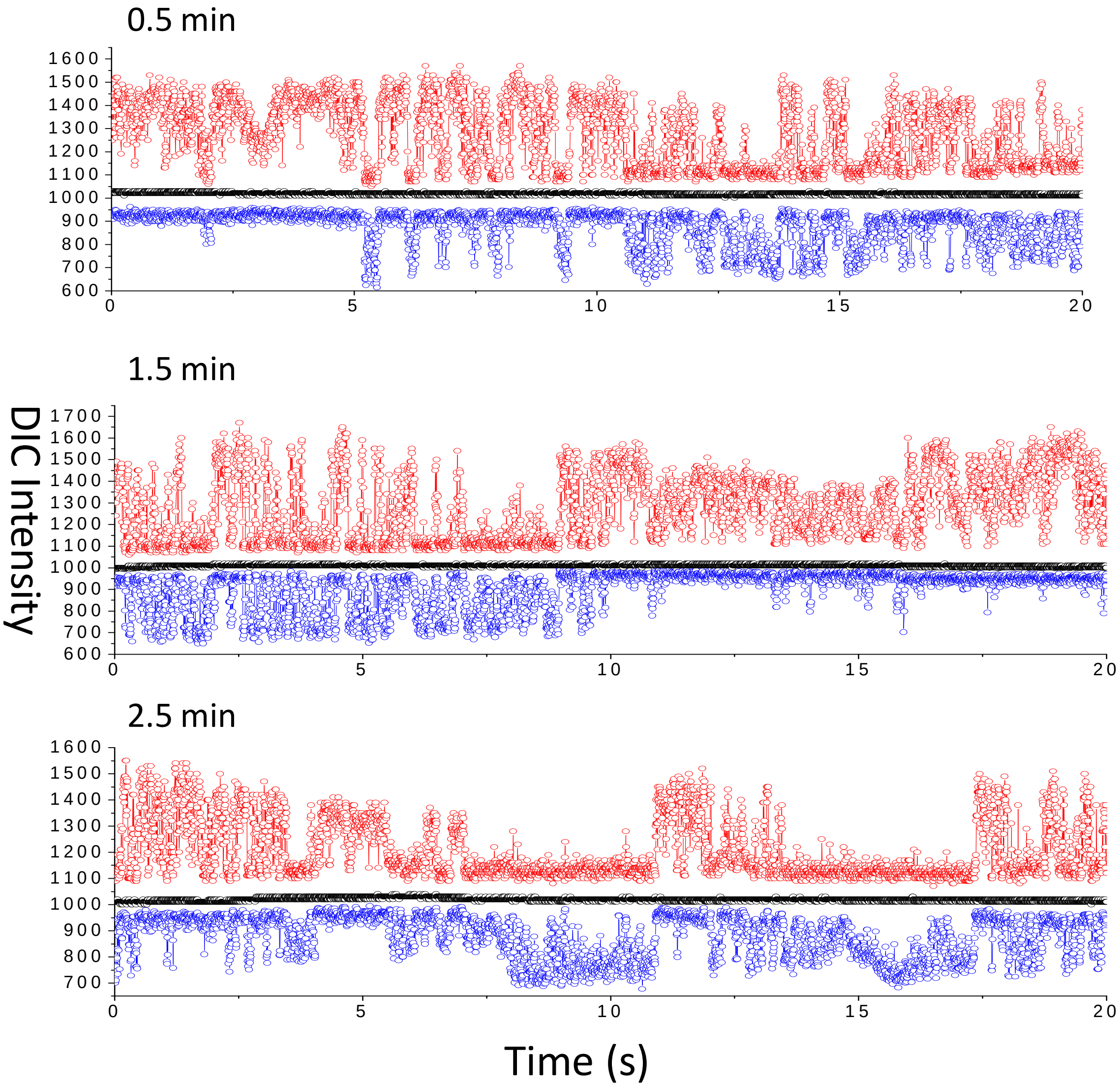
0.5 min
1600
1500
1400
1300
1200
1100
1000
900
800
700
600
0
5
10
15
20
1.5 min
DIC Intensity
1700
1600
1500
1400
1300
1200
1100
1000
900
800
700
600
0
5
10
15
20
2.5 min
1600
1500
1400
1300
1200
1100
1000
900
800
700
0
5
10
15
20
Time (s)

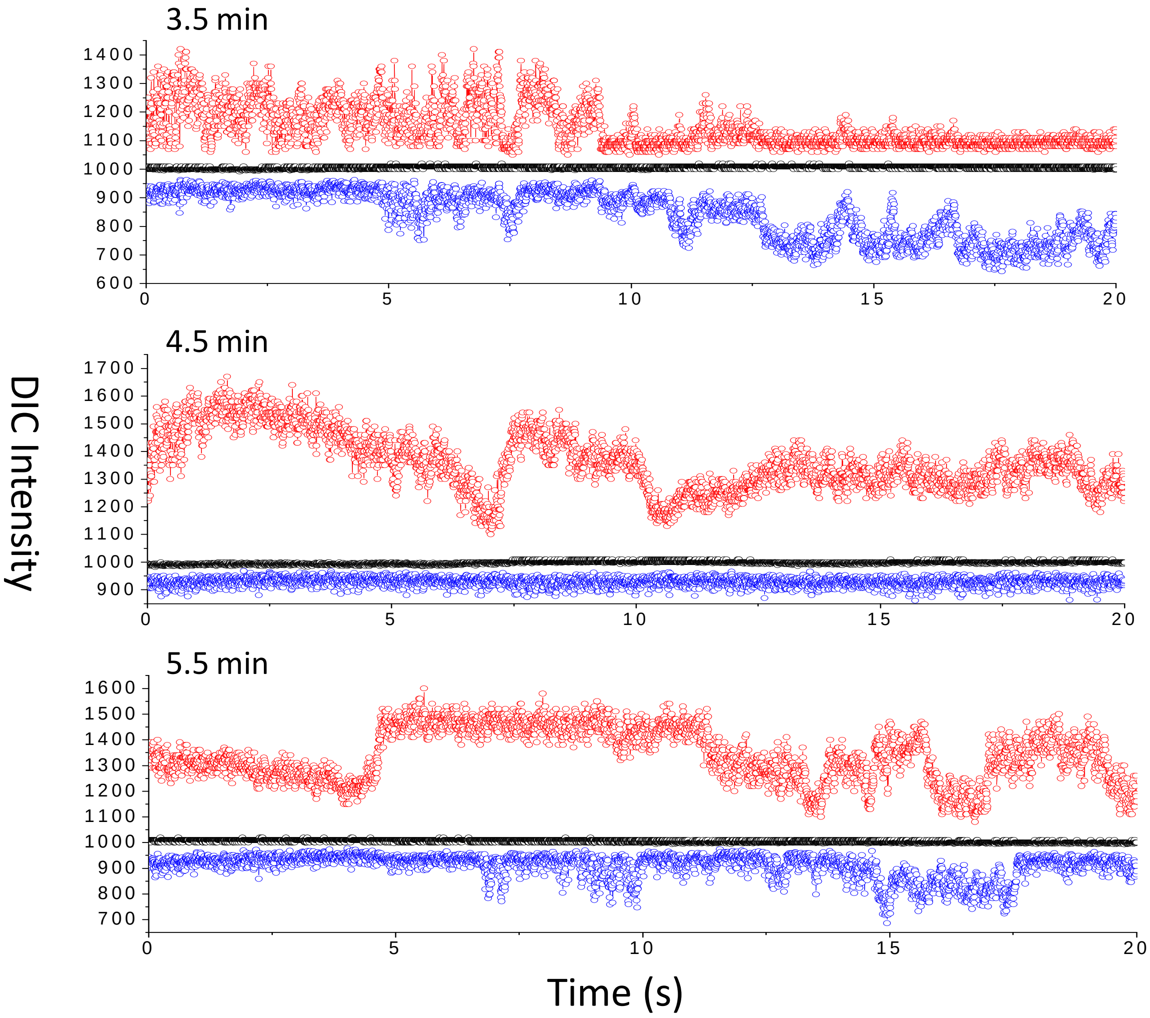

Figure 3.S3. Selected DIC intensity traces of a TAT-modified gold nanorod.

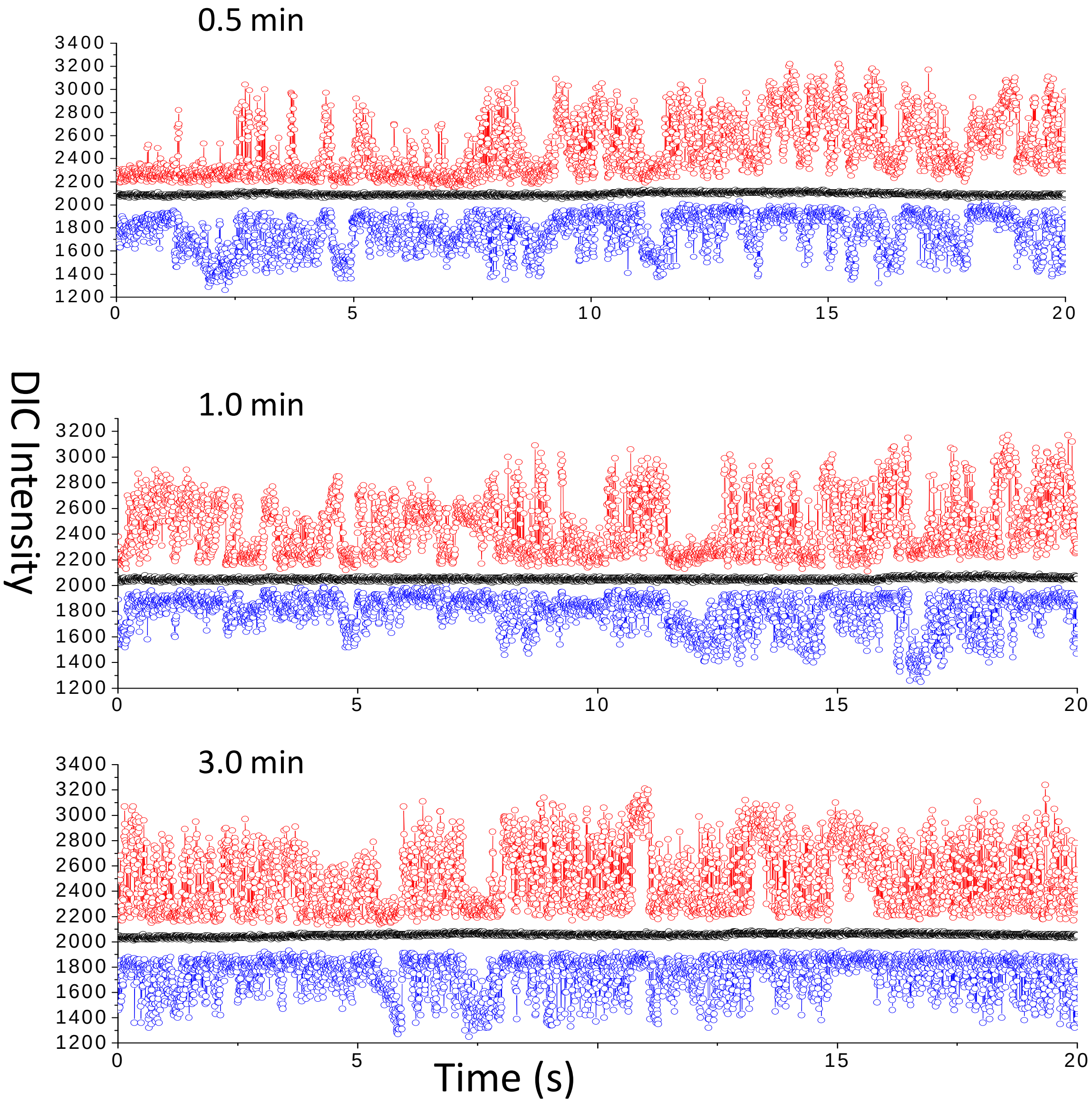
0.5 min
3400
3200
3000
2800
2600
2400
2200
2000
1800
1600
1400
1200
0
5
10
15
20
DIC Intensity
1.0 min
3200
3000
2800
2600
2400
2200
2000
1800
1600
1400
1200
0
5
10
15
20
3.0 min
3400
3200
3000
2800
2600
2400
2200
2000
1800
1600
1400
1200
0
5
15
20
Time (s)

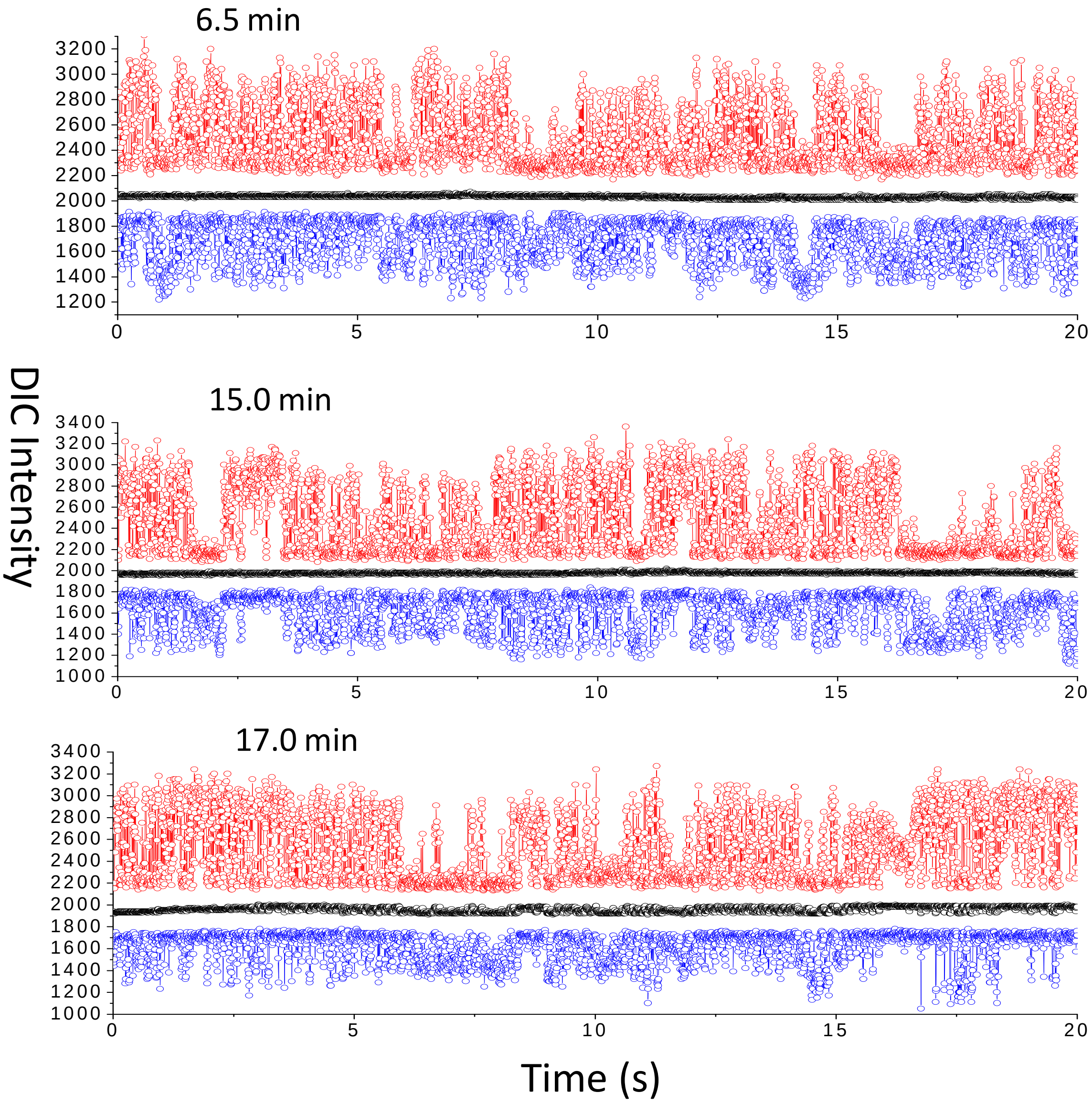

Figure 3.S4. Selected DIC intensity traces of a PEG-modified gold nanorod.

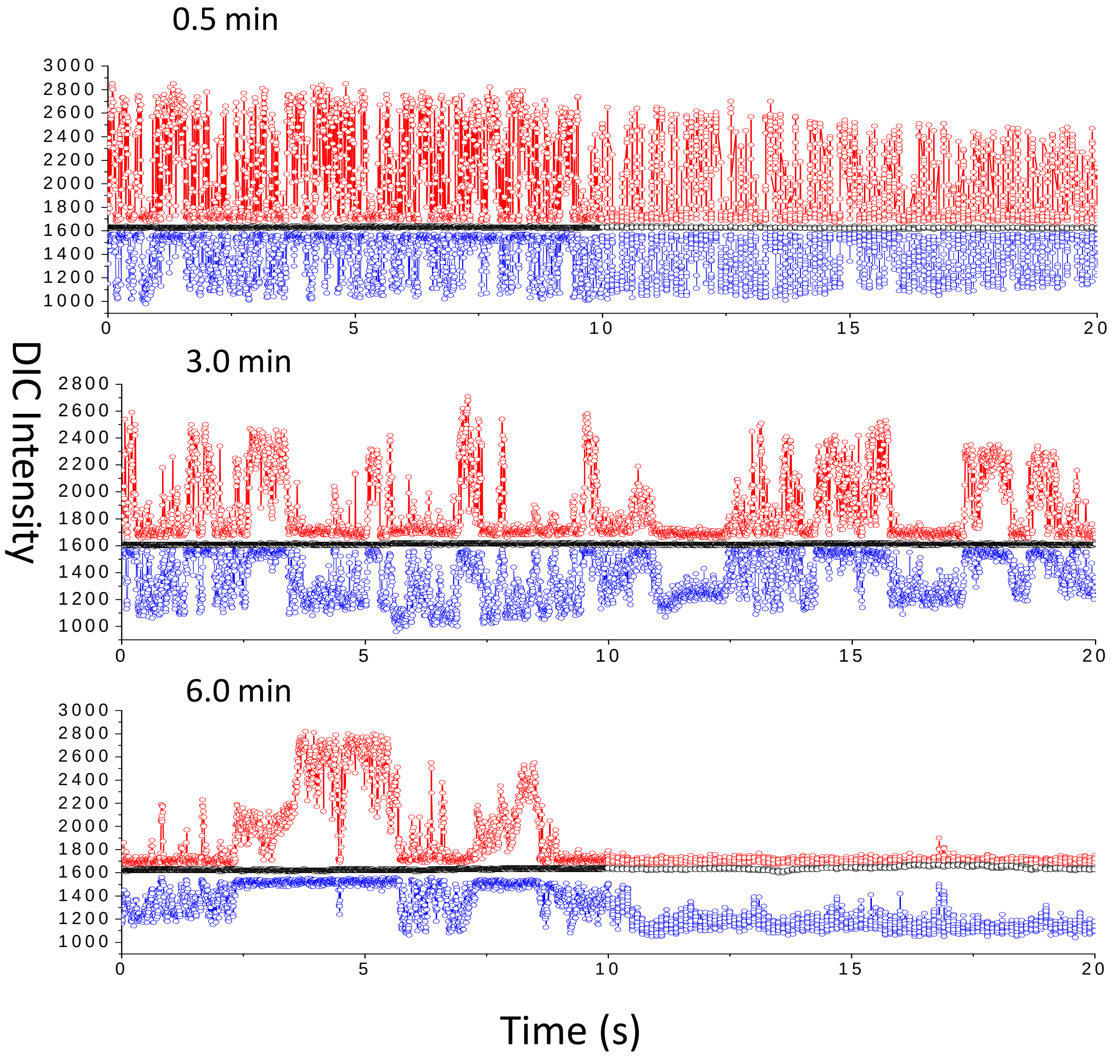
0.5 min
3000
2800
2600
2400
2200
2000
1800
1600
1400
1200
1000
0
5
10
15
20
DIC Intensity
3.0 min
2800
2600
2400
2200
2000
1800
1600
1400
1200
1000
0
5
10
15
20
6.0 min
3000
2800
2600
2400
2200
2000
1800
1600
1400
1200
1000
0
5
10
15
20
Time (s)

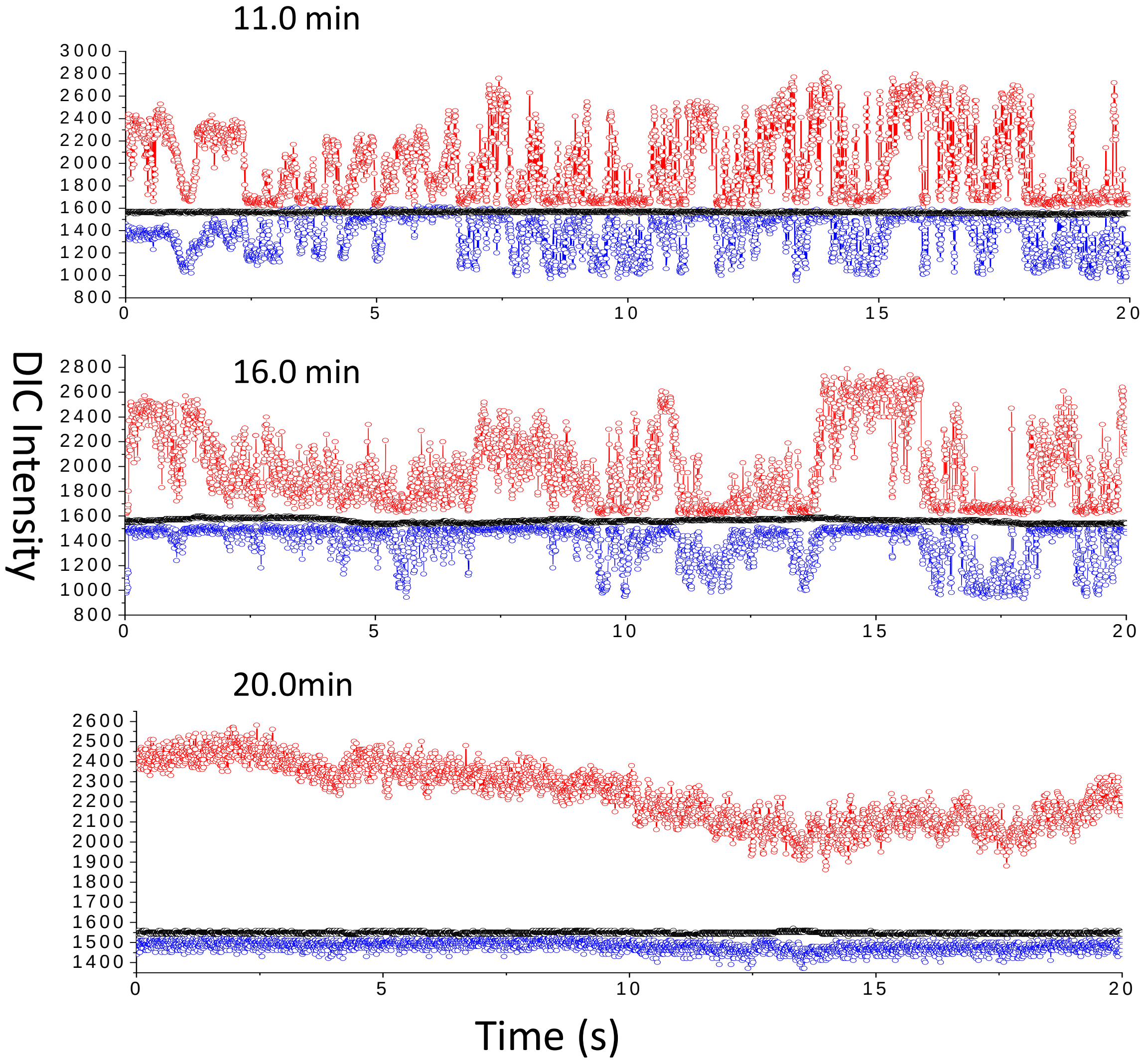

Figure 3.S5. Selected DIC intensity traces of a PEG-CO_2^{2-}-modified gold nanorod.

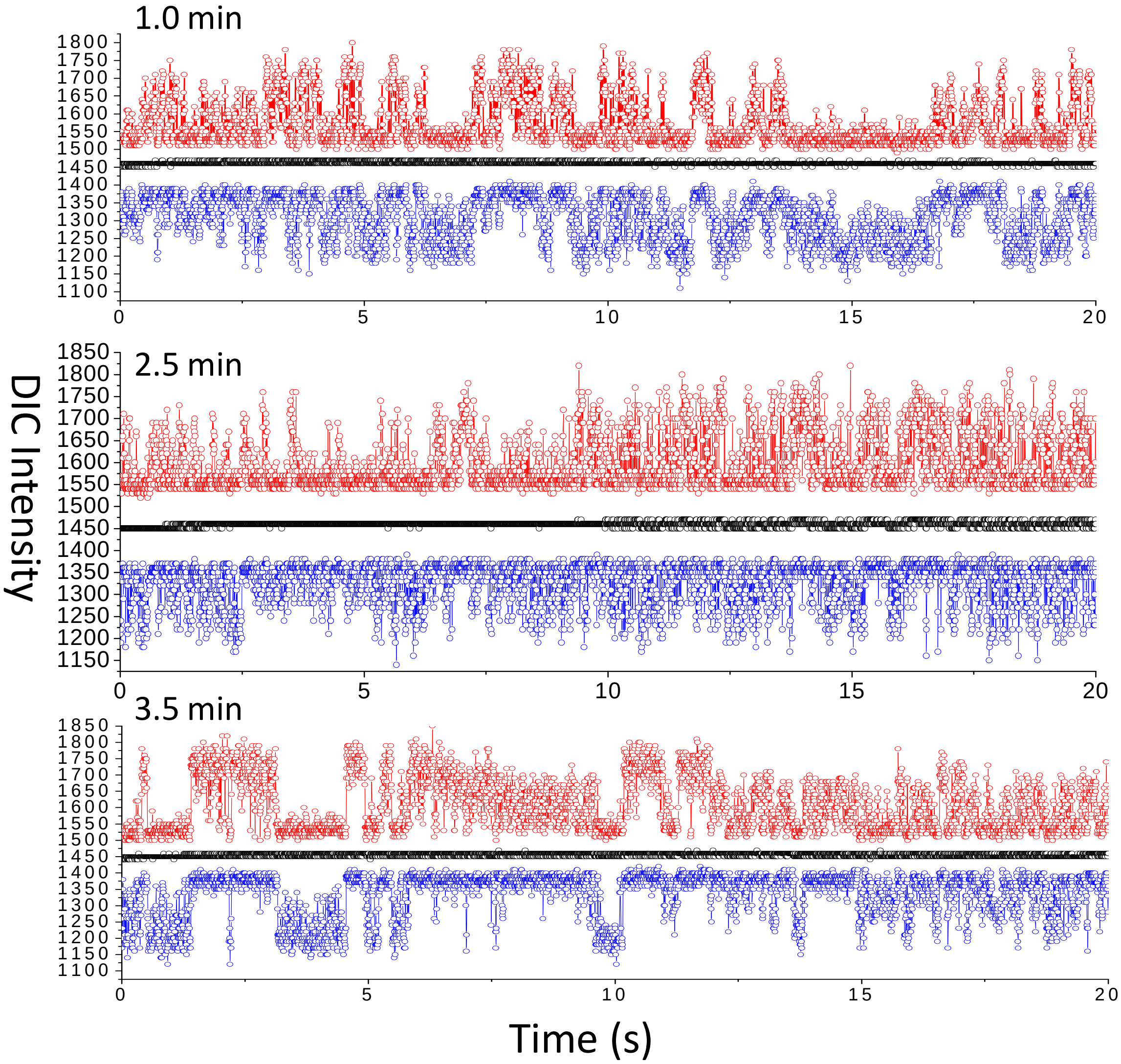
1.0 min
2.5 min
3.5 min
DIC Intensity
Time (s)
1800
1750
1700
1650
1600
1550
1500
1450
1400
1350
1300
1250
1200
1150
1100
1850
0
5
10
15
20

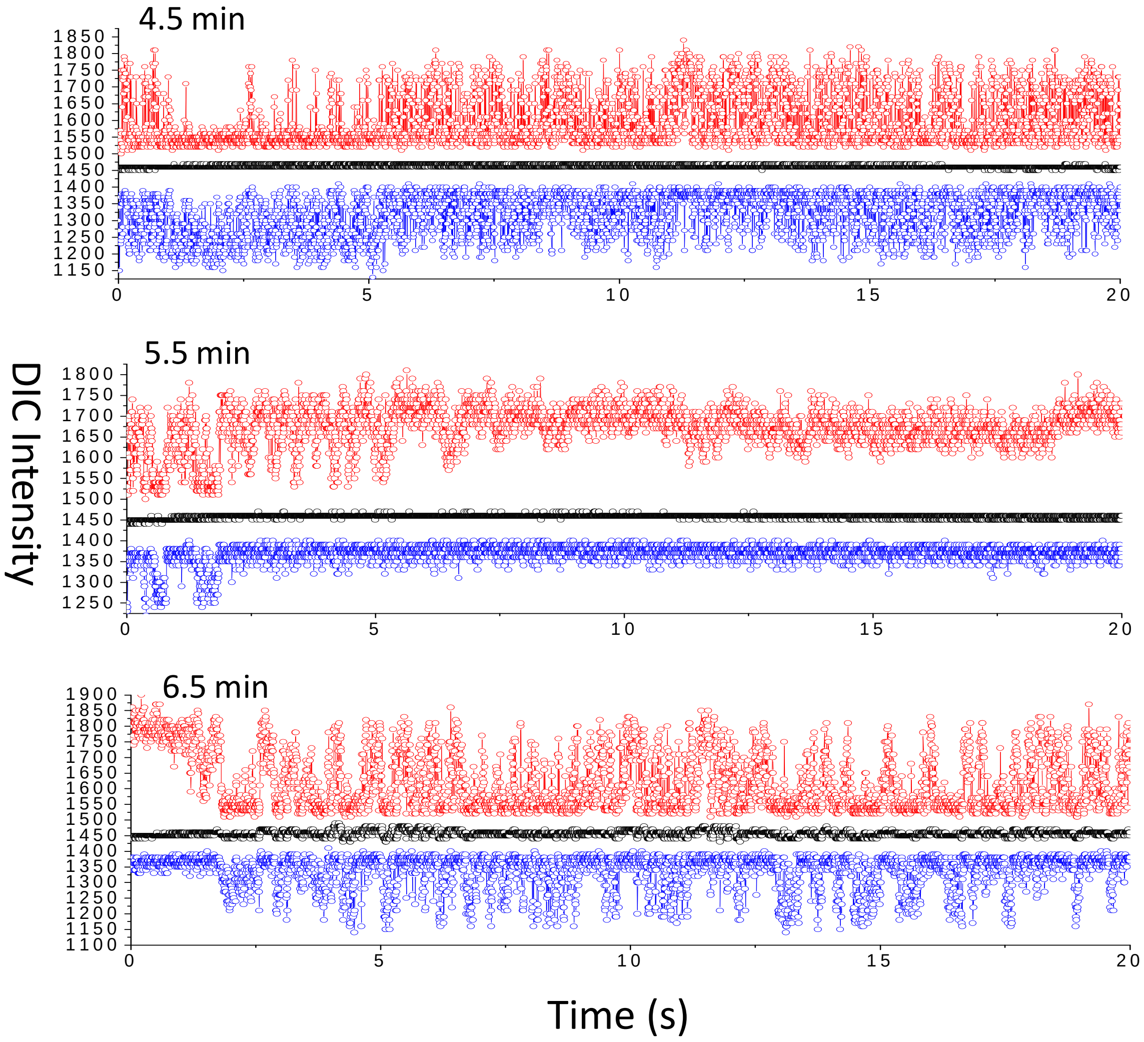

Figure 3.S6. Selected DIC intensity traces of a transferrin-modified gold nanorod.

CHAPTER 4

REVEALING ROTATIONAL MODES OF FUNCTIONALIZED GOLD NANORODS ON LIVE CELL MEMBRANES

A Paper published in *Small*

2013, *9(5)*, 785-792

*Yan Gu, Wei Sun, Gufeng Wang, Michael T. Zimmermann, Robert L. Jernigan and Ning Fang**

Y. Gu, Dr. W. Sun, Dr. G. Wang, Prof. N. Fang
Ames Laboratory, U.S. Department of Energy and Department of Chemistry
Iowa State University, Ames, Iowa, 50011-3111
Dr. M. T. Zimmermann, Prof. R. L. Jernigan
Laurence H. Baker Center for Bioinformatics and Biological Statistics
Department of Biochemistry, Biophysics and Molecular Biology, Iowa State University
Ames, IA 50011-3020
Dr. W. Sun
Current address: Department of Chemistry, the University of Washington, Seattle, WA 98195
Dr. G. Wang
Current address: Department of Chemistry, North Carolina State University, Raleigh, NC 27695

Abstract

A full understanding of cell mechanics requires knowledge of both translational and rotational dynamics. The single particle orientation and rotational tracking (SPORT) technique is combined here with correlation analysis to identify the fundamental rotational modes: in-plane rotation and out-of-plane tilting, as well as other more complex rotational patterns, from the vast image data captured at a temporal resolution of 5 ms for single gold nanorod probes in live cell imaging experiments. The unique capabilities of visualizing and understanding rotational motions of functional nanoparticles on live cell membranes allow us to correlate rotational and translational dynamics in unprecedented detail and provide new insights into complex membrane processes. Particles with functionalized surfaces, which interact with the membrane in fundamentally different ways, can exhibit distinct rotational modes and are, for the first time, directly visualized, and these show the early events for membrane approach and attachment.

Introduction

Fully understanding cell mechanics requires knowledge of not only translational but also rotational motions of biomolecules. Fluorescence polarization techniques have been commonly attempted to probe rotational motions of biomolecules using organic dyes, conjugated polymers, and inorganic semiconductor nanocrystals [1-7]; however, the well-known limitations of fluorescence-based techniques, such as fluorescence intermittency and high photobleaching tendency, have limited their applicability to live cell imaging, especially when long imaging time and high tracking precision are required.

Plasmonic gold nanoparticles have been demonstrated to provide excellent alternatives to fluorescent probes for cell imaging experiments [8-15]. Optically anisotropic gold nanorods are particularly useful for single particle orientation and rotational tracking (SPORT) because of their orientation-dependent optical responses under a variety of imaging tools, including polarization-sensitive dark-field microscopy [16, 17], absorption-based photothermal imaging [18], and differential interference contrast (DIC) microscopy [15]. The DIC microscopy-based SPORT technique provides additional advantages for live cell imaging, such as higher spatial resolution, shallower optical sectioning, and significantly reduced interference from light scattered by cellular components and debris when compared to dark-field microscopy, and faster imaging rate (down to a few milliseconds temporal resolution [19]) than raster-scanning photothermal imaging.

Using the DIC microscopy-based SPORT technique, we have demonstrated that the rotational rate of a nanorod probe resting on the cell membrane can be semi-quantified through autocorrelation analysis of the time series of DIC contrast fluctuations recorded at a temporal resolution of 5 ms [19]. Represented by the characteristic time of the stretched exponential decay that fitted the autocorrelation of the DIC intensities, the rotational rate characterizes how fast the nanorod rotates on the cell membrane. The distinctive changing patterns of rotational rate of surface modified gold nanorods on cell membranes were shown to correlate with their surface charges and the availability of specific membrane receptors, demonstrating the ability of SPORT to interrogate different types of particle-membrane interactions.

In addition to the rotational rate, the rotational mode is another essential property providing important insights into the interactions between nanoparticles and cell membranes. Considering the vast amount of noisy data collected from typical membrane studies, it is challenging to resolve the rotational modes of the nano-objects performing random rotational diffusion on cell membranes. In the present study, the SPORT technique extends its reach through the introduction of statistical correlation coefficient analysis to identify the basic rotational modes: in-plane rotation and out-of-plane tilting, with the cell membrane plane as the reference. All rotational behaviors of gold nanorods on cell membranes can be seen as a combination of the two basic modes, and the two components are mixed in different proportions, exhibiting various degrees of randomness. Random rotational behavior is mentioned with special emphasis because it is associated with distinctively different binding characteristics on the membrane, and corresponds to the various degrees of rotational freedom.

To demonstrate the power of the current method to reveal the characteristic rotational mode on live cell membranes, we study how single functionalized gold nanorods behave during the adhesion process, which is loosely defined in the present work as the first 30 seconds from the moment a nanorod makes the first contact with the cell membrane.

Nanoparticle adhesion to the cell membrane is an important indicator of the internalization efficiency. In these experiments, the gold nanorods with an average size of 25 nm × 73 nm were functionalized with two distinctively different surface modifiers: a cell penetrating peptide (CPP) from the HIV-1 protein Tat [12, 20, 21] (residues 47-57: YGRKKRRQRRR) and transferrin (a glycoprotein used as a drug delivery agent [22]). The cationic Tat CPP interacts with the cell membrane through electrostatic interactions and bidentate hydrogen bonding of the cationic guanidinium groups to anionic cell surface groups, resulting in effective incorporation of CPP-modified gold nanorods into the cell membrane [23-25]. For the other modification, the negatively charged protein transferrin is bound on the cell membrane through specific ligand-receptor binding interactions [26]. The different characteristics of these two surface modifiers give rise to distinctively different rotational behaviors of the bio-conjugated gold nanorods.

Results

Basic Rotational Modes

In our previous reports on the SPORT technique [15, 27], the gold nanorods immobilized on a glass coverslip were positioned at different orientations during a 360° rotation of the sample with 5° steps. This perfect in-plane rotation results in correlated intensity changes in the bright and dark parts of the DIC images. This correlation is also predictable from the simplified mathematical equations derived in the previous report [15] for a gold nanorod oriented with the elevation angle ψ and the azimuthal angle ϕ. In the current study, the correlation analysis is used to extract the rotational information on single gold nanoparticles from the vast DIC intensity data that are otherwise difficult to interpret. Although it has been demonstrated that the **rotational rate** could be derived from methods such as power spectral density analysis [16] or autocorrelation analysis [28], this is the first time that the information about the **rotational mode** is being extracted.

As depicted in **Figure 4.S1** in the Supporting Information, the bright and dark intensities are *correlated*, i.e., the two intensity values increase or decrease together, as the nanorod rotates in a horizontal plane with a fixed angle ψ and a varying angle ϕ, or *anti-correlated*, i.e., the two intensity values change in opposite directions, when the gold nanorod rotates out of the horizontal plane with a fixed angle ϕ and a varying angle ψ. Therefore, the rotational patterns of a single gold nanorod can be characterized by the extent of the correlation of the bright and dark intensities of its DIC images. This is described by Pearson's correlation coefficients r, which have a maximum value of +1 when the two are perfectly correlated, a minimum value of -1 when the two are perfectly anti-correlated, and a value of 0 if two variables are fully independent. It should be noted that the correlated cases illustrated in **Figure 4.S1** do not produce a perfect correlation score of +1 because the two simulated intensities do not have a perfect linear interdependency (**Figure 4.S1h**).

The basic rotational modes – in-plane rotation and out-of-plane tilting – are identified by characterizing the correlation between the bright and dark DIC intensities from both computer simulations and from the live cell imaging experiments (**Figure 4.1**). The computer simulations have been carried out for a rotating nanorod with one end permanently attached to the center of a hemisphere and the other end taking random movements on the surface of the hemisphere. To depict the nanorod's rotational Brownian motion, both the rotation direction and step size are randomized. To account for relative errors of around 10% in the intensity measurement in the actual imaging experiments, a Gaussian noise of 10% was added to the simulated DIC intensities displayed in **Figure 4.**. The simulation results in the presence of different noise levels are shown in **Figure 4.S2-4**.

For the in-plane rotational mode, the nanorod rotates clockwise or counter-clockwise at each step with equal probability while keeping the angle ψ constant. The trace of the moving end of the nanorod is limited within a circle on the hemisphere for the 4000 random steps (**Figure 4.1a**). The generated DIC bright and dark intensities are clearly correlated (an example shown in **Figure 4.1b**). The average correlation coefficient for 100 simulation runs with a fixed angle ψ of 30° is 0.84 with a standard deviation of 0.02. In this mode, the correlation coefficient is not affected either by varying the angle ψ or by limiting the range of the angle ϕ. An example of this rotational mode recorded on the live cell membrane is displayed in **Figure 4.1c and 4.1d**. The correlation coefficient for this example is 0.81, suggesting predominantly in-plane rotational motion. This mode may be interpreted as that the nanorod rotation being restrained to the membrane plane by strong interactions, which might include either specific receptor binding or more general nanorod-membrane interactions.

In the out-of-plane tilting mode, which is describable as a seesaw-like motion, the nanorod's rotating end swings out of the horizontal plane while keeping the azimuthal angle ϕ constant (**Figure 4.1e**). An example with a fixed angle ϕ of 60° is shown in **Figure 4.1f**. At first glance, the bright and dark intensity curves do not appear to be anti-correlated as might be expected based on the curves in **Figure 4.S1g**. This is explained by the fact that when the angle ϕ is fixed at 60°, a nanorod's projection on the dark axis is smaller than its projection on the bright axis resulting in much smaller changes in the dark intensity, which is nearly indistinguishable to the eye because of the 10% Gaussian background noise. The average correlation coefficient for 100 simulation runs at this noise level is -0.54 with a standard deviation of 0.06, still suggesting that there is a significant anti-correlation between the bright and dark intensities. Changing the range of the angle ψ does not significantly affect this correlation coefficient. In the actual live-cell imaging experiments, we encounter almost no negative correlation coefficients. This may be ascribed to two facts. First, a nanorod can easily change its angle ϕ on the relatively flat and fluid cell surface to produce a persistent in-plane rotation component. Second, similarly to other optical microscopic techniques, the vertical angular resolution is far poorer than the lateral angular resolution so that the signals arising from out-of-plane motions are more affected by noise. Nonetheless, the out-of-plane tilting mode can be identified by the visual cue that there are no alternating bright/dark changes, but only changes in either bright or dark intensity. **Figure 4.1g and 4.1h** shows a representative example with a correlation coefficient of 0.26. It is worth noting that it takes much stronger forces to stop the nanorod’s in-plane rotation in the fluid cell membrane; therefore, this motion is likely due to the vertical motions of the nanorod along with the fluctuation of the membrane surface while their rotational motions in the horizontal plane are impeded by strong, multi-point binding interactions.

Other rotational patterns on cell membranes can be treated as a mixture of the in-plane rotation and out-of-plane tilting motions at different ratios and with different restrictions on the rotational angle ranges. One important case is seen where a nanorod rotates completely freely in 3D space, with its rotational motions comprised of equal proportions of the two basic modes. This special case is designated here as “3D wandering” below. **Figure 4.1i** shows a simulated example of the 3D wandering case with the walking trace of the free end covering the entire surface of the hemisphere. The average correlation coefficient for 100 simulation runs with 10% Gaussian noise is 0.39, with a standard deviation of 0.08. A representative example for the live cell membrane, having a correlation coefficient of 0.38, is shown in **Figure 4.1k and 4.1l**. The 3D wandering motion is observed for a nanorod with high rotational freedom in 3D space, while experiencing relatively weak interactions with the membrane.

Another special case occurs when the nanorod is fixed on the membrane with no motion, and then the noise becomes the dominant factor in the correlation analysis and results in correlation scores near 0. This special case can be readily identified by examining the bright and dark DIC intensity traces directly.

A nanorod's full rotational motion in 3D is more complex than the examples shown in **Figure 4.1**, and the next level of complexity arises when the nanorod cannot rotate through the entire 360°, either vertically or horizontally, due to either external forces or steric hindrance. It is challenging to extract additional information about the rotational angle ranges from only the bright and dark DIC intensity traces, especially when the angular resolution is sacrificed for faster temporal resolution. Some examples of more complex rotational patterns are discussed in the Supporting Information and **Figures 4.S5 and 4.S6**.

Although some ambiguity is inevitable for more complex rotational behaviors, the present method still provides important new information about fast rotational Brownian motions. Next, the correlation coefficients of DIC bright and dark intensities will be used to characterize different rotational behaviors of gold nanorods with different surface properties on synthetic lipid bilayers and live cell membranes.

Rotational Dynamics of Gold Nanorods on Synthetic Lipid Bilayers

To elucidate how interactions between functionalized gold nanorods and lipid bilayers affect the rotational behavior, gold nanorods with different surface properties have been introduced onto the synthetic lipid bilayers having various compositions, and their rotational modes were evaluated using correlation analysis of the bright and dark DIC intensities. The detailed discussion and additional methods are provided in the Supporting Information and

Figure 4.S7.

Rotational Modes of Surface Modified Gold Nanorods on Live Cell Membranes at First Contact

In the live cell experiments, the colloidal solution containing gold nanorods having surface-modifications with either Tat CPP or transferrin were introduced to the cell sample slides on a microscope stage. The microscope objective's focal plane was at the membrane surface and the camera began recording before the nanorods appeared on the cell membrane, to ensure that the first contacts were captured. The distinctive rotational behaviors of the Tat CPP and transferrin-modified gold nanorods are described as follows.

The arginine-rich Tat CPP carries positive charges on the peptide. Due to the favorable electrostatic attraction between the Tat CPP-modified gold nanorods and the cell membrane, these nanorods readily adsorb onto the membrane and start fast rotations on the cell membrane.[19] A total of 133 Tat CPP-modified nanorods with first contacts on cell membranes have been recorded and analyzed. The correlation coefficients calculated from the first 200 frames captured within 1 s following the nanorod appearance on the membrane are shown as a histogram (**Figure 4.2a**). The Gaussian fitting of the histogram shows that the distribution of the correlation coefficients is centered around 0.55. The correlation coefficient tends to increase over time, and a histogram of the correlation coefficients calculated from 200 frames captured after the first 35 s is shown in **Figure 4.2c**.

A typical example (available in **Movie 4.1**) is presented in **Figure 4.2b**, where the correlation coefficient increases from 0.54 to 0.85 over a time span of 35 s with its corresponding DIC intensity traces over the same time span shown in **Figure 4.S8**. Such a time span is smaller than the reported time scale before the endocytosis or uncoated cell surface invagination process initiated [29]. The initial smaller correlation coefficient indicates a more random rotational motion on the cell membrane, which coincident with the first stage of rotation due to the resistant interaction with the cell membrane in the simulated results reported elsewhere [30]. The increase in correlation coefficient suggests that the nanorod has an increasing in-plane rotation component, which may be attributed to stronger and more stable interactions forming between the nanorod and the cell membrane and the additional hydrogen-bonding of the cationic guanidinium groups to anionic cell surface groups [25]. In other words, the nanorod's motion becomes more restrained to the in-plane rotational mode as it becomes more tightly bound to the cell membrane with multiple interactions.

Another intriguing observation shown in **Figure 4.2b** is that the correlation coefficient drops twice to about 0.3: the first time at 13-17 s and the second time at 26-27 s. A careful inspection of the DIC intensity traces in **Figure 4.S8** reveals that these two drops correspond to two completely different rotational behaviors of the nanorod. In the first case, the significant changes in both bright and dark intensities suggest frenetic swings and tumbling moves of the nanorod with a large component of out-of-plane tilting. In the second case, the nearly constant bright intensity suggests out-of-plane tilting, where the nanorod has lost most of its rotational freedom and is likely locked onto the membrane transiently by relatively strong interactions and possibly due to the deformation of the cell membrane, since the cationic Tat CPP modified gold nanorods could induce membrane deformation readily due to the disruption of the membrane [31].

The observed fluctuations in correlation coefficients are most likely the consequences of the competition between the thermal motions of the nanorod and the forces from the cell membrane, and have been observed for all of the Tat CPP-modified nanorods that were imaged in our experiments. It is possible for a nanorod to show apparent tilting motion when it actually is undergoing unrestricted random rotations. To obtain semi-quantitative information about the occurrence and duration of the apparent tilting events during unrestricted random rotations, we ran a series of angular random walk simulations (**Figure 4.S9**). The simulations show that the apparent tilting events occur less frequently and their durations become shorter as the rotational rate increases, which demonstrates well the intended application of this method - to study fast rotational dynamics. On the other hand, the tilting motion could also be due to the local cell membrane deformation, especially when the rotation is slowed down. From computer simulation results, it has been reported that the cell membrane could deform because of the embeded nanoparticles [30, 32]. Due to the interplay and elastic deformation of the membrane, the nanorod could be pushed to be tilted as perpendicular as possible to the cell membrane substrate, which also explained our observations. For the drop of the correlation coefficient happened at 26-27 s of the Tat CPP modified gold nanorod, the rotation slowed down, which could also be due to the local deformation of the cell membrane [16]. It is possible that the nanorod caused the local membrane to deform, while the deformed membrane caused the nanorod to slow down its rotation and was oriented perpendicularly to the cell surface, which result in a small correlation coefficient reflecting a tilting motion. Considering that the Tat CPP is cationic, the Tat CPP modified gold nanoparticles could cause membrane defects [33, 34], which facilitates the membrane deformations.

It is well known that negatively-charged transferrin enters the cell through receptor-mediated endocytosis.[26] The unfavorable electrostatic repulsion between the transferrin-modified nanorods and the predominantly negatively-charged cell membrane makes it more difficult for these nanorods to adsorb to the cell membrane.[19] The major forces that these nanorods must overcome are electrostatic repulsions in order to land on the cell membrane and achieve specific ligand-receptor binding or electrostatic interactions with cationic sites on the membrane. The distribution of the correlation coefficients is centered around 0.64 with a larger slope for the left side of the histogram (**Figure 4.2d**) for the 100 transferrin-modified nanorods taken from the first 200 frames following initial contact with the membrane. The specific binding to membrane receptors provides strong forces to restrain the nanorods from swinging out of the membrane plane, which results in a higher proportion of in-plane rotational motions and larger correlation coefficients. The contributions from electrostatic repulsion are evident in many recorded events where the nanorods separate from the membrane within seconds to minutes after their adsorption. A typical example is shown in **Figure 4.S10**. This transferrin-modified gold nanorod showed typical 3D wandering motions for ~5 s with correlation coefficients between 0.40 and 0.55, before it drifted away from the initial adsorption site and eventually left the membrane.

The difference in the distributions of the correlation coefficients of Tat CPP- and transferrin- modified gold nanorods (in **Figure 4.2a and 4.2d**) is shown to be statistically significant with a Student's t-test ($p < 0.005$). Moreover, the distribution of the correlation coefficient is also affected by the randomness of rotation and the noise in the signal, as demonstrated in **Figure 4.S11**.

The histogram of the correlation coefficients calculated from the 200 frames after the first 30 s of observation (**Figure 4.2f**) shows that there is also an increasing trend in the correlation coefficient for the transferrin modified nanorods, although it is not as apparent as for the Tat CPP-modified nanorods, because the initial correlation coefficients are already high. **Figure 4.2e** (**Movie 4.2**) shows a time trace of the correlation coefficient for a transferrin-modified gold nanorod over a time span of 30 s after its first contact with the membrane. The corresponding DIC intensity traces over the same time span are shown in **Figure 4.S12**. The initial correlation coefficient of 0.72 indicates that the in-plane rotational mode is already dominant upon first contact and that the nanorod is most likely adsorbed to the membrane through its specific receptor binding. The correlation coefficient fluctuates between 0.5 and 0.8, except for three occasions where the value drops as low as 0.20, illustrating the dynamic, stochastic nature of the interactions on the membrane, and possibly due to the local membrane deformation caused by the embeded nanoparticle. Each of the three occasions with low correlation coefficients shows typical seesaw motions, suggesting little in-plane rotation presumably because of strong binding to the membrane and possibly confinement from the local deformed membrane.

Discussion

The general trend observed for both Tat CPP- and transferrin-modified gold nanorods can be explained in the following three stages: (1) upon initial contact with the membrane, the nanorods perform 3D rotations with fewer restrictions on the rotation angle ranges and relatively equal contributions from in-plane and out-of-plane components; (2) as the interactions become stronger, the nanorods have less out-of-plane motion and a higher fraction of in-plane motion, with correspondingly larger correlation coefficients; (3) finally, the nanorods settle down onto the membrane with relatively strong, multi-point binding interactions, and they lose the active out-of-plane as well as the in-plane rotational motions, resulting in apparent out-of-plane tilting motions with small correlation coefficients near 0, which may be explained by the intrinsic fluctuations of the cell membrane, the fact that noise becomes a more significant factor when the nanorod shows little or no rotation on the membrane, and the local membrane deformation and contact area of each individual nanoparticle.

Another point for discussion is whether the present imaging technique has sufficient resolving power to overcome the noise from two main sources: the measurement noise and the thermal motion of nanoparticles. The measurement noise is kept consistently throughout our experiments at roughly 10%, which is the noise level used in most simulations. According to the Einstein-Smoluchowski relation, the rotational diffusion coefficient of a rod-shaped nanoparticle in water with a dimension of 75×25×25 nm is ~3500 rad^2/s, and the average rotating angle per μs is ~4.8°. This type of free rotation is undoubtedly too fast for the present technique. However, the rotational motion of nanoparticles on the cell membrane is greatly restricted. According to a model by Fisher *et al*. [35], the rotational diffusion time of a sphere with a volume equivalent to a 75×25×25 nm gold nanorod partially imbeded in the lipid bi-layer to a depth of 2.5 nm is larger than 50 ms [16], which is more than 10 times of the integration time used in our experiments. Additional restraining factors, such as electrostatic interactions and receptor binding, may lead to even slower rotations. Therefore, the present method provides a reliable way to acquire rotational dynamics of nanoparticles on the membrane.

Conclusion

In summary, we have demonstrated that the SPORT technique combined with correlation analysis possesses unique capabilities for visualizing and understanding the rotational modes of bio-conjugated gold nanorods on live cell membranes. Distinctive rotational behaviors, including rotational rates and modes of functional nanoparticles can be directly correlated with chemical and physical properties and the biological functions of surface modifiers, as well as the interactions between nanoparticles and cell membranes. Present and future studies of rotational dynamics of functional nanoparticles will provide more complete fundamental knowledge about complex membrane processes, such as the formation and function of membrane micro- and nanodomains and the internalization of nanoparticle-based drug delivery agents. This method may also be applied to study rotational dynamics involved in other biological processes, such as the motions of viruses on cell membranes at early stages of infection.

Tracking rotational and translational diffusion simultaneously is challenging due to the need for dynamic information on the three spatial coordinates (x, y, z) and the two orientation angles (elevation and azimuthal). Although the method presented here can identify the basic rotational modes for relatively fast rotational Brownian motions, additional information is needed to further remove the ambiguity of the determined rotational modes for other more complex rotational motions with limited ranges of the elevation and azimuthal angles. In addition, for slower rotational motions, a statistical analysis becomes unnecessary and imaging at video rate with higher angular resolution is preferable**.**

Experimental Section

Surface modification of gold nanorods: The cetyltrimethylammonium bromide

(CTAB)-stabilized gold nanorods (25 nm × 73 nm) were purchased from Nanopartz (Salt Lake City, UT).The manufacturer's data show that the in batch size variation is smaller than 10% CV, and the shape monodispersity is proved for more than 95% of the nanorods.

200 µL of the original gold nanorod solution was centrifuged and resuspended in 18.2-MΩ Milli-Q water to remove CTAB. A short NHS-PEG disulfide linker (Sigma-Aldrich, St. Louis, MO) is used for surface modification of gold nanorods by following a published protocol[36]. The NHS-PEG disulfide linker has both disulfide and succinimidyl functionalities for respective chemisorption onto gold and facile covalent coupling of functional molecules. The linker with 7 subunits in the PEG is very short (~ 1 nm) to make sure it would not affect the rotational modes of the gold nanorods on the cell membrane. 4 µL of 20 mM NHS-PEG-thiol in dimethyl sulfoxide (DMSO) is added to the gold nanorod solution and reacts for 3 h at room temperature. After that, the NHS-PEG conjugated gold nanorod solution is separated by centrifugation and resuspended in Milli-Q water.

Preparation of the Tat CPP-modified gold nanorods uses 4 µL of 2 mg·mL^{-1} trans-activating transcriptional activator (Tat) peptide solution (sequence: YGRKKRRQRRR, AnaSpec, San Jose, CA) in water that is added into 200 µL of NHS-PEG conjugated gold nanorod solution left to react for 2 h. The Tat CPP-modified gold nanorods are then washed with Milli-Q water.

Preparation of transferrin-modified gold nanorods: 200 µL of the NHS-PEG conjugated gold nanorod solution is mixed with 20 µg of transferrin (Sigma Aldrich). After 2-h reaction, the gold nanorod solution is centrifuged and resuspended in Milli-Q water.

Preparation of neutravidin-modified gold nanorods: 200 µL of the NHS-PEG conjugated gold nanorod solution is mixed with 4 µL of 20 mM neutravidin biotin-binding protein (Thermo Scientific). After 1-h reaction, the gold nanorod solution is centrifuged and resuspended in Milli-Q water.

The zeta potential (ζ) of nanoparticles refers to the electrostatic potential created as a result of the accumulation of electrons at the surface. The zeta potentials of the Tat CPP- and transferrin- modified gold nanorod colloidal solutions have been measured by Nano-ZS90 Zetasizer (Malvern Instruments, United Kingdom) to be +22.3 mV and -11.2 mV, respectively.

DIC microscopy and data analysis: An upright Nikon Eclipse 80i microscope with a pair of Nomarski prisms and two polarizers was used in this study. The microscope was equipped with a 100× 1.40 numerical aperture (NA) Plan Apo oil immersion objective and 1.4 NA oil immersion condenser. A 700-nm optical filter (Semrock, Rochester, NY) with a bandwidth of 20 nm was inserted at the illumination side. The movies were taken with a Hamamatsu ORCA-flash2.8 scientific CMOS camera. In order to achieve the 200 fps temporal resolution, the image window is limited to 320×256 pixels when the movies are captured.

These collected videos were analyzed using MATLAB and NIH ImageJ. The data analysis included tracking single gold nanorod probes in the recorded movies, extracting bright and dark intensity values from individual DIC images, and calculating Pearson's correlation coefficients. A small square of proper size was defined to enclose a target particle and the bright and dark DIC intensities of this particle were recorded as the highest and lowest intensity values in the square. Pearson's correlation coefficient is defined as the covariance of the two variables divided by the product of their standard deviations.

To track the lateral diffusion of the gold nanorods, the centers of the gold nanorod images were located and observed over time. Compared to the super-localization of fluorescent molecules or isotropic particles, it is much more difficult to localize gold nanorods in DIC microscopy due to the orientation-dependent, disproportionate bright and dark parts in a nanorod's DIC image. The actual localization precision of gold nanorod in a given image frame varies depending on the instantaneous orientation of the nanorod because different orientations give rise to different bright and dark DIC intensities, and thus to different signal-to-noise ratios. The positions of the gold nanorods were determined by locating the centers of their round DIC images. The small pixel size of the Hamamatsu camera (3.63 µm × 3.63 µm) allows us to localize the gold nanorods to the precision of approximately 1-2 pixels or 45-90 nm. Under our experimental conditions, each pixel on the camera chip corresponds to a sample area of 45 nm × 45 nm. The actual localization precision in each image frame varies depending on the nanorod orientation with different orientations giving rise to different bright and dark DIC intensities and thus different signal-to-noise ratios. In the future we plan to develop more robust and accurate localization methods, although these are not required for the present study. This will enable greater nanometer precision in spatial localization to accompany the high angular resolution.

Cell culture and imaging: HeLa cell line was purchased from American Type Culture Collection (CCL-2, ATCC, Manassas, VA). HeLa cells were cultured on 22 mm × 22 mm poly-lysine coated glass coverslips in a six-well tissue culture plate. Minimum essential cell culture medium (ATCC) with 10% fetal bovine serum supplement was added to the plates. The cell culture was incubated at 37°C under 5% CO_2. After the cell culture covered 70% of a coverslip, the coverslip was rinsed with 10 mM PBS buffer at pH 7.4 and then placed on a clean glass slide for observation. Two pieces of double-sided tape act as spacers between the glass slide and the coverslip to form the chamber. 30 μL of minimum essential cell culture medium without bovine serum albumin are added to the chamber to sustain the cells. The surface modified gold nanorod solutions are diluted with Milli-Q water to reach a concentration of 1.0×10^9 particles·mL^{-1}. 20 μL of the diluted surface-modified gold nanorod solution is added to the chamber and with visual observations beginning immediately. Movies of single nanorod rotations are recorded immediately after a single nanorod is adsorbed onto the cell membrane. The region of interest is limited to 320 × 256 pixels in order to increase the recording speed to 200 frames per second. All of the movies were taken at this speed. Each 20 s movie contains 4000 frames, and about 1 s is required between movies.

Computer simulations of the DIC bright and dark intensities of rotating gold nanorods:

Computer simulations are carried out to analyze the correlation coefficient of the bright and dark intensities of a gold nanorod randomly rotating in the 2D plane and swinging in the 3D space. In all simulations, one end of the gold nanorod has been permanently attached to the center of a hemisphere and the other end undergoing random movements on the surface of the hemisphere. Each simulation provides 4000 steps of random rotations in one of the three rotational modes. The relative DIC intensities (*I*) of the bright part and the dark part are calculated using the equations derived in our previous work [15]:

$$I_{\text{bright}} \approx 1 + \cos^2\psi \sin^4\phi, \qquad (3)$$

$$I_{\text{dark}} \approx 1 - \cos^2\psi \cos^4\phi. \qquad (4)$$

The elevation angle ψ and the azimuthal angle ϕ are defined in **Figure 4.S1**. To account for the relative errors of about 10% in the intensity measurement in the actual imaging experiments, a Gaussian noise of 10% has been added to the simulated DIC intensities displayed in **Figure 4.1**. Other simulated results are shown in the Supporting Material.

Acknowledgements

This work was supported by the U.S. Department of Energy, Office of Basic Energy Sciences, Chemical Sciences, Geosciences, and Biosciences Division through the Ames Laboratory (development of the imaging technique) and by the start-up funds from Iowa

State University (membrane studies). The Ames Laboratory is operated for the U.S. Department of Energy by Iowa State University under contract no. DE-AC02-07CH11358. Y.G. and M.T.Z. were supported in part by Plant Sciences Institute at Iowa State University.

References

1. Forkey, J. N.; Quinlan, M. E.; Goldman, Y. E., *Prog. Biophys. Mol. Bio.* **2000,** *74* (1-2), 1-35.
2. Harms, G. S.; Sonnleitner, M.; Schutz, G. J.; Gruber, H. J.; Schmidt, T., *Biophys. J.* **1999,** *77* (5), 2864-2870.
3. Ruiter, A. G. T.; Veerman, J. A.; GarciaParajo, M. F.; vanHulst, N. F., *J. Phys. Chem. A* **1997,** *101* (40), 7318-7323.
4. Stevens, B. C.; Ha, T., *J. Chem. Phys.* **2004,** *120* (6), 3030-3039.
5. Tsay, J. M.; Doose, S.; Weiss, S., *J. Am. Chem. Soc.* **2006,** *128* (5), 1639-1647.
6. Forkey, J. N.; Quinlan, M. E.; Shaw, M. A.; Corrie, J. E. T.; Goldman, Y. E., *Nature* **2003,** *422* (6930), 399-404.
7. Sase, I.; Miyata, H.; Ishiwata, S.; Kinosita, K., *Proc. Natl. Acad. Sci. U. S. A.* **1997,** *94* (11), 5646-5650.
8. Gregas, M. K.; Yan, F.; Scaffidi, J.; Wang, H. N.; Vo-Dinh, T., *Nanomed-Nanotechnol* **2011,** *7* (1), 115-122.
9. Shah, N. B.; Dong, J. P.; Bischof, J. C., *Mol. Pharm.* **2011,** *8* (1), 176-184.
10. Khlebtsov, N.; Dykman, L., *Chem. Soc. Rev.* **2011,** *40* (3), 1647-1671.
11. Zhou, R.; Xiong, B.; He, Y.; Yeung, E. S., *Anal. Bioanal. Chem.* **2011,** *399* (1), 353-359.
12. Tkachenko, A. G.; Xie, H.; Liu, Y. L.; Coleman, D.; Ryan, J.; Glomm, W. R.; Shipton, M. K.; Franzen, S.; Feldheim, D. L., *Bioconjugate Chem.* **2004,** *15* (3), 482-490.
13. Sun, W.; Wang, G.; Fang, N.; Yeung, E. S., *Anal. Chem.* **2009,** *81* (22), 9203-9208.
14. Wang, C. C.; Liang, C. P.; Lee, C. H., *Appl. Phys. Lett.* **2009,** *95* (20).
15. Wang, G.; Sun, W.; Luo, Y.; Fang, N., *J. Am. Chem. Soc.* **2010,** *132* (46), 16417–16422.
16. Pierrat, S.; Hartinger, E.; Faiss, S.; Janshoff, A.; Sonnichsen, C., *J. Phys. Chem. C* **2009,** *113* (26), 11179-11183.
17. Sonnichsen, C.; Alivisatos, A. P., *Nano Lett.* **2005,** *5* (2), 301-304.
18. Chang, W. S.; Ha, J. W.; Slaughter, L. S.; Link, S., *Proc. Natl. Acad. Sci. U. S. A.* **2010,** *107* (7), 2781-2786.
19. Gu, Y.; Sun, W.; Wang, G.; Fang, N., *J. Am. Chem. Soc.* **2011,** *133* (15), 5720-5723.
20. de la Fuente, J. M.; Berry, C. C., *Bioconjugate Chem.* **2005,** *16* (5), 1176-1180.
21. Heitz, F.; Morris, M. C.; Divita, G., *Br. J. Pharmacol.* **2009,** *157* (2), 195-206.

22. Qian, Z. M.; Li, H. Y.; Sun, H. Z.; Ho, K., *Pharmacol. Rev.* **2002,** *54* (4), 561-587.
23. Vives, E., *J. Mol. Recognit.* **2003,** *16* (5), 265-271.
24. Goncalves, E.; Kitas, E.; Seelig, J., *Biochemistry* **2005,** *44* (7), 2692-2702.
25. Lee, H. L.; Dubikovskaya, E. A.; Hwang, H.; Semyonov, A. N.; Wang, H.; Jones, L. R.; Twieg, R. J.; Moerner, W. E.; Wender, P. A., *J. Am. Chem. Soc.* **2008,** *130* (29), 9364-9370.
26. Klausner, R. D.; Vanrenswoude, J.; Ashwell, G.; Kempf, C.; Schechter, A. N.; Dean, A.; Bridges, K. R., *J. Biol. Chem.* **1983,** *258* (8), 4715-4724.
27. Stender, A. S.; Wang, G. F.; Sun, W.; Fang, N., *ACS Nano* **2010,** *4* (12), 7667-7675.
28. Gu, Y.; Sun, W.; Wang, G.; Fang, N., *J. Am. Chem. Soc.* **2011,** (15), 5720-5723.
29. Machy, P.; Truneh, A.; Gennaro, D.; Hoffstein, S., *Eur. J. Cell Biol.* **1987,** *45* (1), 126-136.
30. Yang, K.; Ma, Y.-Q., *Nat. Nanotechnol.* **2010,** *5* (8), 579-583.
31. Piantavigna, S.; McCubbin, G. A.; Boehnke, S.; Graham, B.; Spiccia, L.; Martin, L. L., *BBA-Biomembranes* **2011,** *1808* (7), 1811-1817.
32. Vacha, R.; Martinez-Veracoechea, F. J.; Frenkel, D., *Nano Lett.* **2011,** *11* (12), 5391-5395.
33. Leroueil, P. R.; Berry, S. A.; Duthie, K.; Han, G.; Rotello, V. M.; McNerny, D. Q.; Baker, J. R., Jr.; Orr, B. G.; Holl, M. M. B., *Nano Lett.* **2008,** *8* (2), 420-424.
34. Lin, J.; Zhang, H.; Chen, Z.; Zheng, Y., *ACS Nano* **2010,** *4* (9), 5421-5429.
35. Fischer, T. M.; Dhar, P.; Heinig, P., *J. Fluid Mech.* **2006,** *558*, 451-475.
36. Narayanan, R.; Lipert, R. J.; Porter, M. D., *Anal. Chem.* **2008,** *80* (6), 2265-2271.

Figures

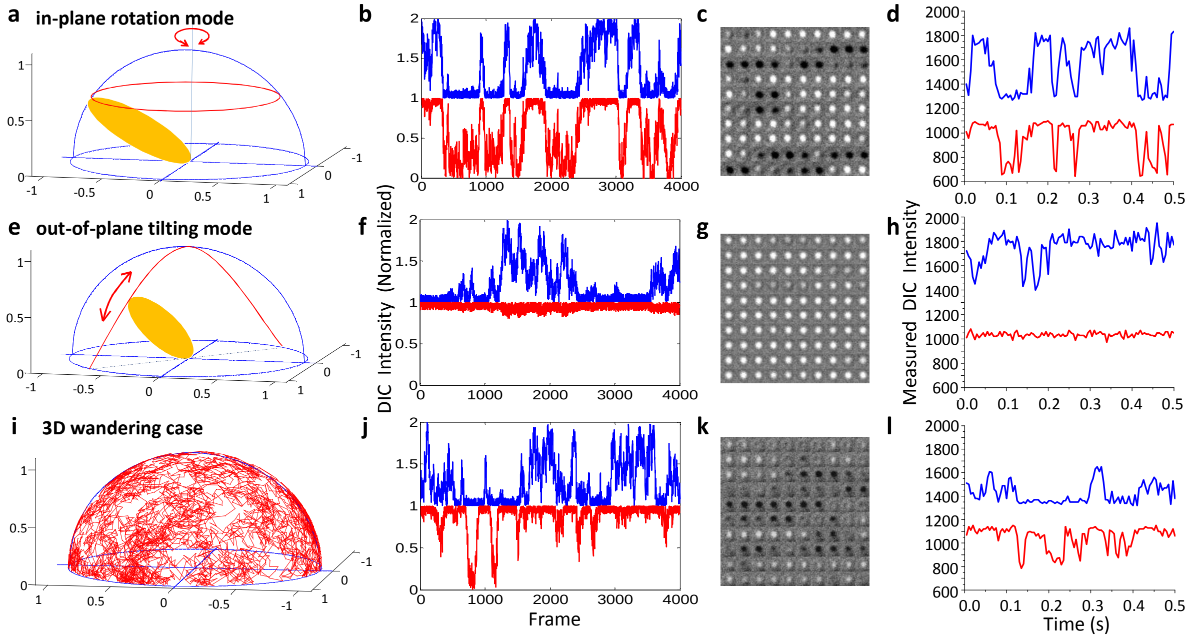

Figure 4.1. Simulations and experimental data for the basic rotational modes for adsorption of particles onto cell membrane surfaces: in-plane rotation (**a-d**), out-of-plane tilting (**e-h**), and a special case of 3D wandering with no restriction on the rotation angles (**i-l**). Computer simulated traces of a single gold nanorod **(a, e** and **i)** are shown together with the corresponding normalized bright and dark DIC intensities (shown in blue and red, respectively in parts **b, f** and **j**). Examples of 100 consecutive images (left to right) captured at 200 frames/s for a single gold nanorod on live cell membranes (**c**, **g** and **k**) are shown together with the corresponding bright and dark DIC intensities (**d**, **h** and **l**).

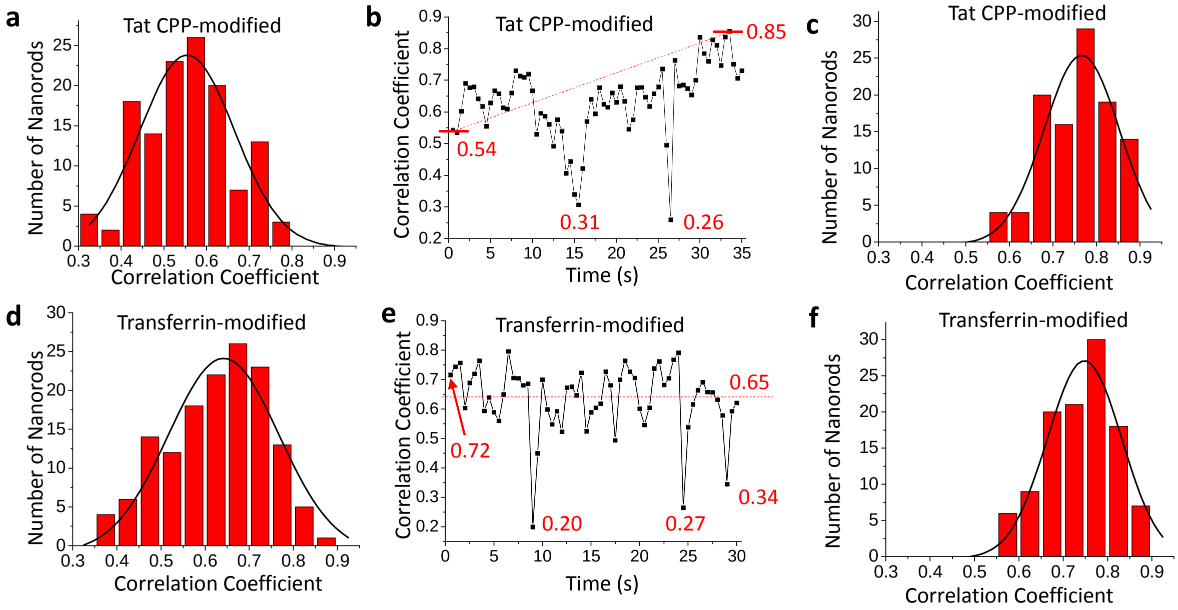

Figure 4.2. Correlation coefficients of the bright and dark intensities of single gold nanorods upon first contact with cell membranes. (**a**) Histogram of the correlation coefficients calculated from the first 200 frames captured within 1 s for 133 Tat CPP-modified gold nanorods. (**b**) Time trace of the correlation coefficient during the first 35 s of contact for a Tat CPP-modified gold nanorod. The correlation coefficient increases from 0.54 to 0.85 in this case. (**c**) Histogram of the correlation coefficients calculated from 200 frames captured after the first 35 s of the landing of the Tat CPP-modified gold nanorods. (**d**) Histogram of the correlation coefficients for 100 transferrin-modified gold nanorods. (**e**) Representative time trace of the correlation coefficients during the first 30 s of contact for a transferrin-modified gold nanorod showing a dominant in-plane rotation component. (**f**) Histogram of the correlation coefficients calculated from 200 frames captured after the first 30 s of contact between the transferrin-modified gold nanorods and the membrane.

Supporting Information

for

Revealing Rotational Modes of Functionalized Gold Nanorods on Live Cell Membranes

Yan Gu[1], *Wei Sun*[1,†], *Gufeng Wang*[1,‡], *Michael T. Zimmermann*[2], *Robert L. Jernigan*[2] *and Ning Fang*[1,]*

[1]Ames Laboratory, U.S. Department of Energy and Department of Chemistry, Iowa State University, Ames, Iowa, 50011-3111

[2]Laurence H. Baker Center for Bioinformatics and Biological Statistics, Department of Biochemistry, Biophysics and Molecular Biology, Iowa State University, Ames, IA 50011-3020

[†]Current address: Department of Chemistry, the University of Washington, Seattle, WA 98195

[‡]Current address: Department of Chemistry, North Carolina State University, Raleigh, NC 27695

Additional Methods For Experiments On Synthetic Lipid Bilayers

Preparation of synthetic lipid bilayers

The synthetic phospholipid blend (1,2-dioleoyl-*sn*-glycero-3-phosphoethanolamine (DOPE) : 1,2-dioleoyl-*sn*-glycero-3-phospho-L-serine (DOPS) : 1,2-dioleoyl-*sn*-glycero-3-phosphocholine (DOPC) at a ratio of 5:3:2) is dissolved in chloroform to reach a concentration of 25 mg/mL. The lipid mixture is dried under a stream of nitrogen followed by at least 3 h under vacuum at room temperature to remove the residual solvent. The dry lipids have then been stored in a -20°C freezer until use.

To prepare the large unilamellar vesicles (LUVs), 0.5× phosphate buffered saline (PBS) at pH 7.4 is added to swell the lipids, and the concentration of the lipids in the PBS buffer reaches 1mg/mL. After incubation for 1 h at room temperature, with occasional vortexing, the lipids form a cloudy suspension. The suspension is extruded at least 21 times with a mini-extruder (Avanti Polar Lipids) assembled with a polycarbonate membrane having a pore diameter of 100 nm. The resulting clear LUVs suspensions is then stored at 4°C.

The formation of planar bilayer is achieved by incubating the LUVs with freshly cleaned glass coverslips for 20 min. The excess lipids were removed by washing with PBS buffer. Nanorods with Tat CPP or transferrin modifiers are added onto the membranes and rotational motions captured after 5-min incubation.

Artificial membranes composed of 1-palmitoyl-2-oleoyl-sn-glycero-3-phosphocholine (POPC) and 1% wt biotin-DOPE are prepared using the same method. After washing with PBS buffer, either neutravidin modified or bare gold nanorods are added onto the membranes. The neutravidin modified gold nanorods are incubated with the membranes for 30 min followed by extensively washing with PBS buffer. For the control experiment, bare gold nanorods have been added onto the membranes and movies were collected after 5 min incubation.

For the preparation of the POPC membranes with different cholesterol content, the synthetic phospholipid 1-palmitoyl-2-oleoyl-*sn*-glycero-3-phosphocholine (POPC, Avanti

Polar Lipids) supplemented with 10%, 20%, 30% and 40% (wt.) cholesterol (Avanti Polar Lipids) is dissolved in chloroform to reach a concentration of 25 mg/ml. The lipid mixture is dried under a stream of nitrogen followed by at least 3 h under vacuum at room temperature to remove the residual solvent. The dry lipids have then been stored in a -20°C freezer until use. The synthetic membranes are prepared in the same way as discussed above.

Fluorescence recovery after photobleaching (FRAP)

To prepare for the FRAP experiments, the lipids mixtures containing various concentrations of cholesterol were supplemented with 1% (wt.) Texas Red 1,2-Dihexadecanoyl-sn-Glycero-3-Phosphoethanolamine, Triethylammonium Salt (Texas Red® DHPE) (Invitrogen).The lipid bi-layers were prepared as described above.

A 532-nm 80-mW laser (B&W TEK Inc. Lasers, Newark, DE) was coupled with the Nikon 80i Eclipse upright microscope and the excitation light was directed through the epi-fluorescence pathway, focused to 8 μm in diameter by the 100× oil immersion objective. A neutral density filter that reduces the light intensity by 95% was inserted in the light path. After a short movie of the original fluorescence from the lipid bi-layers excited with the reduced light was recorded, the neutral density filter was flipped away from the light path to allow the strong laser to photobleach the small patch of the lipid membrane that is within the laser spot. After that, the neutral density filter was then flipped back for imaging fluorescence recovery. An external shutter was synchronized with the CCD shutter to reduce the photobleaching during the recovery process and the integration time of each frame was 200 ms. Fluorescent signalswere recorded by an Photometrics Evolve EMCCD camera (Tucson, AZ). The FRAP data were analyzed using the Hankel transform method[1] by running a MATLAB code.

Discussion Of Complex Rotational Patterns With Limited Ranges Of Rotation Angles

A typical limitation for a nanorod on the cell membrane is that it is more difficult to stand up, that is, the angle ψ may be limited to a range from 0° to less than 90° in the hemisphere. This limitation effectively reduces the proportion of the out-of-plane tilting component. The simulation results shown in **Figure 4.S5** quantify the influences of different ranges of the angle ψwhile keeping the in-plane rotation fully random. A decrease in the correlation coefficient is observed as the upper limit of the angle ψ increases resulting in more out-of-plane tilting.

The restriction on the in-plane rotation angle leads to even more complicated situations, partly because the in-plane rotation generates more significant intensity changes than the out-of-plane tilting. The main challenge is depicted in **Figure 4.S6**. When the angle ϕ is limited to small values near one of the optical axes, either the bright or dark DIC intensity is weak and nearly buried in the grey background while the other intensity is close to its maximum. Noise becomes a dominant factor in the measurement of the weak intensity. The resulting correlation coefficient can decrease drastically in the presence of noise and some out-of-plane tilting. This situation is nonetheless informative about the angle ψ. This is an inherent limitation of all orientation probes: the orientation-dependent signals become too small at certain positions, which results in low accuracy in the data analysis. This problem can be partially circumvented by the statistical analysis of a large number of data points if the nanorod does not reach these positions sufficiently often. This is generally true for the random and relatively fast rotational motions. Thus it is important to state that the statistical analysis presented here is intended for relatively fast rotational Brownian motions, and not for highly restrained slower motions (e.g., the rotational motions of cargos in kinesin gliding assays that we reported previously[2]), where the statistical analysis is unnecessary and imaging at slower rates with higher angular resolution is appropriate.

Discussion Of Rotational Dynamics Of Gold Nanorods On The Synthetic Lipid Bilayers

To elucidate how interactions between functionalized gold nanorods and lipid bilayers affect the rotational behavior, gold nanorods with different surface properties have been introduced onto the synthetic lipid bilayers having various compositions, and their rotational modes were evaluated using correlation analysis of the bright and dark DIC intensities.

The negatively charged lipid bilayers were prepared from a synthetic phospholipid blend (1,2-dioleoyl-*sn*-glycero-3-phosphoethanolamine (DOPE) : 1,2-dioleoyl-*sn*-glycero-3-phospho-L-serine (DOPS) : 1,2-dioleoyl-*sn*-glycero-3-phosphocholine (DOPC) at a ratio of 5:3:2). The positively-charged Tat CPP-modified gold nanorods adsorbed onto the synthetic membrane much more rapidly than the negatively-charged transferrin-modified gold nanorods. Using the same concentration of the gold nanorod solution (~10^9 nanoparticles/mL) and the same incubation time (5 min), the density of the Tat CPP-modified gold nanorods on the synthetic membranes was more than 20 times greater than the density of the transferrin-modified gold nanorods. Over 30 nanorods with each surface modifier have been recorded and analyzed. Due to the favored electrostatic interactions with the lipid bilayers, the Tat CPP-modified gold nanorods tend to lie flatter on the membranes and perform more in-plane rotations to exhibit large correlation coefficients centered around 0.7-0.8 (**Figure 4.S7a**). By contrast, the transferrin-modified gold nanorods were characterized by smaller correlation coefficients centered at 0.3-0.4 (**Figure 4.S7b**) and perform more random 3D wandering motions on the synthetic membranes, showing their reluctance to anchoring.

We then evaluated the impact of specific binding on the rotational mode of nanorod probes. To circumvent the effects of electrostatic interactions, bilayers formed by zwitterionic POPC lipid (ζ = ~ -4.3 mV) mixed with 1% biotin-DOPE were used as the substrate. Gold nanorods modified with neutravidin were incubated with the lipid bilayers and washed to remove most of the nonspecific binding. The correlation coefficients for these rotating nanorods are generally large (again centered at 0.7-0.8) (**Figure 4.S7c**), reflecting the strong binding interactions of the nanoprobes with the synthetic membranes. As a control, bare gold nanorods stabilized with positively-charged surfactant cetyltrimethylammonium bromide

(CTAB) were introduced onto the same biotin labeled POPC membrane. The correlation coefficients for the CTAB-stabilized gold nanorods are centered at 0.6-0.7 (**Figure 4.S7d**), which is smaller than the values for neutravidin-modified nanorods, but is still larger than that of the typical 3D wandering motion. This can be attributed to favorable electrostatic interactions between the positively-charged CTAB-modified nanorods (ζ = +20 mV) and the slightly negatively-charged POPC membranes.

After assuming equal variance of the two samples, the statistical significance of the difference in the correlation coefficients between the neutravidin-modified nanorods and the CTAB stabilized bare nanorods is evaluated with Student's t-test.The p value is smaller than 0.05, indicating the correlation coefficients are significantly different. .

The artificial membranes are simple in composition and their conformations should not have large curvatures or rigid structures, as manifested by the real cell membranes; thus, the nanorods interacting with flat membrane surfaces result in simpler rotational dynamics. The experiments on synthetic membranes clearly demonstrate the ability of the present method to identify different rotational modes of gold nanorods under the control of electrostatic interactions and specific binding interactions. These results show that when the surface charges of gold nanorods are favored by the membranes or when the functional molecules can provide specific binding interactions with the membranes, the gold nanorods are more likely to perform in-plane rotations when they have stronger interactions with the membranes. Note that the distribution of the correlation coefficient should be due to the randomness of the rotation of the nanoparticles, and depends on probably the membrane deformation, contact area and number of ligands attached to the nanorods, as discussed in the main text for the live cell experiments.

To test the effect of membrane viscosity on the rotational dynamics, the rotational behaviors of CTAB-capped gold nanorods on POPC lipid bilayers with various cholesterol concentrations have been recorded. Cholesterol plays a major role in moderating the membrane fluidity in animal cells and changing the cholesterol content in the membranes changes the membrane viscosity.[3] The change of the viscosity of the POPC lipid bilayer could be reflected by the change of the lipid mobility, which is characterized by the lateral diffusion coefficient of the molecules in the lipid bilayer. According to the Saffman–Delbrück model[4], the diffusion coefficient of a cylindrical inclusion in a lipid membrane is correlated with the viscosity of the membrane:

$$D = \frac{k_B T}{4\pi\eta_m}\left[\ln\left(\frac{2L_{sd}}{a}\right) - \gamma\right],$$

where η_m is the viscosity of the membrane, a is the radius of the cylindrical inclusion, γ (≈ 0.577) is the Euler-Mascheroni constant, and L_{sd} is the Saffman-Delbrück length, which is defined as:

$$L_{sd} = \frac{h\eta_m}{2\eta_f},$$

where h is the thickness of the membrane and η_f is the viscosity of the bulk fluid. It has been reported that an increase in the cholesterol concentration reduces the lateral diffusion coefficient of lipids in synthetic lipid bilayers.[5, 6]The influence of the concentration of cholesterol on the lateral diffusion coefficient of the POPC lipid bi-layers was tested by Fluorescence Recovery after Photobleaching (FRAP). The decrease of the diffusion coefficient with the increase of the cholesterol content is shown in **Figure 4.S7e**.

The rotational behaviors of the CTAB-capped gold nanorods were recorded after 5-min incubation with the synthetic lipid bilayers. To semi-quantify the rotational rate of the gold nanorods, the autocorrelation of the DIC intensities is fitted with a stretched exponential function, and the mean relaxation time for decay is determined from the fitting as the characteristic rotation time [7]. The characteristic times of 45 or more gold nanorods were calculated and averaged for each cholesterol concentration (from 0 to 40% wt.). The characteristic rotation time is plotted against the cholesterol levels in **Figure 3.S7f**. An increase in the characteristic rotation time is observed when the cholesterol concentration becomes higher. These results demonstrate that the present method affords sufficient sensitivity to report the apparent changes in membrane viscosity.

References

1. Jonsson, P.; Jonsson, M. P.; Tegenfeldt, J. O.; Hook, F. *Biophys. J.* **2008,** 95, (11), 5334-5348.
2. Wang, G.; Sun, W.; Luo, Y.; Fang, N. *J. Am. Chem. Soc.* **2010,** 132, (46), 16417–16422.
3. Goodwin, J. S.; Drake, K. R.; Remmert, C. L.; Kenworthy, A. K. *Biophys. J.* **2005,** 89, (2), 1398-1410.
4. Saffman, P. G.; Delbruck, M. *Proc Natl Acad Sci U S A. 1975 Aug;72(8):3111-3.*
5. Ladha, S.; Mackie, A. R.; Harvey, L. J.; Clark, D. C.; Lea, E. J. A.; Brullemans, M.;

Duclohier, H. *Biophys. J.* **1996,** 71, (3), 1364-1373.

6. Filippov, A.; Oradd, G.; Lindblom, G. *Biophys. J.* **2003,** 84, (5), 3079-3086.
7. Gu, Y.; Sun, W.; Wang, G.; Fang, N. *J. Am. Chem. Soc.* **2011**, (15), 5720-5723.

Figures

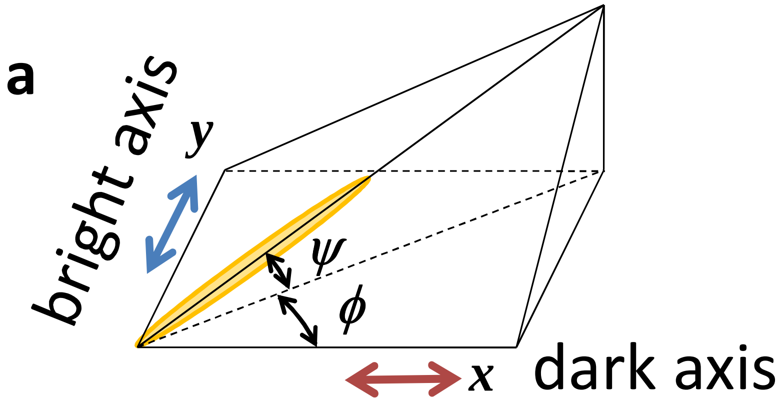

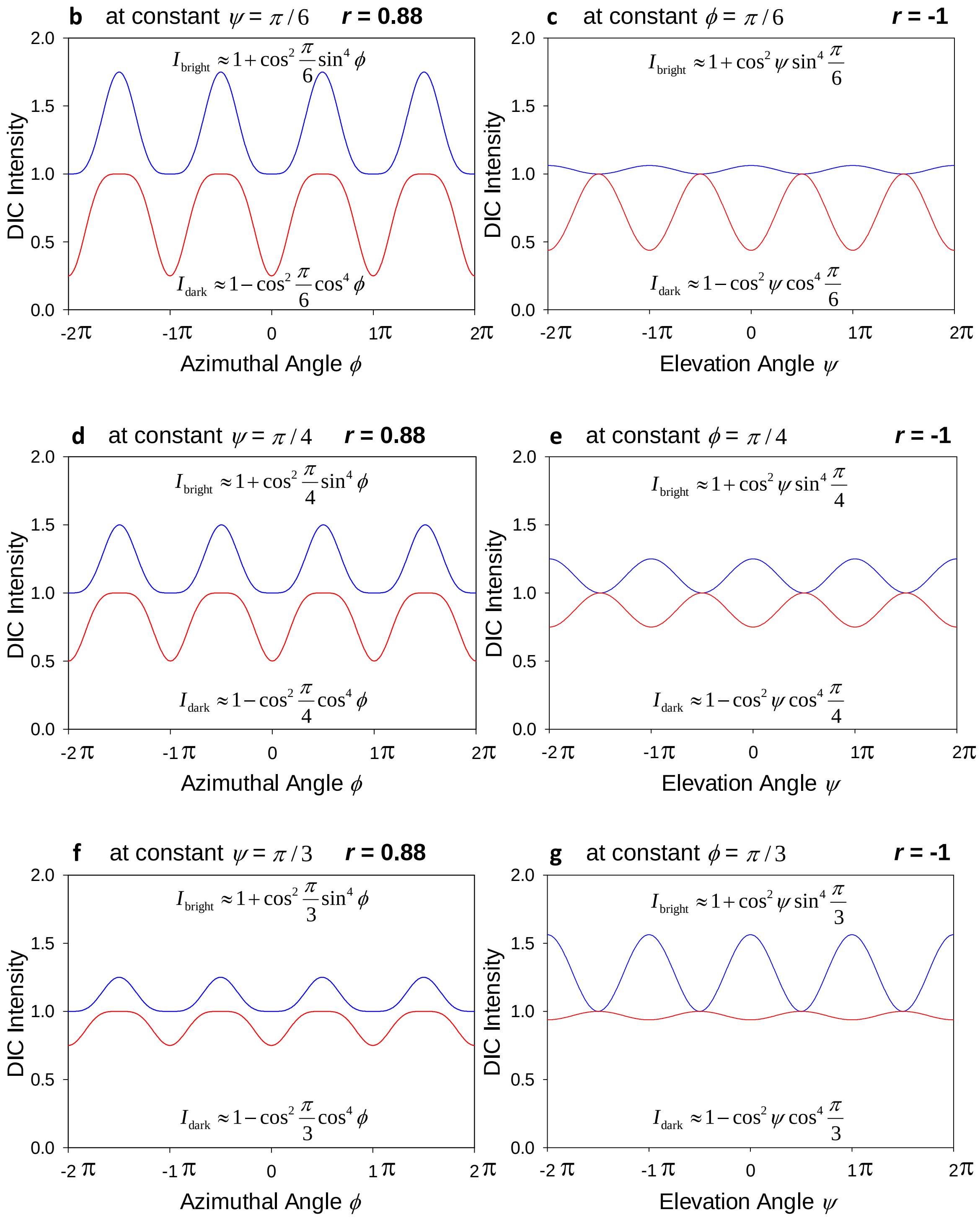
b at constant $\psi = \pi/6$ r = 0.88
$I_{\text{bright}} \approx 1 + \cos^2\frac{\pi}{6}\sin^4\phi$
$I_{\text{dark}} \approx 1 - \cos^2\frac{\pi}{6}\cos^4\phi$
DIC Intensity
Azimuthal Angle ϕ
c at constant $\phi = \pi/6$ r = -1
$I_{\text{bright}} \approx 1 + \cos^2\psi\sin^4\frac{\pi}{6}$
$I_{\text{dark}} \approx 1 - \cos^2\psi\cos^4\frac{\pi}{6}$
DIC Intensity
Elevation Angle ψ
d at constant $\psi = \pi/4$ r = 0.88
$I_{\text{bright}} \approx 1 + \cos^2\frac{\pi}{4}\sin^4\phi$
$I_{\text{dark}} \approx 1 - \cos^2\frac{\pi}{4}\cos^4\phi$
DIC Intensity
Azimuthal Angle ϕ
e at constant $\phi = \pi/4$ r = -1
$I_{\text{bright}} \approx 1 + \cos^2\psi\sin^4\frac{\pi}{4}$
$I_{\text{dark}} \approx 1 - \cos^2\psi\cos^4\frac{\pi}{4}$
DIC Intensity
Elevation Angle ψ
f at constant $\psi = \pi/3$ r = 0.88
$I_{\text{bright}} \approx 1 + \cos^2\frac{\pi}{3}\sin^4\phi$
$I_{\text{dark}} \approx 1 - \cos^2\frac{\pi}{3}\cos^4\phi$
DIC Intensity
Azimuthal Angle ϕ
g at constant $\phi = \pi/3$ r = -1
$I_{\text{bright}} \approx 1 + \cos^2\psi\sin^4\frac{\pi}{3}$
$I_{\text{dark}} \approx 1 - \cos^2\psi\cos^4\frac{\pi}{3}$
DIC Intensity
Elevation Angle ψ
0.0
0.5
1.0
1.5
2.0
-2π
-1π
0
1π
2π

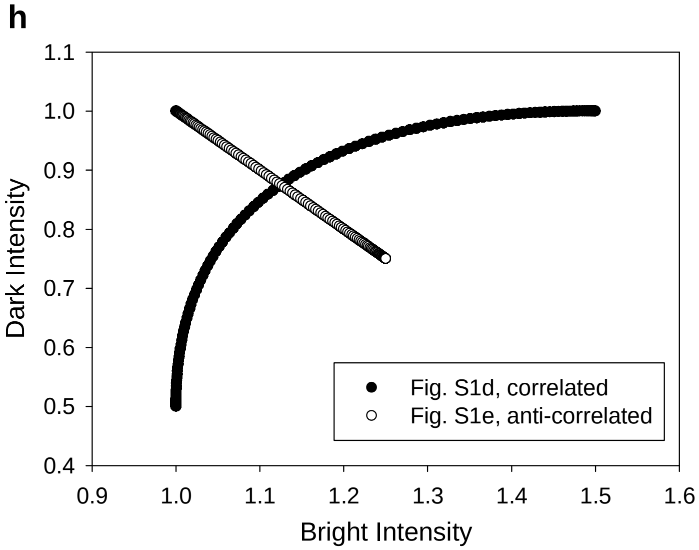

Figure 4.S1. Computer simulated bright and dark DIC intensities of a gold nanorod rotating with variouscombinations of the azimuthal angle ϕ and the elevation angle ψ.

***a**. Definitions of the orientation angles ϕ and ψ of a nanorod in 3D space. These definitions are identical to the ones used in our previous work.*[2]

b. The angle ψ is fixed at π/6 while the angle ϕ varies from -2π to 2π.

c. The angle ϕ is fixed at π/6 while the angle ψ varies from -2π to 2π.

d. The angle ψ is fixed at π/4 while the angle ϕ varies from -2π to 2π.

e. The angle ϕ is fixed at π/4 while the angle ψ varies from -2π to 2π.

f. The angle ψ is fixed at π/3 while the angle ϕ varies from -2π to 2π.

g.The angle ϕ is fixed at π/3 while the angle ψ varies from -2π to 2π.

In **b, d,** and **f**, the correlation coefficients are around 0.88. This slight deviation from perfect correlation originates from the $\sin^4$ and $\cos^4$ relations for the angle ϕ as explained in **h**.

In **c, e,** and **g**, the correlation coefficients are -1, suggesting a perfect anti-correlation between the bright and dark intensities.

h. Plots of the bright intensity vs. the dark intensity for **c** and **d**. The perfect correlation coefficients of +1 and -1 can only be achieved in Pearson's correlation coefficient analysis when the two variables are on linear dependency, which is true for the anti-correlated case. For the correlated case, the two variables are not on linear dependency, and this results in a smaller correlation coefficient.

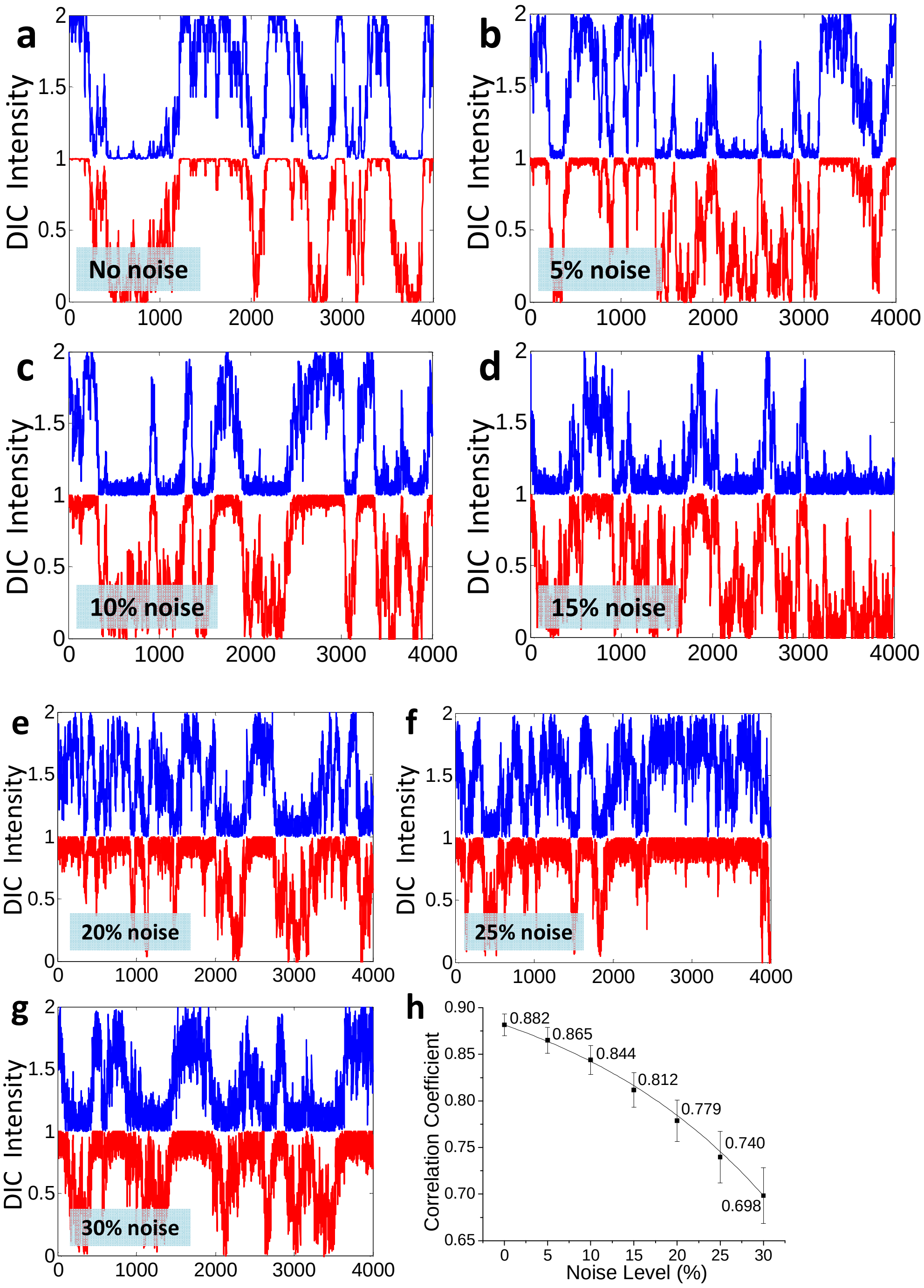

Figure 4.S2. Computer simulated DIC bright and dark intensities of a gold nanorod rotating in the **in-plane rotation mode** in the presence of various levels of noise.

a-g. Simulated DIC intensities with 0%, 5%, 10%, 15%, 20%, 25% and 30% noise, respectively.

h. Plot of the correlation coefficient versus the noise level.

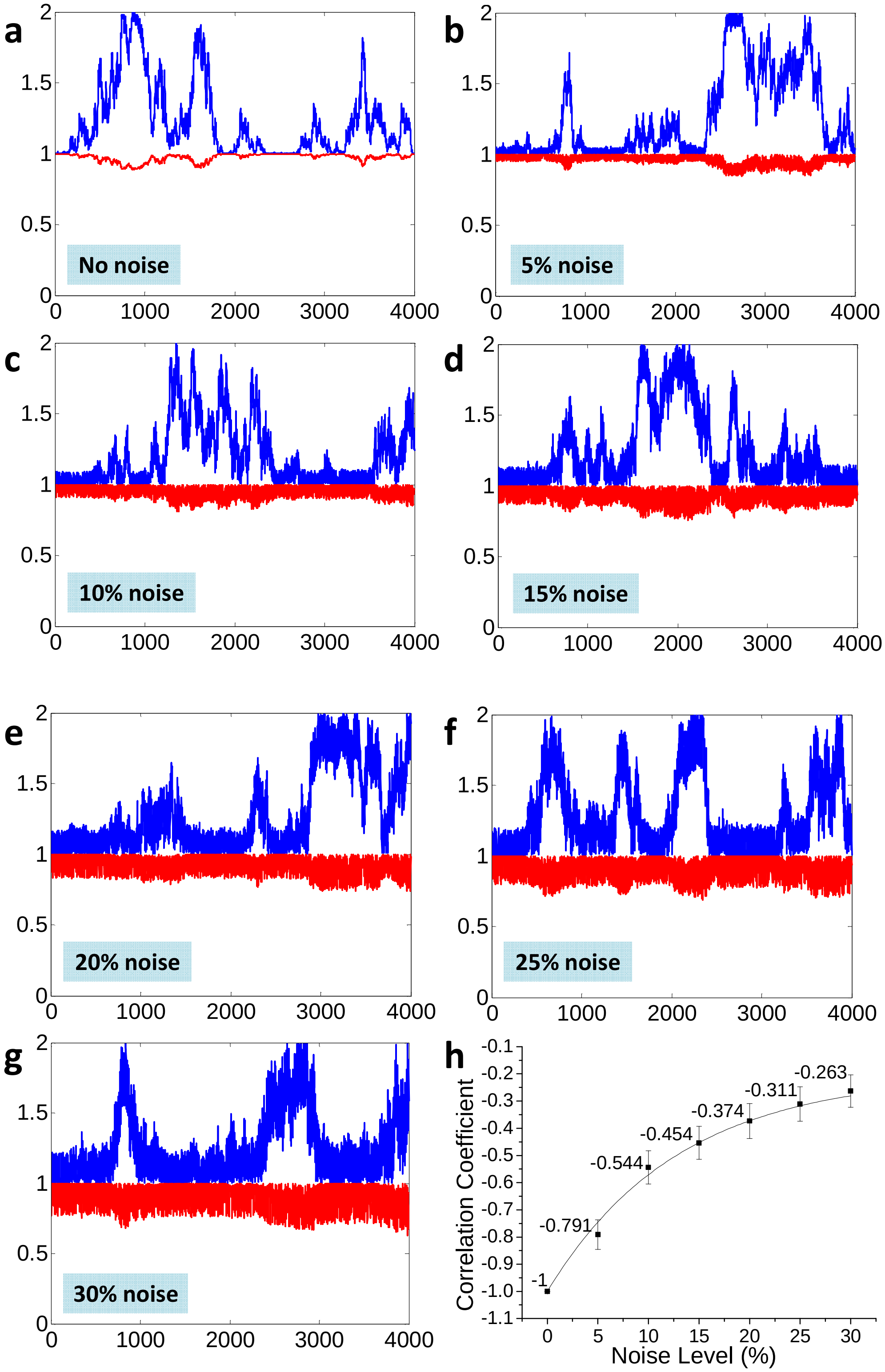

Figure 4.S3. Computer simulated DIC bright and dark intensities of a gold nanorod rotating

in the **out-of-plane tilting mode** in the presence of various levels of noise.

a-g. Simulated DIC intensities with 0%, 5%, 10%, 15%, 20%, 25% and 30% noise, respectively.

h. Plot of the correlation coefficient versus the noise level.

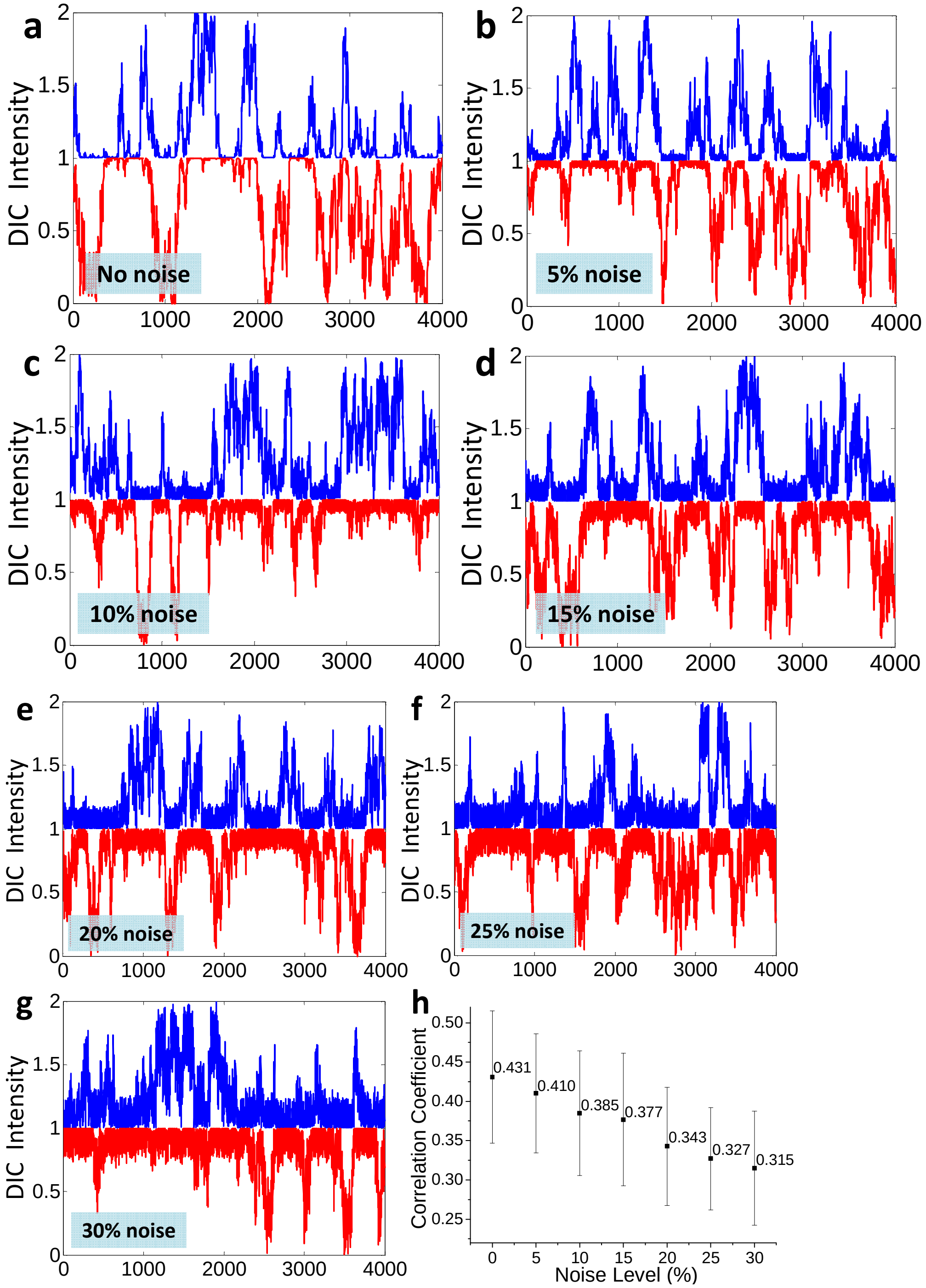

Figure 4.S4. Computer simulated DIC bright and dark intensities of a gold nanorod rotating in the **3D wandering mode** in the presence of various levels of noise.

a-g. Simulated DIC intensities with 0%, 5%, 10%, 15%, 20%, 25% and 30% noise, respectively.

h. Plot of the correlation coefficient versus the noise level.

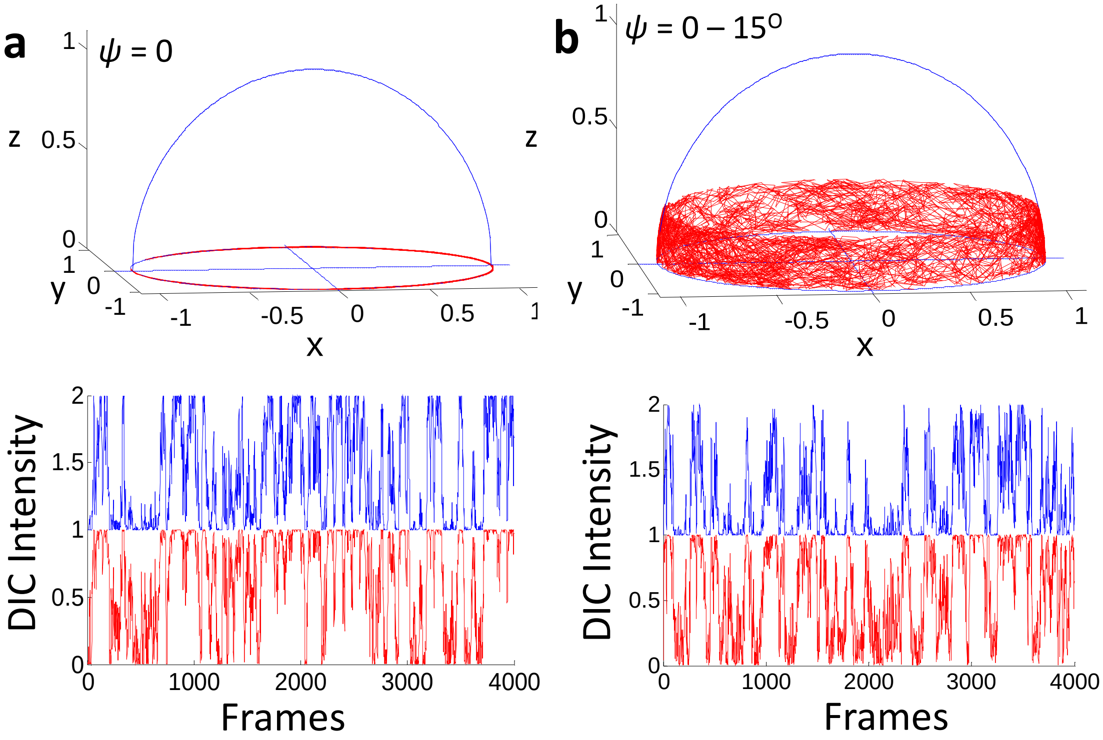
a
ψ = 0
z
1
0.5
0
y
1
0
-1
-1
-0.5
0
0.5
1
x
b
ψ = 0 – 15°
z
1
0.5
0
y
1
0
-1
-1
-0.5
0
0.5
1
x
DIC Intensity
2
1.5
1
0.5
0
0
1000
2000
3000
4000
Frames
DIC Intensity
2
1.5
1
0.5
0
0
1000
2000
3000
4000
Frames

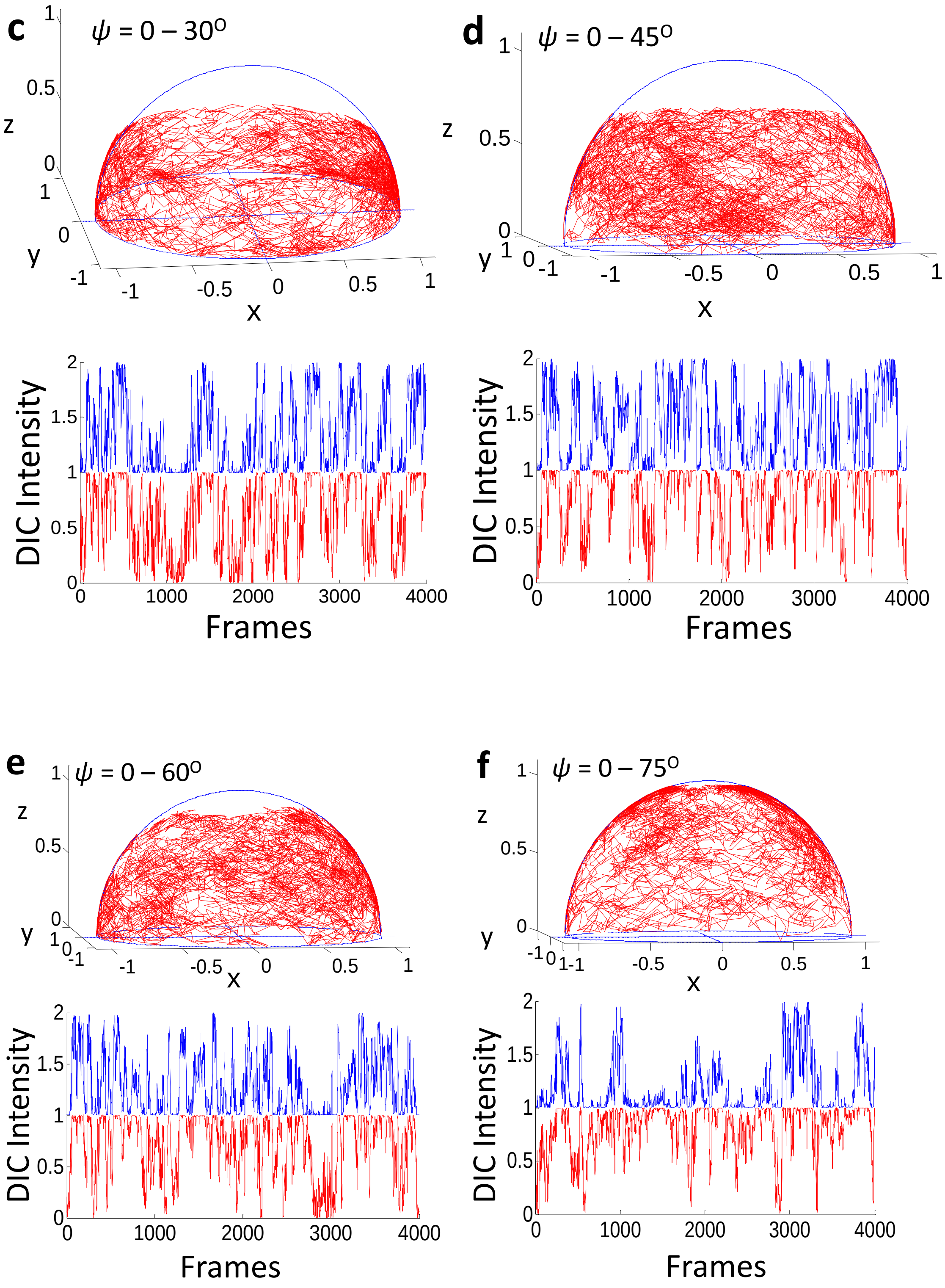
c
ψ = 0 – 30°
d
ψ = 0 – 45°
e
ψ = 0 – 60°
f
ψ = 0 – 75°
x
y
z
DIC Intensity
Frames
0
1000
2000
3000
4000
0.5
1
1.5
2
-1
-0.5

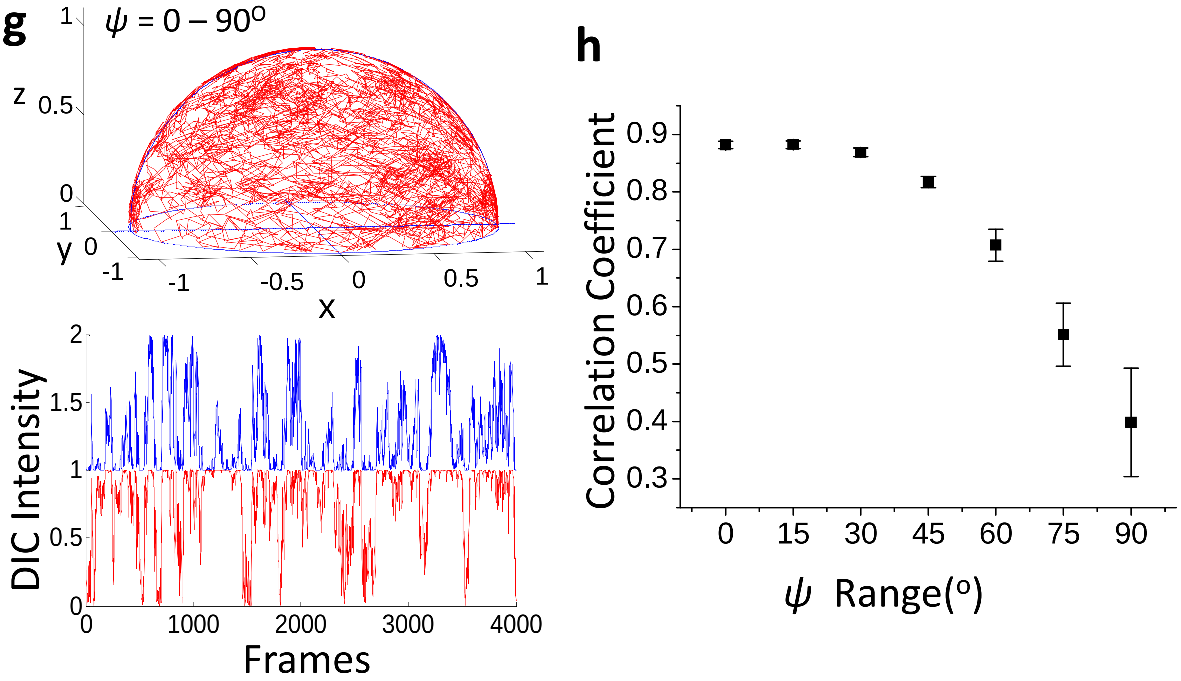

Figure 4.S5. (a-g) Computer simulated moving traces of the free end of a gold nanorod with the other end attached atthe center of the hemisphere, and the corresponding simulated bright and dark DIC intensities. The upper limit of the elevation angle ψincreases from 0° to 90°. **(h)** Plot of the correlation coefficient versus the range of the angle ψ.

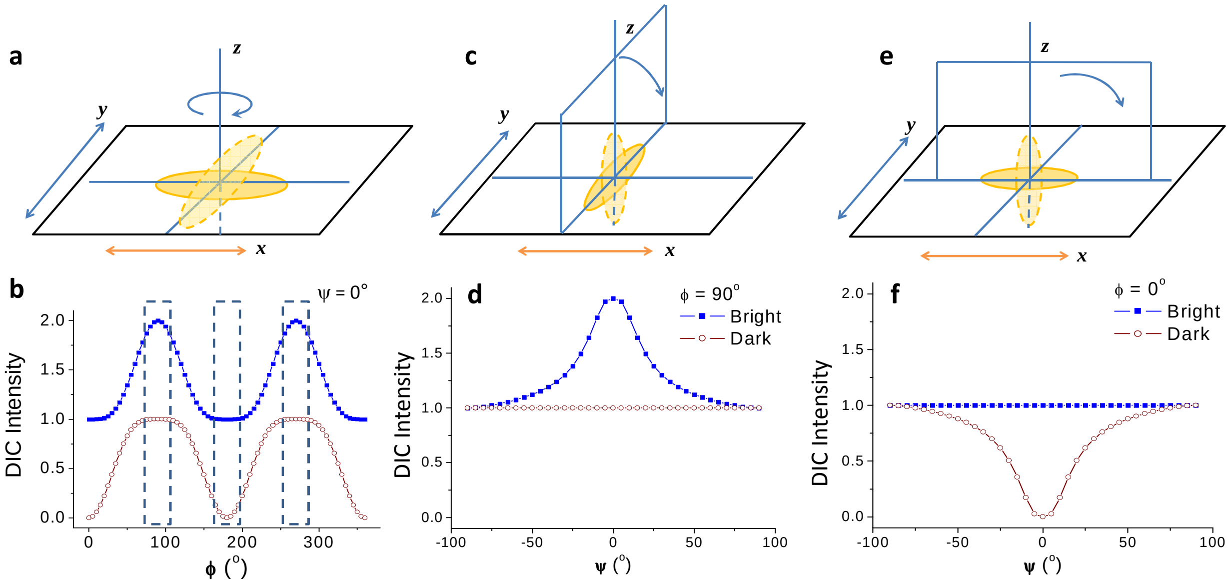

Figure 4.S6. Computer simulated bright and dark DIC intensities of a gold nanorod rotating in constant directions to demonstrate the intensity patterns when the nanorod rotates around the optical axes. **(a, b)** In-plane rotation mode and the corresponding DIC intensity trace. Close to the optical axes where θ equals 90^{o}, 180 ^{o} and 270 ^{o} (highlighted by the boxes in **b**), the amplitude of either the bright or dark intensity is very small while the other is near its maximum. The noise becomes a dominant factor in the measurement of the weak intensity and the resulting correlation coefficient can decrease drastically in the presence of noise and some out-of-plane tilting component. **(c, d)** Out-of-plane tilting mode with the rotation plane parallel to the bright axis and the corresponding DIC intensity trace.**(e, f)** Out-of-plane tilting mode with the rotation plane parallel to the dark axis and the corresponding DIC intensity trace. The correlation coefficients for (**d**) and (**f**) are 0. The inclusion of these last two special cases would result in unsatisfactorily resolved rotational modes.

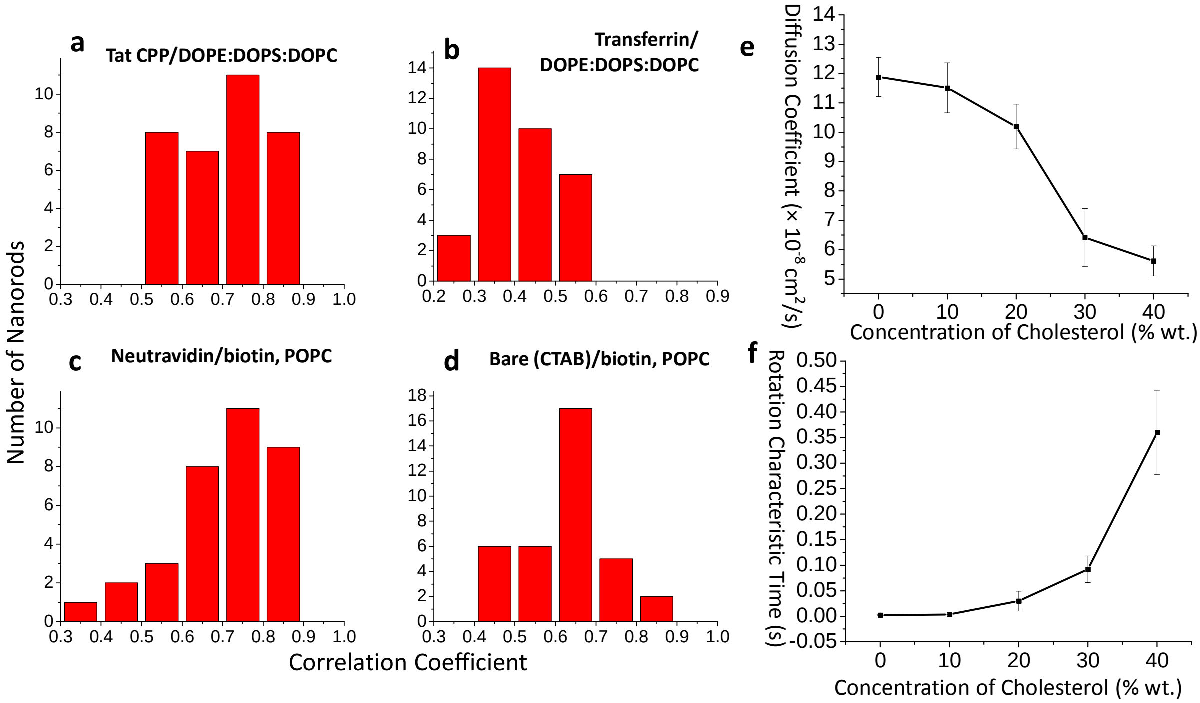

Figure 4.S7. **Histograms of correlation coefficients for single gold nanorods adsorbed on artificial lipid bilayers.** Each correlation coefficient is calculated from 2000 frames (10 s) of a single movie. (**a**) Tat CPP-modified gold nanorods on negatively-charged lipid bilayers. (**b**) Transferrin-modified gold nanorods on negatively-charged lipid bilayers. (**c**) Neutravidin-modified gold nanorods on zwitterionic lipid bilayers with biotin labels. (**d**) Bare (CTAB-capped) gold nanorods on zwitterionic lipid bilayers with biotin labels. (**e**) The translational diffusion coefficient of POPC synthetic lipid bilayers with various cholesterol concentrations (from 0 to 40% wt.) derived from the FRAP experiment. Each data point represents the average of the diffusion coefficient calculated from 5 FRAP experiments.(**f**) The change of the rotation characteristic times of the bare gold nanorods on POPC synthetic lipid bilayers with various cholesterol concentrations (from 0 to 40% wt.). Each data point represents a characteristic rotation time from an average over observations on at least 45 gold nanorods.

Part 1: 0.0 - 15.0 s

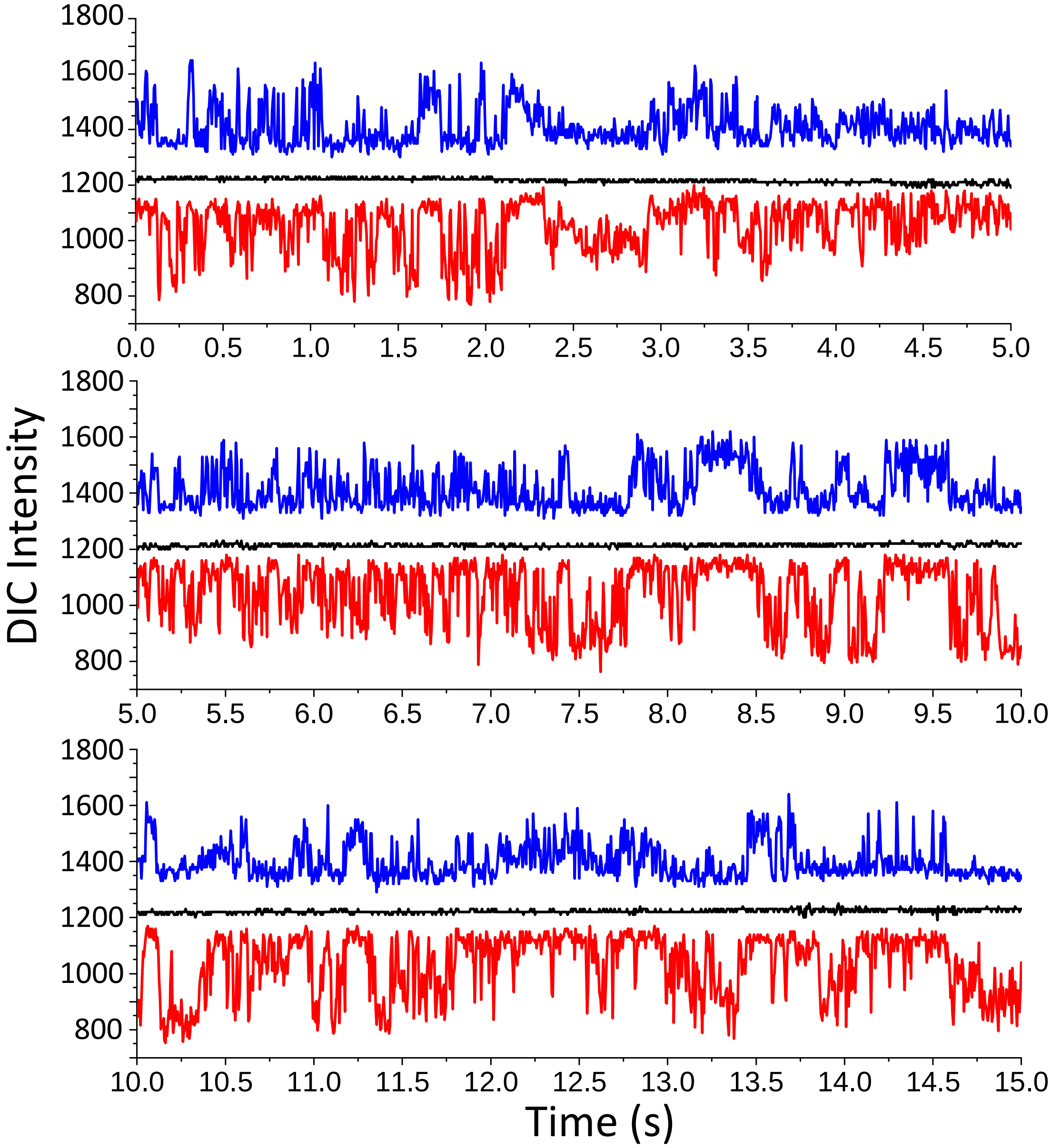

Part 2: 15.0 – 35.0 s

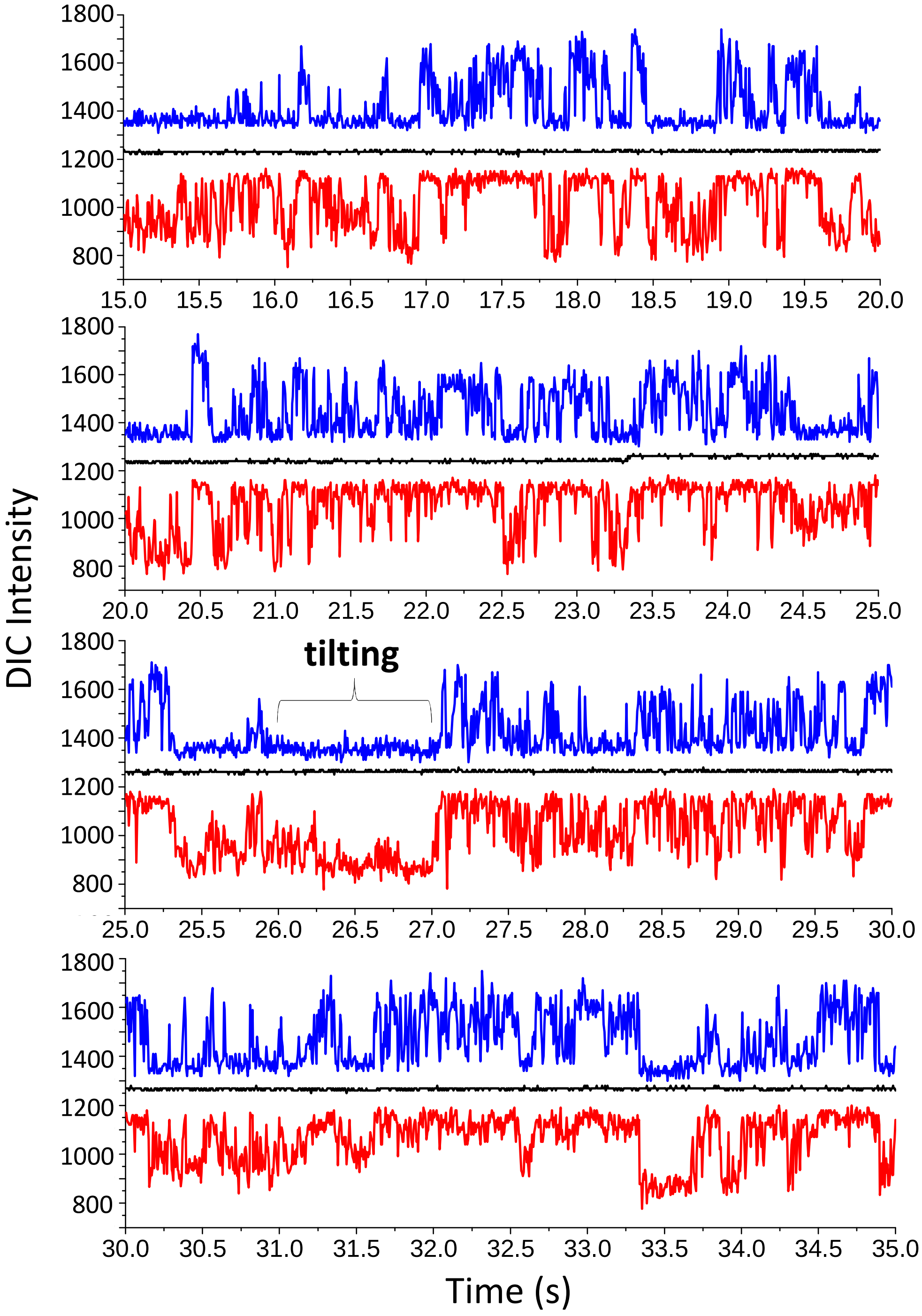

Figure 4.S8. DIC intensity traces of the Tat CPP-modified gold nanorod (**Movie 3.1**) producing the correlation coefficient trace shown in **Figure3.2b** in the main text. The bright and dark intensities are shown in blue and red, respectively, with the average background intensities are shown in black.

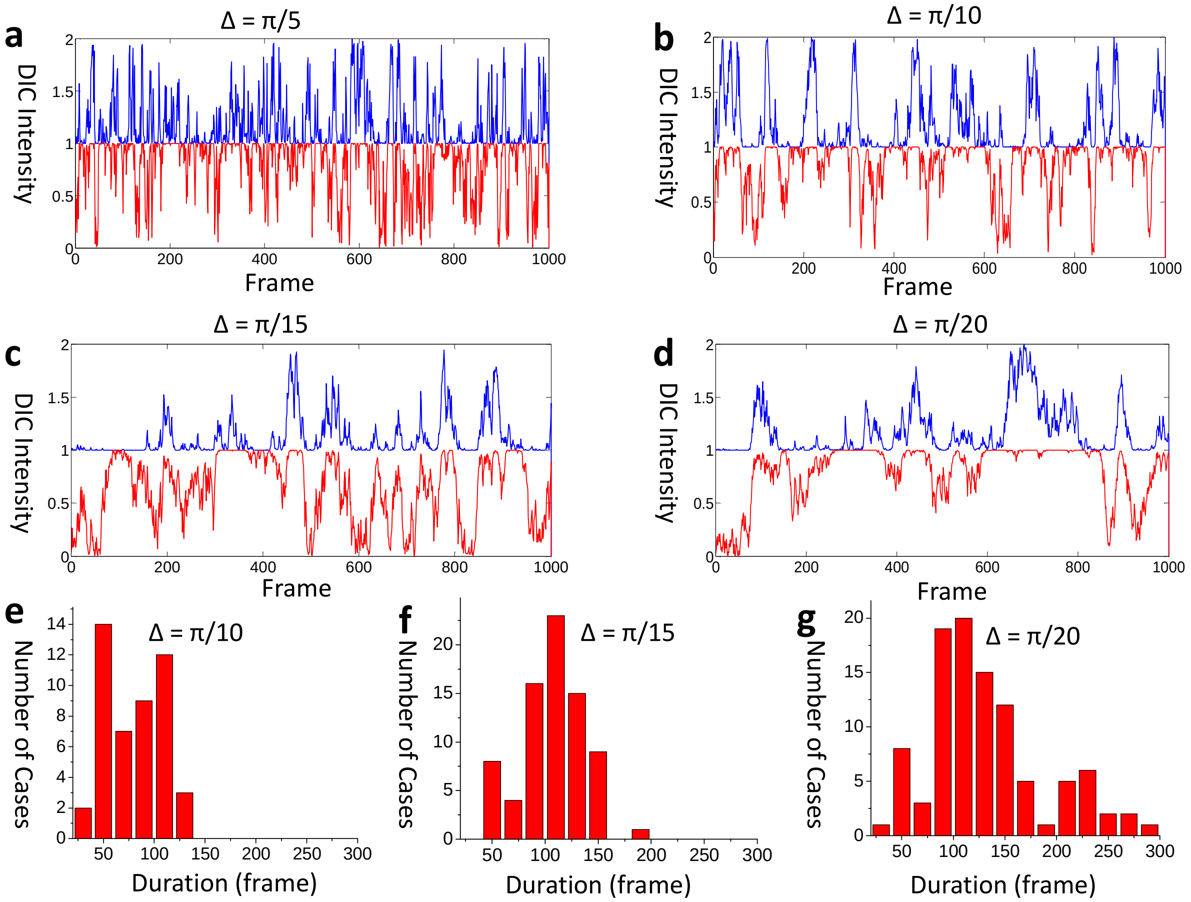

Figure 4.S9. The occurrence and duration of the tilting eventsare related to the step size. **(a-d)**Simulated DIC intensities of angular random walks with step sizes of π/5, π/10, π/15 and π/20 respectively.**(e-g)**Histograms of the durations of the tilting events in random walk simulations. Each histogram is generated with 20 simulation runs.

The tilting events occur more frequently when the step size is smaller. More explicitly, no simpletilting eventsareidentified in angular random walk simulations with a step size of π/5. 47 tilting eventsare observed in 20 simulations with a step size of π/10. 76 tilting eventsare observed in 20 simulations with a step size of π/15. 100 titling eventsare observed in 20 simulations with a step sized of π/20. In addition, as the step size decreases, the durations of the tilting events become longer. The histograms of the durations show that when the step size becomes as small as π/20 (which corresponds to a rotation period of 200 ms), the duration of the cases begin to exceed 200 frames.

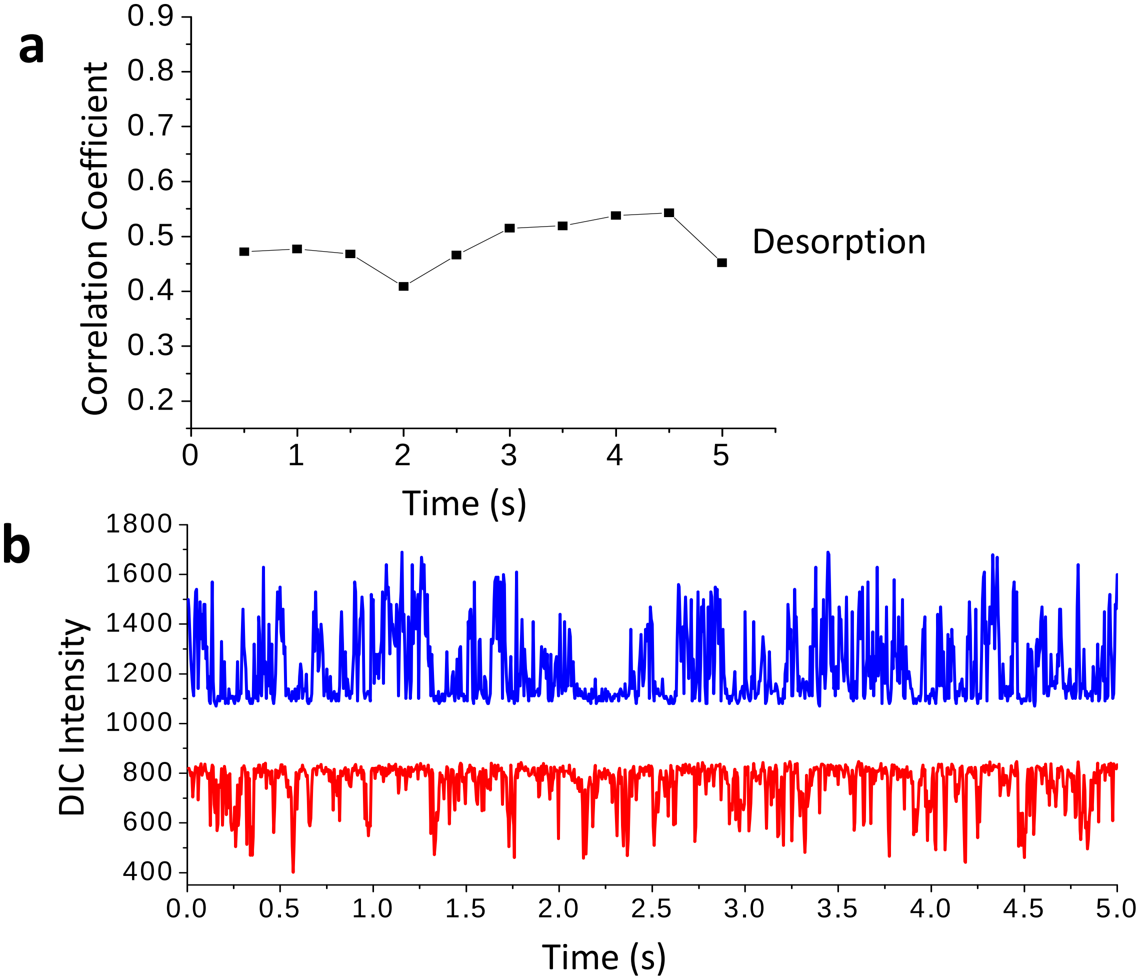

Figure 4.S10. Time traces of the correlation coefficient (**a**) and the corresponding DIC intensities (**b**) for a transferrin-modified gold nanorod for 5 s. The nanorod then drifted to a different location about 2 µm away from the initial adsorption spot, and eventually disappeared from the membrane.

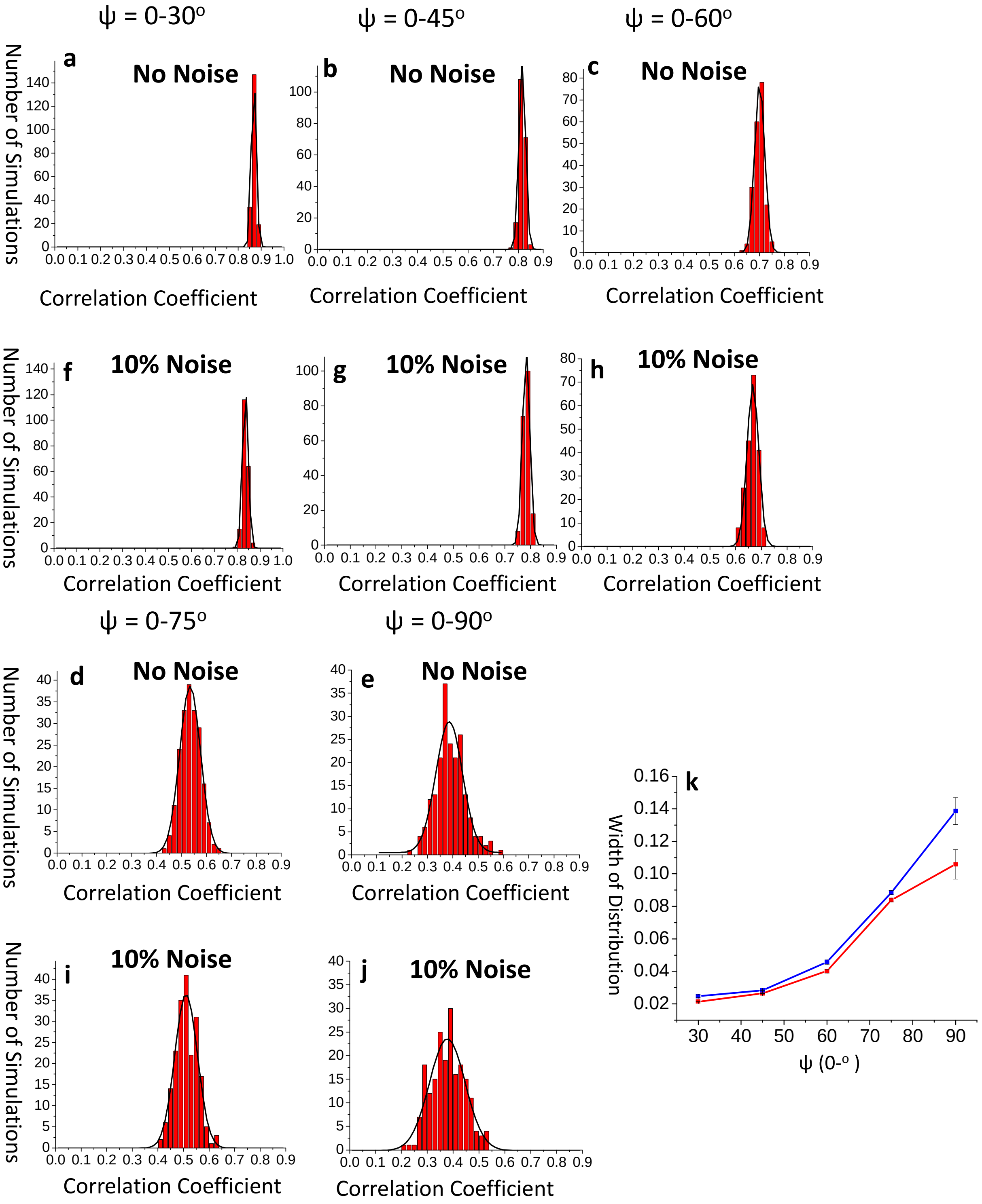

Figure 4.S11. (a-e) Histograms of the correlation coefficient generated from simulated rotations without Gaussian noise. **(f-j)** Histograms of the correlation coefficient generated

from simulated rotations with 10% Gaussian noise. All the histograms are plotted from 200 simulations and fitted with Gaussian functions. (**k)** Plot of the full width at half maximum (FWHM) of the Gaussian functions versus the upper limit of the elevation angle range. The blue curve is the data without noise, and the red one is the data with 10% noise.

The peak width increases from 0.02-0.11 as the elevation angle range changes from 0-30° to 0-90°. This is expected because a higher randomness should result in a larger distribution.

There is not a big difference in the width of the fitted Gaussian peaks with and without noise when the elevation angle ranges is between 0-30° and 0-75°; however, an obvious difference can be observed for the case of 0-90°.

Part 1: 0.0 - 15.0 s

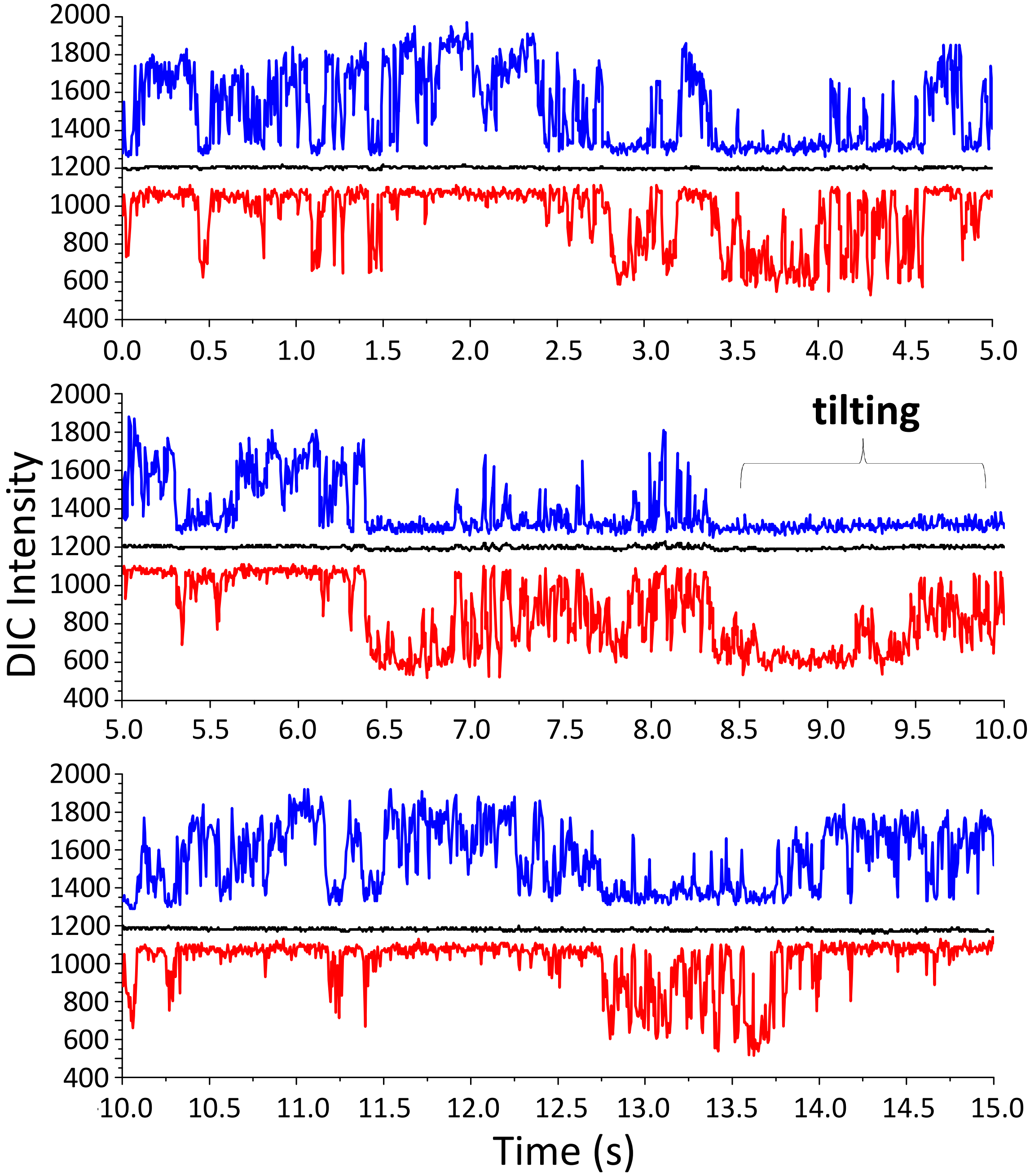

Part 2: 15.0 - 30.0 s

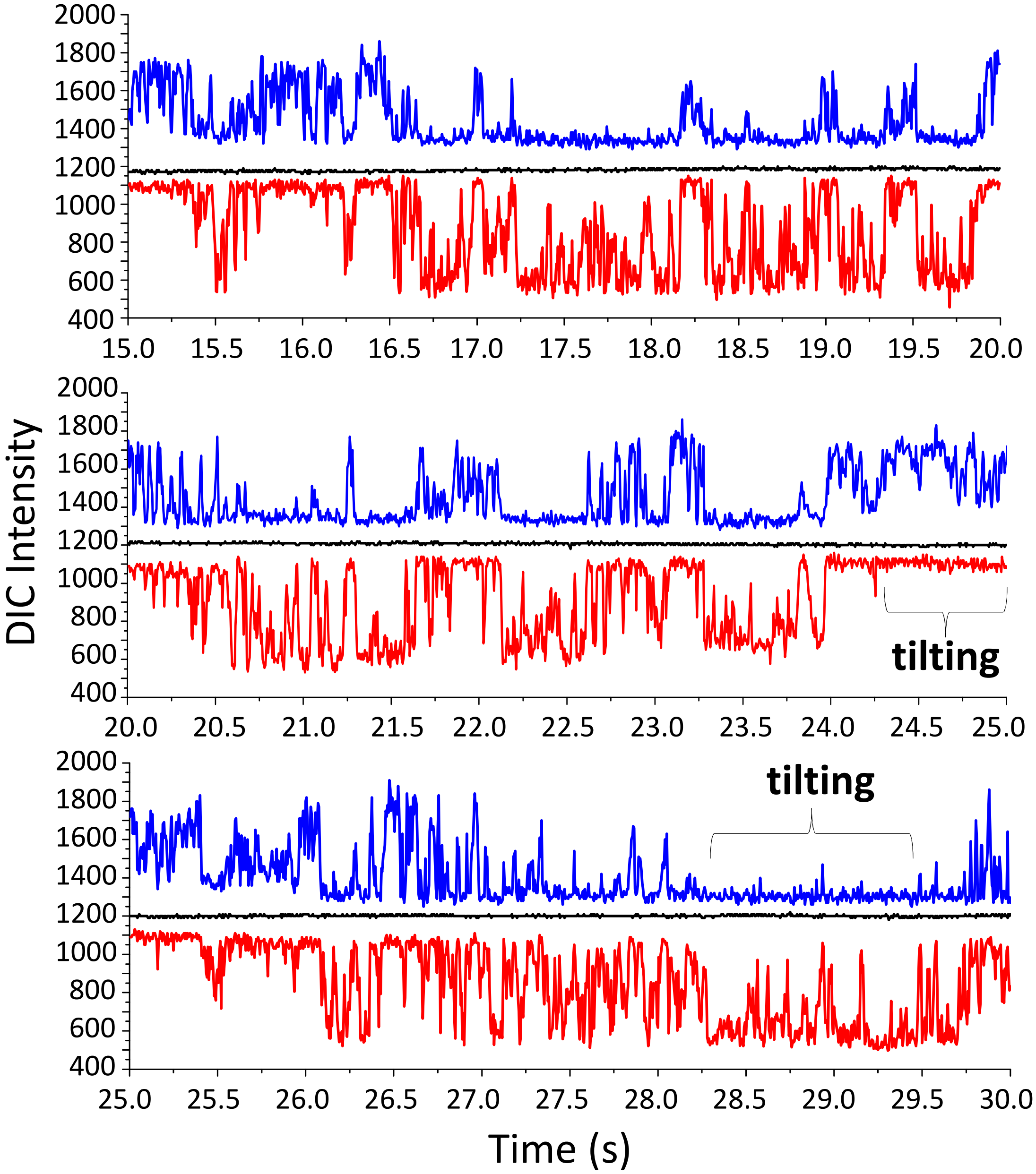

Figure 4.S12. DIC intensity traces of the transferrin-modified gold nanorod that produced the correlation coefficient trace shown in **Figure3.2e** in the main text. The bright and dark intensities are shown in blue and red, respectively, and the average background intensities are shown in black.

CHAPTER 5

ROTATIONAL DYNAMICS OF CARGOS AT PAUSES DURING AXONAL TRANSPORT

A paper published in *Nature Communications*

2012, *3*, 1030

Yan Gu[1,§], *Wei Sun*[1,§,†], *Gufeng Wang*[1,‡], *Ksenija Jeftinija*[2], *Srdija Jeftinija*[2]*and Ning Fang*[1,*]

Ames Laboratory, U.S. Department of Energy and Department of Chemistry, Iowa State University,
Ames, Iowa, 50011

Department of Biomedical Sciences, College of Veterinary Medicine, Iowa State University, Ames,
Iowa, 50011

[§]These authors contributed equally to this work.

[†]Current address: Department of Chemistry, the University of Washington, Seattle, WA 98195

[‡]Current address: Department of Chemistry, North Carolina State University, Raleigh, NC 27695

Abstract

Direct visualization of axonal transport in live neurons is essential to learn about the neuronal functions and the working mechanisms of microtubule-based motor proteins. In this paper, the high-speed single particle orientation and rotational tracking (SPORT) technique was developed for direct visualization of the rotational dynamics of cargos in both active directional transport and pausing stages of axonal transport with a temporal resolution of 2 ms. Both long and short pauses were imaged, and the correlations between the pause duration, the rotational behavior of the cargo at the pause, and the moving direction after the pause

were established. Furthermore, the rotational dynamics leading to switching tracks were visualized in detail. These first-time observations of cargo's rotational dynamics provide new insights on how kinesin and dynein motors take the cargo through the alternating stages of active directional transport and pause.

Introduction

Axonal transport of proteins and materials inside the cytoplasm of the slender axon is essential to a neuron's growth and function. For example, proteins manufactured by ribosomes need to be delivered anterogradely from the cell body and distributed along the axon, while extracellular materials internalized through endocytosis at the distant axon outposts are moved retrogradely towards the cell body for degradation. Dysfunction of axonal transport may lead to serious neuronal disorders such as the Alzheimer's disease, which is related to the abnormal depolymerization of microtubules inside the axon.[1] Besides its physiological significance, axonal transport is a model system for studying the mechanisms of intracellular transport by motor proteins in mammalian cells. The microtubule arrays located inside the axon have the same polarity with the minus end facing the cell body. The motor proteins kinesin and dynein transport cargos in the anterograde and retrograde directions, respectively, by "walking" on the microtubule arrays.[2]

The underlying mechanism of axonal transport has been studied intensively for several decades.[3-8] Cargos are moved between the cell body and the synapse via fast and slow axonal transport. It has been found that membranous cargos are generally fast transport components,[8] while cytoskeletal structures[9-11] and non-membrane bound proteins[6,12] are slow transport components. Both slow- and fast-transport cargos move at comparable speeds when they are actually moving, and the transport efficiency is determined mainly by the fraction of time they spend in moving.[8] Cargos pause much more frequently and for longer durations in the slow transport than in the fast transport. The "Stop and Go" model suggests that the pauses are caused by the varying affinities between the cargo and motor proteins in slow axonal transport.[5,13,14] When the coupling between the cargo and the motor proteins is deficient, the cargo can fall off the microtubule to pause the transport. Another hypothesis suggests that the pauses are a result of tug-of-war among motor proteins of opposing directionality.[15-17]

Understanding the mechanism of axonal transport relies on our knowledge on how the two motor proteins of opposing directionality move a cargo. The tug-of-war model supports the idea that the two motor proteins compete with each other to move the cargo in their desired direction.[16-19] On the contrary, the coordination model suggests that the two types of motor proteins are coordinated by certain molecular signals so that only one is activated while the other is deactivated during transport,[20-25] and a coordination complex might exist to regulate the motors,[26,27] although this coordination complex was proved unnecessary to explain the bidirectional cargo transport.[17] It was also proposed that the two models coexist in the microtubule-based transport, while tug-of-war can be deemed as one mechanism of “coordination”.[15] In this model, multiple kinesin and dynein motors bind to the cargo at the same time, and communication and coordination are achieved through the engaging and disengaging of motor proteins under competing pulling forces; the moving direction of the cargo is directly decided by the number of motors that engage in the tug-of-war.[28-30] Recently, Schuster *et al.* showed that the change in the transport direction is influenced by the binding and unbinding of dynein motors to the organelles,[31] and Kunwar *et al*. used the theoretical “mean field” model to show that an additional level of regulation is necessary to combine with “tugs-of-war” to explain the *in vivo* transport data,[32] while the “sharp maxima approximation” approach was also shown to be able to quantitatively describe the stochastic dynamics of the tug-of-war model.[19]

Direct visualization of the transport events in living neurons has led to the current understanding of the mechanism of axonal transport. For example, the axonal transport of organelles has been visualized in real-time using fluorescence-based techniques[9,12,33] Pseudo total internal reflection fluorescence (pseudo-TIRF) microscopy has been applied in tracking the axonal transport of nerve growth factor-modified quantum dots incorporated in endosomes.[34] However, the mechanics of the pauses in the transit of cargos are still largely unknown, mainly because of the limitations of the molecular or nanoparticle probes used in the previous studies. No orientation or rotational information of the cargo at the pauses was disclosed. The cargo’s rotational dynamics at the pauses is the direct consequence of motor protein competition and regulation and thus is essential to fully understand axonal transport.

In all of the previous reports, the cargo itself or the labels on the cargo gave constant image contrasts at a seemingly fixed location during a pause. It was unclear whether the cargo was completely fixed in space with no motion at all or it was still rotating at various speeds.

Recently, we introduced the single particle orientation and rotational tracking (SPORT) technique[35-37] to follow the rotational motion of plasmonic gold nanorods[38] under a differential interference contrast (DIC) microscope. Working in the principle of interferometry,[39] a DIC microscope generates disproportionate bright and dark interference patterns for gold nanorods in different orientations. The relative bright and dark intensities are independent measures of the effective projections of the nanorods onto the two polarization axes, from which the gold nanorod’s 3D orientation can be resolved in each DIC image. By measuring the bright and dark DIC intensities of the gold nanorod continuously, it becomes possible to dynamically track the nanorod’s orientation and rotational patterns. Using the SPORT technique with an electron multiplying charge coupled device (EMCCD) running at a temporal resolution of 30 ms, we observed that a cargo tends to keep the same orientation relative to the microtubule tracks during the active transport in living cells.[35]

In the current study, we acquired for the first time the orientation and rotational information of the cargo during both the moving (directional transport) and pausing stages of axonal transport at a high temporal resolution of 2 ms. This high temporal resolution was achieved by using a scientific complementary metal-oxide-semiconductor (CMOS) camera when limiting the region of interest to a narrow stripe that was aligned with the axon where the transport events occurred. Such a high temporal resolution is necessary to resolve the motions of cargo in unprecedented detail and answer some of the outstanding questions on the mechanism of axonal transport.

Rotational motion of endocytic vesicles reported by gold nanorods. The gold nanorods with an average size of 25 nm × 73 nm were used as orientation and rotational nanoprobes**.** **Supplementary Figure 5.S1** shows a set of DIC images for a gold nanorod that was immobilized on a glass slide and rotated to different orientations with an interval of 10°. The gold nanorods were surface-modified with transferrin (a glycoprotein used as a drug delivery agent[40]) through a polyethylene glycol (PEG) linker to facilitate receptor-mediated endocytosis. After endocytosis, these nanorods were transported inside the endocytic vesicles by motor proteins along the cytoskeletal tracks. Some of the nanorod-containing vesicles were found to be transported in the axons anterogradely or retrogradely.

For a gold nanorod to report the vesicle's rotational motion accurately, the nanorod is required to be stationary with respect to the vesicle on the time scale of the transport events. This requirement is generally met when a single nanorod is contained within the lipid membranes of a small endocytic vesicle, which has a size comparable to the size of the nanorod, and is bound to the transferrin receptors imbedded in the lipid membrane. **Supplementary Figure 5.S2** is a transmission electron micrograph showing gold nanorod-containing vesicles in a PC12 cell.

However, after the endocytic vesicle fuses with an early or late endosome, there is more room for the nanorod to rotate randomly, losing its ability to report the rotational motions of the vesicles. An example that the nanorods cannot be used as the orientation and rotational reporter is provided in **Supplementary Movie 5.1**. Apparently, the two nanorods in this movie were transported together inside the same endosome, and they were free to perform rotational and translational Brownian motions.

The qualification of each individual nanorod as orientation and rotational reporter must be verified by checking whether the nanorod maintained a constant DIC image pattern during the undisrupted linear transport. This criterion is based on the fact that cytoplasmic microtubules in mammalian cells, including PC12 cells, are composed of 13 linear protofilaments,[41] and that kinesin and dynein motor proteins pull the cargos along the linear protofilament tracks if there are no interruptions (e.g., obstacles, dissociation of motors from the tracks or degraded microtubules) to the transport.[42,43] A constant DIC image pattern during the linear transport events suggests that the nanorod and its lipid vesicle maintain their orientation relative to one another and to the microtubule tracks as we have reported previously.[35] The restriction on the cargo's rotational motion during the directional transport is believed to be caused by tension applied by multiple motor proteins bound to the cargo. All of the nanorods that were analyzed and discussed in the rest of the paper showed the linear directional transport without noticeable cargo rotations.

Paused nanocargos undergoing restricted rotations. During the axonal transport, the cargo can be in two stages: first, the directional (anterograde or retrograde) transport driven by the motor proteins kinesin and dynein and second, the pausing stage, in which the cargo shows little or no directional movement. The pause durations vary from tens of milliseconds to tens of seconds. The cargo undergoes different motions depending on the binding status of the motor proteins to the cargo and the microtubules.

The first type of motion at the pausing stage is demonstrated in **Supplementary Movie 5.2**, in which a nanorod paused for ~6.2 s before it reversed its moving direction. The corresponding bright and dark DIC intensities of the nanorod during the whole pause period are displayed in **Figure 5.1A**. The significant DIC intensity fluctuations indicate the fast rotational motion of the cargo during this long pause. To the best of our knowledge, this type of rotational motion has not been visualized in living cells by using any other imaging techniques.

In order to better understand how the nanocargo's rotational motion is affected by the motor proteins and other associate proteins, the unrestricted rotational Brownian motion was analyzed as shown in **Figure 5.1B**. This nanorod-containing cargo diffused freely in the axon of a differentiated PC12 cell, which had been treated with cochicine to destroy the microtubules (**Supplementary Figure 5.S3**).[44] Since the cargo could no longer attach to the intact microtubules, it performed random translational and rotational diffusion.

The difference in these two rotational patterns is revealed by an analysis of the degree of correlation for the bright and dark intensities. The correlated bright and dark intensity changes indicate the nanorod’s in-plane rotation, while the anti-correlated intensity changes correspond to the out-of-plane rotation (see **Supplementary Figure 5.S4** for details). Pearson’s correlation coefficient (*r*) was thus used to analyze the DIC intensity traces with a maximum value of +1 for perfectly correlated cases, a minimum value of -1 for perfectly anti-correlated case, and the value 0 for uncorrelated cases.

The correlation analysis showed that the rotational motion during the long pause (**Figure 5.1A**) is distinctively different from the unrestricted rotational Brownian motion (**Figure 5.1B**). The correlation coefficient for the time traces during the long pause was calculated to be 0.79. The average correlation coefficient for 26 recorded long pauses that lasted for at least 3 s was 0.70 ± 0.06 (**Figure 5.1C**). Such a large correlation coefficient suggests a high proportion of the in-plane rotational component. On the contrary, the correlation coefficient for this example of rotational Brownian motion was found to be 0.11 (close to 0, uncorrelated), suggesting the random 3D rotations with roughly equal proportions of the in-plane and out-of-plane rotational components. The average correlation coefficient for 29 recorded time traces of unrestricted rotational Brownian motion (**Figure 5.1D**) was 0.26 ± 0.09. The rotation dynamics can also be characterized using the power spectral density (PSD) function. By fitting the PSD of the intensity traces with the Lorentzian function (**Supplementary Figure 5.S5**),[45] we found that the rotation characteristic time of the in-plane rotation at the pauses (8.7 – 14.3 ms) is longer than that of the random Brownian motion (2.1

± 0.3 ms), indicating the rotation at these long pauses is slower than the Brownian motion.

The in-plane rotational motion of the cargo at the long pause leads to two new findings.

First, the fast rotational motion provides direct evidence that the confinement of the rotational motions of the cargos caused by the binding of kinesin and dynein motors and possibly other associated proteins have been significantly weakened and the nanorod has gained more freedom to rotate randomly during the pauses of this type.

Second, the mostly in-plane rotational motion suggests that the cargo was still tethered to the microtubule track. Otherwise, if the cargo was fully detached from the microtubule track, it would perform largely unrestricted rotational Brownian motion to generate uncorrelated bright and dark DIC intensity changing patterns (similar to **Figure 5.1B**) at a faster speed. The restraint could come from kinesin and dynein motors or other associated proteins such as dynactin.[46,47] One possibility is that the motor proteins could be deactivated by regulatory molecules but still bound to both the cargo and microtubule. The other possibility is that dynactin, which provides extra docking sites on the cargos and link the cargos to cytoplasmic dynein and microtubule tracks,[48-50] could also tether the cargos to the microtubules, independent of the molecular motors, and also restrict the rotational motions. In either way, the observation that the cargos performed restricted rotational motions show that they were still tethered to the microtubule tracks at the pauses.

Pause duration and rotation and change of moving direction. Movie 4.3 provides a complex example of cargo's behaviors at the directional transport and pausing stages. The corresponding bright and dark DIC intensity curves and the nanorod's lateral displacement are displayed in **Figure 5.2**. The nanorod-containing vesicle was transported for a distance of 4 µm retrogradely by dynein motors at ~1.0 µm/s in the time window of 1-5 s, paused for 5 s, and then moved again in the opposite direction by kinesin motors at a lower velocity of ~0.3 µm/s until the end of the recording. During both directional transport segments, the nanorod generated rather constant DIC intensities with noise expected from the DIC intensity measurements at the fast temporal resolution of 2 ms. The speed of cargo transport varied quite dramatically even in the same directional transport event as revealed by different slopes of the displacement curve. For example, the transport in **Figure 5.2C** is much faster than that in **Figure 5.2D**.

When the cargo showed rotational motion during the 5-s pause, the bright and dark DIC intensities display a similar level of correlation (r = 0.68) as the example shown in **Figure 5.1A**. In addition to this long pause, there were shorter pauses that lasted for tens to hundreds of milliseconds. Due to these short pauses and other random motions, the displacement curve is far from smooth, suggesting a number of probable factors, including the competition between kinesin and dynein motors and the steric hindrance, affect the transport process continuously and result in the stochastic nature of cargo transport.

The short pauses were accompanied by different cargo movement. The pink boxes in **Figures 5.2B and D** highlight a 0.5-s pause with almost no changes in the DIC intensities, suggesting that the cargo came to a full stop without apparent rotational motion. After the pause the cargo continued to move in the same direction. The blue arrows in **Figure 5.2B** point out another type of short pause characterized by fast reversal in the transport direction (back-and-forth movement).

Many pauses of different durations were recorded. More examples are shown in **Supplementary Figures 5.S6-5.S9.** *A statistical analysis was carried out to find the correlation between the pause duration, the rotational motion, and the subsequent transport direction.*

For the pauses that incorporated no rotational information, the time was generally short (**Figure 5.3A**), and 61 out of the 93 recorded pauses (65.6%) ended with the cargos moving in the same direction. During this type of pauses, the tension applied by motor proteins likely remained high and balanced to keep the cargos from rotating freely. The time required to resume active directional transport was generally short, and the cargos tended to maintain the original transport direction.

For the pauses with rotation, the pause durations were generally longer with a second maximum at 5-6 s (**Figure 5.3B**). During this type of pauses, the tension exerted by the motors was weakened due to the uncoupling of some motors. It is plausible that the pauses caused by the extensive uncoupling and reattachment of motors required a longer time to return to the active directional transport stage.

Another important finding is that the majority of the pauses with rotation (76%, 62 out of

81 cases) were followed by the cargo transport in the reversed direction. Such a significant bias in favor of the reversed transport direction after pause indicates that the bi-directional transport of cargos should be affected by some regulatory mechanisms, instead of working in a simple unregulated stochastic manner.[32] The regulations could result in the change of single motor parameters, since the cargo transport is highly sensitive to the change of motor properties induced by regulatory mechanisms.[17] Other than the regulatory mechanisms, the long pauses observed with high occurrence of rotational motions and reversals could also be possibly due to obstacles that impede the cargos from moving forward smoothly. The unbinding and binding of the motors when confronted with an obstacle could result in extended pauses and also involve the rotational motions of the cargos. Future work to correlate these new experimental observations with computational models of motor proteins may eventually lead to a fuller understanding of the complicated mechanisms.

Cargo motions at track-switching. Track-switching is an important consequence of pause during axonal transport. Kinesin and dynein motors frequently encounter obstacles, such as other cargos, microtubule-associated proteins, and intersecting microtubules, which obstruct their way in the transport direction.[42,51-56] The motors may pause until the track becomes available again to continue the transport, or they may overcome these obstacles by switching to other microtubules. Using SPORT, the cargo's motions during the track-switching processes were elucidated in detail.

Figure 5.4 and **Supplementary Movie 5.4** show the moving trace of a gold nanorod-containing vesicle that switched to another microtubule and reversed its moving direction after a pause. Three steps were visualized and identified for this track-switching process. The cargo was initially transported anterogradely by kinesin. Step 1 was a short pause with no apparent rotational motion. The nanorod moved to a new location of ~100 nm away from the original location in only 2-3 frames (4-6 ms) at ~2.5 s, and started the rotation and random translational movement within a 400 nm × 200 nm region in Step 2 until ~8.1 s. In Step 3, the cargo stopped the rotational motion for ~1 s before it finally started the retrograde transport along another microtubule that was 170 nm away from the original one. The correlation coefficients of the bright and dark DIC intensities in Steps 2 was 0.75, suggesting that the cargo was still tethered to the microtubule tracks and underwent the in-plane rotation.

Apparently, the cargo “strode” from one microtubule to another and reversed the moving direction. Based on the distance between the two microtubule tracks, the rotational behavior of the gold nanorod and its positions during this process, the cargo possibly went through the following steps to switch the microtubule track and reverse the moving direction: First, the cargo encountered an obstacle and stopped proceeding. Second, Some motor proteins were then detached from the microtubule track to give enough freedom to the cargo to allow it to rotate and swing away from the original track; in the meantime, the detached motor proteins or newly recruited ones attempted to bind to other neighboring tracks. This was the time when both rotational and translational movements were observed in Steps 2. The cargo was always tethered to the microtubules to result in the mostly in-plane rotational motion. Then, The rotational and translational movements stopped in Step 3 when enough kinesin and dynein motors and possibly other associated proteins were bound to the microtubules to prohibit the cargos from moving. At last, at the end of Step 3, the active retrograde transport was finally initiated by the dynein motors on a microtubule that was ~170 nm away from the original one.

Additional examples of gold nanorods switching tracks can be found in **Supplementary Figures 5.S10 and 5.S11**. In both examples, the cargos showed rotational behavior during the pauses before switching tracks. This can be attributed to the requirement of cargo getting loose from the original microtubule and being attached to a different one.

In summary, the SPORT technique with a temporal resolution of 2 ms has been developed and used to study the axonal transport of membranous cargos. The behaviors of gold nanorod-containing cargos in both active transport and pausing stages have been elucidated in unprecedented detail. During the active transport, multiple motor proteins bind to the cargo to provide a sufficient tension to maintain the cargo’s orientation. Between the active directional transport stages, the cargo experiences long and short pauses and undergoes different motions dependent upon the binding status of the kinesin and dynein motors together with other possible associated proteins such as dynactin to the cargo and the microtubule. The pauses sometimes are followed by the cargo switching to a different microtubule track. These first-time observations on the rotational dynamics of the cargo by the SPORT technique reveal how motor proteins and other associated proteins take the cargo through the alternating stages of active directional transport and pause.

As a future direction, the high-speed SPORT technique will provide new evidence for understanding the mechanism of the differential modulation of kinesin and dynein motor proteins by regulating factors, such as microtubule-associated protein tau.[57-59] The combination of SPORT and fluorescence microscopy will be able to correlate the rotational dynamics of cargo with interactions between motor proteins and fluorescence-labeled microtubule-associated proteins.

Cell culture. PC12 cells (CRL 1721.1, ATCC, Manassas, VA) were cultured on 22 mm × 22 mm poly-l-lysine coated coverslips in six-well cell culturing plates. The complete cell culture medium was composed of F12K cell culturing medium (ATCC), 15% horse bovine serum (ATCC) and 2.5% Fetal Bovine Serum (ATCC) and was added to the plates. After the cells covered 70% of the coverslips, F12K medium supplemented with 200 ng/mL 2.5S neuron growth factor (NGF) (Bioproducts for Science, Madison, WI) was added to the plates. The cells were incubated in 37°C incubator with 5% CO_2 for 48 h. The cell culturing medium was then changed to F12K medium supplemented with 200 ng/mL NGF and 0.05 mM foskolin (Catalog #344270, CalBiochem/EMD Biosciences). Rapid neurite extension was observed within 20 min. The differentiated PC12 cells were left in the incubator for another 48 h before use to allow the growth of intact microtubules in the axons.

Preparation of transferrin-modified gold nanorods. To facilitate their internalization into PC12 cells, the gold nanorods were modified with transferrin. Cetyltrimethylammonium bromide (CTAB)-capped (25 nm ×73 nm, 1.3×10^{11} particles/mL, Nanopartz) gold nanorods were used. An N-hydroxylsuccinimide-polyethylene glycol (NHS-PEG) disulfide linker (Sigma-Aldrich) was used by following a published protocol.[60] The NHS-PEG disulfide linker has both disulfide and succinimidyl functionalities for respective chemisorption onto gold and facile covalent coupling of transferrin molecules. Briefly, excessive surfactant was first removed from 1.0 mL of gold nanorod solution by centrifugation at 3000 g for 10 min and the particles were resuspended in 1.0 mL of 2 mM borate buffer. A proper amount of fresh NHS-PEG disulfide solution (in dimethyl sulfoxide) was added to reach a final thiol concentration of 0.2 mM and reacted with gold nanorods for 2 h. The solution was then cleaned up by centrifugation and resuspended in 2 mM borate buffer. 2.0 μg of transferrin was added to the gold colloidal solution and allowed to react for 8 h. Before use, the colloidal gold nanorod probes were cleaned up by centrifugation and resuspended in 2 mM borate buffer. The concentrated gold colloidal solution was diluted to a final concentration of 4.3×10^{9} particles/mL for incubation with cells.

Live cell imaging. 40 μL of diluted transferrin modified gold nanorod solution were added to the cell cultures and incubated for 45 min. The coverslip was rinsed with PBS buffer (10 mM, pH 7.4) and then placed on a clean glass slide for observation. Two pieces of double-sided tape served as spacers between the glass slide and the coverslip to form a chamber. 30μL of fresh complete cell culturing medium was added to the chamber. An upright Nikon Eclipse 80i microscope with a pair of Nomarski prisms and two polarizers was used for the imaging. The microscope was equipped with a 100× 1.40 numerical aperture (NA) Plan Apo oil immersion objective and a 1.4 NA oil immersion condenser. A 700-nm optical filter (Semrock, Rochester, NY) with a bandwidth of 20 nm was inserted at the illumination side. The movies were taken by a Hamamatsu ORCA-Flash2.8 CMOS camera at 500 frames/s. The collected videos were analyzed with MATLAB and NIH ImageJ.

Microtubule destruction and fluorescence immunostaining. The cells were incubated with transferrin-modified gold nanorods for 45 min and then in the cell culturing medium containing 200 μg/mL colchicine for 1 h in the incubator (37°C, 5% CO_2). The effect of colchicine on the microtubule network was confirmed by fixing both the treated and untreated cells with 4% paraldehyde in PBS solution and staining with the 1st antibody (mouse anti-alpha tubulin) and the 2nd antibody (Alexa 488 goat anti-mouse). The fluorescent images of the destroyed microtubules after treated with colchicine and the intact microtubules in the untreated cells were observed under the Nikon Eclipse 80i microscope.

Transmission electron microscopy of gold nanorod-containing vesicles. The PC12 cells were plated on 22 mm × 22 mm coverslips in 3.5 cm petri-dishes and incubated with the complete cell culture medium until the cells reached over 90% confluency on the coverslips.

The transferrin modified gold nanorod solution were added into the petri-dishes to reach a final concentration of 3.7 × 10^{10} nanoparticles/mL and the cells were incubated with the nanoparticles for 50 min at 37°C in a cell incubator. After that, the cells were removed from the cell culturing medium and incubated with the fixative solution containing 2.0% glutaraldehyde and 2.0% paraformaldehyde for 15 min and kept in a 4°C fridge overnight. The cells were then post-fixed with 1% osmium tetroxide in pH 7.2 PBS buffer for 1.5 h, and dehydrated in ethanol solutions with increasing concentrations of ethanol (ethanol/water v/v: 50%, 60% 70%, 80%, 90%, and 100%) for 15 min each and stained with 2% uranyl acetate in 70% ethanol solution at room temperature overnight. After that, the cells were washed three times with acetone and embedded in Epon resin. The embedded samples were removed from the coverslips and sectioned into 100 nm thick slices on a sliding ultramicrotome. The thin slices supported on the copper grids were examined with a JEOL 1200EX transmission electron microscope.

Data analysis. A MATLAB script was written to track the location and the DIC intensities of the gold nanorods. The constant image patterns of the gold nanorod during the directional transport facilitate the precise localization of the gold nanorods when being transported. The nanorods were localized by looking for the center of the images. However, at the pauses when rotations occurred, the varying DIC image patterns reduced the localization precision. The actual localization precision in each image frame varies depending on the nanorod's orientation at that moment as different orientations give rise to different bright and dark DIC intensities and thus different signal-to-noise ratios. The small pixel size of the Hamamatsu CMOS camera (3.63 μm × 3.63 μm) allows the localization of gold nanorod to a precision of about 1-2 pixels or 45-90 nm.

The rotation modes of the nano-cargo during the pauses were determined by calculating the Pearson's correlation coefficient of the bright and dark part intensities of the DIC images. Pearson's correlation coefficient is defined as the covariance of the two variables divided by the product of their standard deviations. It should be noted that the correlation coefficients were only calculated for the periods when the nanocargoes underwent rotational motions. When a nanocargo showed no apparent rotational motion, the noise would strongly affect the correlation analysis to result in mostly uncorrelated (close to 0) correlation coefficients.

Acknowlegements

The authors gratefully acknowledge the Microscopy and NanoImaging Facility at Iowa State University for taking transmission electron micrographs of nanorod-containing vesicles.

References

1. S. Roy, B. Zhang, V. M. Y. Lee et al., *Acta Neuropathol.* **109** (1), 5 (2005).
2. N. Hirokawa and R. Takemura, *Nat. Rev. Neurosci.* **6** (3), 201 (2005).
3. M. M. Black and R. J. Lasek, *J. Cell Biol.* **86** (2), 616 (1980).
4. R. J. Lasek, J. A. Garner, and S. T. Brady, *J. Cell Biol.* **99** (1), S212 (1984).
5. J. V. Shah and D. W. Cleveland, *Curr. Opin. Cell Biol.* **14** (1), 58 (2002).
6. S. Roy, M. J. Winton, M. M. Black et al., *J. Neurosci.* **27** (12), 3131 (2007).
7. A. B. Dahlstrom, *Prog. Neurobiol.* **90** (2), 119 (2010).

8. A. Brown, *J. Cell Biol.* **160** (6), 817 (2003).
9. S. Roy, P. Coffee, G. Smith et al., *J. Neurosci.* **20** (18), 6849 (2000).
10. L. Wang and A. Brown, *Mol. Biol. Cell* **12** (10), 3257 (2001).
11. A. Brown, L. Wang, and P. Jung, *Mol. Biol. Cell* **16** (9), 4243 (2005).
12. B. Droz and C. P. Leblond, *Science* **137** (3535), 1047 (1962).
13. K. E. Miller and S. R. Heidemann, *Exp. Cell Res.* **314** (10), 1981 (2008).
14. A. V. Kuznetsov, A. A. Avramenko, and D. G. Blinov, *Int. Commun. Heat Mass Transf.* **36** (4), 293 (2009).
15. A. G. Hendricks, E. Perlson, J. L. Ross et al., *Curr. Biol.* **20** (8), 697 (2010).
16. V. Soppina, A. K. Rai, A. J. Ramaiya et al., *Proc. Natl. Acad. Sci. U. S. A.* **106** (46), 19381 (2009).
17. M. J. I. Muller, S. Klumpp, and R. Lipowsky, *Proc. Natl. Acad. Sci. U. S. A.* **105** (12), 4609 (2008).
18. M. J. I. Muller, S. Klumpp, and R. Lipowsky, *Biophysical Journal* **98** (11), 2610 (2010).
19. M. J. I. Muller, S. Klumpp, and R. Lipowsky, *Journal of Statistical Physics* **133** (6), 1059 (2008).
20. E. L. F. Holzbaur and Y. E. Goldman, *Curr. Opin. Cell Biol.* **22** (1), 4 (2010).
21. S. P. Gross, M. A. Welte, S. M. Block et al., *J. Cell Biol.* **156** (4), 715 (2002).
22. C. Kural, H. Kim, S. Syed et al., *Science* **308** (5727), 1469 (2005).
23. A. G. Larson, E. C. Landahl, and S. E. Rice, *Phys. Chem. Chem. Phys.* **11** (24), 4890 (2009).
24. S. Ally, A. G. Larson, K. Barlan et al., *J. Cell Biol.* **187** (7), 1071 (2009).
25. J. A. Laib, J. A. Marin, R. A. Bloodgood et al., *Proc. Natl. Acad. Sci. U. S. A.* **106** (9), 3190 (2009).
26. S. P. Gross, *Physical Biology* **1** (1-2), R1 (2004).
27. Michael A. Welte, *Current biology : CB* **14** (13), R525 (2004).
28. M. A. Welte, *Curr. Biol.* **20** (9), R410 (2010).
29. Y. X. Zhang, *Physical Review E* **83** (1) (2011).
30. G. T. Shubeita, S. L. Tran, J. Xu et al., *Cell* **135** (6), 1098 (2008).
31. M. Schuster, R. Lipowsky, M. A. Assmann et al., *Proc. Natl. Acad. Sci. U. S. A.* **108** (9), 3618 (2011).
32. A. Kunwar, S. K. Tripathy, J. Xu et al., *Proc. Natl. Acad. Sci. U. S. A.* **108** (47), 18960 (2011).
33. X. L. Nan, P. A. Sims, P. Chen et al., *J. Phys. Chem. B* **109** (51), 24220 (2005).
34. B. X. Cui, C. B. Wu, L. Chen et al., *Proc. Natl. Acad. Sci. U. S. A.* **104** (34), 13666 (2007).
35. G. Wang, Wei Sun, Yong Luo et al., *J. Am. Chem. Soc.* **132** (46), 16417 (2010).
36. Ji Won Ha, Wei Sun, Gufeng Wang et al., *Chem. Commun.* **47**, 7743 (2011).
37. A. S. Stender, G. Wang, W. Sun et al., *ACS Nano* **4** (12), 7667 (2010).
38. C. Sonnichsen and A. P. Alivisatos, *Nano Lett.* **5** (2), 301 (2005).

39. Wei Sun, Gufeng Wang, Ning Fang et al., *Anal. Chem.* **81** (22), 9203 (2009).
40. Z. M. Qian, H. Y. Li, H. Z. Sun et al., *Pharmacol. Rev.* **54** (4), 561 (2002).
41. L. G. Tilney, J. Bryan, D. J. Bush et al., *J. Cell Biol.* **59** (2), 267 (1973).
42. A. Seitz and T. Surrey, *Embo Journal* **25** (2), 267 (2006).
43. K. M. Ori-McKenney, J. Xu, S. P. Gross et al., *Nat. Cell Biol.* **12** (12), 1228 (2010).
44. J. D. Gunstream, G. A. Castro, and E. T. Walters, *J. Neurosci.* **15** (1), 439 (1995).
45. S. Pierrat, E. Hartinger, S. Faiss et al., *J. Phys. Chem. C* **113** (26), 11179 (2009).
46. R. D. Vale, *Cell* **112** (4), 467 (2003).
47. C. Valetti, D. M. Wetzel, M. Schrader et al., *Mol. Biol. Cell* **10** (12), 4107 (1999).
48. S. J. King and T. A. Schroer, *Nat. Cell Biol.* **2** (1), 20 (2000).
49. N. J. Quintyne, S. R. Gill, D. M. Eckley et al., *J. Cell Biol.* **147** (2), 321 (1999).
50. T. A. Schroer, *Annu. Rev. Cell Dev. Biol.* **20**, 759 (2004).
51. M. Vershinin, B. C. Carter, D. S. Razafsky et al., *Proc. Natl. Acad. Sci. U. S. A.* **104** (1), 87 (2007).
52. I. A. Telley, P. Bieling, and T. Surrey, *Biophys. J.* **96** (8), 3341 (2009).
53. J. L. Ross, H. Shuman, E. L. F. Holzbaur et al., *Biophys. J.* **94** (8), 3115 (2008).
54. T. Korten and S. Diez, *Lab Chip* **8** (9), 1441 (2008).
55. J. L. Ross, M. Y. Ali, and D. M. Warshaw, *Curr. Opin. Cell Biol.* **20** (1), 41 (2008).
56. S. L. Reck-Peterson, A. Yildiz, A. P. Carter et al., *Cell* **126** (2), 335 (2006).
57. K. Stamer, R. Vogel, E. Thies et al., *J. Cell Biol.* **156** (6), 1051 (2002).
58. E. M. Mandelkow, K. Stamer, R. Vogel et al., *Neurobiology of Aging* **24** (8), 1079 (2003).
59. Ram Dixit, Jennifer L. Ross, Yale E. Goldman et al., *Science* **319** (5866), 1086 (2008).
60. R. Narayanan, R. J. Lipert, and M. D. Porter, *Anal. Chem.* **80** (6), 2265 (2008).

Figures

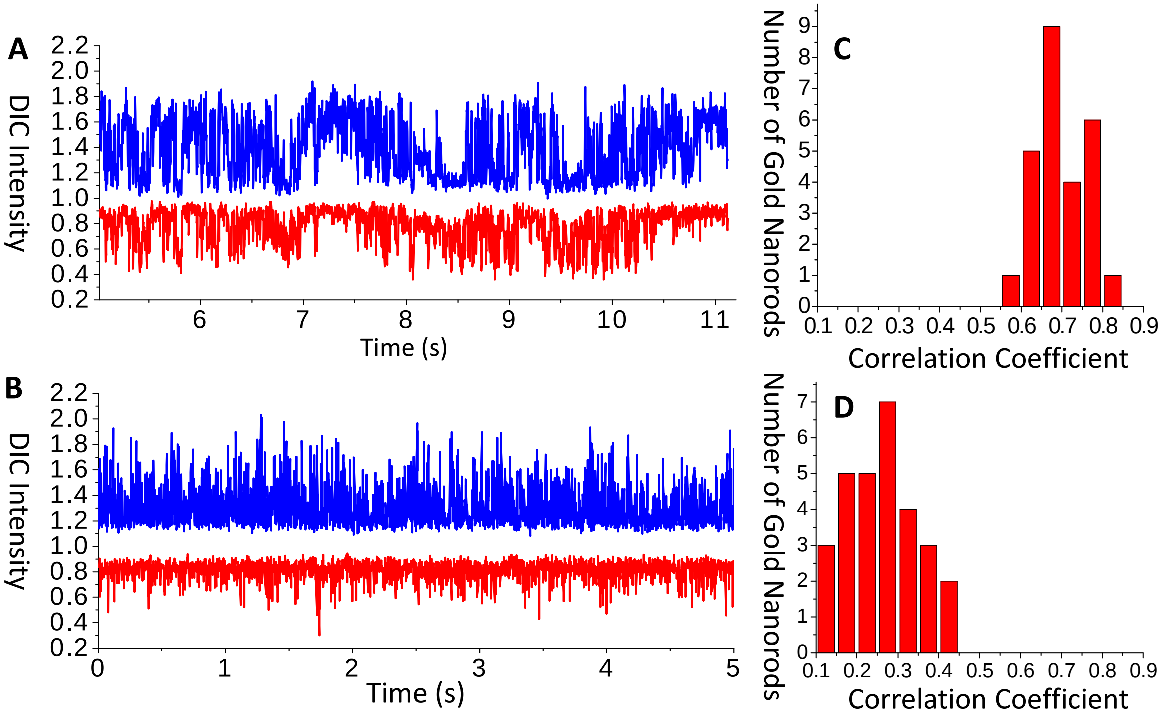

Figure 5.1. (A) Normalized DIC intensities of a gold nanorod-containing cargo at a long pause during the axonal transport. The bright and dark intensities are shown in blue and red, respectively. The x-axis (time) corresponds to the recording time of **Movie 4.2**. Before and after this pause, the cargo took on the directional transport. (B) Normalized DIC intensities of a gold nanorod-containing cargo freely diffusing in an axon where the microtubule arrays have been destroyed by colchicine. (C) Histogram of the correlation coefficients of the intensities of the gold nanorod-containing cargos at pauses. (D) Histogram of the correlation coefficients of the intensities of the gold nanorod-containing cargos freely diffusing in axons where the microtubule arrays have been destroyed by colchicine.

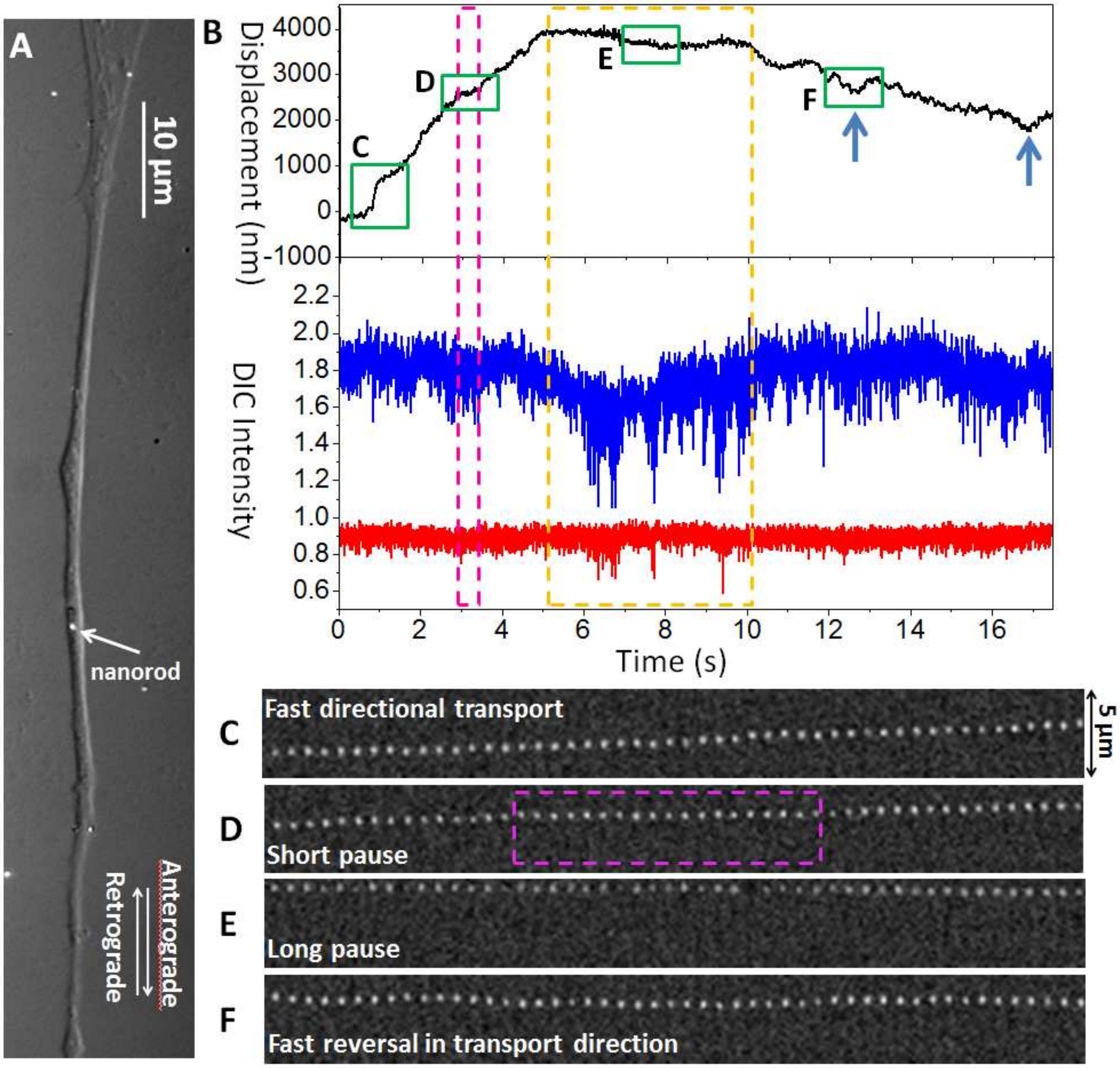

Figure 5.2. (A) DIC image of an axon of a differentiated PC 12 cell. A transferrin-modified gold nanorod is marked by the white arrow. The scale bar represents 10 µm. (B) Lateral displacement and normalized DIC intensities of a gold nanorod-containing cargo that was transported retrogradely, then paused, and finally was transported retrogradely again. The long pause is identified in the yellow frame, and a short pause in the pink frame. The fast reversals are highlighted by the blue arrows. (C-F) 50 images taken from **Supplementary Movie 4.3** at a time interval of 30 ms for each of the four regions highlighted in the green frames in (B), including (C) fast retrograde transport, (D) short pause without rotation, (E) long pause with rotation, and (F) fast reversal.

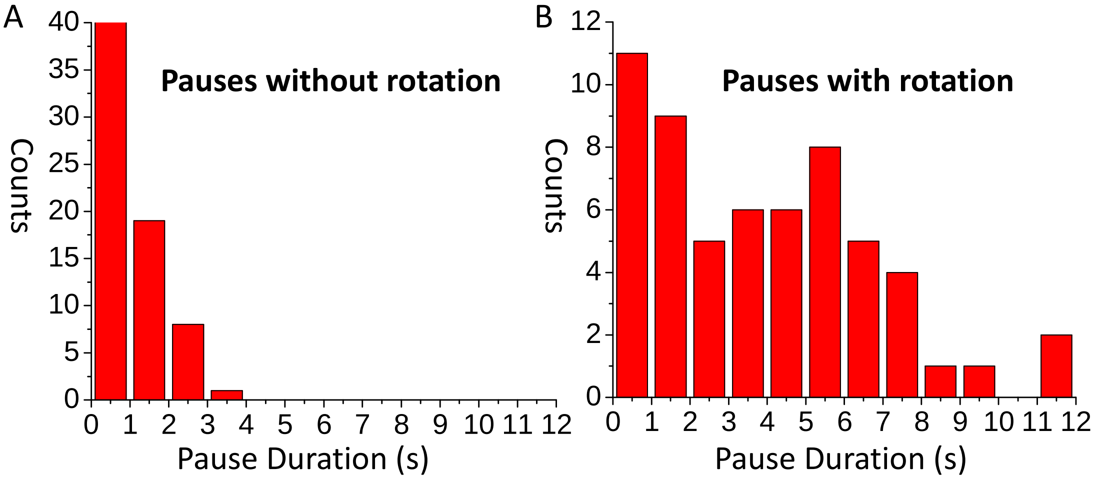

Figure 5.3. (A) Histograms of the pause durations for 93 pauses with no apparent rotational motion. (B) Histograms of the pause durations for 81 pauses with rotational motion.

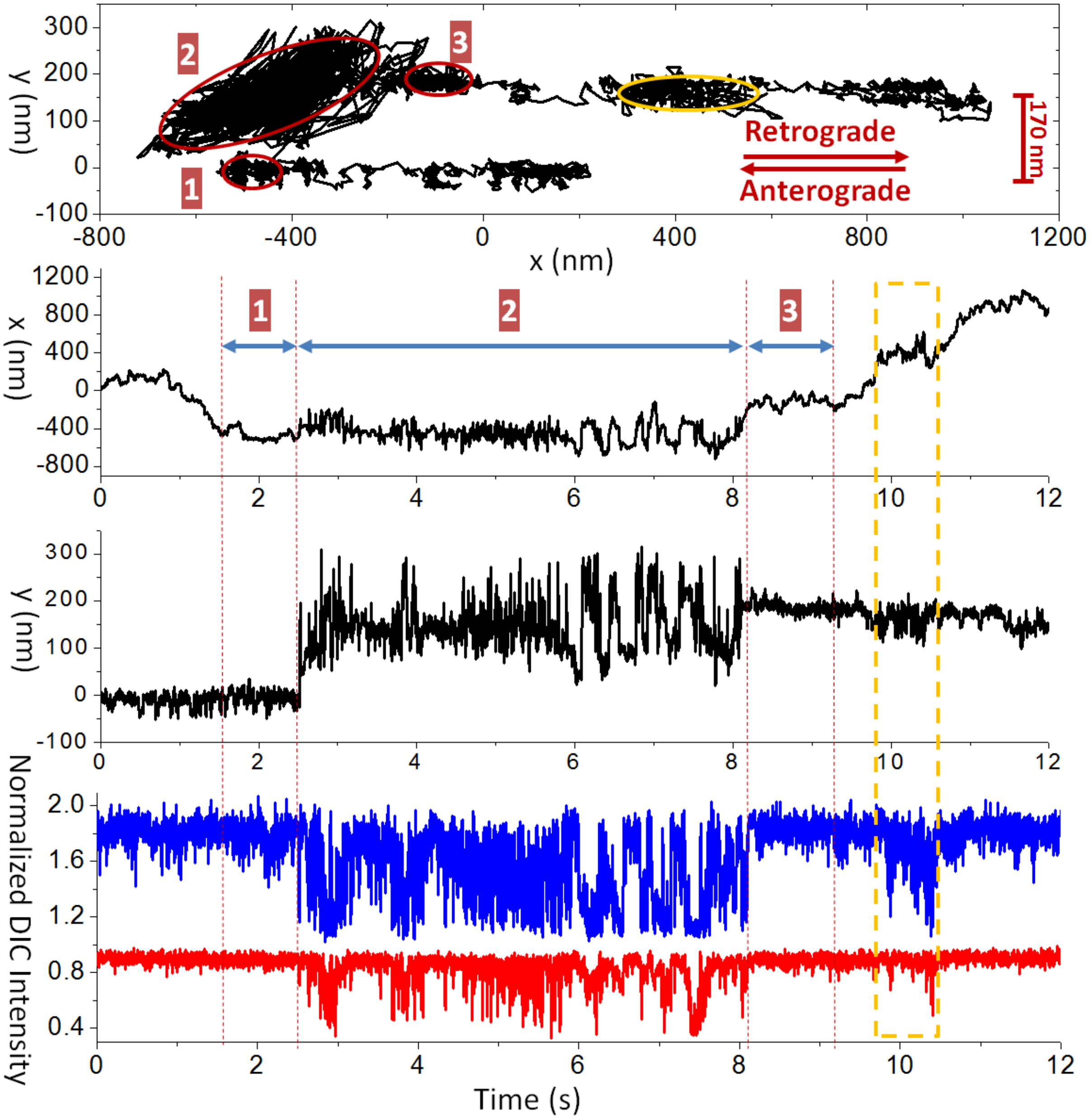

Figure 5.4. (A) The 2D trajectory that starts at the origin. (B) The x and y trajectories and the normalized DIC intensity traces. The bright and dark intensities are shown in blue and red, respectively. The three steps are labeled with numbers. Another short pause with rotational motion is highlighted in the yellow frame.

Supporting Information

for

Rotational Dynamics of Cargos at Pauses during Axonal Transport

Yan Gu[1,§], *Wei Sun*[1,§,†], *Gufeng Wang*[1,‡], *Ksenija Jeftinija*[2], *Srdija Jeftinija*[2] *and Ning Fang*[1,]*

Ames Laboratory, U.S. Department of Energy and Department of Chemistry, Iowa State University,
Ames, Iowa, 50011

1. College of Veterinary Medicine, Iowa State University, Ames, Iowa, 50011

[§] These authors contributed equally to this work.

[†] Current address: Department of Chemistry, the University of Washington, Seattle, WA 98195

[‡] Current address: Department of Chemistry, North Carolina State University, Raleigh, NC 27695

Supplementary Figures

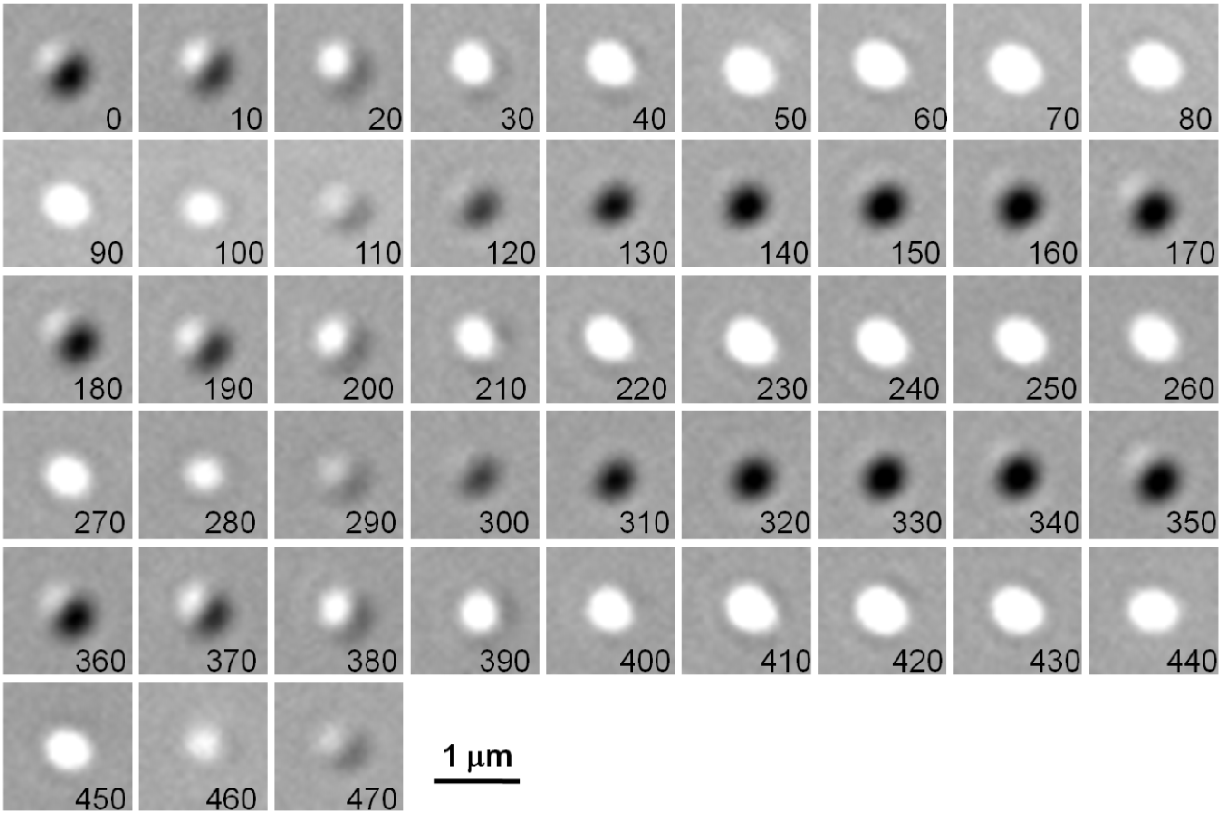

Figure 5S1. DIC images of a 25 nm ×73 nmgold nanorod illuminated at 720 nm (longitudinal plasmon resonance mode) at different orientations. The nanorod was placed on a rotating stage and imaged at an interval of 10°. The orientation angle of the nanorod is showed in each image. The periodic changes of DIC image patterns are clearly demonstrated in this set of images.

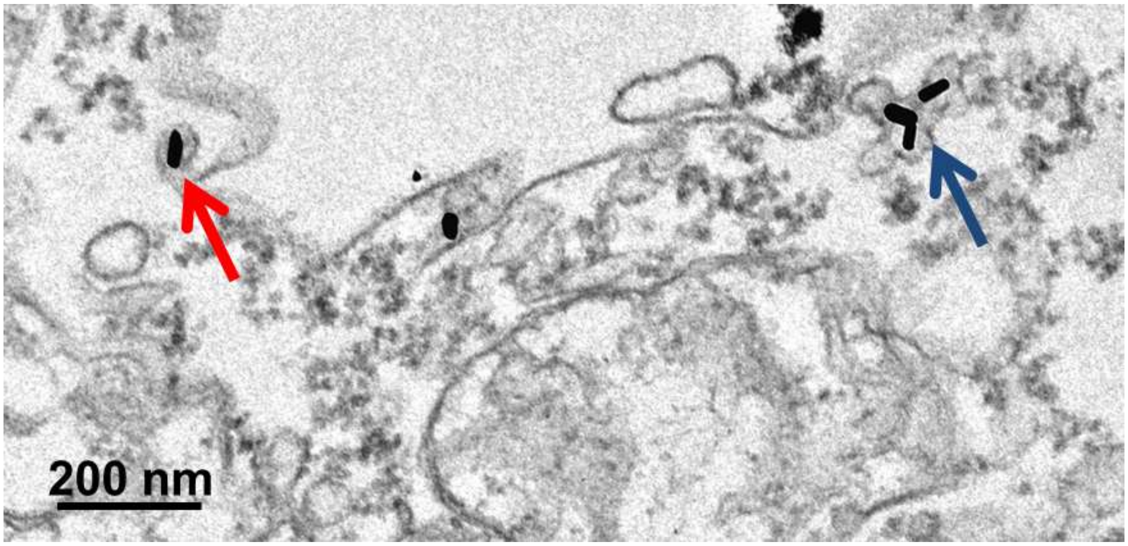

Figure 5.S2. The red arrow points out a nanorod that is wrapped around tightly by the lipid membrane of the endosome. The blue arrow points out three other nanorods that are also contained inside small vesicles, although it is more difficult to identify individual vesicle boundaries as these vesicles are positioned close to each other.

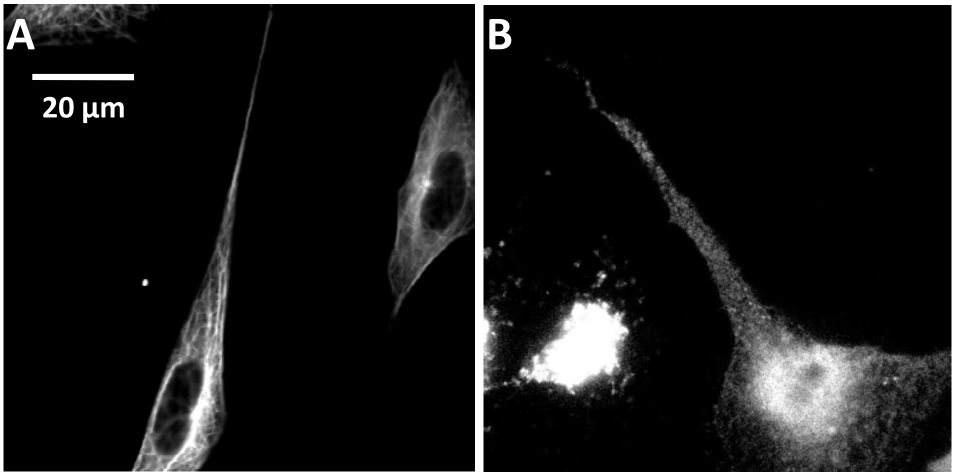

Figure 5.S3. (A) The fluorescent image of the microtubule network in a healthy differentiated PC12 cell. **(B)**The fluorescent image of the destroyed microtubule network in a differentiated PC12 cell treated with colchicine.

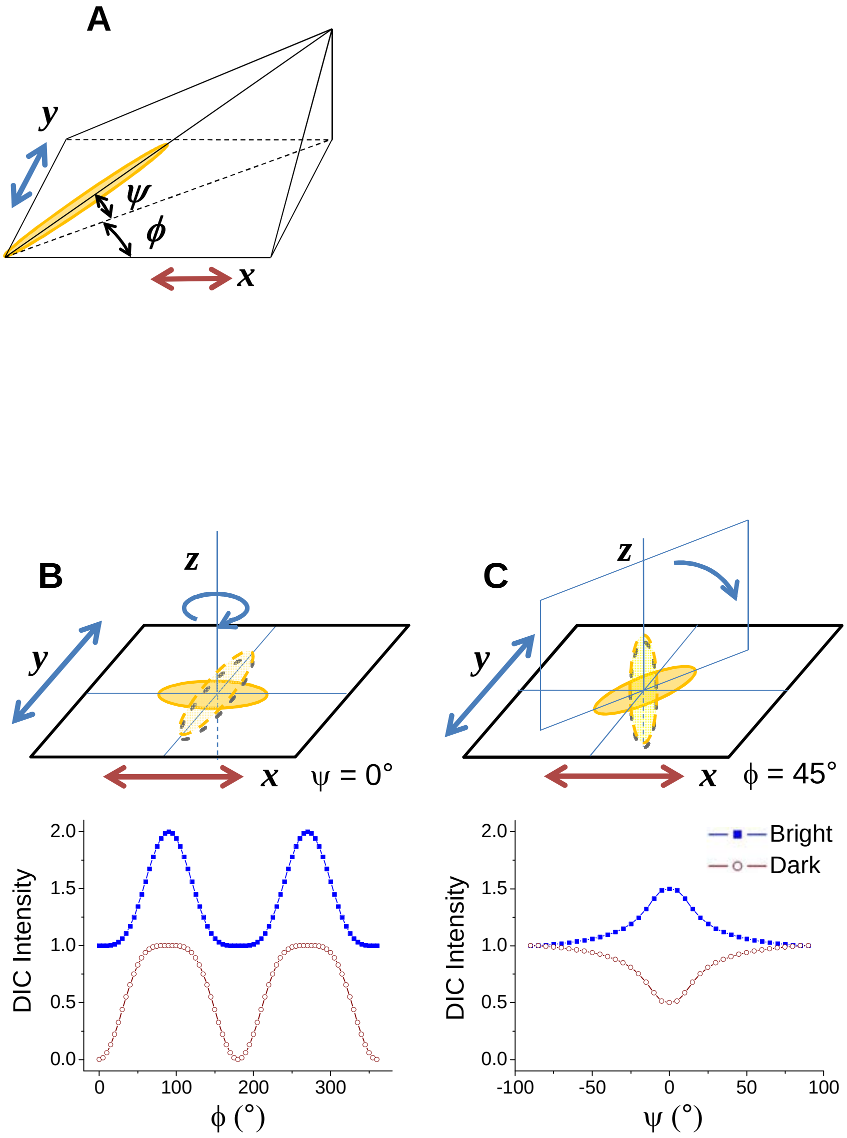

Figure 5.S4. Two examples of computer simulated DIC intensity changing patterns of a gold nanorod. (**A**) Definitions of the elevation angle *ψ* and the azimuthal angle *ϕ*.(**B**) In-plane rotation of a nanorod lying flat on the surface (*ψ* = 0°). This is identical to the rotation of the real sample shown in **Supplementary Figure 5.1**. The correlation is evident as the bright and dark intensities move up and down together. The correlation coefficient for this case is close to +1. (**C**) Out-of-plane rotation in a vertical plane that is 45^{o} to both *x*- and *y*-polarization directions (*ϕ* = 45°). The anti-correlation is evident as the two intensity values change in the opposite directions. The correlation coefficient for this case is -1.

The relative DIC intensities of the bright part and the dark part were calculated using the simplified equations derived in **ref. 33** (*J. Am. Chem. Soc.***132**, 16417–16422, (2010)):

$$I_{\text{bright}} \approx 1 + \cos^2 \psi \sin^4 \phi , \tag{S1}$$

$$I_{\text{dark}} \approx 1 - \cos^2 \psi \cos^4 \phi . \tag{S2}$$

It is worth noting that the noise in the actual imaging experiments, which gives typically 10-15% relative errors in the DIC intensity measurement, provides a constant source of uncorrelation to the experimental correlation coefficients.

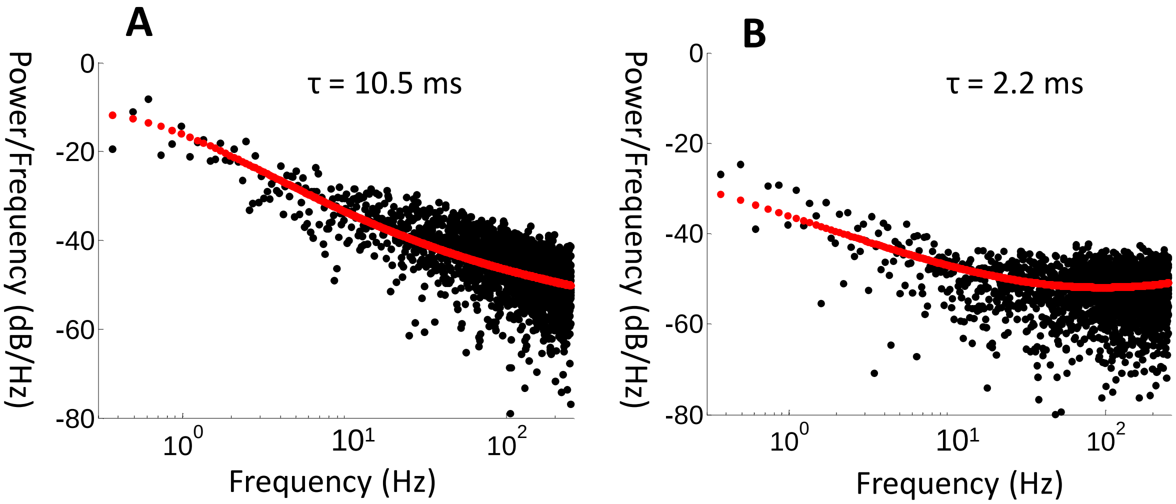

Figure 5.S5. Rotation characteristic time analysis using power spectral density followed by Lorentzian curve fitting. The power spectral density is the Fourier transform ofthe autocorrelation function according to the Wiener-Khintchine theorem. The single-side power spectral density spectra were plotted with the imbedded function in MATLAB. The spectra converted on the logarithm scale were fitted with the Lorentzian Function:

$$y = y_0 + \frac{2A}{\pi} \frac{w}{4(x - x_0)^2 + w^2} , \qquad \text{(S3)}$$

where y_0 is an offset from noise, A is a constant relative to the amplitude of the signal,x_0 is the peak position of the Lorentizian curve, and $w$is the width of the Lorentzian curve, with the unit of Hz. The rotation characteristic time can be calculated as $\tau = 1/w$.

The rotation characteristic times of the rotation at the long pause **(A)** and of the random Brownian diffusion **(B)** shown in **Figure 5.1A and 4.1B**are 10.5 ms and 2.2 ms respectively.

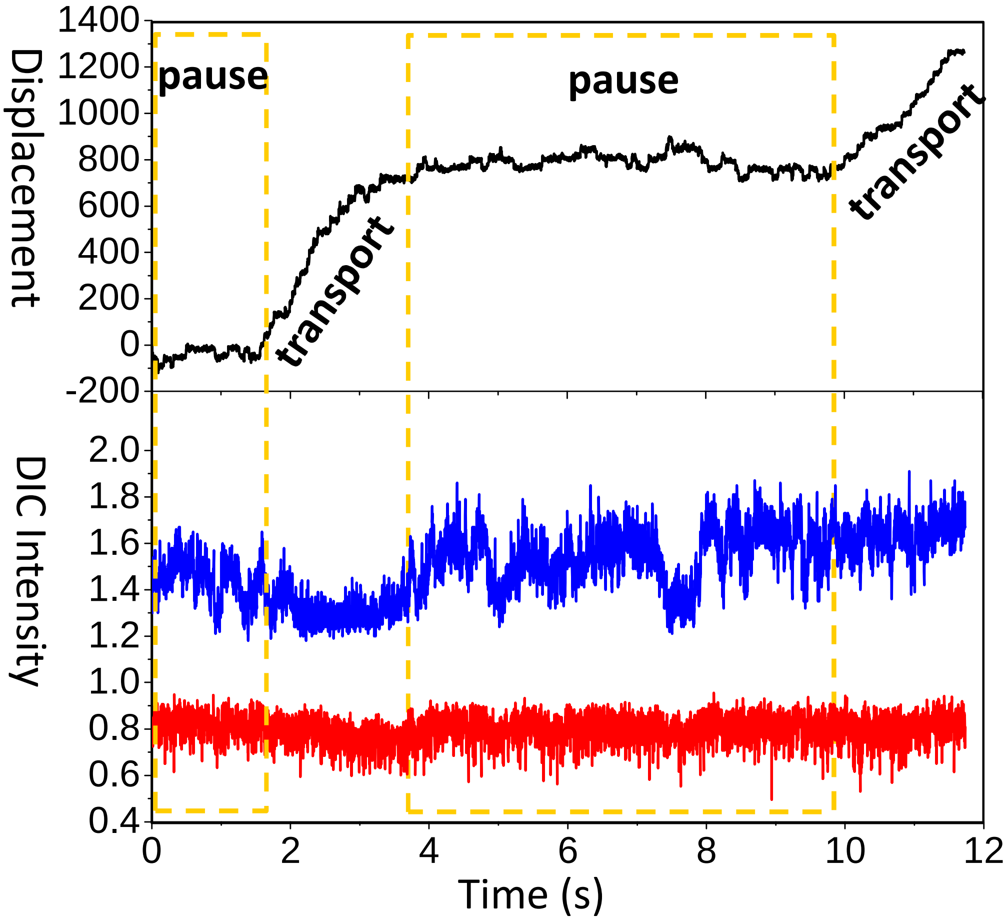

Figure 5.S6. A cargo showed rotational behavior at two pauses (0-1.7 s and 3.7-9.8 s) and maintained the same transport direction after both pauses. The displacement of transferrin-modified gold nanorods and their bright (blue) and dark (red) DIC intensities are plotted in this set of figures. The pauses are highlighted in the yellow frames. In these events, the cargoes were transported on the linear microtubules without much curvature, so the displacement from the original location of the cargo is plotted against the time.

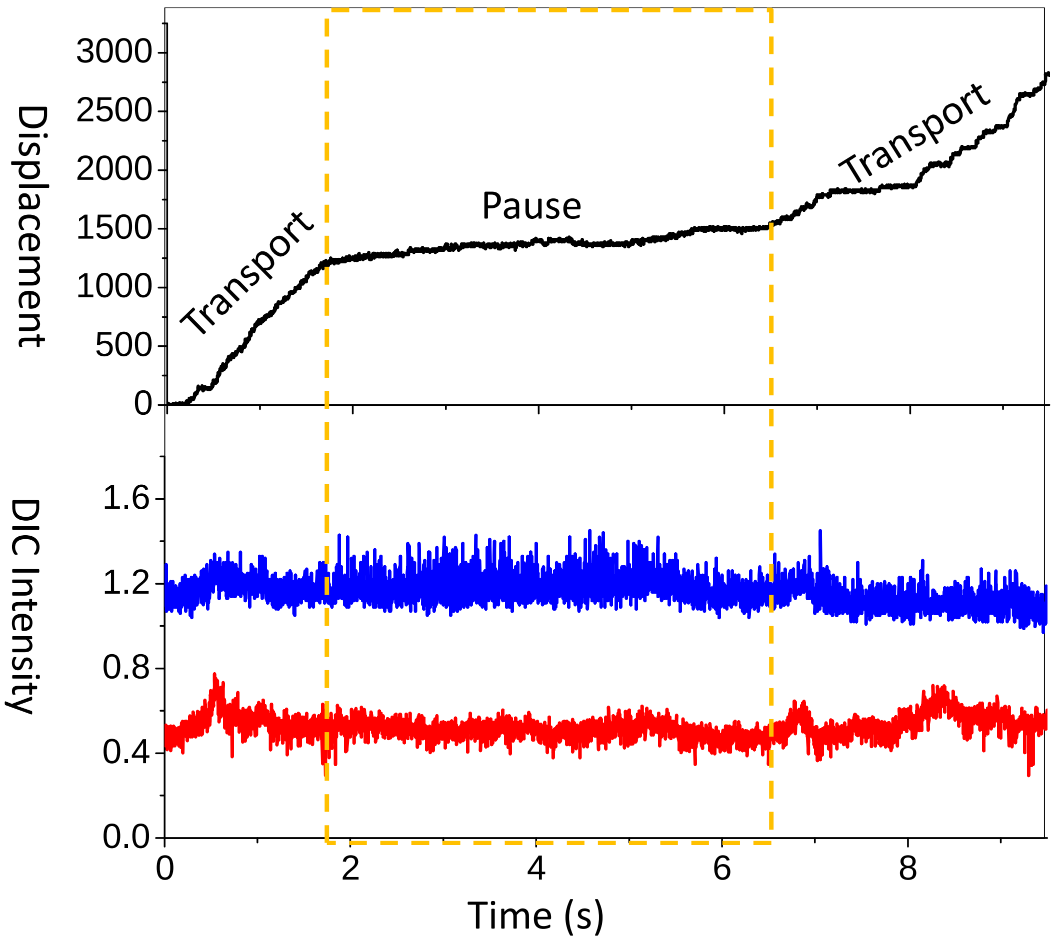

Figure 5.S7. A cargo showed no significantrotational behavior during the pause (2.2-6.6 s), and then was transported in the same direction. The displacement of transferrin-modified gold nanorods and their bright (blue) and dark (red) DIC intensities are plotted in this set of figures.The pauses are highlighted in the yellow frames. In these events, the cargoes were transported on the linear microtubules without much curvature, so the displacement from the original location of the cargo is plotted against the time.

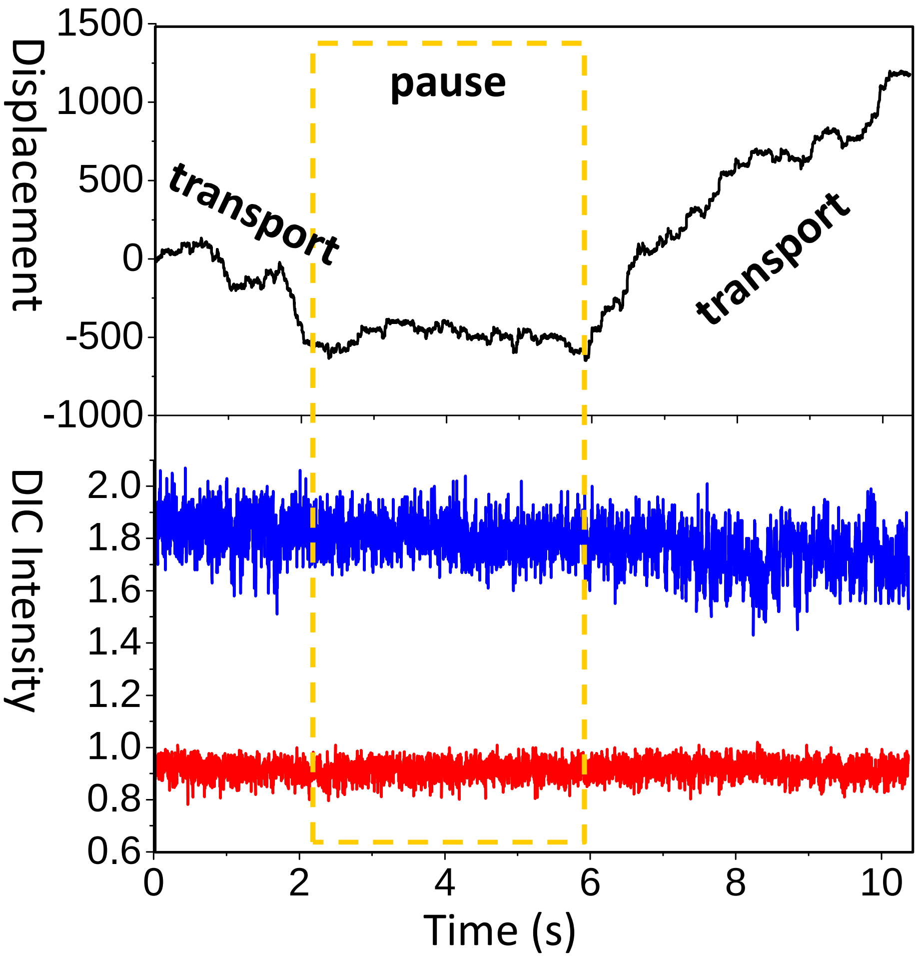

Figure 5.S8. A cargo showed no apparentrotational behavior during the pause (2.1-5.9 s), and then was transported in the opposite direction. The displacement of transferrin-modified gold nanorods and their bright (blue) and dark (red) DIC intensities are plotted in this set of figures.The pauses are highlighted in the yellow frames. In these events, the cargoes were transported on the linear microtubules without much curvature, so the displacement from the original location of the cargo is plotted against the time.

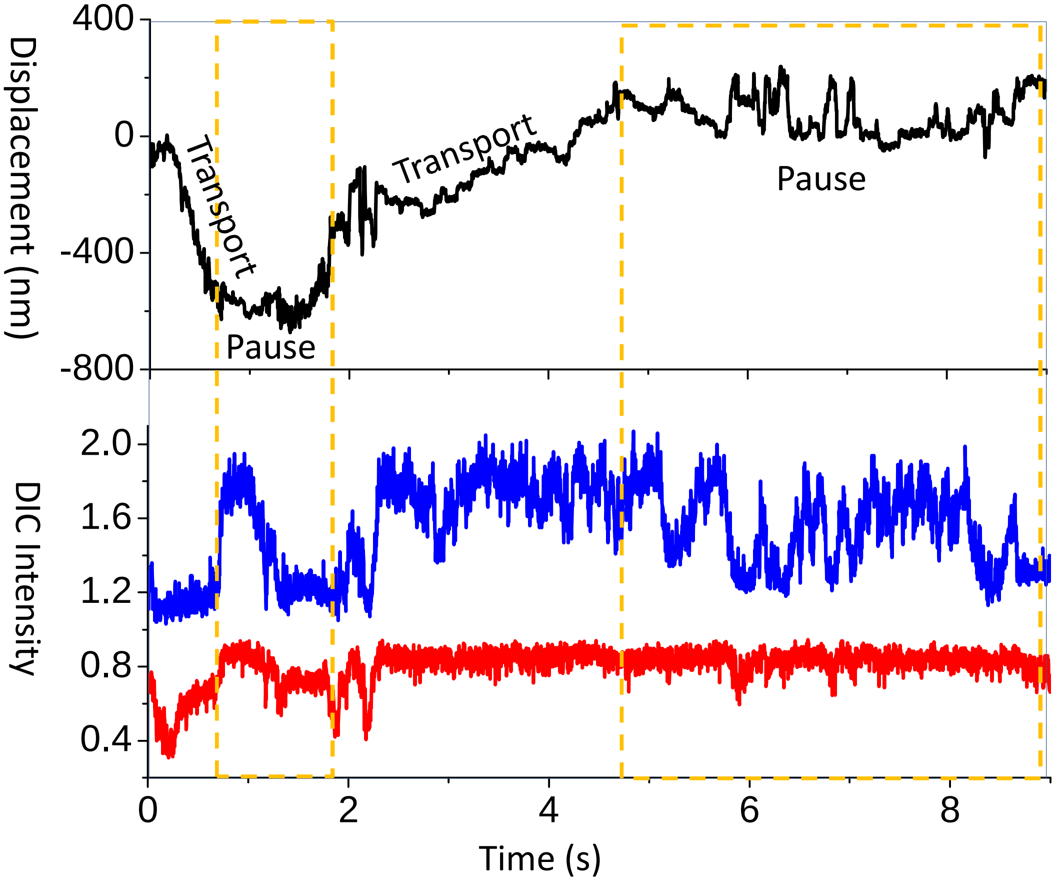

Figure 5.S9. A cargo showed rotational behavior at the pause (0.7-1.8 s), and then was transported in the opposite direction. Later, the cargo paused again from 4.8 s to the end of the movie. During this second pause, the cargo showed significant translational and rotational motions. The displacement of transferrin-modified gold nanorods and their bright (blue) and dark (red) DIC intensities are plotted in this set of figures. The pauses are highlighted in the yellow frames. In these events, the cargoes were transported on the linear microtubules without much curvature, so the displacement from the original location of the cargo is plotted against the time.

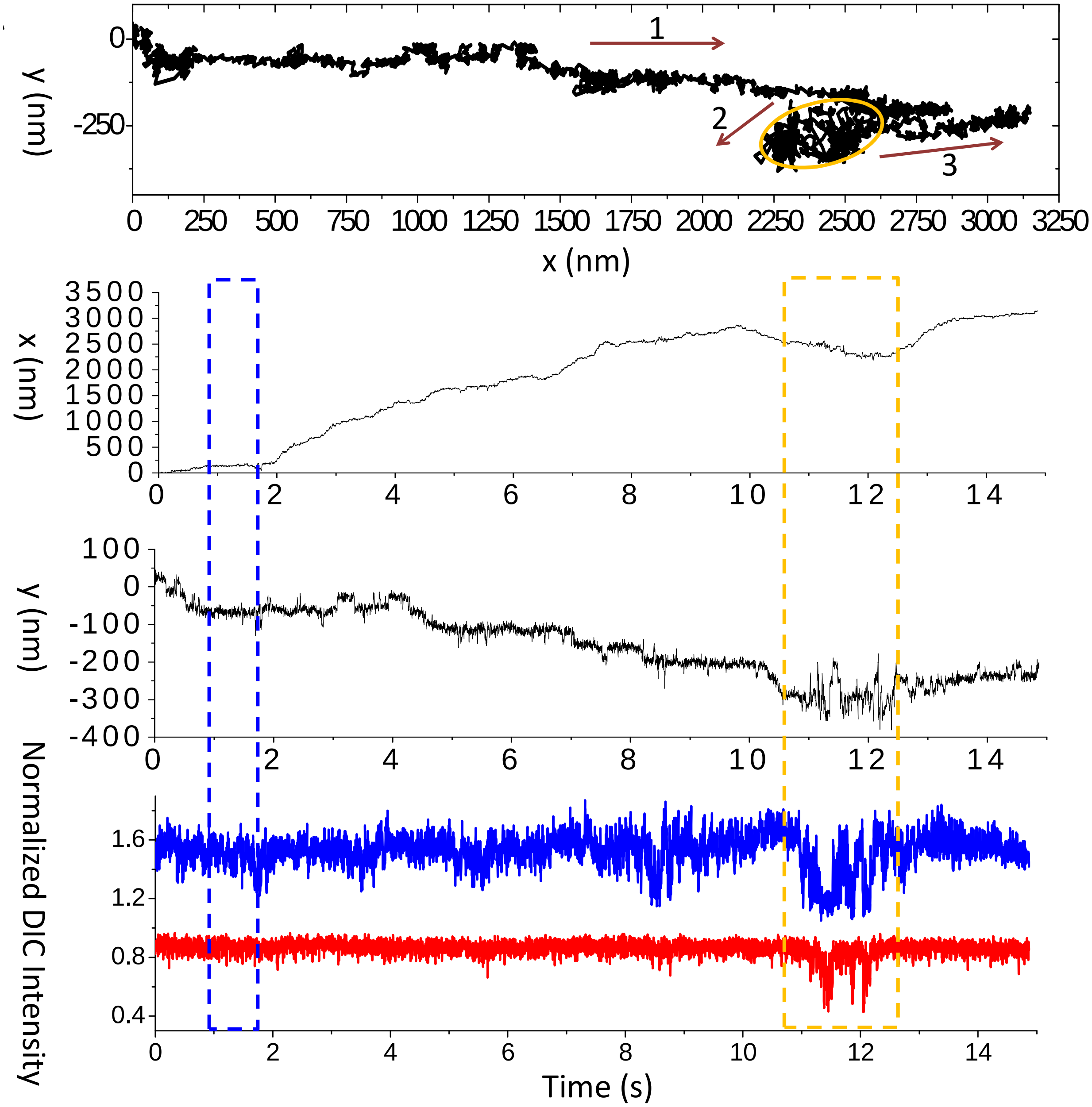

Figure 5.S10. (A) The moving trace of the gold nanorod. The red arrows point towards the moving direction and the numbers indicate the sequence of these transport routes. **(B)**The traces of the gold nanorods along the x- and y-axes and DIC intensity traces.The bright and dark intensities are shown in blue and red, respectively.To clear show the movement of the cargoes from one microtubule to another, both x and y positions, instead of the displacement, are plotted against time in these figures.

The gold nanorod paused from ~0.8-1.8s (highlighted by the blue frame, no apparent rotational motion), transported from 1.8-10 s for a distance of ~2.8 μm with an average velocity of 300 nm/s, and reversed the transport direction at 10 s. Then it paused and showed mostly in-plane rotational motion (correlation coefficient $r = 0.78$) during the track-switching process (10.7-12.3 s) (highlighted in the yellow frame). The in-plane rotational motion of the cargo indicates a loosened attachment of the motor proteins to the microtubule track when the motors looked for another docking site. The pause where the track-switching occurred is highlighted by the yellow circle in the 2D trajectory. The two tracks are ~80 nm apart.

During the directional transport stages, the gold nanorods did not show apparent rotational motion.

During the track-switching for all the three examples, the gold nanorods paused while showing rotational motion, indicating that the cargoes confronted with road blocks and loosened their attachment with the microtubule track in order to move to another track.

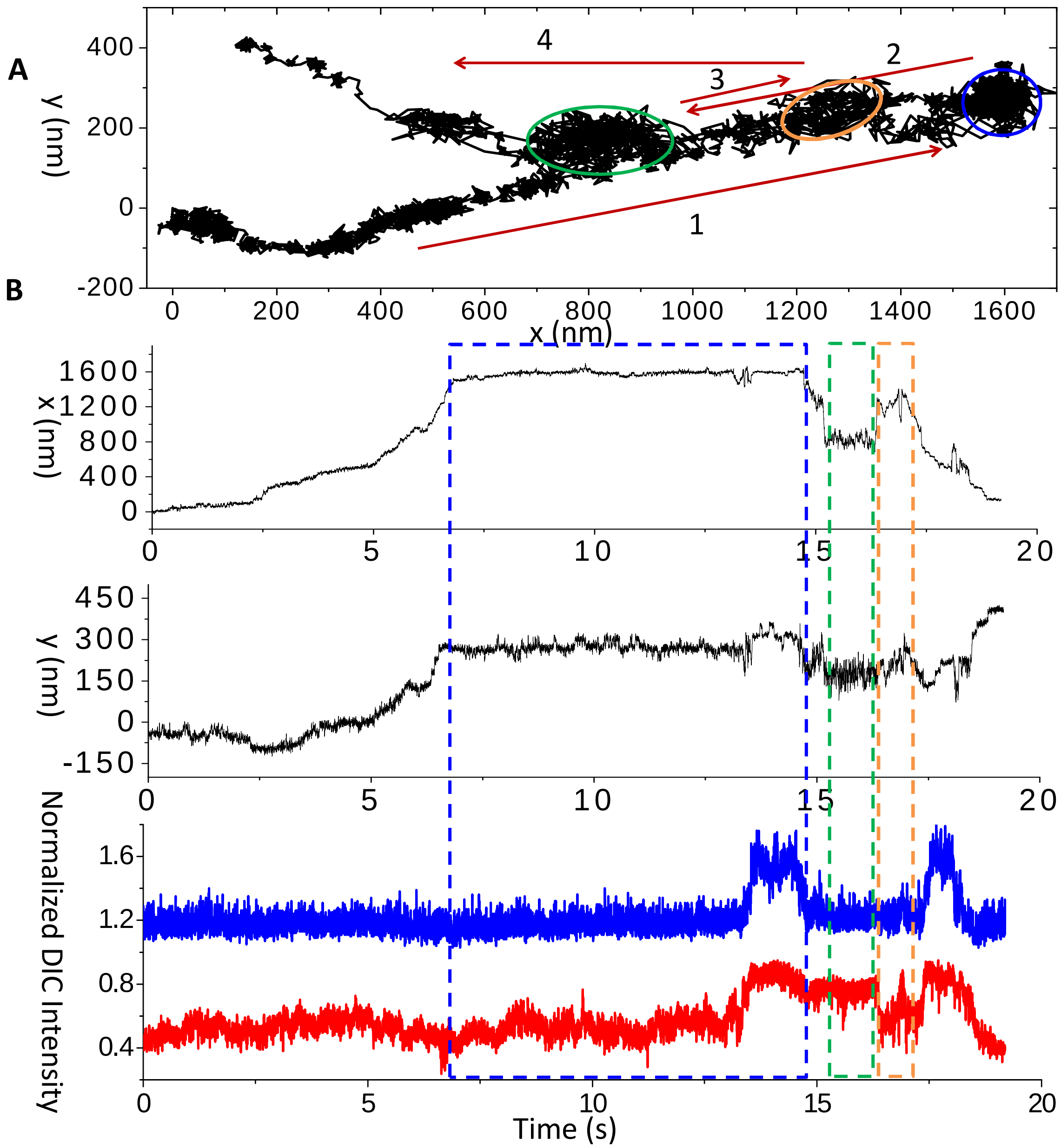

Figure 5.S11. This gold nanorod-containing cargo was first transported for a distance of ~1.6 µm at 250 nm/s (Route 1) and paused from 7.0-14.6 s. The pause was highlighted in the blue circle in **A** and the blue frame in **B**. The nanorod showed very little rotational motion in the first 6.5 s of the pause. At the end of this pause, the nanorod showed rotational motion (13.5-14.6 s) and then reversed its transport direction. After being transported for a distance of ~700 nm (Route 2), the nanorod paused again from 15.3-16.5 s with very little rotational motion (highlighted in the green circle and frame). The nanorod was then transported in the opposite direction rapidly for a distance of ~400 nm (Route 3) and paused again from 16.6-17.3 s with rotational motion (highlighted in the yellow circle and frame). After the

pause, the nanorod reversed its transport direction and then moved along another intersecting microtubule track (Route 4). From the last segment of Route 4(towards the top left corner), it was clear that the cargo moved on a new microtubule track, but it was unclear at which point, the green or yellow circle, the cargo switched track.

CHAPTER 6

THREE-DIMENSIONAL SUPER-LOCALIZATION AND TRACKING OF SINGLE GOLD NANOPARTICLES IN CELLS

A paper published in *Analytical Chemistry*
2012, *84*, 4111-4117

Yan Gu[†], *Xiaowei Di*[‡], *Wei Sun*[†], *Gufeng Wang*[§]* *and Ning Fang*[†]*

†Ames Laboratory, U.S. Department of Energy, and Department of Chemistry, Iowa State University, Ames, Iowa 50011, United States

§Department of Chemistry, North Carolina State University, Raleigh, NC 27695

‡College of Chemistry and Chemical Engineering, Inner Mongolia University, Hohhot 010021, China

Abstract

We introduce a precise three-dimensional (3D) localization method of spherical gold nanoparticle probes using model-based correlation coefficient mapping. To accomplish this, a stack of sample images at different z-positions are acquired and a 3D intensity profile of the probe serving as the model is used to map out the positions of nanoparticles in the sample. By using this model-based correlation imaging method, precise localization can be achieved in imaging techniques with complicated point spread functions (PSF) such as differential interference contrast (DIC) microscopy. We demonstrated the localization precision of 4-7 nm laterally and 16 nm axially for 40-nm gold nanospheres at an imaging rate of 10 frames

per second. The 3D super-localization method was applied to tracking gold nanospheres during live endocytosis events.

Introduction

Many biological activities involve motions at the nanoscale, e.g., DNA polymerization,[1] motor protein stepping,[2,3] and self-rotation of ATP synthase.[4] Precisely locating and tracking optical probes are of vital importance in understanding these biological processes. Single fluorescent molecules and nanoparticles have been widely applied in these studies. For example, 8-nm steps of motor proteins have been resolved in live cells by tracking individual fluorescent particles.[2,5] Ultrafine membrane compartments with a size ranging from 30-230 nm, which limits membrane protein diffusion, were revealed by single fluorescent molecule tracking.[6] The localization precision of single molecules in such complex samples was typically 10-20 nm laterally and ~50 nm in the axial direction.[7-11] It is worthwhile to point out that the localization precision of individual fluorescent molecules is directly relevant to the optical resolution in imaging photo-switchable dyes as these single-molecule fluorescence events are temporally separated by being alternatively switched “on” and “off”. The small fractions of fluorophores that are turned “on” in each imaging cycle allow the localization of each fluorophore with nanometer accuracy. This stochastic photoactivation and optical reconstruction approach has been recently used to break the diffraction limit of far-field optical microscope in both 2D and 3D.[9,12-14]

The major disadvantages of fluorescence-based imaging including photo-instability of fluorescent labels, e.g., photobleaching[15,16] and blinking,[16,17] and the interference to the natural cellular processes are caused by fluorescent labels.[8,18] An alternative approach is to use plasmonic gold nanoparticle probes, which display large optical cross-sections near their surface plasmon resonance (SPR) frequencies, excellent photo- and chemical-stability, and good biocompatibility.[19-22] In addition, they can be engineered into different sizes and shapes and their controllable surface chemistry allows them to be modified with a variety of chemically and biologically active molecules.

Gold nanoparticles have been imaged and tracked in live cells with a variety of techniques including bright-field microscopy,[23,24] dark-field microscopy,[25,26] photothermal interference contrast technique,[27-29] differential interference contrast (DIC) microscopy,[30,31] confocal Raman microscopy,[32] and dynamic surface-enhanced Raman spectroscopy.[33] Among these techniques, DIC microscopy exhibits excellent detectability of small gold nanoparticles, thus the potential of serving as a powerful tool in single particle tracking studies. We recently used DIC microscope to track the endocytosis process of gold nanoparticles[31] and visualized the rotational motion of gold nanorods in live cells and on cell membranes.[34,35]

DIC microscope works on the principle of two-beam interferometry to gain information about the optical density of the sample. The interference nature makes it sensitive to see small features that display different refractive indices from its environment while insensitive to scattered light from surrounding cellular components. The result is that it enables the user to image both the nanoprobes and live cells with superior quality. A variety of cellular organelles that are invisible in other conventional microscopy such as bright-field microscopy becomes observable under a DIC microscope.[36] The excellent detectability of nanoparticles and wide-field configuration gives excellent temporal resolution that are unparalleled by detection techniques based on raster scanning. Compared to scattering-based dark-field microscopy,[25,26,37,38] imaging nanoparticles under the DIC microscope is less affected by other strong light scatterers, such as large vesicles and the edge of the nucleus, in the sample media.[39]

More importantly, DIC microscopy allows for the use of the full numerical aperture (NA) of the microscope objective and condenser, resulting in the highest possible lateral and axial resolutions.[40,41] The optical resolutions, defined as the full width at half maximum (FWHM) of the intensity distribution of a point spread function (PSF), are:[42]

$$FWHM_{Lateral} = 0.51 \times \frac{\lambda}{NA} \qquad (1)$$

laterally, and

$$FWHM_{Axial} = \frac{0.88 \times \lambda}{n - \sqrt{n^2 - NA^2}} \qquad (2)$$

axially, where λ is the illumination wavelength, *n* is the refractive index of the immersion oil, and NA is the numerical aperture of the objective. In dark-field microscopy, the illumination is provided by a center-blocked, high-NA condenser (usually NA 1.2-1.4). The objective NA must be restricted (smaller than the condenser NA) to reject transmitted illumination beam, resulting in lower spatial resolution. Taking an oil-immersion (n = 1.519) objective with the NA restricted to 1.0 as an example, and assuming the illumination wavelength to be 545 nm, the lateral resolution in dark field microscopy is 278 nm, as compared to 199 nm in DIC microscopy (NA 1.4 for both condenser and objective). The axial resolution in dark field microscopy is 1277 nm, nearly 2.5 times the DIC axial resolution of 516 nm. Therefore, the image spot of a nanoparticle appears expanded both laterally and axially in dark-field microscopy when compared to the image spot in DIC microscopy (**Supplementary Figure 6.1**). In this sense, using DIC microscopy will yield much better precision in locating the centroids of the diffraction limited image spots of nanoparticle probes, especially in the axial direction.

Due to DIC microscopy's reliance on the principle of interference, nanoparticles show a half-bright and half-dark image superimposed on a gray background, which complicates the particle localization because simple Gaussian fitting of the image profile does not apply to the more complicated DIC PSF. To solve this problem, Gelles *et al.* developed a localization method by evaluating the cross correlation of the sample image with the kernel portion of a model particle image.[43] They demonstrated 1-2 nm precision laterally in tracking 190-nm plastic beads driven by kinesin motors under a DIC microscope. To the best of our knowledge, precisely tracking gold nanoparticles in 3D space to a few nanometer precision has not been demonstrated although there is an increasing demand to achieve this in the 3D matrix of biological samples.

In the present study, we systematically investigated the 3D PSF of gold nanoparticles in DIC microscopy and introduced an algorithm to locate gold nanoparticles in 3D space. The localization precision of 4-7 nm laterally and 16 nm axially for 40-nm gold nanospheres was achieved with an imaging rate of 10 frames per second and a vertical step size of 40 nm. The temporal resolution of 3D localization was in the range of seconds, which was the time needed to record a stack of z-slices through the sample volume. We also demonstrated the application of this method in the tracking of gold nanoparticles in live cells during the endocytosis events.

Experimental Section

Sample slides. 40-nm gold nanoparticle colloid solutions were purchased from BBInternational (Cardiff, UK). Positively-charged amino silane-coated glass coverslips were prepared by modifying 22 mm × 22 mm No. 1.5 coverslips (Corning) with 1% 3-aminopropyl triethoxy-silane (Sigma-Aldrich) ethanol solution. The colloid solutions were first diluted with 18.2-MΩ pure water to proper concentrations. Then the diluted solution was sonicated for 15 mins at room temperature. After sonication, 6 μL of the gold nanoparticle solution was added onto the modified coverslip and the particles (citrate-capped, negatively charged) adsorb to the coverslip surface through electrostatic interactions.

Imaging system. An upright Nikon Eclipse 80i microscope was used in our investigations. The DIC mode used a pair of Nomarski prisms, a 100× Plan Apo/1.40 oil-immersion objective, and an NA 1.40 oil condenser, while the dark-field mode used a 100× Plan Fluor NA 0.7-1.3 oil objective and an NA 1.20-1.43 oil dark-field condenser. A high transmission 540-nm optical filter (Semrock, Rochester, NY) with a bandwidth of 20 nm was inserted at the illumination side. Before imaging, in order to differentiate gold nanoparticles from sub-cellular organelles, a high transmission 720-nm optical filter (Semrock, Rochester, NY) with a bandwidth of 13 nm was used because gold nanospheres that were visible at 540 nm would become nearly invisible at 720 nm as we have demonstrated previously.[44] The images and movies were taken by either a CoolSnap ES CCD camera (Photometrics, CA) or a Hamamatsu ORCA-Flash2.8 CMOS camera. An optimal combination of image contrast, spatial resolution and temporal resolution was achieved with the imaging rate of 10 frames per second, which was used in all of our imaging experiments unless noted.

3D Imaging. A motorized rotary stage from Sigma Koki (model no. SGSP-60YAM) was coupled to the fine-adjustment knob on the microscope. The motor was controlled by Intelligent Driver, CSG-602R (Sigma Koki). The camera and stage were synchronized by adjusting the scanning speed and imaging rate. At the imaging rate of 10 frames per second, the distance between two successive images was 40 nm. MATLAB and NIH ImageJ were used to analyze and process the collected images and videos. The 3D images were rendered in Visage Imaging Amira (Berlin, Germany).

Surface modification of gold nanoparticles. To facilitate their internalization into A549 cells, the gold nanoparticles were modified with either transferrin[45] or a cell penetrating peptide (CPP) from the HIV-1 protein Tat[30,46,47] (sequence: YGRKKRRQRRR, AnaSpec, San Jose, CA). A NHS-PEG disulfide linker (Sigma-Aldrich) was used by following a published protocol.[48] The NHS-PEG disulfide linker has both disulfide and succinimidyl functionalities for respective chemisorption onto gold and facile covalent coupling of transferrin molecules. Briefly, a proper amount of fresh NHS-PEG disulfide solution (in dimethyl sulfoxide) was added to reach a final thiol concentration of 0.2 mM and reacted with gold nanoparticles for 2 h. The solution was then cleaned up by centrifugation and resuspended in 2 mM borate buffer. 2.0 μg of transferrin (or 2.0 μg of Tat CPP) was added to the gold colloidal solution and reacted for 8 h. Before use, the colloidal gold nanoparticles were cleaned up by centrifugation and resuspended in 2 mM borate buffer. The concentrated gold colloidal solution was diluted to a final concentration of 4.3×10^9 particles/mL for incubation with cells.

Cell cultures and imaging. For the localization of gold nanoparticles inside fixed cells, HeLa cells (ATCC, Manassas, VA) were cultured on 22 mm × 22 mm poly-L-lysine coated glass coverslips in petri dishes. 1.5 mL of minimum essential cell culture medium (ATCC) with 10% fetal bovine serum supplement was added to the plates. The cell culture was incubated at 37°C under 5% CO_2. After the cell culture covered 70% of a coverslip, 30 μL of TAT CPP-modified gold nanoparticle solution was added into the petri dish and incubated with the cells for an hour. The gold nanoparticles were naturally internalized by the HeLa cells. The coverslip was then rinsed with 10 mM phosphate buffered saline (PBS) at pH 7.4 and then the cells were fixed with 4% paraldehyde in the same PBS buffer. After that, the cell coverslip was placed on a clean glass slide for observation. Two pieces of double-sided tape served as spacers between the glass slide and coverslip to form a chamber.

For the localization of gold nanoparticles during the endocytosis process, A549 human lung cancer cells (ATCC, CCL-185) were cultured on 22 mm × 22 mm poly-L-lysine coated glass coverslips in petri dishes. Minimum essential cell culture medium (ATCC) with 10% fetal bovine serum supplement was added to the plates. The cell culture was incubated at 37°C under 5% CO_2. After the cell culture covered 70% of a coverslip, the cell coverslip was taken out for imaging and a chamber was made using two pieces of double-sided tape. 20 μL of transferrin-modified gold nanoparticle solution was added into the chamber. The back-and-forth vertical scans and movie recording started immediately.

Results and discussion

Complexity of 3D DIC point spread function. The 2D amplitude PSF of a DIC microscope adopts the form of:[44,49]

$$h(x,y)=(1-R)e^{-i\theta}k(x-\Delta x,y)-Re^{i\theta}k(x+\Delta x,y) \qquad (3)$$

where (x, y) is a point in the image plane, R is the amplitude ratio of the 2 illumination beams, $k(x, y)$ is the amplitude PSF for transmission optics under coherent illumination, 2θ is the additional phase bias, and the shear distance $2\Delta x$ is assumed to be along the x direction without losing generality. In the image plane, the intensity distribution of a DIC image is the square modulus of the convolution of the DIC PSF and the object amplitude and phase distribution.

The 3D DIC PSF has been modeled by Preza and coworker using eq 3 and the defocused PSF for transmission optics.[49,50] Their work shows that under ideal conditions, i.e., the two illumination beams are of equal intensity and the phase bias 2θ is $\pi/2$, the 3D PSF is anti-symmetric, i.e., it has a 2-fold rotation-reflection axis. However, due to non-ideal experimental parameters, the actual 3D DIC PSF is more complicated. To demonstrate this, we collected the 3D intensity profile of a 40-nm gold nanosphere immobilized on a piece of glass coverslip with a z-step size of 40 nm. **Figure 6.1A** shows the 3D intensity profile, where the "hot" part shows the bright DIC intensities and the "cold" part shows the dark DIC intensities. Interestingly, the 3D PSF is elongated due to the lower resolution in the *z*-direction than in the *x*-, *y*-directions. **Figures 6.1B and C** show the ortho-slices of the 3D intensity profile in the x-y and x-z planes, respectively. The dark part of the DIC image shows two minima in the focal plane, and apparently not following the ideal anti-symmetric pattern. In addition, the 3D DIC intensity profile is not symmetric along the *z*-direction with respect to the focal plane, and the bright and dark portions have different maximum/minimum at different z-positions.

Model-based correlation imaging. To precisely locate 40-nm gold nanoparticle probes in biological samples, an experimental 3D DIC intensity profile of a nanoprobe is used as the model to map the nanoparticle probes in a stack of z-sectioned sample images. In practice, the sample containing the model nanoparticle and other nanoparticle probes are scanned vertically until a z-stack of images of a volume of interest is collected. The 3D model is cropped and then overlaid with a portion of the volume of interest. A correlation score is calculated to evaluate how likely the overlaid volume contains a nanoprobe. The model is then moved pixel by pixel, line by line and frame by frame to cover the whole volume of interest. The correlation scores are calculated at each position and used to construct a 3D correlation map. The correlation scores can be defined through a variety of ways[51] and herein Pearson's correlation coefficient was used. The correlation coefficient *p* between a 3D model and the sub-volume that the model overlays is defined as:

$$p(model, sub\text{-}volume) = \frac{1}{m-1}\sum_{i=1}^{m}\frac{[I_{model}(i)-I_{model}(avg)]}{\sigma_{model}}\frac{[I_{sub\text{-}volume}(i)-I_{sub\text{-}volume}(avg)]}{\sigma_{sub\text{-}volume}},(4)$$

where the summation is over all the pixels in the 3D model or the sub-volume, and m is the total number of pixels in the model; I is intensity; *avg* and σ denote the average and standard deviation of all intensities in the model or the sub-volume, respectively. From the 3D correlation map, the position of a nanoparticle can be precisely located. The center of a nanoparticle can be computed by weighting all the coordinates that the particle covers with their corresponding p values:

$$X_{center} = \frac{\sum_{i=1}^{m} X_i [p(i) - Threshold]}{\sum_{i=1}^{m} [p(i) - Threshold]} \quad , \qquad (5)$$

where *X* can denote any Cartesian coordinates, *x*, *y*, or *z*, and a threshold is usually applied to cut off the noise contribution. The summation is over all the pixels that a particle covers. Through this weighting procedure, all intensities in the 3D profile are considered and a sub-pixel precision can be obtained.

Figures 6.1D-H show the localization of a 40-nm gold nanosphere using this model-based correlation imaging technique. In the localization, one stationary particle is selected as the reference in order to eliminate the error caused by the drifting of the sample relative to the microscope optics. That is, the position of the target particle relative to the reference particle is recorded. **Figure 6.1E** shows the 3D correlation map of the 40-nm gold nanoparticle and its surrounding area. High correlation scores close to its center are clearly identifiable (hot part). Similar to the 3D PSF, the 3D correlation coefficient map is also elongated along the z-direction. By setting a proper display threshold, the correlation scores appear as a spheroid shaped volume. **Figures 6.1F and G** show the ortho-slices of the 3D map in the *x*-*y* and *x*-*z* planes, respectively. It is interesting to note that the central high correlation portion is flanked by two regions with low correlation scores (cold parts). The negative correlation scores mean anti-correlation, which is originated from the overlap of the bright part of the model and the dark part of the sample, or vice versa.

The centroid of the particle is determined by weighting the coordinates with the correlation scores using eq 5. In practice, a threshold is set to remove the interference from noise. Since the position is acquired from the whole image volume, high lateral and axial precisions are achieved. **Figure 6.1H** shows 42 repeated measurements of the position of particle *a* with respect to particle *b*. The standard deviations of the relative *x*, *y* and *z* positions of particle *a* are 4.4 nm, 6.5 nm and 16.0 nm, respectively. The axial localization precision is ~3 times of that in the x or y direction, consistent with the fluorescence-based methods.

The signal to noise ratio of DIC images plays an important role in localization precision. In the current study, DIC images of fixed 40-nm gold nanospheres were captured at 10 frames per second, which gave a signal-to-noise ratio of ~20. Here the signal is defined as the intensity difference between the bright part and dark part for an in-focus 40-nm gold nanoparticle, and the noise is simply the standard deviation of the non-signal background. Correspondingly, the temporal resolution of 3D super-localization was in the range of seconds for taking stacks of *z*-slices at 40-nm steps through the sample volume. It is expected that the precision can be improved if the temporal resolution requirement is relaxed. For example, when the frame rate was halved to 5 frames per second, the *x*, *y*, and *z* localization precisions were improved to 3.1 nm, 3.8 nm and 12.9 nm, respectively.

It is worthwhile to note that the model-based mapping algorithm requires that the gold nanospheres are uniform in shape and size; otherwise, the 3D model generated from one particle may not fit accurately with other particles. The 40-nm gold nanoparticles used in the present study were sufficiently uniform to meet this requirement.

3D localization of gold nanoparticles in fixed cells. Gold nanoparticles have been reported to serve as carriers in targeted drug delivery,[52,53] gene regulation[54] and photothermal therapies.[55] It is important to follow their distribution, trajectory and final fate after they enter the host cell. To demonstrate the capability of the 3D correlation imaging, we further applied this 3D correlation mapping method in locating and tracking 40-nm gold nanospheres in cells. We first demonstrated super-localization of 40-nm gold nanoparticles in fixed HeLa cells.

The cells were incubated with Tat CPP-modified 40-nm gold nanoparticles for an hour to allow natural internalization to occur. The cells were then fixed using 4% glutaraldehyde for 20 min. Z-sections of the HeLa cells with gold nanoparticles were recorded (**Supplementary Movie 6.1**). **Figure 6.2A** shows the 3D distribution of mapped particles in a thin layer from the glass slide surface to ~2 µm above and their corresponding positions to a z-sectioned DIC image. It should be noted that the viewing angle is from above and gold nanoparticles below the cell image are covered up and invisible. Gold nanospheres are displayed as elongated, golden iso-surfaces in the figure. All of the visible gold nanoparticles are in cell plasma and outside of the nucleus, with a few residing at locations very close to the nucleus membrane. This is consistent with the literature reports that gold nanoparticles larger than 20 nm will not go through the nucleus membrane.[30] **Figure 6.2B** shows the same cell viewed from the side. In the lower left corner, there are a group of gold nanoparticles in the same plane. Those are adsorbed particles on the glass coverslip.

One thing to note is that the automated localization procedure can also pick up other spherical sub-cellular organelles that have a 3D DIC intensity profile similar to that of the gold nanoparticle model. In order to discriminate single gold nanoparticle probes from these spherical structures, as well as nanoparticle aggregates, with high confidence, we also imaged the cell at 720 nm at which single gold nanoparticles could be “switched off” to manually exclude those cellular structures and larger aggregates.[31]

3D localization of gold nanoparticles in live cells. The applicability of the 3D correlation mapping algorithm to single particle tracking in live cells was further demonstrated by tracking 40-nm transferrin-modified gold nanoparticles continuously during their internalization by live A549 cells. Transferrin and transferrin-modified gold nanospheres are known to be internalized by cells mainly through clathrin-mediated endocytosis.[57,58] When incubated with cells, the negatively-charged nanoparticles can be adsorbed on the cell membrane through non-specific adsorption and/or specific receptor binding and perform active translational diffusion on the cell membrane. The particles then either dissociate from the cell surface or are temporarily fixed at one location presumably by specific interactions with transferrin receptors before the internalization occurs. The endocytosis process usually takes several minutes, after which the nanoparticles restore active translational motion, including intracellular transport and random diffusion, inside the cell.

In our tracking experiment, some of the negatively-charged gold nanoparticles were firmly adsorbed on the positively-charged poly-L-lysine-modified coverslip surface through electrostatic attraction. One such particle was chosen as the reference (**Figure 6.3A**) to eliminate the effect of sample drifting during the repeated vertical scans. The relative 3D position of the particles of interest (**Figure 6.3B**) was tracked continuously by repeatedly scanning between the coverslip surface and the top cell surface.

The tracking started when the particle stopped active translational diffusion on cell membrane and stayed at a relatively fixed position, allowing its location to be measured with sufficient accuracy. The 3D moving trace of the gold nanoparticle (**Figure 6.3C**) shows clearly that the particle moved significantly before it finally entered the cells. The movement in the *z*-direction was as large as several hundred nanometers between data points, much larger than the cell membrane thickness (5~10 nm). The big position changes in the *z*-direction are possibly due to the movement of the cell membrane or the change of the cell surface morphology. At the end of the endocytosis, the nanoparticle went into the cells and diffused away from the original entry spot.

Achievable temporal resolution. Temporal resolution is an important consideration in tracking dynamic biological events. The temporal resolution for a recorded sequence of nanoparticle movement is simply the time spent on one vertical scan through the sample of interest. In the endocytosis study, the whole depth of the cell (~6.4 µm) was scanned with a step size of 40 nm and an image exposure time of 100 ms. This yields a temporal resolution of 16 s for each particle position in order to achieve a sub-20 nm spatial resolution. This temporal resolution may not be sufficient for fast dynamics, such as the Brownian motion or intracellular transport on the cytoskeleton tracks. However, it is generally adequate for localizing nanoparticles with restricted movement when they are imbedded in viscous media such as cell membranes or bound to relatively stationary organelles. Because this method has minimal intrusion to biological systems and no photobleaching, it is ideal for long-term high-precision tracking of nanoprobes in living systems.

The temporal resolution of this method can be improved to ~1 s without sacrificing localization precision. Note that a large fraction of time was spent in scanning through the non-signal regions (area contains no probe or target of interest). If we reduce the scanning depth to ~400 nm, which is sufficient to cover the image volume of a visible nanoparticle, we can achieve a temporal resolution of 1 data point per second under the same experimental conditions (100 ms exposure time and 40 nm vertical step size). This temporal resolution is comparable to most commercially available confocal fluorescence microscopes with a temporal resolution on the order of 1 frame per second for collecting 2D images.

Limitations of the Technique. Just like other localization techniques, the 3D mapping technique also has its limitations. First, because this technique requires a high consistency of the geometry of the nanoparticles, it cannot be applied on gold nanoparticles when they form aggregates. Second, this technique also requires that the distances between each two nanoparticles are satisfactory. When the distances between the nanoparticles are within the diffraction limit, the individual images of the nanoparticles cannot be distinguished. However, that is an intrinsic limitation for far field light microscopy techniques. Even if the distances between the nanoparticles are larger than the diffraction limit, the mapping could still be affected when the distance between the nanoparticles is smaller than the size of the model image that is used to map the images of interest. When the model image is moved pixel by pixel and frame by frame to cover one nanoparticle of interest, to some degree it will cover part of another nanoparticle. The centroid generated from the weighting may not be precise in this case.

Conclusions

In summary, a 3D model-based correlation mapping method was developed to locate gold nanoparticles through vertical scans of the sample volume of interest. This localization method provides sub-20-nm axial precision. Using this method, 40-nm gold nanoparticles in a fixed HeLa cell were detected and their positions were mapped in the 3D cellular environment. Dynamic tracking of gold nanoparticles on the live cell membrane during the endocytosis process was also demonstrated. Although with limitations, this 3D localization method allows long-term single particle tracking with high precision, and thus has a high potential in studying biological processes where precise localization is essential in learning the mechanisms.

Acknowledgment

This work was supported by a grant from U.S. Department of Energy, Office of Basic Energy Sciences, Division of Chemical Sciences, Geosciences, and Biosciences through the Ames Laboratory and in part by the North Carolina State University start-up funds to G.W. The Ames Laboratory is operated for the U.S. Department of Energy by Iowa State University under contract no. DE-AC02-07CH11358.

References

(1) Waga, S.; Stillman, B. *Annu. Rev. Biochem.* **1998**, *67*, 721.
(2) Kural, C.; Kim, H.; Syed, S.; Goshima, G.; Gelfand, V. I.; Selvin, P. R. *Science* **2005**, *308*, 1469.
(3) Forkey, J. N.; Quinlan, M. E.; Shaw, M. A.; Corrie, J. E. T.; Goldman, Y. E. *Nature* **2003**, *422*, 399.
(4) Yasuda, R.; Noji, H.; Yoshida, M.; Kinosita, K.; Itoh, H. *Nature* **2001**, *410*, 898.
(5) Nan, X. L.; Sims, P. A.; Chen, P.; Xie, X. S. *J. Phys. Chem. B* **2005**, *109*, 24220.
(6) Murase, K.; Fujiwara, T.; Umemura, Y.; Suzuki, K.; Iino, R.; Yamashita, H.; Saito, M.; Murakoshi, H.; Ritchie, K.; Kusumi, A. *Biophys. J.* **2004**, *86*, 4075.
(7) Thompson, R. E.; Larson, D. R.; Webb, W. W. *Biophys. J.* **2002**, *82*, 2775.
(8) Toprak, E.; Balci, H.; Blehm, B. H.; Selvin, P. R. *Nano Lett.* **2007**, *7*, 2043.
(9) Huang, B.; Wang, W. Q.; Bates, M.; Zhuang, X. W. *Science* **2008**, *319*, 810.
(10) Juette, M. F.; Gould, T. J.; Lessard, M. D.; Mlodzianoski, M. J.; Nagpure, B. S.; Bennett, B. T.; Hess, S. T.; Bewersdorf, J. *Nat. Methods* **2008**, *5*, 527.

(11) Shtengel, G.; Galbraith, J. A.; Galbraith, C. G.; Lippincott-Schwartz, J.; Gillette, J. M.; Manley, S.; Sougrat, R.; Waterman, C. M.; Kanchanawong, P.; Davidson, M. W.; Fetter, R. D.; Hess, H. F. *Proc. Natl. Acad. Sci. U. S. A.* **2009**, *106*, 3125.

(12) Bates, M.; Huang, B.; Dempsey, G. T.; Zhuang, X. W. *Science* **2007**, *317*, 1749.

(13) Betzig, E.; Patterson, G. H.; Sougrat, R.; Lindwasser, O. W.; Olenych, S.; Bonifacino, J. S.; Davidson, M. W.; Lippincott-Schwartz, J.; Hess, H. F. *Science* **2006**, *313*, 1642.

(14) Westphal, V.; Rizzoli, S. O.; Lauterbach, M. A.; Kamin, D.; Jahn, R.; Hell, S. W. *Science* **2008**, *320*, 246.

(15) Xie, X. S.; Dunn, R. C. *Science* **1994**, *265*, 361.

(16) Moerner, W. E.; Orrit, M. *Science* **1999**, *283*, 1670.

(17) Nirmal, M.; Dabbousi, B. O.; Bawendi, M. G.; Macklin, J. J.; Trautman, J. K.; Harris, T. D.; Brus, L. E. *Nature* **1996**, *383*, 802.

(18) Derfus, A. M.; Chan, W. C. W.; Bhatia, S. N. *Nano Lett.* **2004**, *4*, 11.

(19) Wang, G. F.; Stender, A. S.; Sun, W.; Fang, N. *Analyst* **2010**, *135*, 215.

(20) West, J. L.; Halas, N. J. *Annual Review of Biomedical Engineering* **2003**, *5*, 285.

(21) Murphy, C. J.; Gole, A. M.; Stone, J. W.; Sisco, P. N.; Alkilany, A. M.; Goldsmith, E. C.; Baxter, S. C. *Accounts of Chemical Research* **2008**, *41*, 1721.

(22) De, M.; Ghosh, P. S.; Rotello, V. M. *Advanced Materials* **2008**, *20*, 4225.

(23) Saxton, M. J.; Jacobson, K. *Annu. Rev. Biophys. Biomol. Struct.* **1997**, *26*, 373.

(24) Debrabander, M.; Nuydens, R.; Geuens, G.; Moeremans, M.; Demey, J. *Cell Motil. Cytoskeleton* **1986**, *6*, 105.

(25) Hu, M.; Novo, C.; Funston, A.; Wang, H. N.; Staleva, H.; Zou, S. L.; Mulvaney, P.; Xia, Y. N.; Hartland, G. V. *J. Mater. Chem.* **2008**, *18*, 1949.

(26) Rong, G. X.; Wang, H. Y.; Skewis, L. R.; Reinhard, B. M. *Nano Lett.* **2008**, *8*, 3386.

(27) Boyer, D.; Tamarat, P.; Maali, A.; Lounis, B.; Orrit, M. *Science* **2002**, *297*, 1160.

(28) Cognet, L.; Tardin, C.; Boyer, D.; Choquet, D.; Tamarat, P.; Lounis, B. *Proc. Natl. Acad. Sci. U. S. A.* **2003**, *100*, 11350.

(29) Lasne, D.; Blab, G. A.; Berciaud, S.; Heine, M.; Groc, L.; Choquet, D.; Cognet, L.; Lounis, B. *Biophys. J.* **2006**, *91*, 4598.

(30) Tkachenko, A. G.; Xie, H.; Liu, Y. L.; Coleman, D.; Ryan, J.; Glomm, W. R.; Shipton, M. K.; Franzen, S.; Feldheim, D. L. *Bioconjugate Chem.* **2004**, *15*, 482.

(31) Sun, W.; Wang, G.; Fang, N.; Yeung, E. S. *Anal. Chem.* **2009**, *81*, 9203.

(32) Shah, N. B.; Dong, J.; Bischof, J. C. *Mol. Pharm.* **2010**, *8*, 176.

(33) Ando, J.; Fujita, K.; Smith, N. I.; Kawata, S. *Nano Lett.* **2011**, *11*, 5344.

(34) Wang, G. F.; Sun, W.; Luo, Y.; Fang, N. *J. Am. Chem. Soc.* **2010**, *132*, 16417.

(35) Gu, Y.; Sun, W.; Wang, G. F.; Fang, N. *J. Am. Chem. Soc.* **2011**, *133*, 5720.

(36) Sun, W.; Fang, N.; Trewyn, B. G.; Tsunoda, M.; Slowing, II; Lin, V. S. Y.; Yeung, E. S. *Anal. Bioanal. Chem.* **2008**, *391*, 2119.

(37) Sherry, L. J.; Chang, S. H.; Schatz, G. C.; Van Duyne, R. P.; Wiley, B. J.; Xia, Y. N. *Nano Lett.* **2005**, *5*, 2034.

(38) Lee, K. J.; Nallathamby, P. D.; Browning, L. M.; Osgood, C. J.; Xu, X.-H. N. *ACS Nano* **2007**, *1*, 133.

(39) Tsunoda, M.; Isailovic, D.; Yeung, E. S. *J. Microsc.-Oxf.* **2008**, *232*, 207.

(40) Li, H. W.; McCloskey, M.; He, Y.; Yeung, E. S. *Anal. Bioanal. Chem.* **2007**, *387*, 63.

(41) Tsunoda, M.; Isailovic, D.; Yeung, E. S. *J. Microsc-Oxford* **2008**, *232*, 207.

(42) Pluta, M. *Advance light microscopy*; Elsevier Science Publishing Co. Inc.: New York, 1989; Vol. 2.

(43) Gelles, J.; Schnapp, B. J.; Sheetz, M. P. *Nature* **1988**, *331*, 450.

(44) Sun, W.; Wang, G. F.; Fang, N.; Yeung, E. S. *Anal. Chem.* **2009**, *81*, 9203.

(45) Qian, Z. M.; Li, H. Y.; Sun, H. Z.; Ho, K. *Pharmacol. Rev.* **2002**, *54*, 561.

(46) de la Fuente, J. M.; Berry, C. C. *Bioconjugate Chem.* **2005**, *16*, 1176.

(47) Heitz, F.; Morris, M. C.; Divita, G. *Br. J. Pharmacol.* **2009**, *157*, 195.

(48) Narayanan, R.; Lipert, R. J.; Porter, M. D. *Anal. Chem.* **2008**, *80*, 2265.

(49) Preza, C.; Snyder, D. L.; Conchello, J. A. *J. Opt. Soc. Am. A* **1999**, *16*, 2185.

(50) Gibson, S. F.; Lanni, F. *J. Opt. Soc. Am. A* **1989**, *6*, 1357.

(51) Wang, G. F.; Geng, L. *Anal. Chem.* **2005**, *77*, 20.

(52) Qian, X. M.; Peng, X. H.; Ansari, D. O.; Yin-Goen, Q.; Chen, G. Z.; Shin, D. M.; Yang, L.; Young, A. N.; Wang, M. D.; Nie, S. M. *Nature Biotechnology* **2008**, *26*, 83.

(53) Liong, M.; Lu, J.; Kovochich, M.; Xia, T.; Ruehm, S. G.; Nel, A. E.; Tamanoi, F.; Zink, J. I. *Acs Nano* **2008**, *2*, 889.

(54) Rosi, N. L.; Giljohann, D. A.; Thaxton, C. S.; Lytton-Jean, A. K. R.; Han, M. S.; Mirkin, C. A. *Science* **2006**, *312*, 1027.

(55) Lal, S.; Clare, S. E.; Halas, N. J. *Accounts of Chemical Research* **2008**, *41*, 1842.

(56) De Jong, W. H.; Hagens, W. I.; Krystek, P.; Burger, M. C.; Sips, A.; Geertsma, R. E. *Biomaterials* **2008**, *29*, 1912.

(57) Klausner, R. D.; Vanrenswoude, J.; Ashwell, G.; Kempf, C.; Schechter, A. N.; Dean, A.; Bridges, K. R. *J. Biol. Chem.* **1983**, *258*, 4715.

(58) Chithrani, B. D.; Chan, W. C. W. *Nano Lett.* **2007**, *7*, 1542.

Figures

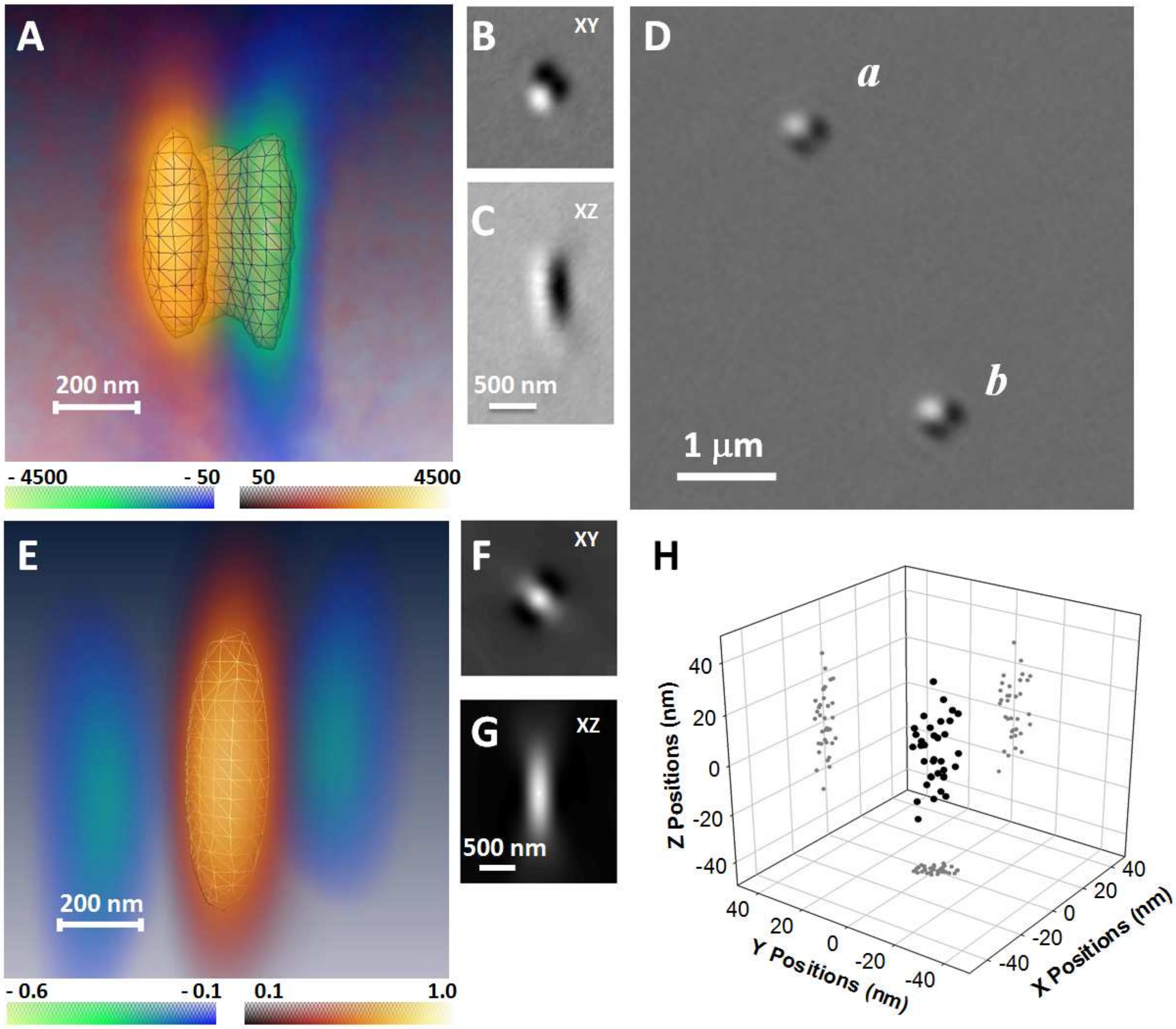

Figure 6.1. Model-based 3D correlation imaging for 3D super localization of gold nanoparticles. (A) 3D intensity profile of a 40-nm spherical gold nanoparticle immobilized on glass surface (shown in (D)) imaged with a 100× objective. The model is comprised of a bright portion shown in orange and a dark portion shown in blue. The 3D intensity profile was built from 65 equally spaced 2D DIC images along the optical axis. The pixel size was 36.3 nm, and the z-step was 40 nm. Ortho-slices of the image volume were shown in (B) and (C). (E) Model-based 3D correlation map of a 40-nm gold nanoparticle and its surrounding area. Ortho-slices of the correlation map were shown in (F) and (G). (H) Variations on the

measured distance between two 40-nm gold particles from 42 sets of z-scans. The distance, rather than the absolute positions, was determined in order to eliminate the sample drifting in high precision microscopy. A correlation coefficient threshold of 0.6 (the shaded iso-surface in (E)) was used in the calculation.

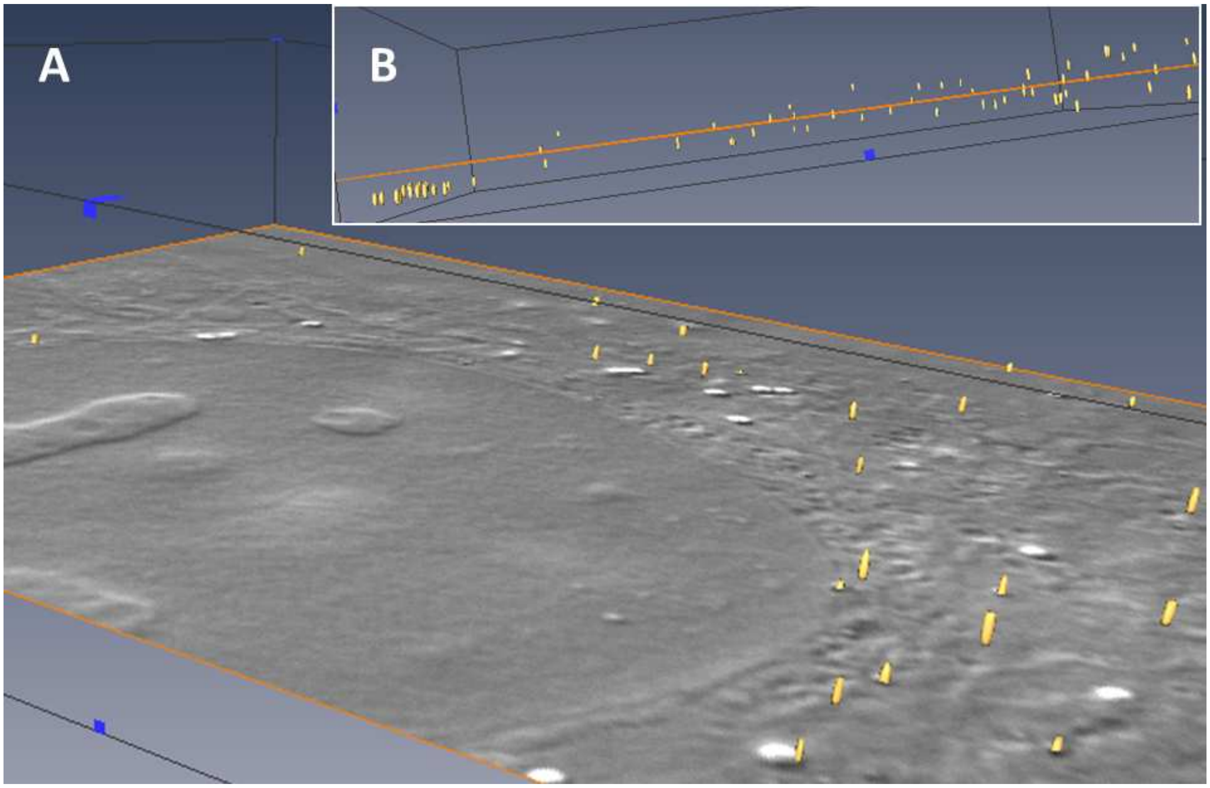

Figure 6.2.3D localization of 40-nm gold nanoparticles inside a fixed HeLa cell. (A) The positions of mapped particles are presented as spheroid iso-correlation surfaces of 0.6 in the 3D correlation map. The cross section shows the DIC cell image at the corresponding position. (B) The same volume is viewed from a different angle to show that mapped particles are vertically distributed inside the cell. More slices of the cell image with vertically distributed gold nanoparticles were shown in Supplementary Figure 6.2.

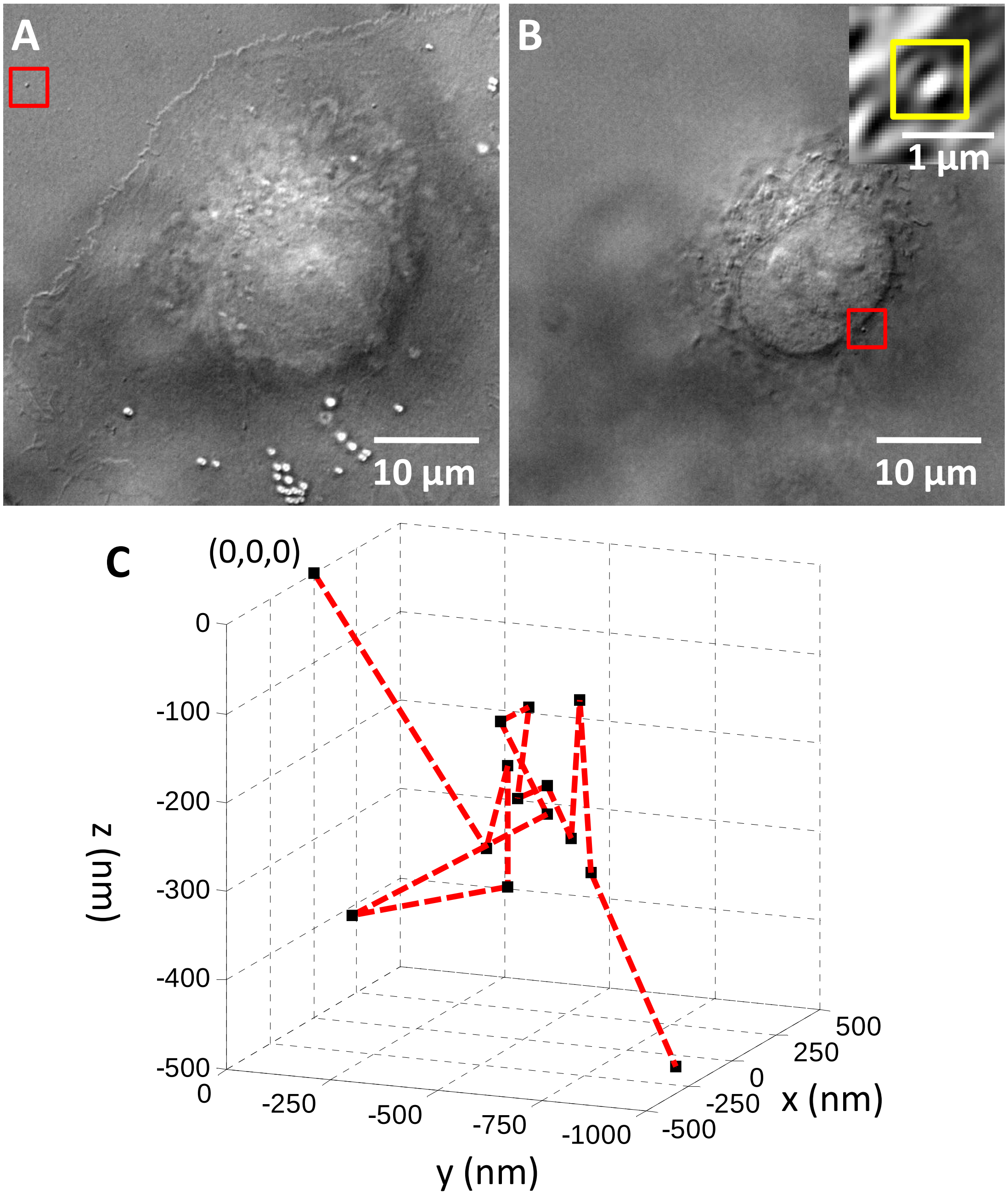

Figure 6.3. The 3D trajectory of a gold nanoparticle on the membrane of an A549 cell. (A) The reference particle adsorbed on the coverslip. (B) The particle of interest on the cell membrane. The correlation map of the particle of interest is shown in the square box appended to the image. The reference particle and the particle of interest are imaged at different focal planes. (C) The moving trace of the nanoparticle. The initial position of the

particle was (0, 0, 0). Larger z coordinates indicate the particle was closer to the cell surface and farther away from the coverslip.

Supporting Information

for

Three-Dimensional Super-Localization and Tracking of Single Gold Nanoparticles in Cells

Yan Gu[†], *Xiaowei Di*[‡], *Wei Sun*[†], *Gufeng Wang*[§]* *and Ning Fang*[†]*

†Ames Laboratory, U.S. Department of Energy, and Department of Chemistry, Iowa State University, Ames,
Iowa 50011, United States

§Department of Chemistry, North Carolina State University, Raleigh, NC 27695

‡College of Chemistry and Chemical Engineering, Inner Mongolia University, Hohhot 010021, China

Supplementary Figures

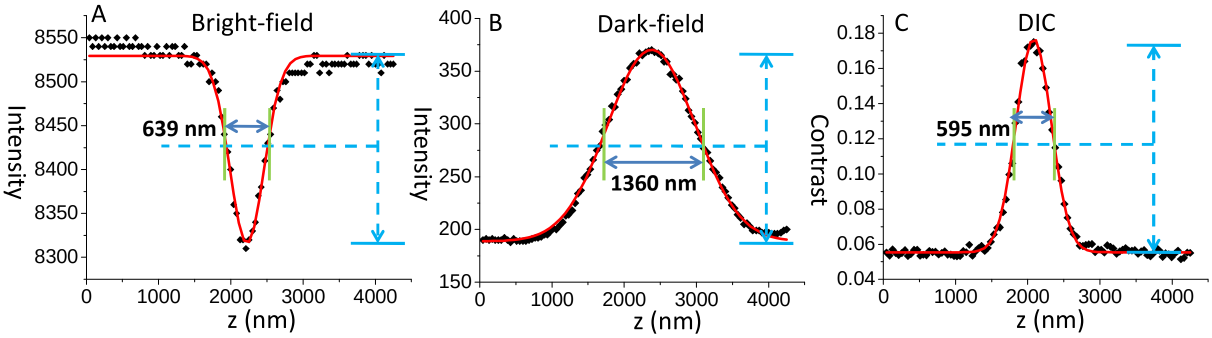

Figure 6.S1. Z-profiles of single gold nanoparticles under (A) bright-field (NA 1.4 for both objectiveand condenser), (B) dark-field (objective NA ~1.0, condenser NA 1.2-1.4), and (C) DIC microscope(NA 1.4 for both objective and condenser), respectively.

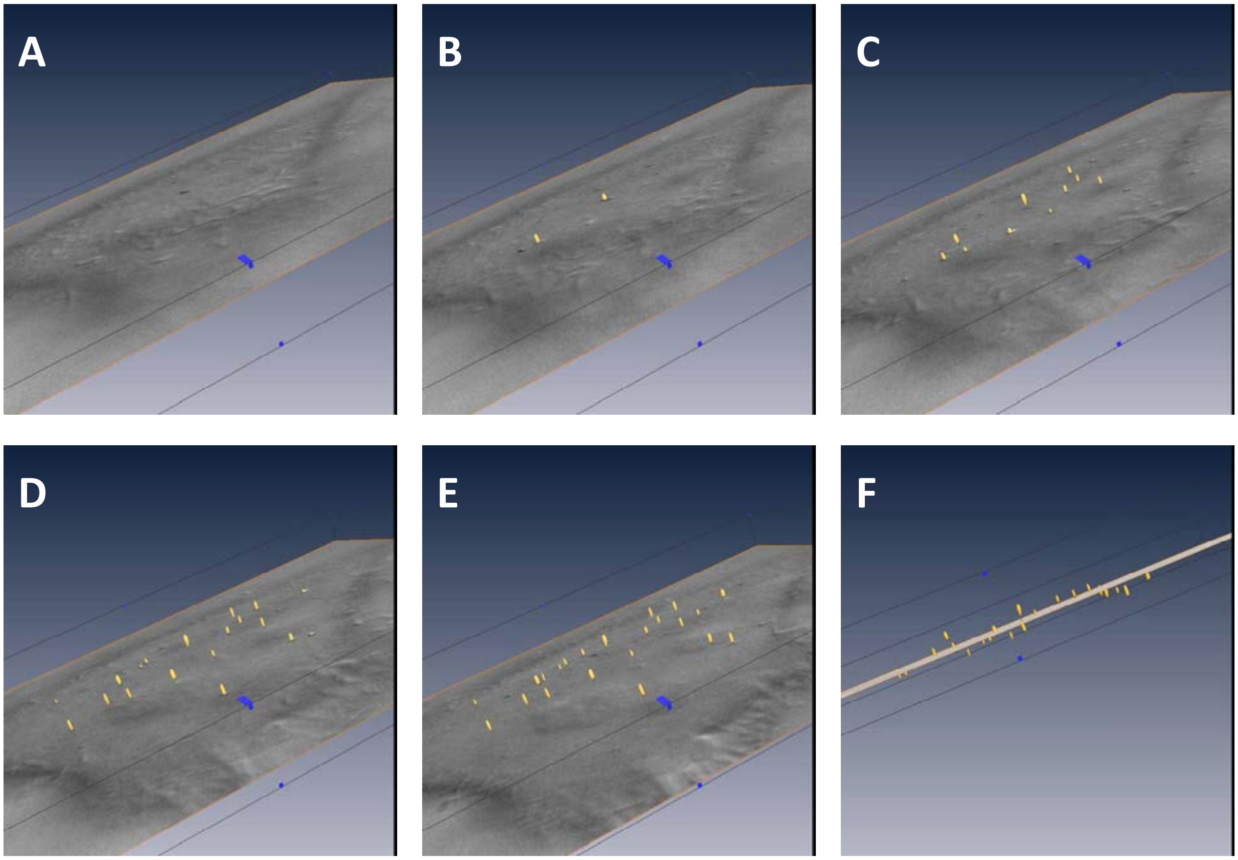

Figure 6.S2. A-E.Slices of the volume of the cell images with 40-nm gold nanoparticles distributed at different axial positions.F. Side view of the distribution of the gold nanoparticles.

CHAPTER 7

SIMULTANEOUS SINGLE PARTICLE SUPER-LOCALIZATION AND ROTATIONAL TRACKING

A paper published in ACS Nano

2013, *7(2)*, 1658-1665

Yan Gu[†], *Gufeng Wang**[‡], *and Ning Fang**[†]

[†]Ames Laboratory, U.S. Department of Energy, and Department of Chemistry, Iowa State University, Ames, Iowa 50011, United States

[‡]Department of Chemistry, North Carolina State University, Raleigh, North Carolina 27695, United States

Abstract

Super-localization of single molecules and nanoparticles has become an essential procedure to bring new insights into nanoscale structures and dynamics of biological systems. In the present study, super-localization is combined with the newly introduced differential interference contrast (DIC) microscopy-based single particle orientation and rotational tracking (SPORT). The new technique overcomes the difficulty in localization of the anti-symmetric DIC point spread function by using a dual-modality microscope configuration for simultaneous rotational tracking and localization of single gold nanorods with nanometer-scale precision. The new imaging setup has been applied to study the steric hindrance induced by relatively large cargos in the microtubule gliding assay and to track

nanocargos in the crowded cellular environment. This technique has great potential in the study of biological processes where both localization and rotational information are required.

Introduction

Localization of single molecules and particles in optical microscopy with a precision of one to three orders of magnitude smaller than the diffraction limit of light is often referred to as super-localization. Nanometer-scale localization precision has been demonstrated for single fluorophores[1-8] and non-fluorescent particles.[9-11] In single molecule or particle tracking experiments, super-localization has brought new insights into various biological questions, e.g., the stepping mechanisms of motor proteins kinesin and myosin.[10-13] In single-molecule-based super-resolution fluorescence microscopy, such as stochastic optical reconstruction microscopy (STORM)[14-15] and photoactivated localization microscopy (PALM),[16-18] the localization precision determines the spatial resolution as individual molecules are separated temporally.

In most super-localization analyses the centroids of single molecules/particles are found by fitting their images to the point spread function (PSF) of the optical imaging system, which is usually approximated as a 2D Gaussian function. Beyond these relatively simple cases, however, there are more complicated situations where the PSF does not resemble the Gaussian profile. For example, special cares are required to minimize the localization errors when the intensity distribution of an emitting molecule is significantly affected by the emission dipole's 3D orientation.[3-4] In differential interference contrast (DIC) microscopy, the anti-symmetric PSF, which is composed of apposed bright and dark parts over a grey background, cannot be fitted with a simple mathematical function; therefore, the correlation mapping algorithm has been implemented to provide nanometer-scale localization for spherical particles in 2D[10] and 3D.[9]

While tracking precise trajectories of single molecules and particles has become more attainable, a thorough understanding of a biological process frequently requires additional information such as the orientation and rotational motion of target molecules. Current techniques for acquiring orientation and rotational information of nano-objects are based on optical anisotropy of the probes. The polarized fluorescence[19-20] or dark-field scattering imaging[21] techniques converts the orientation information to image intensity, which is determined by the angle between the transition dipole of the probe and the polarization direction of the illumination beam. Most of these methods are not directly compatible with superlocalization microscopy. For example, in defocused imaging, it is challenging to locate the center of the defocused image patterns; therefore, switching back and forth between focused and defocused imaging[22] or taking focused and defocused images simultaneously using a dual-wavelength setup[23] is necessary to obtain the accurate centroid and orientation. More recently, Ohmachi *et al.*developed a simultaneous 3D orientation and position tracking technique forhighly fluorescent quantum rods by splitting fluorescence signals to four polarization channels.[24]

We have recently developed the single particle orientation and rotational tracking (SPORT) technique[25-26] to visualize the motions of single rod-shaped plasmonic gold nanoparticles in DIC microscopy. The SPORT technique is especially useful in biological studies with gold nanorods as the probes because of their low cytotoxicity, large optical cross section resulted from surface plasmon resonance (SPR), and excellent photo-stability. However, the SPORT technique faces similar challenges of super-localization as other rotational tracking techniques, as well as the difficulties originated from the anti-symmetric PSF of DIC microscopy.

In this study, we demonstrate a novel dual-modality approach for SPORT, which allows for the simultaneous rotational tracking and localization of single gold nanorods with nanometer-scale precision in engineered environments and in live cells. This is realized by inserting an additional arm into the optical path of the DIC microscope for imaging at two modes simultaneously. In the additional optical arm, gold nanorod probes form modified bright-field images, allowing their positions to be determined with nanometer-scale precision. At the same time, the original DIC scheme allows for the rotational tracking of gold nanorods, thus keeping all the essential traits of the SPORT technique. Using this set-up, the localization precision of less than 10 nm has been achieved for gold nanorods with an average size of 25 nm × 73 nm at a temporal resolution of 74 ms. The usefulness of the novel particle tracking strategy is demonstrated by tracing gold nanorod cargos in the *in vitro* microtubule gliding assays and in live cells under the influence of steric hindrance.

DIC/Bright-field dual-modality microscopy

The dual-modality setup is modified from a Nikon Eclipse 80i DIC microscope equipped with two Nomarski prisms (**Figure 7.1A**) for taking images in DIC and bright-field modes simultaneously. The first Nomarski prism splits the illumination white light to two beams that are mutually orthogonally polarized and laterally shifted by a small shear distance *d*. These two beams result in two intermediate bright-field images behind the microscope objective and tube lens. The presence of the second Nomarski prism shifts the two intermediate images back by the same shear distance *d*. In the dual-modality imaging, instead of intercepting the images behind the tube lens, the intermediate images are collimated again and divided by a 560-nm long pass dichroic mirror into two channels. Proper band pass filters are inserted into the two light paths to select a wavelength of 700 nm for DIC imaging and 540 nm for bright-field imaging. These two wavelengths correspond to the longitudinal and transverse SPR modes of the gold nanorods (25 nm × 73 nm), respectively.

In the 700-nm DIC channel, the second polarizer projects the two intermediate bright-field images to the same polarization plane and interference occurs, yielding typical bright/dark DIC images on a gray background (**Figure 7.1B**). This channel tracks the 3D orientation of the nanorod's longitudinal SPR mode.

In the 540-nm bright-field channel, the two mutually shifted intermediate images are projected onto the camera without interference *in the absence of the second polarizer*, forming an overlaid bright-field image for the gold nanorod's transverse SPR mode. A gold nanorod shows as two partially overlapped dark lobes, mutually shifted by the shear distance *d*, on a bright background (**Figure 7.1C**). The presence of two Nomarski prisms in this modified bright-field microscopy imaging results in a new PSF that can be approximated as a double-peak Gaussian profile; therefore, the centroid of a single particle can be located by non-linear least squares fitting of the two dark lobes with the following double-peak Gaussian function:

$$I = I_b - A_1 \cdot e^{-\left[\frac{(x-x_0)^2}{2\sigma_{x1}^2} + \frac{(y-y_0)^2}{2\sigma_{y1}^2}\right]} - A_2 \cdot e^{-\left[\frac{\left(x-x_0 \pm d/\sqrt{2}\right)^2}{2\sigma_{x2}^2} + \frac{\left(y-y_0 \pm d/\sqrt{2}\right)^2}{2\sigma_{y2}^2}\right]}, \qquad (1)$$

where I_b is the background intensity, which is determined by the exposure time and the camera gain; A_1 and $A_2$are the amplitudes of the two Gaussians; x_0 and y_0 are the coordinates of the centroid of the first Gaussian; *d* is the shear distance assuming the shear is along the northwest-southeast direction (**Figure 7.1C**); σ_{x1}, σ_{y1}andσ_{x2}, $\sigma_{y2}$are the standard deviations of the *x* and *y* components, respectively, for the two Gaussian peaks (**Figure 7.1D**).

The shear distance *d* is an intrinsic property of the Nomarski prisms and the focusing optics, and also depends on the illumination wavelength. Two pairs of Nomarski prisms with different shear distances were tested by taking images of a gold nanorod and a 200-nm polystyrene particle at different orientations (**Supplementary Figure 7.1**). The shear distances of these Nomarski prisms were measured by fitting the modified bright-field images of the polystyrene particle with **Equation 7.1**. The shear distances of these two sets of Nomarski prisms at the wavelength of 540 nm were found to be 290 ± 3 nm and 189 ± 3 nm, respectively. The Nomarski prisms with a larger shear distance generate more accurate results in double-peak Gaussian fitting because they separate the two peaks farther apart.

The relative intensity of the two dark lobes (the ratio of A_1 to A_2) is dependent on the orientation of the gold nanorod and the bias retardation, which is intentionally introduced as a phase shift between the two wavefronts passing through the specimen by adjusting the polarizer and quarter-wave plate settings to increaseDIC image contrast.[27] **Supplementary Figure 7.2** shows an example of the DIC and modified bright-field images of the same gold nanorod at three different orientations using the pair of Nomarski prisms with the larger shear distance.

In the rest of discussion in this paper, this modified bright-field microscopy imaging mode will be referred to as the *double-Gaussian* method for super-localization of gold nanorods.

Alternative configuration

In the Nomarski DIC mode, the second polarizer is set at 90° with respect to the first polarizer so that final DIC images are generated with equal contributions from two orthogonally polarized light beams passing through the sample. When the second polarizer is removed from the light path, we obtain the modified bright-field images with two dark lobes, as described in the previous section. When the second polarizer is set at 45° with respect to the first polarizer, one of the two orthogonally polarized beams is blocked, leaving only one dark spot in the final image of a gold nanorod. This alternative approach for localizing gold nanorods will be referred to as the *single-Gaussian* method.

The images of a gold nanorod and a 200-nm polystyrene particle during a 360° rotation under each of these different polarizer settings are shown in **Supplementary Figure 7.3A**. With the second polarizer setting of 45°, the remaining dark spot can be non-linear least squares fitted with a 2D Gaussian function to locate the particle (**Supplementary Figures 7.3B-C**), and the intensity changes with respect to the orientation of the nanorod's short axis as the observation wavelength corresponds to the transverse SPR mode of gold nanorod (**Supplementary Figure 7.4**). The two 45^{o} polarization configurations result in slightly different signal intensities once again due to the intentionally introduced bias retardation.[27]

The comparison of the *double-* and *single-Gaussian* methods is done by measuring the distances between the two particles at different orientations as shown in **Supplementary Figure 7.3A**. The two sets of measured distances are virtually identical. Therefore, the *single-Gaussian* method will be used exclusively in the rest of our discussions because of its mathematical simplicity.

The localization precision of the *single-Gaussian* method is obtained by recovering the positions of gold nanorods in a stepping experiment on a high-precision piezoelectric stage (**Supplementary Figure 7.5**). The measured step sizes by localizing the particles are consistent with the designated values. The localization precision from non-linear least squares fitting is determined to be 2-5 nm at a temporal resolution of 74 ms, similar to those obtained for 40-nm gold nanospheres.[9]

Dual-modality imaging in microtubule gliding assays

The microtubule gliding assays have shown great potential to serve as transport system for shuttling and sorting nanocargos in engineered environments.[28-31] In these assays, motor proteins, such as kinesin, are pre-coated on a substrate and propel microtubule fragments. A microtubule can rotate along its longitudinal axis when it glides on the substrate, depending on the number of protofilaments it is composed of. We have previously demonstrated that the gold nanorods with an average size of 10 nm × 35 nm attached on the gliding/rotating non-13-protofilament microtubules displayed periodic bright and dark DIC image patterns, while the nanorods attached on the 13-protofilament microtubules displayed nearly constant DIC intensities.[26] The measurements by fluorescence interference contrast microscopy have shown that full-length kinesin motors elevate gliding microtubules by only 17 ± 2 nm over the surface.[32] Small cargos such as 20 nm quantum dots[33] or 10 nm × 35 nm gold nanorods[26] do not impede the self-rotation of microtubules; however, larger cargos such as micro-beads do obstruct the self-rotation, but have a minimal effect on the forward speed of the microtubule carrier.[33]

In order to utilize molecular motors as nanoengines to transport cargos in engineered systems, it is important to understand how the transport system responds to the steric hindrance created by relatively large cargos in the gliding assay. In the current study, we carry out similar microtubule gliding experiments with larger gold nanorods with an average size of 25 nm × 73 nm. The short axis of these nanorods is the same as the outer diameter (25 nm) of the microtubules. The orientation and location of gold nanorods are obtained simultaneously at a temporal resolution of 74 ms using the *single-Gaussian* method.

In our experiments, the gold nanorods are surface-modified with neutravidin and the microtubules are made from a mixture of unlabeled tubulin and biotinylated tubulin at a ratio of 93 to 7. The number of biotin-neutravidin bindings between a nanorod and a microtubule is a key factor that affects the nanorod's motions during the transport. When a nanorod's long axis is aligned parallel to a microtubule, the contact area of the two rod-shaped objects is maximized to allow an average of 4 biotin-neutravidin bindings. When a nanorod's long axis is perpendicular to a microtubule, the contact area is minimized to result in as few as 1 binding. (See Supplementary Information for detailed calculations.)

The parallel geometry does not create significant steric hindrance, and the nanorods in this geometry will behavior similarly as in the previous reports.[26, 33] The perpendicular geometry with a single binding will likely result in a loosely-bound nanorod and give rise to "blinking" (fast switching between bright and dark DIC image patterns). Such anexample is given in **Supplementary Figure 7.6 (Movie 7.1)**. The current temporal resolution of 74 ms is likely too slow to fully resolve this type of fast, random rotation.

The more common and interesting case, which will be elucidated in greater detail here, is when a nanorod and a microtubule are aligned at an angle (neither perpendicular nor parallel) with multiple bindings (likely 2-4 bindings under our experimental conditions). In this case, a nanorod is more strongly bound to a microtubule, and its motion is no longer determined predominately by the thermal noise as the steric hindrance created from the nanorod/microtubule geometry and the obstacles present in the course of transport becomes an important factor. **Figure 7.2 (Movie 7.2)** shows an example where a gold nanorod travels nearly half a circle with a distance of ~24 μm on a gliding microtubule. The nanorod shows a mainly bright image while travelling southwest, then a mainly dark image after turning ~90° toward northwest, and finally a mainly bright image again after making another turn toward northeast. The relatively stable DIC intensities on the time scale of seconds suggest that the nanorod was rather firmly attached to the microtubule through multiple biotin-neutravidin bindings. However, the recorded DIC intensity traces still show significant fluctuations, indicating that the nanorod changes its orientation

orientation intermittently from time to time due to the steric hindrance. These rotational motions are often accompanied by the movement of the nanorod to new positions found in the x and y trajectories.

Two interesting segments of this transport event are explained in detail as follows. In the first segment (14-22 s, **Figure 7.2C, Supplementary Figure 7.7A**), the microtubule glides at a nearly constant speed of 0.35 μm/s, which is evident from the constant slopes observed in both the x and y trajectories. The x trajectory is smoother than the y trajectory, which can be explained by the fact that the microtubule moves in the x direction and it is much more likely for the nanorod to swing from side to side (y) than to move back and forth (x). Interestingly, the gold nanorod changes its orientation drastically when the microtubule changes its gliding direction at 15-16 s or when the trajectory shows a sudden "jump" (a distance of ~70 nm in the y trajectory) at ~18.5 s. The moving directions of the gold nanorod before and after the drastic orientation changes are guided by the pink dashed lines on the y trajectory. The nanorod changes its orientation possibly because they are shunted by road blocks, such as other microtubules,aggregates of kinesin molecules or un-polymerized tubulin monomers.[34-35] The microtubule and nanorod is caused to rotate in order to evade the steric hindrance, which results in the sudden changes in the nanorod's orientation and position. In the second segment (44-52 s, **Figure 7.2D, Supplementary Figure 7.7B)**, the microtubule moves mainly in the y direction, which results in a rather smooth y trajectory. The rotations of the gold nanorod are accompanied by a shift of the trace at 47.5 s and a change in the moving direction at 50.0 s.

Super-localization and rotational tracking of endocytosed gold nanorods in live cell

The cytoskeleton in a live mammalian cell is composed of interweaving microtubules and actin filaments.[36-37] Cargos are transported by molecular motors including kinesin, dynein and myosin along the microtubule and actin filament tracks.[34] How the cargos are transported in the complex cytoskeleton system and in a crowding environment is intriguing because it is closely related with the cooperation and cross-talk among the motor proteins and the intracellular transport mechanism, but requires further understandings. The transport of a cargo in a complex cytoskeleton environment has been studied using bright-field microscopy with pigment granules as the cargos[38] and fluorescent microscopy with fluorescence-labeled organelles.[39] The directed transport of cargos is affected in the region where space is limited by the crowded cytoskeleton such as the cortex of the cell.[39-40] We previously reported that nanocargos tend to keep their orientation during the directed transport along the microtubule tracks using the SPORT technique.[26, 41] In this study, we visualized the fluctuation of the cargo's orientation caused by the steric hindrance of the surrounding environment.

We imaged the transport of the endocytosed transferrin-modified gold nanorods in live PC12 cells using the new imaging setup. The DIC images of the nanorods show that the rotation of the gold nanorods was common when they are transported in the cortical area where the cytoskeleton is rather crowded. One example is shown in **Figure 7.3** (**Movie 6.3)**. The gold nanorod in this example was transported by a distance of ~2 µm in the x direction. The nanorod wiggled from side to side of the microtubule track during the transport, reflected by the 80-170 nm lateral displacements in the y direction, e.g., at 11 s, 20 s, and 36 s (**Figure 7.3B**). The lateral displacements are comparable to the diameter of early endosomes. It is interesting to note that at the moments of the wiggling motion, the DIC intensities also indicate a wiggling motion by displaying non-correlated bright/dark intensity changes (**Supplementary Figure 7.8**). The correlation of DIC intensity with the lateral displacement and the slow rotation pattern show that the rotation of the nanorod is not caused by rotational diffusion of the vesicle.[42]

The correlated wiggling motion and the orientation changes of the gold nanorod indicate that the transport of the cargo is far from a smooth process. An important factor could be the steric hindrance caused by the crowded environment since there are interweaving actin filaments and microtubules around the cortical area of the cells. The cargo has to evade the obstruction from the interweaving microtubules and actin filaments in order to move forward. Note that the overall transport velocity is around 0.05 µm/s, much smaller than the directed transport rate on microtubule tracks[43] and actin filaments,[11-12] which also provides the evidence that the transport is hindered.

Conclusions

In summary, a novel dual-modality imaging technique has been developed to super-localize a single gold nanorod while providing its orientation and rotational information. The super-localization of the gold nanorod was achieved by curve fitting the modified bright-field images generated by one of the two beams laterally shifted by the Nomarski prism in a DIC microscope. The orientation and rotational information is derived from the DIC images of the gold nanorods. The new single particle tracking technique is a significant improvement over the existing non-fluorescent particle tracking techniques. Due to the advantages of this technique, it can be applied in the study of many biological processes which require both precise localization and the orientation and rotational information of the nanoprobes.

It should be noted that the temporal resolution is currently limited by the achievable signal to noise ratio (SNR) in the modified bright-field channel. Unlike the dark background on fluorescence images, the high background on bright-field images leads to greatly reduced SNR; therefore, the temporal resolution of 74 ms is required to achieve the reported nanometer-scale localization precision with a 100W halogen lamp. By switching to a more intense laser light source or allowing lower localization precision, a higher temporal resolution can be achieved.

The usefulness of this technique has been demonstrated by dynamic tracking of single gold nanorod cargos in microtubule gliding assays and in live cells. The new imaging technique makes it possible in future studies to acquire critical knowledge in order to realize the transport of larger and heavier cargos in micro transport systems using molecular motors. On the other hand, the hustle of the cargo by the obstacles is an important observation associated with intracellular transport where steric hindrance exists in the crowded cellular environment. Further studies will lead to our understanding on how competing kinesin and dynein motors work together to overcome constant obstacles in intracellular transport.

Sample preparation

The cetyltrimethylammonium bromide (CTAB)-capped 25 nm × 73 nm gold nanorods (Nanopartz) were washed and resuspended in 18.2 Ω Milli-Q water before surface modification. To change the surface charge from positive to negative, the gold nanorods were modified with transferrin through a polyethylene glycol (PEG)-thiol linker. The detailed procedures of nanorod surface modifications and polystyrene beads sample preparations can be found in the Supporting Information.

Precision and accuracy measurement on the piezo-stage

A 3D piezoelectric stage was installed on an inverted Zeiss Axiovert 100 TV microscope. The microscope was equipped with two Nomarski prisms, two polarizers, a condenser and a 100× oil immersion objective. Gold nanorods dispersed in Milli-Q water were immobilized on a clean coverslip, and the sample slide was stepped in either the x or y direction by the piezoelectric stage with sub-nanometer precision. The DIC images were captured at 700 nm and the bright field images were captured at 540 nm. Three particles at different orientations were captured, which show completely dark, completely bright, and half dark/half bright DIC images, respectively. The averaged signal-to-noise ratio of the bright-field images of the three nanorods is better than 10. The step size for each movement was 40 nm. At each position, 50 frames of images were taken at a temporal resolution of 74 ms. The coordinates of each gold nanorod in each frame was determined using the single-peak 2D Gaussian fitting of the bright-field images, and 50 x or y coordinates were plotted as one step. The precision of the single particle tracking was calculated as the standard deviation of the x or y coordinates in each step, and the accuracy of the step measurements was determined as the standard deviation of the step sizes calculated as the difference between the averaged x or y coordinates for each two steps.

Microtubule gliding assays

The protocol was modified from the procedures reported in our previous publication.[25] Detailed procedures of the extraction of full-length kinesin, surface modification of gold nanorods with neutravidin, and preparation of biotinylated 12-protofilament microtubules can be found in the Supporting Information. A chamber was formed by placing a clean glass coverslip on top of a clean glass slide with two pieces of double-sided tape serving as spacers. BRB80 solution containing 0.5 mg/mL casein (Sigma, St. Louis, MO) was flowed into the chamber, and the chamber was kept at room temperature for 5 min. BRB80 solution containing 0.2 mg/mL casein, 0.2 mM MgATP, and kinesin was then introduced into the chamber to replace the previous solution. After 5 min, BRB80 solution containing 0.2 mg/mL casein, 0.2 mM MgATP, 10 µM Taxol, and microtubules was introduced into the chamber and kept at room temperature for 5 min. After that, BRB80 solution containing 0.2 mg/mL casein, 0.2 mM MgATP, 10 µM Taxol, and neutravidin-modified gold nanorods was flowed into the chamber and incubated at room temperature for 7 min. Finally, the chamber was filled with BRB80 solution containing 0.2 mg/mL casein, 1 mM MgATP, and 10 µM Taxol with an oxygen scavenging system [50 µg/mL glucose oxidase (Sigma), 4 µg/mL catalase (Sigma), 1% (w/v) glucose (Sigma), and 0.1% (v/v) mercaptoethanol (Fluka)]. Between the steps, the chamber was washed twice with BRB80 solution containing 0.2 mg/mL casein and 0.2 mM MgATP. The motions of the gold nanorods attached with the microtubules were then imaged under our dual-modality microscope.

Cell cultures and live cell imaging

PC 12 cells (CRL 1721.1, ATCC, Manassas, VA) were cultured on 22 mm × 22 mm poly-l-lysine coated coverslips in six-well cell culturing plates. Complete cell culturing medium composed of F12K cell culturing medium (ATCC), 15% horse bovine serum (ATCC) and 2.5% Fetus Bovine Serum (ATCC) was added to the plates. After the cell culture covered 70% of a coverslip, 40 µL of transferrin modified gold nanorod solution was added to each of the plate and incubated for 1 hour. After that, the cell coverslip was placed on a clean glass slide for imaging. Two pieces of double-sided tape act as spacers between the glass slide and the coverslip to form the chamber. 30 µL of F12K cell culture medium was added to the chamber to sustain the cells.

Dual mode imaging and data analysis

Movies of gliding assays and live cell experiments were taken under the dual-mode microscope modified from an upright Nikon 80i microscope. All movies were taken at the temporal resolution of 74 ms. The images and movies were all processed in ImageJ and Matlab. The 2D Gaussian fitting and single particle tracking (including position and orientation) were all done automatically by running the programs written in MATLAB.

References

1. Gordon, M. P.; Ha, T.; Selvin, P. R., Single-Molecule High-Resolution Imaging with Photobleaching. *Proc. Natl. Acad. Sci. USA* **2004,***101*, 6462-6465.
2. Yildiz, A.; Selvin, P. R., Fluorescence Imaging with One Manometer Accuracy: Application to Molecular Motors. *Acc. Chem. Res.* **2005,***38*, 574-582.
3. Enderlein, J.; Toprak, E.; Selvin, P. R., Polarization Effect on Position Accuracy of Fluorophore Localization. *Opt. Express* **2006,***14*, 8111-8120.
4. Mortensen, K. I.; Churchman, L. S.; Spudich, J. A.; Flyvbjerg, H., Optimized Localization Analysis for Single-Molecule Tracking and Super-Resolution Microscopy. *Nat. Methods* **2010,***7*, 377-381.
5. Churchman, L. S.; Okten, Z.; Rock, R. S.; Dawson, J. F.; Spudich, J. A., Single Molecule High-Resolution Colocalization of Cy3 and Cy5 Attached to Macromolecules Measures Intramolecular Distances through Time. *Proc. Natl. Acad. Sci. USA* **2005,***102*, 1419-1423.
6. Toprak, E.; Balci, H.; Blehm, B. H.; Selvin, P. R., Three-Dimensional Particle Tracking Via Bifocal Imaging. *Nano Lett.* **2007,***7*, 2043-2045.
7. Agrawal, A.; Deo, R.; Wang, G. D.; Wang, M. D.; Nie, S. M., Nanometer-Scale Mapping and Single-Molecule Detection with Color-Coded Nanoparticle Probes. *Proc. Natl. Acad. Sci. USA* **2008,***105*, 3298-3303.
8. Pertsinidis, A.; Zhang, Y.; Chu, S., Subnanometre Single-Molecule Localization, Registration and Distance Measurements. *Nature* **2010,***466*, 647-651.
9. Gu, Y.; Di, X.; Sun, W.; Wang, G.; Fang, N., Three-Dimensional Super-Localization and Tracking of Single Gold Nanoparticles in Cells. *Anal. Chem.* **2012**.
10. Gelles, J.; Schnapp, B. J.; Sheetz, M. P., Tracking Kinesin-Driven Movements with Nanometre-Scale Precision. *Nature* **1988,***331*, 450-453.
11. Levi, V.; Gelfand, V. I.; Serpinskaya, A. S.; Gratton, E., Melanosomes Transported by Myosin-V in Xenopus Melanophores Perform Slow 35 Nm Steps. *Biophys. J.* **2006,***90*, L7-L9.
12. Pierobon, P.; Achouri, S.; Courty, S.; Dunn, A. R.; Spudich, J. A.; Dahan, M.; Cappello, G., Velocity, Processivity, and Individual Steps of Single Myosin V Molecules in Live Cells. *Biophys. J.* **2009,***96*, 4268-4275.
13. Yildiz, A.; Forkey, J. N.; McKinney, S. A.; Ha, T.; Goldman, Y. E.; Selvin, P. R., Myosin V Walks Hand-over-Hand: Single Fluorophore Imaging with 1.5-Nm Localization.

Science **2003,***300*, 2061-2065.

14. Rust, M. J.; Bates, M.; Zhuang, X. W., Sub-Diffraction-Limit Imaging by Stochastic Optical Reconstruction Microscopy (Storm). *Nat. Methods* **2006,***3*, 793-795.
15. Huang, B.; Wang, W. Q.; Bates, M.; Zhuang, X. W., Three-Dimensional Super-Resolution Imaging by Stochastic Optical Reconstruction Microscopy. *Science* **2008,***319*, 810-813.
16. Betzig, E.; Patterson, G. H.; Sougrat, R.; Lindwasser, O. W.; Olenych, S.; Bonifacino, J. S.; Davidson, M. W.; Lippincott-Schwartz, J.; Hess, H. F., Imaging Intracellular Fluorescent Proteins at Nanometer Resolution. *Science* **2006,***313*, 1642-1645.
17. Manley, S.; Gillette, J. M.; Patterson, G. H.; Shroff, H.; Hess, H. F.; Betzig, E.; Lippincott-Schwartz, J., High-Density Mapping of Single-Molecule Trajectories with Photoactivated Localization Microscopy. *Nat. Methods* **2008,***5*, 155-157.
18. Shroff, H.; Galbraith, C. G.; Galbraith, J. A.; Betzig, E., Live-Cell Photoactivated Localization Microscopy of Nanoscale Adhesion Dynamics. *Nat. Methods* **2008,***5*, 417-423.
19. Sabido-David, C.; Brandmeier, B.; Craik, J. S.; Corrie, J. E. T.; Trentham, D. R.; Irving, M., Steady-State Fluorescence Polarization Studies of the Orientation of Myosin Regulatory Light Chains in Single Skeletal Muscle Fibers Using Pure Isomers of Iodoacetamidotetramethylrhodamine. *Biophys. J.* **1998,***74*, 3083-3092.
20. Inoue, S.; Shimomura, O.; Goda, M.; Shribak, M.; Tran, P. T., Fluorescence Polarization of Green Fluorescence Protein. *Proc. Natl. Acad. Sci. USA* **2002,***99*, 4272-4277.
21. Sonnichsen, C.; Alivisatos, A. P., Gold Nanorods as Novel Nonbleaching Plasmon-Based Orientation Sensors for Polarized Single-Particle Microscopy. *Nano Lett.* **2005,***5*, 301-304.
22. Toprak, E.; Enderlein, J.; Syed, S.; McKinney, S. A.; Petschek, R. G.; Ha, T.; Goldman, Y. E.; Selvin, P. R., Defocused Orientation and Position Imaging (Dopi) of Myosin V. *Proc. Natl. Acad. Sci. USA* **2006,***103*, 6495-6499.
23. Xiao, L.; Wei, L.; Liu, C.; He, Y.; Yeung, E. S., Unsynchronized Translational and Rotational Diffusion of Nanocargo on a Living Cell Membrane. *Angew. Chem. Int. Ed.* **2012,***51*, 4181-4184.
24. Ohmachi, M.; Komori, Y.; Iwane, A.; Fujii, F.; Jin, T.; Yanagida, T., Fluorescence Microscopy for Simultaneous Observation of 3d Orientation and Movement and Its Application to Quantum Rod- Tagged Myosin V. *Proc. Natl. Acad. Sci. USA* **2012,***109*, 5294-5298.
25. Gu, Y.; Sun, W.; Wang, G. F.; Fang, N., Single Particle Orientation and Rotation Tracking Discloses Distinctive Rotational Dynamics of Drug Delivery Vectors on Live Cell Membranes. *J. Am. Chem. Soc.* **2011,***133*, 5720-5723.
26. Wang, G.; Sun, W.; Luo, Y.; Fang, N., Resolving Rotational Motions of Nano-Objects in Engineered Environments and Live Cells with Gold Nanorods and Differential Interference Contrast Microscopy. *J. Am. Chem. Soc.* **2010,***132*, 16417-16422.

27. Stender, A. S.; Augspurger, A. E.; Wang, G.; Fang, N., Influence of Polarization Setting on Gold Nanorod Signal at Nonplasmonic Wavelengths under Differential Interference Contrast Microscopy. *Anal. Chem.* **2012,***84*, 5210-5215.
28. Saxton, W. M.; Porter, M. E.; Cohn, S. A.; Scholey, J. M.; Raff, E. C.; McIntosh, J. R., Drosophila Kinesin - Characterization of Microtubule Motility and Atpase. *Proc. Natl. Acad. Sci. USA* **1988,***85*, 1109-1113.
29. Berliner, E.; Mahtani, H. K.; Karki, S.; Chu, L. F.; Cronan, J. E.; Gelles, J., Microtubule Movement by a Biotinated Kinesin Bound to a Streptavidin-Coated Surface. *J. Biol. Chem.* **1994,***269*, 8610-8615.
30. Friedman, D. S.; Vale, R. D., Single-Molecule Analysis of Kinesin Motility Reveals Regulation by the Cargo-Binding Tail Domain. *Nat. Cell Biol.* **1999,***1*, 293-297.
31. Kaseda, K.; Higuchi, H.; Hirose, K., Alternate Fast and Slow Stepping of a Heterodimeric Kinesin Molecule. *Nat. Cell Biol.* **2003,***5*, 1079-1082.
32. Kerssemakers, J.; Howard, J.; Hess, H.; Diez, S., The Distance That Kinesin-1 Holds Its Cargo from the Microtubule Surface Measured by Fluorescence Interference Contrast Microscopy. *Proc. Natl. Acad. Sci. USA* **2006,***103*, 15812-15817.
33. Nitzsche, B.; Ruhnow, F.; Diez, S., Quantum-Dot-Assisted Characterization of Microtubule Rotations During Cargo Transport. *Nat. Nanotechnol.* **2008,***3*, 552-556.
34. Ross, J. L.; Ali, M. Y.; Warshaw, D. M., Cargo Transport: Molecular Motors Navigate a Complex Cytoskeleton. *Curr. Opin. Cell Biol.* **2008,***20*, 41-47.
35. Seitz, A.; Surrey, T., Processive Movement of Single Kinesins on Crowded Microtubules Visualized Using Quantum Dots. *EMBO J.* **2006,***25*, 267-277.
36. Fuchs, E.; Yang, Y. M., Crossroads on Cytoskeletal Highways. *Cell* **1999,***98*, 547-550.
37. Klymkowsky, M. W., Weaving a Tangled Web: The Interconnected Cytoskeleton. *Nat. Cell Biol.* **1999,***1*, E121-E123.
38. Rodionov, V.; Yi, J.; Kashina, A.; Oladipo, A.; Gross, S. P., Switching between Microtubule- and Actin-Based Transport Systems in Melanophores Is Controlled by Camp Levels. *Curr. Biol.* **2003,***13*, 1837-1847.
39. Lang, T.; Wacker, I.; Wunderlich, I.; Rohrbach, A.; Giese, G.; Soldati, T.; Almers, W., Role of Actin Cortex in the Subplasmalemmal Transport of Secretory Granules in Pc-12 Cells. *Biophys. J.* **2000,***78*, 2863-2877.
40. Rudolf, R.; Salm, T.; Rustom, A.; Gerdes, H. H., Dynamics of Immature Secretory Granules: Role of Cytoskeletal Elements During Transport, Cortical Restriction, and F-Actin-Dependent Tethering. *Mol. Biol. CELL* **2001,***12*, 1353-1365.
41. Sun, W.; Gu, Y.; Wang, G.; Fang, N., Dual-Modality Single Particle Orientation and Rotational Tracking of Intracellular Transport of Nanocargos. *Anal. Chem.* **2012,***84*, 1134-1138.
42. Gu, Y.; Sun, W.; Wang, G.; Jeftinija, K.; Jeftinija, S.; Fang, N., Rotational Dynamics of Cargos at Pauses During Axonal Transport. *Nat. Commun.* **2012,***3*, 1030.
43. Herold, C.; Leduc, C.; Stock, R.; Diez, S.; Schwille, P., Long-Range Transport of Giant

Vesicles Along Microtubule Networks. *Chemphyschem* **2011,***13*, 1001-6.

Figures

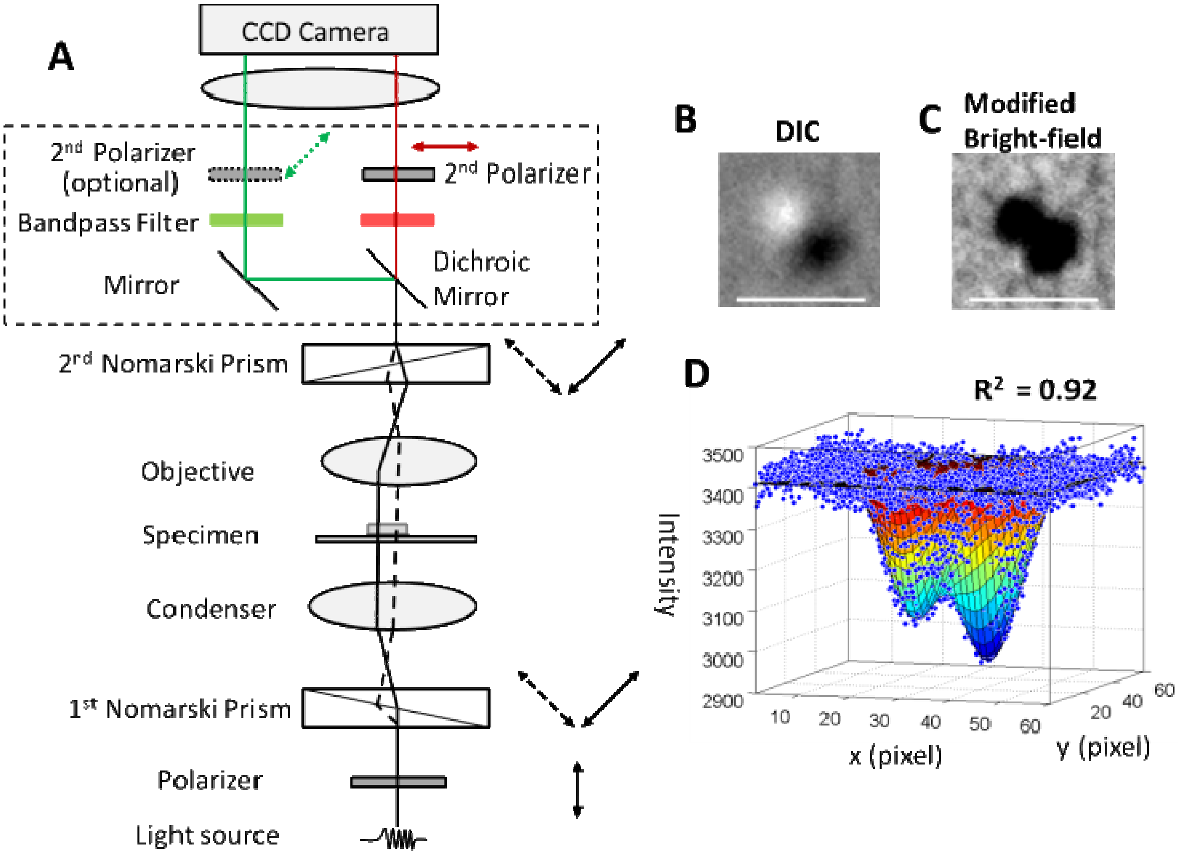

Figure 7.1. The dual-modality single particle localization and rotational tracking technique. **(A)** Schematic diagram of the dual-modality microscope. **(B)** ADIC image of a 200-nm polystyrene bead captured under the modified microscope. **(C)** A double-Gaussian bright-field image. **(D)**Fitting of the image in (C) with a 2D inverse double-peak Gaussian function. The blue dots are the intensities at each coordinate. The scale bars in (B) and (C) represent 1 µm.

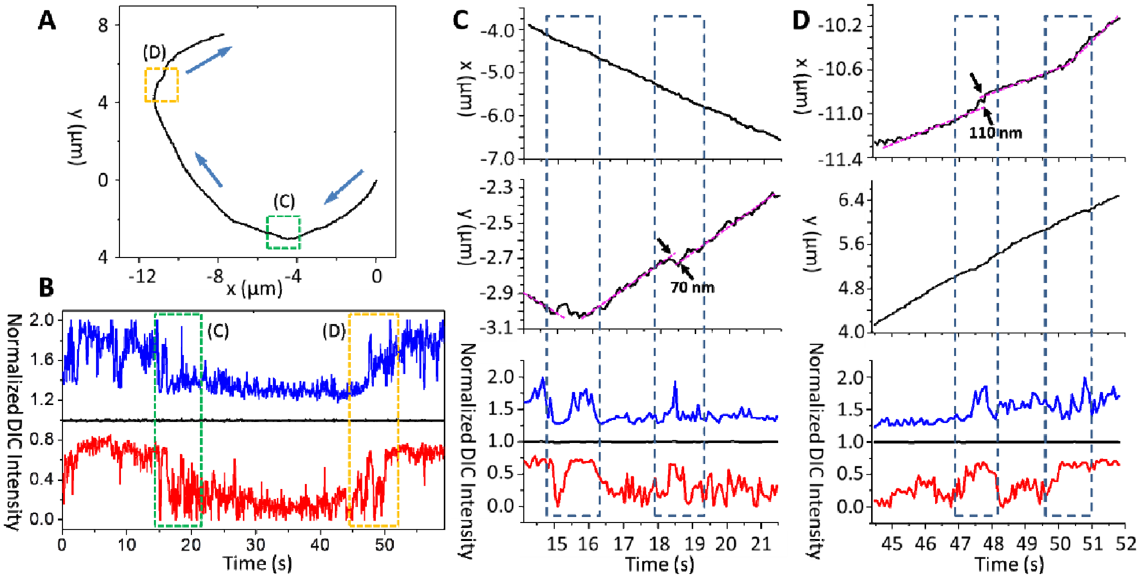

Figure 7.2. Motions of a gold nanorod attached to a gliding microtubule. **(A)** The moving trace of the gold nanorod over a time span of 59.2 s. The positions of the gold nanorod are determined by using the single-Gaussian method. **(B)** The DIC intensity traces of the nanorod under the dual-modality microscope. The bright and dark intensities are shown in blue and red, respectively, and the average background intensities are shown in black. The green (C) and orange (D) boxes highlight two interesting segments where the transport direction is being changed and significant rotational motions are observed. **(C, D)** The x and y displacements and the corresponding DIC intensity traces of the gold nanorod from the two highlighted segments. The transition points with significant rotational behaviors are highlighted in the blue rectangles. The trajectories of the gold nanorod before and after the rotations are highlighted by the pink dashed lines. The calculated azimuthal and polar angles of the gold nanorods during these two segments are shown in **Supplementary Figure 7.7**.

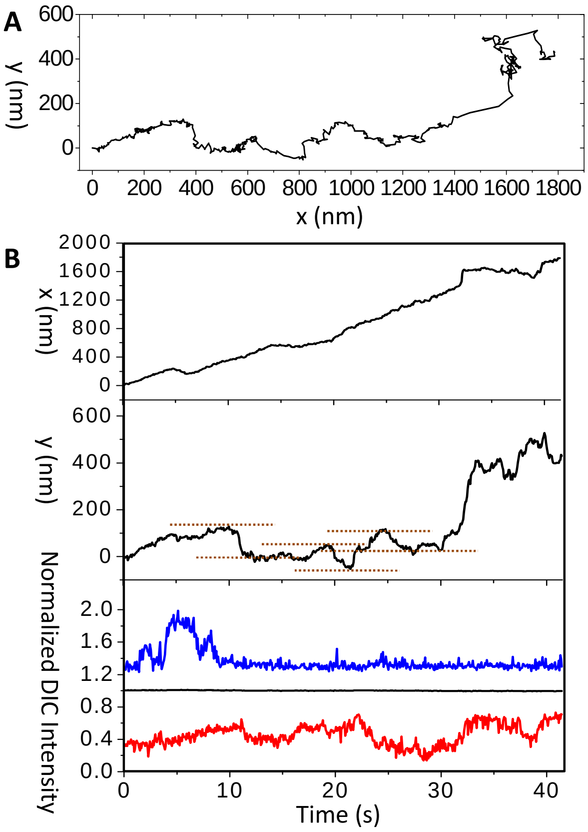

Figure 7.3. Lateral displacement and DIC intensities of a gold nanorod transported in a live cell. **(A)** The moving trace of the gold nanorod. **(B)** The x and y displacements and the DIC intensity traces. The lateral shifts are guided by the horizontal dashed lines. The nanorod's coordinate is set to (0, 0) at time 0.

Supporting Information

for

Simultaneous Single Particle Super-Localization and Rotational Tracking

Yan Gu[†], Gufeng Wang[‡], and Ning Fang*[†]*

[†]Ames Laboratory, U.S. Department of Energy, and Department of Chemistry, Iowa State University, Ames, Iowa 50011, United States

[‡]Department of Chemistry, North Carolina State University, Raleigh, North Carolina 27695, United States

Additional Experimental Methods

Sample preparation: positively-charged gold nanorods.

25 nm × 73 nm gold nanorods were purchased from Nanopartz (Salt Lake City, UT). The gold nanorods were stabilized in cetyltrimethylammonium bromide (CTAB) solution. Before used in our experiments,thecolloidal gold nanorod solutionwas centrifuged and resuspended in Millli-Q water twice to remove most of the CTAB.After that, 10 µL of gold nanorod solution was added on to a pre-cleaned glass slide and covered with a clean glass coverslip. To prevent evaporation, the coverslip was then sealed with nail polisher. The gold nanorods carry positive charges. Due to the electric static interaction with the negatively charged glass surface of the coverslip, the gold nanorods were adsorbed to the coverslip in a short period of time.

Sample preparation: negatively-charged gold nanorods and polystyrene beads.

The 200-nm negatively-charged polystyrene beads were purchased from Duke Scientific (Palo Alto, CA) and diluted to the same concentration as the gold nanorods.

The gold nanorods were then surface-modified with transferrin through a polyethylene glycol (PEG)linker by following the procedure described below:1mL of the gold nanorod solution was reacted with 20-mM N-hydroxylsuccinimide (NHS)-polyethylene glycol (PEG)-thiol (M.W. 119.26, Sigma-Aldrich # 671630, St. Louis, MO) for 1.5 h. After that, the gold nanorod solution was centrifuged and resuspended in 18.2 Ω Millli-Q water again to remove excess NHS-PEG-thiol. After that, 20 μL of 2mg/mL transferrin in dimethyl sulfoxide (DMSO)was added to the gold nanorod solution and react for 3 h. The gold nanorods were then centrifuged and resuspended in Millli-Q water to the concentration of ~1.0×10^{11} nanoparticles/mL.

The gold nanorod and the polystyrene bead solutions were then mixed at 1:1 ratio and diluted by a factor of 10 in Milli-Q water. 10 μL of the mixture was added onto a clean glass substrate and covered by a 3-aminopropyltriethoxysilane modified glass coverslip. The nanoparticles were adsorbed onto the glass coverslip due to electrostatic interactions. The coverslip was then sealed with nail polisher to prevent evaporation.

Localization precision measurement using DIC/bright-field dual-modality imaging and

simplified DIC/bright-field dual-modality imaging

The sample slide of the mixture of gold nanorods (25 nm × 73 nm) and polystyrene beads (200 nm) was fixed on the rotation stage. When the second polarizer is polarized at 45° in either of the two configurations shown in **Supplementary Figure 7.3A**, it blocks one of the intermediate images, giving only one dark spot in the bright-field image. The bright-field image can be then non-linear least squares fitted with a single-peak, 2D Gaussian function:

$$I = I_{Background} - A \times e^{-[\frac{(x-x_0)^2}{2\sigma_x{}^2} + \frac{(y-y_0)^2}{2\sigma_y{}^2}]},$$

where $I_b$is the background intensity; A is the amplitudes of the two Gaussians; x_0 and y_0 are the coordinates of the centroid; $\sigma_x$and $\sigma_y$are the standard deviations of the x and y components of the Gaussians. The centroid of the 2D Gaussian (x_o, y_o) is the location of the nanorod. The localization of the gold nanorod and the polystyrene bead was carried out both without the 2nd polarizer in the bright-field arm and with the 2nd polarizer placed at 135°with respect to the 1st polarizer. The sample slide was rotated by 360° with 15° steps. At each orientation, 10 images were acquired and the particles in each image were localized and their positions were averaged.

Single Particle Tracking in Microtubule Gliding Assay.

Extraction of the full-length kinesin motor proteins.

BL21 (DE3) *Escherichia coli* with the full-length His-tagged kinesin plasmid were kindly provided by Dr. Will Hancock atPennsylvania State University. The kinesin motor proteins was extracted and purified on a Ni column according to the protocol published elsewhere.[1]

Preparation of biotin-conjugated microtubules.

The tubulin proteins, GTP and Taxol were purchased from Cytoskeleton (Denver, CO). The protocol of the preparation of 12-protofilament microtubules was reported in our previous publication.[2] Generally, 10 μL of BRB80 buffer supplemented with 9 μM tubulin mixture of unlabeled tubulin, Rhodamine labeled tubulin and biotinylated tubulin (86:7:7), 4 mM $MgCl_2$, 0.5 mM GTP, and 10 μM Taxol in 10 μL of BRB80 buffer was incubated at 37°C for 3 h; microtubules were then diluted and stabilized in 100 μL of BRB80 buffer supplemented with 10 μM Taxol. The microtubule solution was then pipette up and down to shorten the microtubules to the proper length.

Neutravidin conjugationof gold nanorods.

1 mL of 25 nm × 73 nm gold nanorod solution was centrifuged and resuspended in Millli-Q water twice to remove most of the CTAB. The gold nanorod solution was then reacted with 20 mM NHS-PEG-Thiol (M.W. 119.26, Sigma-Aldrich # 671630, St. Louis, MO) for 1.5 hrs. After that, the gold nanorod was centrifuged and resuspended in Millli-Q water again to remove excess NHS-PEG-Thiol. After that, 40 μL of 1mg/mL Neutravidin in pH 7.4 PBS (Phosphate Buffer Saline) buffer was added to the gold nanorod solution and let react for 3 hrs. The gold nanorods were then centrifuged and resuspended in Millli-Q water and

ready to use.

Calculation of the number of neutravidin-biotin ligands between the gold nanorods and the microtubules.

The labeling stoichiometry of biotin-tubulin was determined to be approximately one biotin per tubulin heterodimer by the manufacturer (Cytoskeleton). The percentage of the biotin-tagged tubulin in the tubulin mixture is 7%. The size of the tubulin heterodimer is 8 nm^3. Assuming the nanorod binds to the microtubule by 2 tubulin units in the transverse direction of each protofilament and bind to the microtubule via 3 protofilaments, for the AuNR with a length of 73 nm, the number of binding sites when it's parallel with the microtubule is 73 nm /8 nm $\times 2 \times 3 \times$ 7% $\approx$ 4.When the nanorod is perpendicular to the microtubule, the number of binding sites would be 25 nm /8 nm $\times 2 \times 3 \times$ 7% $\approx$ 1.

Figures

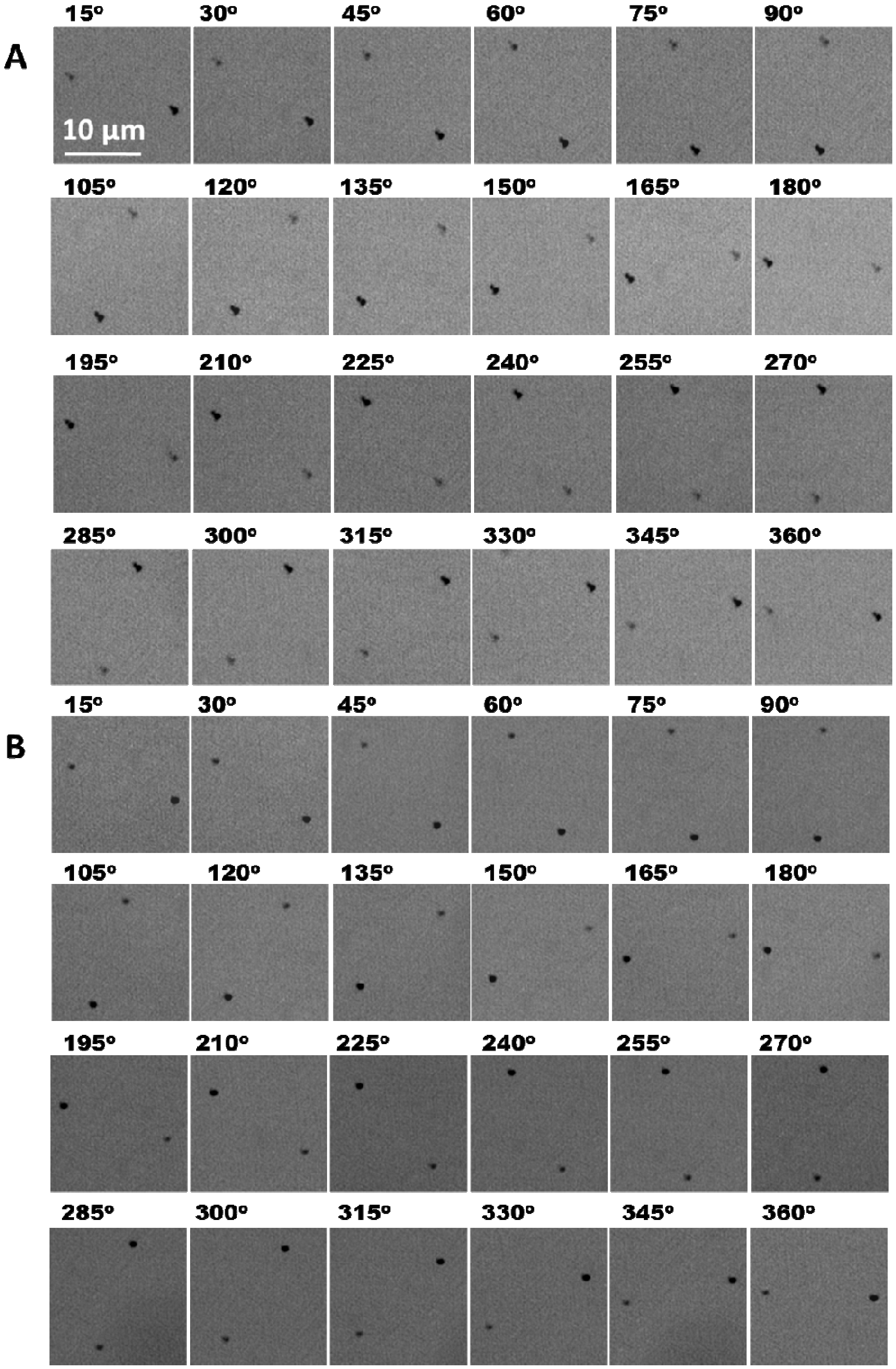

Supplementary Figure 7.1. Bright-field images of a gold nanorod and a 200-nm polystyrene bead captured by the dual-modality microscope equipped with (A) a pair of Nomarski prismsthat generates a larger shear distance or (B) a pair of Nomarski prisms that generates a smaller shear distance. The second polarizeris removed from the light path for the double-Gaussian method. The sample was rotated for 360° with 15° steps.

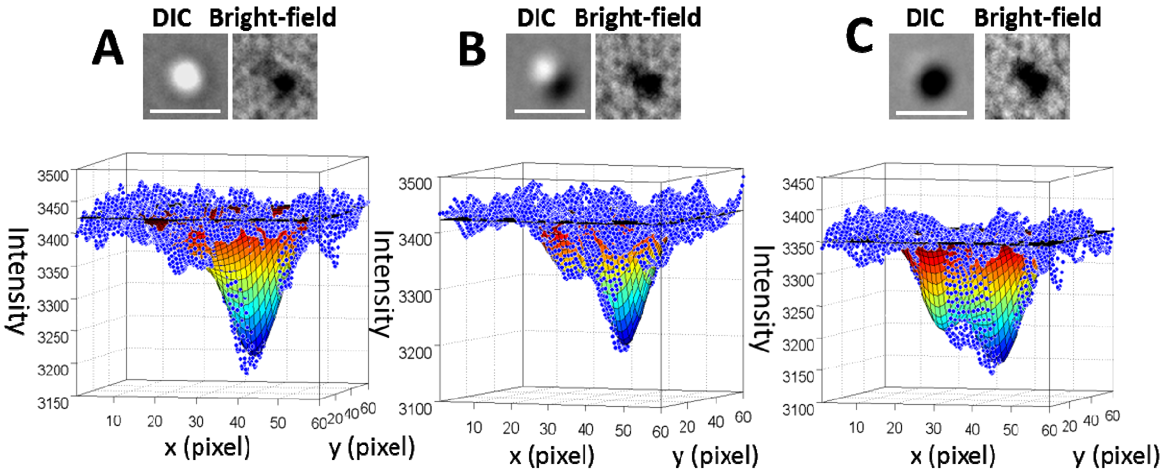

Supplementary Figure 7.2. DIC and bright-field images and the 2D double-peak Gaussian fitting of a 25 nm × 73 nm gold nanorod at three different orientations, where the DIC patterns (left) are bright (A), grey (B),and dark (C), respectively.

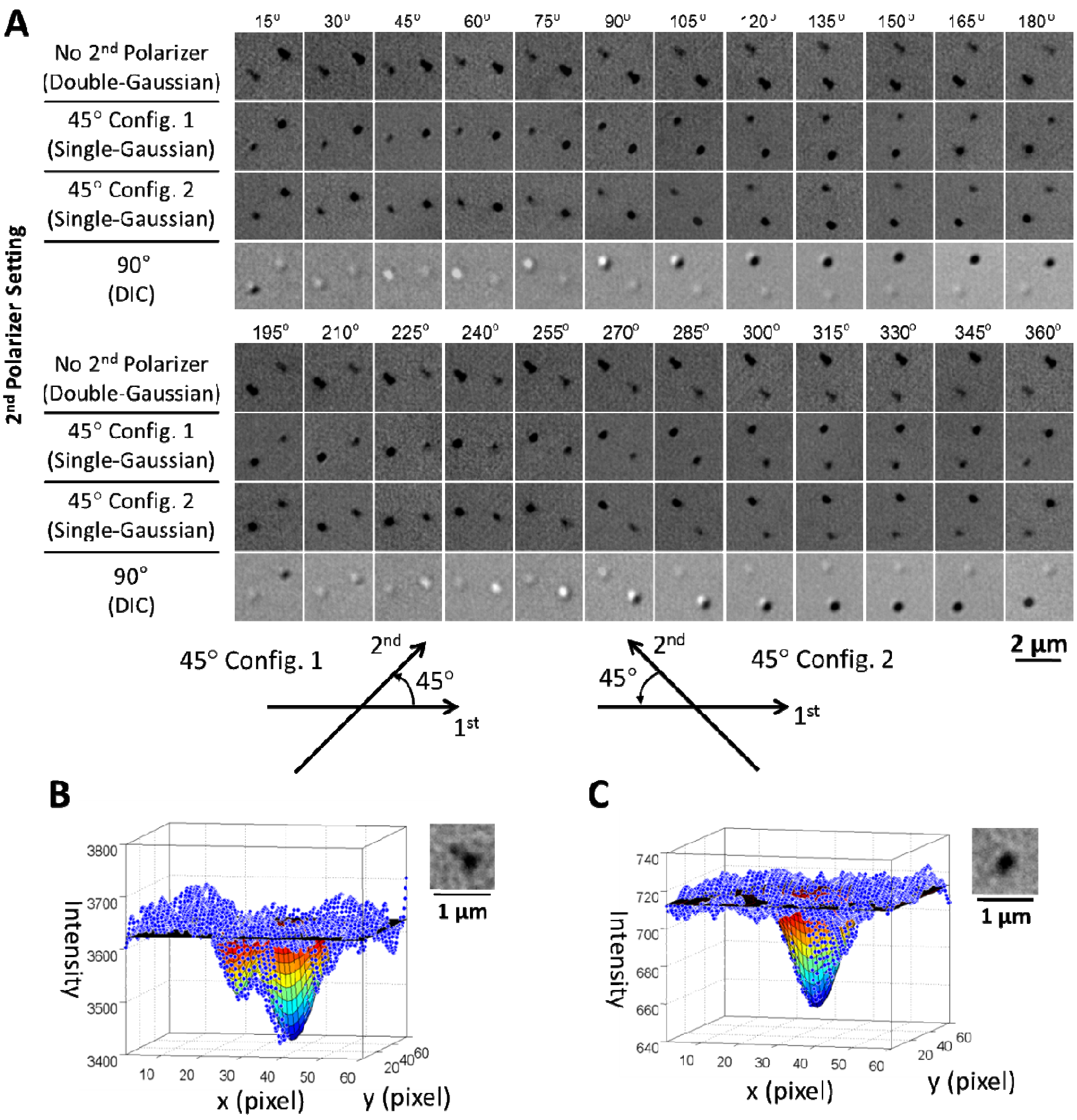

Supplementary Figure 7.3. Comparison of the double-Gaussian and single-Gaussian methods.

(**A**) The bright-fieldand DIC imagesof a gold nanorod and a 200-nm polystyrene particle at different orientations. From top to bottom: the double-Gaussian configuration without the second polarizer, **two** single-Gaussian configurations withthe second polarizer set at 45°, and the Nomarski DIC configuration with the second polarizer at 90° with respect to the first polarizer. The sample slide was rotated from 0-360° at an interval of 15°. The two 45° polarization configurations do not result in the same contrast due to the intentionally introduced bias retardation. Under our microscope settings, Configuration 1 is preferred for its offering of higher contrast. (**B**) The bright-field image without a polarizer and its double-peak Gaussian fitting. (**C**) The bright-field image with a polarizer set at 45° and its single-peak Gaussian fitting.

The distances between the two particles measured at all orientation angles using the double-Gaussian (the "No 2nd Polarizer" row) and the single-Gaussian (the "45°Config. 1" row) methods are 1595 ± 10 nm and 1590 ± 10 nm, respectively. The difference between the two sets of measured distances is showed to be statistically insignificant at the 95% confidence level by Student's t-test. The standard deviation of the distances measured at the same orientation is 3-6 nm for both the double-Gaussian and single-Gaussian methods.

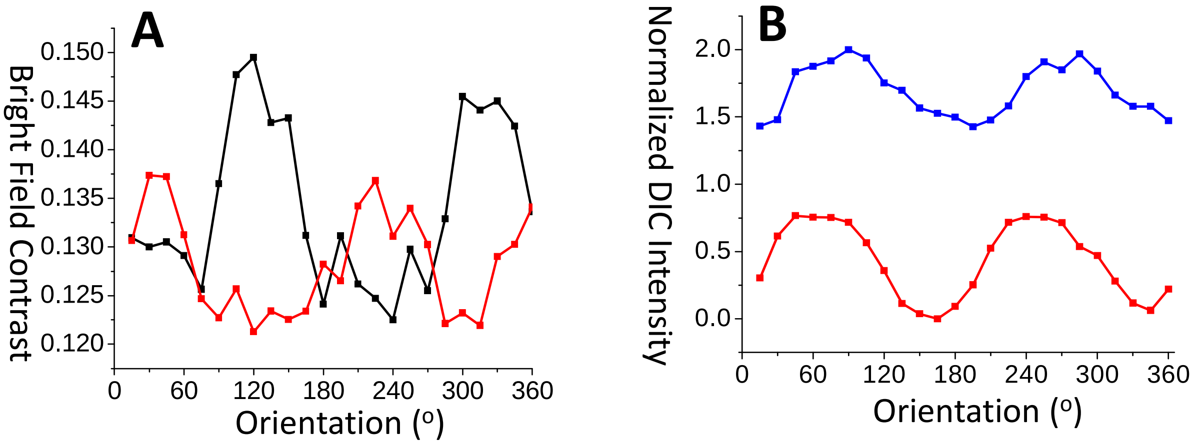

Supplementary Figure 7.4.(**A**) The contrast of the modified bright field images of the gold nanorod captured with the analyzer at two 45^{o}configurations (black – Config. 1; red – Config. 2). (**B**) Normalized DICintensities of the gold nanorod at different orientations.

Note that the contrast of the modified bright field images when the analyzer is placed at 45^{o} is generally larger than that when the analyzer is placed at 135^{o}.The reason accounting for such phenomenon is that the ordinary (o) beam and extraordinary (e) beam generated by the Nomarski prism own a bias because of the quarter wave plate (QWP). For a de Sénarmont type Nomarski DIC microscope, the QWP introduced the phase retardation of the beams. The fast axis of the QWP is aligned at 90^{o} to the transmission axis of the analyzer. In practice, the QWP is also orientated at an orientation in order to get the best DIC contrast. According to the Nikon manufacturer's website, the bias retardation introduced by the QWP causes a change in path length, also causes the unevenness of the o beam and e beam. The same thing happens for the older types of the DIC microscopes when one Nomarski prism is translated laterally with respect to the other. Detailed discussion of how the QWP and polarizer settings affect the imaging of the de Sénarmont type Nomarski DIC microscope can be found in our recent paper.[4]

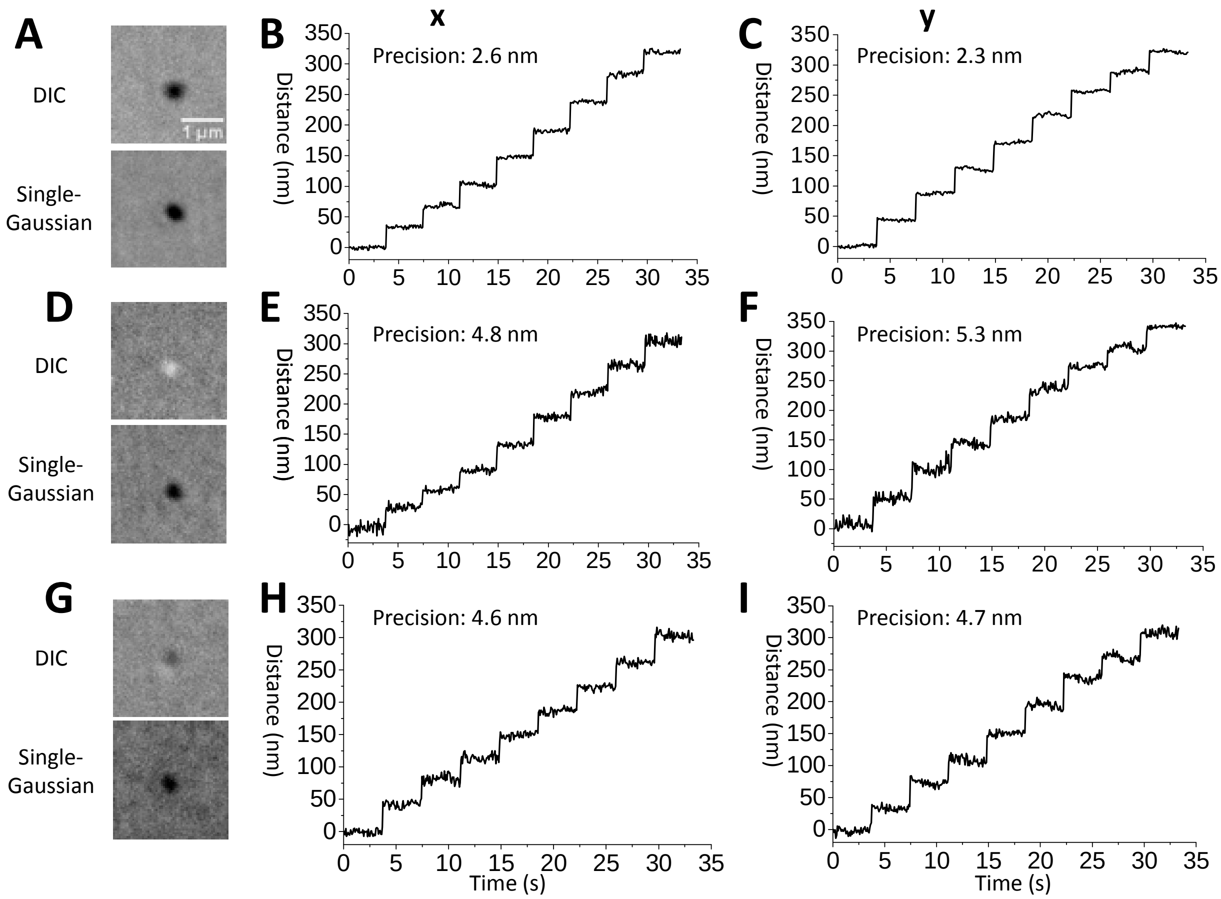

Supplementary Figure 7.5. Super-localization of three gold nanorods on a piezo-electric translational stagetaking 40 nm steps in the *x* or *y* direction. The three nanorods are in different orientations because their DIC images show different contrasts.**(A-C)**A nanorod shows a nearly completely dark DIC image.**(D-F)**A nanorod shows a mostly bright DIC image; **(G-I)**A nanorod shows a half bright/half dark DIC image.

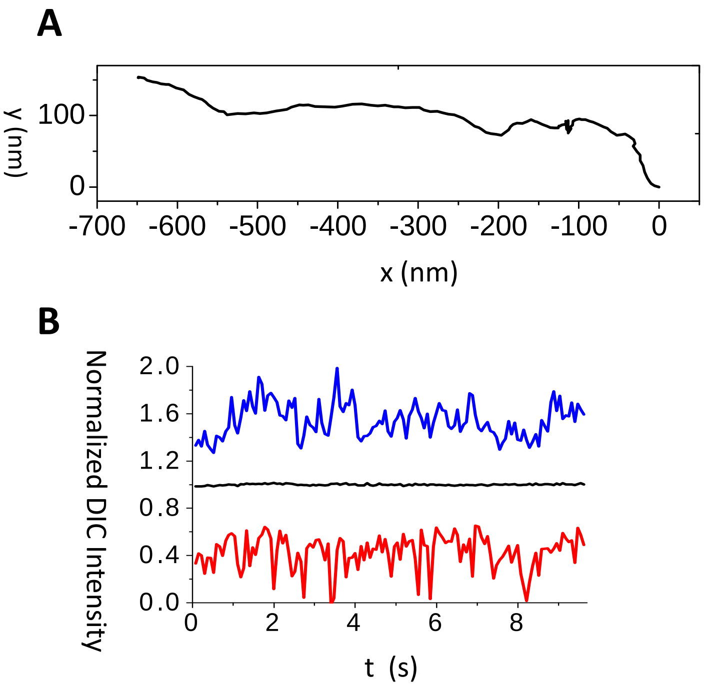

Supplementary Figure 7.6. An example of a loosely-bound gold nanorodtransporting with a microtubule and exhibiting fast, random DIC intensity fluctuations.**(A)**The trajectory of the gold nanorod. **(B)** The corresponding bright (blue) and dark (red) DIC intensities.

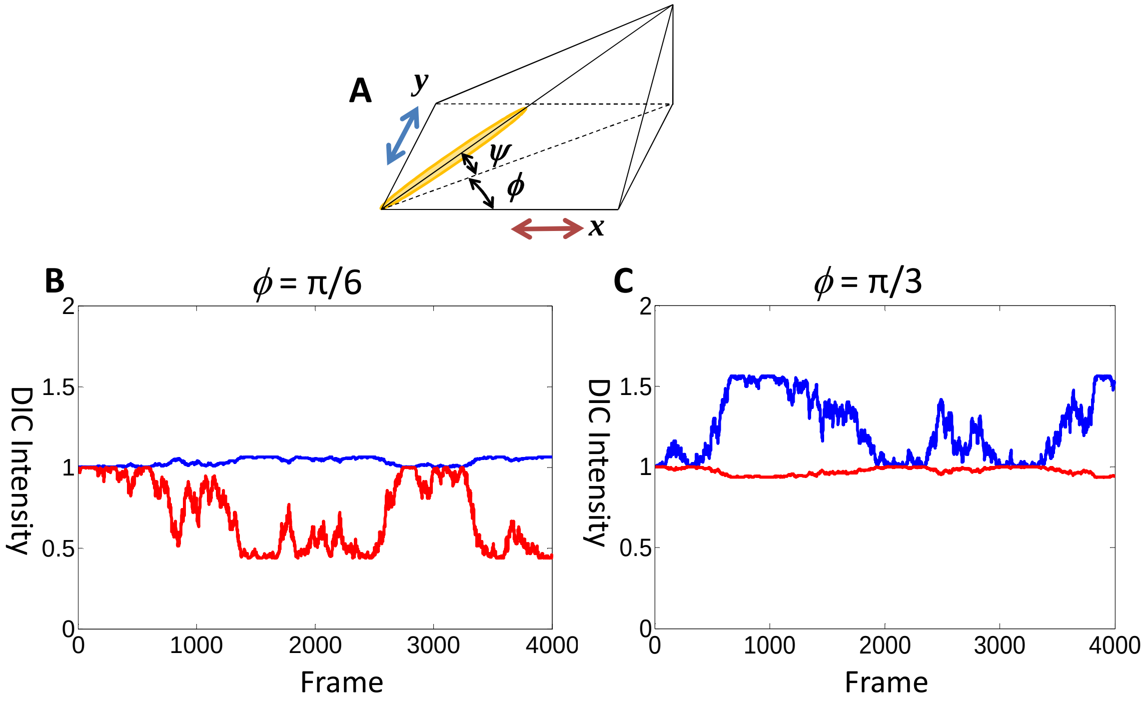

Supplementary Figure 7.7. Simulations of the DIC intensities of a gold nanorod performing out-of-plane wiggling motion with the rotation axis parallel with the imaging plane and perpendicular with the long axis of the nanorod. The nanorod maintains the same azimuthal angle in the simulation. The change of the elevation angle of the nanorod is defined as π /10 per frame, and the wiggling direction is randomized. (**A**) The schematic illustration of a gold nanorod oriented with the elevation angle ψ and the azimuthal angle ϕ. (**B**) Simulated DIC intensities of a gold nanorod performing wiggling motion with an azimuthal angle of π/3. (**C**) Simulated DIC intensities of a gold nanorod performing wiggling motion with an azimuthal angle of π/6.

The DIC intensities are simulated using the equations:

$I_{bright} \approx 1 + \cos^2 \psi \sin^4 \phi$,

$I_{dark} \approx 1 - \cos^2 \psi \cos^4 \phi$.

The wiggling motion is reflected by the DIC intensity pattern that either the bright or the dark intensity fluctuates significantly while the other intensity changes only slightly. These simulated DIC intensity traces are similar to the experimental traces reported in **Figure 7.3** in the main text.

A full discussion on the nanorod’s rotational modes can be found in our recent paper.

References

1. Hancock, W. O.; Howard, J. *J. Cell Biol.* **1998**, *140*, 1395-1405.
2. Wang, G. F.; Sun, W.; Luo, Y.; Fang, N. *J. Am. Chem. Soc.* **2010**, *132*, 16417-16422.
3. Mozziconacci, J.; Sandblad, L.; Wachsmuth, M.; Brunner, D.; Karsenti, E. *Plos One* **2008**,
4. Stender, A. S.; Augspurger, A. E.; Wang, G.; Fang, N. *Anal. Chem.* **2012**, *84*, 5210-5215.
5. Gu, Y.; Sun, W.; Wang, G.; Zimmermann, M.T.; Jernigan, R.L.; Fang, N**.** *Small*, **2012**, in press, DOI: 10.1002/smll.201201808.

CHAPTER 8

GENERAL CONCLUSIONS AND OUTLOOK

8.1 General Conclusions

Equipped with new technical advances and data analysis methods, the DIC-microscopy-based SPORT technique has been applied in biophysical studies to reveal biological processes with unprecedented details.

1) The rotation rate of single gold nanorods is semi-quantified as the characteristic rotation time by fitting the autocorrelation of noisy DIC intensities with the stretched exponential decay function. With this information, we have studied the rotational dynamics of several surface-modified gold nanorods from the first contact with the cell membranes to the point when the nanorods are imbedded and fixed in the cell membranes. The correlations between the rotational dynamics of surface modified gold nanorods and the properties of the surface modifiers are being established.

2) A method to extract rotational mode from the vast DIC intensities of single gold nanorods has been developed by calculating the correlation coefficient of the bright and dark DIC intensities. The gold nanorods are modified with either Tat cell penetrating peptide (CPP) or transferrin. Because of the distinctive properties of the two modifiers, surface-modified gold nanords exhibit different rotational modes at first contact with the live cell membrane.

The calibration of the rotational modes of gold nanorods with various surface modifications have been carried out on synthetic lipid bilayers with different compositions.

3) The temporal resolution of the SPORT technique with DIC microscopy has been improved to 500 frames/s to image fast transport dynamics. Transferrin modified gold nanorods (25 nm × 73 nm) are endocytosed by differentiated PC 12 cells and incorporated in the endosomes during the imaging. The orientation of gold nanorod-containing cargos during the directional intracellular transport is kept generally constant relative to the microtubules track, indicating the tight wrapping of nanoparticles by the endosome vesicles. The rotational motions of cargos during short and long pauses have been captured and analyzed. The correlation analysis of the bright and dark DIC intensities of the nanorods performing rotational motions during the pauses compared with free rotational diffusion indicates that the cargos are still tethered to the microtubule tracks during the pauses. The rotational motion and the transport directions following a pause are also correlated with the pause duration, indicating that some regulatory mechanisms exist in the cargo transport by kinesin and dynein motors.

4) In order to raise the single particle tracking precision with DIC microscopy, a 3D correlation mapping method has been developed to localize gold nanospheres. The optimized experimental conditions allow the 3D localization of 40-nm gold nanoparticles with a precision of 4-7 nm laterally and 16 nm axially. The technique has been applied in localizing

the 3D position of a single transferrin-modified 40-nm gold nanosphere during the uptake process by a lung cancer cell.

5) The complicated orientation-dependent DIC PSF makes it difficult to localize gold nanorods with high accuracy under a DIC microscope. A dual-mode microscope that combines bright-field and DIC imaging techniques has been devised to simultaneously super-localize gold nanorods while obtaining their orientation and rotational information simultaneously. This technique has been applied to study steric hindrance affecting the transport of relateive large cargos by motor proteins.

8.2 Outlook

The SPORT techniques are emerging promising tools in biophysical studies to disclose many biological functions in unprecedented detail. A number of key improvements are still necessary in order to fully realize the potential of SPORT. First, dynamic tracking in the axial direction remains challenging and the axial localization precision is still more than an order of magnitude worse than the lateral precision. As such, it is necessary to develop new SPORT techniques that provide accurate measurements of both 3D position and orientation of rotational probes. Second, the temporal resolution of SPORT is usually much worse than the conventional SPT, as a larger number of photons need to be collected in order to resolve the orientation. Faster image rates and innovative data analysis methods are desirable to elucidate fast rotational motions encountered in live biological systems. The current state-of-the-art

SPORT techniques are mainly applicable to study rotational probes that are restrained by certain factors, such as being tethered to membrane receptors or encapsulated inside small compartments.

Most of the current biophysical studies using SPORT are technical demonstrations or reports of direct observations of rotational motions. Future SPORT studies should be focused on elucidating the underlying mechanisms that govern the observed rotational motions. The arguably most important topic of SPORT is nanoparticle-based drug delivery. Functionalized nanoparticles can be fashioned as model systems to allow the studies on the detailed mechanisms of membrane diffusion/interactions, internalization, targeted delivery to the diseased organ, controlled drug release, and nanotoxicity.

Finally, live rotational motions captured by SPORT provide a significant new dimensionality to the computational efforts. As the translational freedom does not necessarily correlate directly with the rotational freedom, the new dimension in experimental and simulated data will provide a more accurate interpretation of the influences of individual factors.